5-2024

Development and evaluation of a modeling platform for evaluating immunotherapeutic efficacy in the tumor microenvironment.

Dylan Andrew Goodin

DEVELOPMENT AND EVALUATION OF A MODELING PLATFORM FOR
EVALUATING IMMUNOTHERAPEUTIC EFFICACY IN THE TUMOR
MICROENVIRONMENT

By

Dylan Andrew Goodin

B.S., University of Louisville, 2018

M.Eng., University of Louisville, 2019

A Dissertation

Submitted to the Graduate School

At the University of Louisville,

In Partial Fulfillment of the Requirements

For the Degree of

Doctor of Philosophy in Interdisciplinary Studies,

Specialization in Translational Bioengineering

Interdisciplinary Studies

University of Louisville

Louisville, KY

May 2024

DEVELOPMENT AND EVALUATION OF A MODELING PLATFORM FOR
EVALUATING IMMUNOTHERAPEUTIC EFFICACY IN THE TUMOR
MICROENVIRONMENT

By

Dylan Andrew Goodin
B.S., University of Louisville, 2018
M.Eng., University of Louisville, 2019

A Dissertation Approved on

March 29th, 2024

By the following Dissertation Committee:

_____
Hermann Frieboes, Ph.D.

_____
Ayman El-Baz, Ph.D.

_____
Nihat Altiparmak, Ph.D.

_____
Joseph Chen, Ph.D.

_____
Joshua Hood, M.D., Ph.D.

DEDICATION

To El Roi

ABSTRACT

DEVELOPMENT AND EVALUATION OF A MODELING PLATFORM FOR
EVALUATING IMMUNOTHERAPEUTIC EFFICACY IN THE TUMOR
MICROENVIRONMENT

Dylan A. Goodin

March 29th 2024

The tumor microenvironment (TME) represents the complex outcome of numerous

tumor, stromal, and immune interactions, and whose composition can significantly affect

treatment response. Particularly, immunotherapeutic efficacy is subject to multiple tumor-

specific TME interactions that may be difficult to evaluate/predict clinically.

Mathematical modelling has been formulated to evaluate specific aspects of the TME,

including vasculature, ECM deposition, and immune-tumor interactions. However, the

computational challenge of simulating multiple TME interactions has led to sacrificing

varying degrees of model generalizability and clinical relevance. This work describes

increased computational performance of a 3D continuum model that simulates tumor

tissue, ECM, and vasculature using a Message Passing Interface (MPI) CUDA-

accelerated framework (Chapter 2) and expanding biological scope to include TME

immune interactions (Chapter 3). Model performance is scaled to 2.56x2.56x2.56 cm^3 domain sizes while preserving mm-resolution interactions. The model's host tissue phase is expanded to include an immune component. This component includes multiple innate and adaptive immune species whose local activation influences the TME into varying degrees of pro- or anti-tumor states. This model is applied to simulate the effect of a macrophage-mediated immunotherapeutic regimen against multiple breast cancer liver metastases (BCLM) simultaneously in a simulated mouse liver lobe (Chapter 4). The model results indicate that tumor burden could be potentially curbed with treatment intervals lasting less than 7 days. The effects of anti-Programmed Death Ligand 1 and antigen-loaded chitosan nanoparticle immunotherapies were quantified against primary and liver-metastatic pancreatic ductal adenocarcinoma (PDAC), finding that applying both therapies simultaneously may synergistically decrease tumor burden (Chapter 5). Lastly, as a first step towards evaluating the patient-specific TME immune landscape for BCLM, a machine learning workflow is presented that classifies expression of BCLM imaging mass cytometry (IMC) data from paired primary IMC data, with validation subset AUROC $\geq$0.75. Longer-term, this overall work could be applied across a broad spectrum of tumor types and therapeutic approaches to identify optimal strategies tailored to specific tumors. Chapter 2 is published in *Computers in Biology and Medicine*. Chapter 3 is published in the *Journal of Theoretical Biology*. Chapter 4 is published in *Immunology*. Chapters 5 and 6 are in preparation for submission.

TABLE OF CONTENTS

LIST OF TABLES

LIST OF FIGURES

CHAPTER 1: INTRODUCTION

Metastatic formation is a hallmark of advanced staged cancers that can carry 5-year survival rates ~25% or lower [1-6]. The liver is a common site for metastatic formation, being diagnosed at breast cancer diagnosis in up to 25% of cases [2, 5, 7-9], and present in nearly 80% of pancreatic ductal adenocarcinoma (PDAC) patient autopsies [10]. Further, 47% of PDAC patients are diagnosed at stage IV and have a 5-year survival rate of <5% [5]. Breast cancer liver metastases (BCLM) are poor, with a 5-year survival rate of ~20%, and a median survival <28 months [2-4]. Thus, there is a critical need for developing treatment strategies that are effective at both primary and metastatic sites.

The tumor microenvironment (TME) is a major contributor to reduced patient survival, hosting a complex array of interactions between the tumor, extracellular matrix, vasculature within the extracellular matrix, and innate and adaptive immune species, which poses a challenge to successful therapy [11-25]. Primary PDAC lesions, exhibit desmoplastic growth characterized by a high stromal concentration that lowers immune species penetration [14-16] and sparser vascularization that reduces availability of systemically administered chemotherapeutics [16, 21-23, 25]. Breast cancer liver metastases (BCLM) preserve normal stromal concentration [26] and are avascular [17], creating physiological drug resistance [11-13].

Immunotherapies have shown promise in treating a variety of cancer types by exploiting various events in the TME [27-31]. Cytokines can be administered to promote an unspecific immune response and have seen success in treating metastatic renal cell carcinoma [32, 33] and metastatic melanoma [34, 35]. Adoptive cell therapy involves training immune species, such as cancer-infiltrating lymphocytes, to eliminate tumor burden [36]. Antibody therapies promote an anti-tumor immune response, such as Trastuzumab to treat human epidermal growth factor receptor 2 (HER2) positive breast cancer [37, 38]. Immune checkpoint inhibitors target pathways that regulate immune response, such as Ipilimumab (anti Cytotoxic T-lymphocyte associated protein 4 [CTLA-4]) to treat metastatic melanoma [39] or Tremeliumab (anti-CDLA-4) with Durvalumab (anti Programmed Death Ligand 1 [PD-L1]) in a STRIDE (Single Trmelimumab Regular Interval Durvalumab) regimen to treat hepatocellular carcinoma [40]. Cancer vaccines, such as Sipuleucel-T to treat minimally symptomatic metastatic castration-resistant prostate cancer [41, 42], aim to promote an adaptive immune system response using antigen-presenting cells [43]. Oncolytic viruses, such as Nadofaragene firadenovec in bacillus Calmette-Guerin (BCG) unresponsive non-muscle invasive bladder cancer [44], selectively infect and lyse tumor cells and can invoke both innate and adaptive immune responses [45]. Thus, the difficulty of improving cancer prognosis across a diverse set of TME pathophysiologies has been targeted with a plethora of immunotherapeutic approaches that often rely on interactions within the TME.

However, despite continued progress in immunotherapeutic development, the TME remains an obstacle to successful therapies for many cancer types. Cytotoxic T-cells (CTL), a common cell species targeted by immunotherapy [46-50], can be hampered by PD-L1 expression in the TME [51-53] which promotes CTL exhaustion, a condition noted for reduced CTL cytotoxicity [54-56]. However, a recent clinical trial observed that an immunotherapeutic strategy targeting PD-L1, Tremelimumab and Durvalumab in a STRIDE regimen, was ineffective in treating metastatic PDAC [24]. A recent proposal for BCLM treatment entailed nanoalbumin-bound paclitaxel (nab-PTX) encapsulated in porous silicon multistage nanovector vehicles (MSV) taken up by macrophages in the BCLM TME [57-60]. These macrophages remain within the vicinity of the tumor, releasing the nab-PTX and increasing cytotoxicity. This approach has shown promise *in vitro* [57, 59, 60] and *in vivo* [58].

Evaluating tumor response to current immunotherapy strategies necessitates a comprehensive evaluation of the affinity of a particular cancer's TME to a specific treatment regimen. Given the complex nature that the TME presents to predicting treatment response, a critical need has emerged to complement *in vitro* and *in vivo* studies with a systems-level analysis in which patient-specific tumors and the corresponding TME may be repeatedly and consistently evaluated in a low-risk environment to identify promising candidate therapeutic types and regimens. Furthermore, biopsy and resection of liver metastases are generally discouraged for liver metastases [12, 61-63], making acquisition of patient-specific TME data an ongoing challenge.

Mathematical modelling offers an opportunity to fulfill this role by simulating the interactions between the tumor and the TME [64-71]. Previous work has grown *in silico* tumors to evaluate therapeutic properties to complement *in vitro* and *in vivo* studies [57-60]. A recent model was developed to simulate multiple phenomena in the TME, including subcellular metabolism, discrete tumor, normal, and endothelial cells, diffusion of oxygen, glucose, vascular endothelial growth factor, and therapeutics, and creation and spread of blood vasculature [70]. However, two major hurdles must be overcome for wider use of mathematical models of the TME as a therapeutic platform: (1) evaluating the aggregate effect of immune species interactions and (2) computational performance required to simulate centimeter-scale tumors seen clinically [72, 73] while preserving cell-scale interactions. In response to the former, mathematical models have emphasized specific interactions to make therapeutic predictions, potentially neglecting many immune-tumor interactions in the TME that may affect tumor response [64, 65, 67, 74-79]. For the latter, models that have simulated centimeter domains have either sacrificed model resolution [80] or model complexity [80, 81], depending on the study's objective. Additionally, recent mathematical models that simulate an increasing number of TME interactions have been limited to millimeter-scale volumes [70, 71]. Thus, evaluating immunotherapeutic efficacy on patient specific tumors, both primary and metastatic, by simulating TME interactions necessitates a cm-scale simulation that acknowledges cell-scale (sub-millimeter resolution) interactions and is informed by TME composition.

Previously, a 3D model of the TME was developed to simulate tumor and ECM interactions [82, 83]. This model includes tumor growth, oxygen and glucose release

4

from vasculature and carbon dioxide and lactic acid release from tumor tissue, solid pressure gradients that influence said growth, ECM production by myofibroblasts and degradation by matrix degrading enzymes, angiogenesis in response to release of tumor angiogenic factors by the tumor, and release of tumor growth factors. However, the model did not simulate immune species, and its computation time hindered applicability, being limited to sub-centimeter domain sizes. Ideally, improving model performance while including immune interactions would make this model applicable to immunotherapeutic evaluation.

Here, the journey of increasing 3D model performance, laying a foundation for assessment of TME interactions and evaluating tumor response to novel immunotherapies, is documented. Chapter 2 of this dissertation describes the implementation of a Message Passing Interface (MPI) framework that interfaces with Compute Unified Device Architecture (CUDA)-capable graphics processing units (GPUs) to increase model performance. Chapter 3 describes the addition of an immune species component to the model, including monocytes, macrophages, neutrophils, natural killer cells, dendritic cells, helper and cytotoxic T-cells, B-cells, and myeloid derived suppressor cells (MDSC), as well as local immune-immune, immune-tumor, and immune-ECM interactions. This model is then extended to simulate treatment of multiple breast cancer liver metastases via nanotherapy in an *in silico* mouse liver lobe in Chapter 4. The 3D model is used to simulate treatment of a cm-scale PDAC and a mm-scale PDAC liver metastasis using anti-PDL1 therapeutic and antigen-loaded chitosan nanoparticles (CNP) in Chapter 5. Finally, as a first step to creating a platform to inform

simulations of immunotherapies of BCLM with patient-specific TME data, Chapter 6

documents the development of a machine learning workflow that predicts patient BCLM

TME from paired primary tumor breast data.

CHAPTER 2: SIMULATION OF 3D CENTIMETER-SCALE CONTINUUM TUMOR

GROWTH AT SUB-MILLIMETER RESOLUTION VIA DISTRIBUTED

COMPUTING[1]

2.2 Introduction

Representation of tumor growth in clinically-relevant contexts has generally been

explored via three main types of models: continuum models that simulate tissue-scale

behavior, discrete models that define individual cells and their interactions, and hybrid

models utilizing a combination of both approaches. These efforts have been traditionally

constrained by the computational cost to numerically solve the associated equations, with

the results limited to representing mm-sized or smaller tumors. For discrete models the

challenge has been to simulate billions of cells and their interactions, while for continuum

models the cost of representing cm-scale domains becomes computationally prohibitive.

In particular, models based on continuum mixture theory to simulate tumor growth have

been developed [84-88] and analyzed [89-91], building upon earlier work to represent

tumor tissue as different phases of a mixture [92-112]. However, more complex

continuum models have struggled to achieve high performance simulations at patient-

scale (cm) resolution.

Lorenzo et al. used a continuum two-phase model to simulate a prostate tumor with 2.66 cm^3 volume from CT-scan [81]. Antonopoulos et al represented a 4.2 x 4.2 x 4.2 cm^3 domain for 3 simulated months with 2.2 mm^3 resolution [80]. While both models reached cm scale, multispecies representation and vascularization were not incorporated. Wise et al. developed an adaptive multigrid framework for simulating a continuum multispecies tumor model using a single-core computer process, finding that time required to simulate a single day of tumor evolution at $1*10^{-2}$ days per time step increases from ~12 min during early time steps to ~400 min by end of simulation [113]. In [66] the model of [84] was coupled with a lattice-free random walk angiogenesis model [114-117]. Recently, a mixture model with continuum 3D representation of tumor, vasculature, and extracellular matrix (ECM) was presented in [118, 119]. Open Multi-Processing (OpenMP) parallelization benefits were offset in [118] by increased model complexity: early model performance was 156 min per simulated day to ~280 min per simulated day for $1*10^{-2}$ days per time step. In these models, coupling of tumor and vasculature in a biologically realistic 3D representation to simulate clinically-relevant tumor growth incurs a high computational cost. Consequently, the numerical implementation to solve the coupled equations has hindered these models from reaching practical application, especially in terms of simulating patient tumor response to potential courses of treatment in a timely manner to drive clinical decision-making.

Outside of the context of continuum models, several parallelized implementations have been developed over the past decade to improve performance. In [120], a tumor

model parallelization saw a 5.2x performance increase over a single-process approach using eight processors. OpenMP implementations have improved tumor modeling performance, as shown in [121, 122]. An early effort at parallelizing a Cellular Potts model used Message Passing Interface (MPI) but remained a 2D simulation [123]. Models have benefitted from multiple approaches, including an MPI-based parallel solver named NAStJA [124-126] and Compute Unified Device Architecture (CUDA) based solvers [127, 128]. A near 30x uplift over CPU-based implementations using a CUDA-based solver was seen in [127]. Likewise, cellular automata tumor modeling has benefited from CUDA and CPU-based parallelization approaches [129-131]. A tumor simulation using finite element methods leveraged an MPI framework to attain ~4x performance improvement by spanning the simulation across 16 processes [132]. Performance gains for a finite-element method were also realized using Galois, a software package that employs an amorphous data-parallelism model [133]. Recently, a hybrid model was parallelized using the framework to simulate ~1 cm^3 melanoma evolution [134]. Of note, Antonopoulos et al.'s continuum model in MATLAB emphasized macroscopic tumor phenomena, simulating a cubic 4.2 cm length domain at 2 mm^3 resolution. By simulating fewer equations at a lower resolution than in [118], the model was capable of simulating ~3 months of tumor evolution in 10-12min [80].

Complementing these previous efforts, this study presents a distributed computing implementation of the mixture model in [118, 119] via a combined MPI-CUDA implementation to simulate cm-scale vascularized 3D tumor growth tissue at sub-millimeter resolution.

2.2 Materials and Methods

2.2.1 Model of Tumor Growth

We fully parallelize the continuum 3D model presented in [118, 119], which used openMP. Briefly, the model simulates evolution of a single tumor cell phenotype in an environment with host cells and ECM. Tumor tissue vies for resources against healthy tissue while balancing the need for nutrients, metabolites, and ionic species, including oxygen, carbon dioxide, lactate, bicarbonate, sodium ions, chloride, and H^+ ions. Crowding in a limited tissue space is abstracted into solid mass pressure and pressure from surrounding fluids. These pressures drive velocity in the solid tissue mass and create buildup of elastic energy on the surrounding ECM. Matrix degrading enzymes and myofibroblast concentrations increase due to remodeling of surrounding ECM to compensate for strain induced by tumor growth.

During tumor growth, tissue distal from vasculature can be deprived of resources. The tumor releases angiogenic factors to encourage growth of surrounding vasculature towards hypoxic tissue. Increased vessel leakiness has been well-documented from such relatively quick vasculature changes; the body compensates for edema by increasing lymphatic growth [135]. Therefore, the model simulates lymphatic growth with independent terms to the vasculature, although both are closely related mathematically and physiologically. However, vasculature effectiveness is limited physiologically by the diffusion rate of oxygen. Thus, interior hypoxic regions in sufficiently large tumors will operate at varying levels of anaerobic glycolysis, building up lactic acid. In a sufficiently

hypoxic state, tumor cells become apoptotic or necrotic, represented as dead cell volume fraction.

Numerically, this model is solved using a geometric multigrid solver. At its finest multigrid level, the solver uses evenly-spaced points to define model solution resolution. By increasing the number of points per side of the cubic domain and using a point-to-point distance <100 μm, sub-mm precision is retained while increasing the domain size beyond a centimeter on a side. At each point on a cubic domain, a solution for model variables is generated, with solution generation occurring after θ units of simulated time elapse. Key equations in non-dimensionalized form and the numerical solver are summarized further in **Supplementary Material**.

2.2.2 Limitations of openMP-based solver

Three limitations of openMP-based solver in [118, 119] include:

1. When tested using 128^3 grids, maximum performance was obtained using only 8 cores out of 32 on a 32-core processor on the University of Louisville Cardinal Research Cluster (CRC), potentially due to insufficient memory bandwidth. Further testing on an AMD 2990WX exhibited more promising results, indicating that nascent CPUs may fare better from openMP. However, limitations to core counts would further constrain gains.

2. openMP is a shared-memory architecture that runs on non-distributed systems, limiting performance gains to a single PC, workstation, or High Performance Computing (HPC) node.

3. Many PCs have insufficient RAM to hold larger tumor model spaces. **Table 1** summarizes expected RAM footprint for varying model sizes.

	Level Size	
	256^3	512^3
Points on a Side	130	258
Maximum Level size Simulated (#Points on a side)	256	512
Upper Bound RAM Required per process with eight processes on the finest level with an equal distribution of level data (GB)	3.3	25.5
Total RAM Required for single process on the finest level (GB)	13.6	107.6
Maximum spherical tumor diameter that could be simulated with 50 µm point resolution (mm)	12.8	25.6

Table 1 Memory footprint for varying model sizes using model in [118, 119].

2.2.3 Distributed computing solution

To simulate tumors at patient tissue cm-scales, model in [118, 119] requires sufficient computational resources to function at a 512^3 sized domain and, according to **Table 1**, over 100GB RAM are necessary. Because single-socket computers do not typically possess this much RAM, a new solution generator is required for long-term parallel computing.

For this purpose, this study implements the numerical solving scheme of [119] using a two-stage parallelization framework. First, numerical computations were rewritten for GPU computation using CUDA. This framework handles all Multigrid-related computations, including Gauss-Seidel red-black smoothing, restriction, prolongation, and error correction. MPI handles distribution of information across multiple processes, freeing the program from the RAM and processing limitations found on single-system parallelization frameworks. On each system, Nvidia's CUDA library

allows for faster processing of model data using GPU-bound computing on fewer systems. Thus, the new model framework is a two-part MPI-CUDA model.

The type of simulation being considered, generally known as HPC, requires consistent communication between multiple data processors Architectures configured for Big Data, in which data processors are designed to perform tasks at a coarser resolution, are unideal for datapoint-level communication [136]. Further, common Big Data platforms, such as Hadoop and Apache Spark, rely on either disk-based queries or exhibit possess significantly more overhead than comparable MPI-based HPC implementations, respectively, making MPI a more viable distributed computing framework for our purposes [136-139].

Overall algorithm in MPI-CUDA tumor model is identical to model in [118, 119], save that the conditions for block generation have changed. Under the previous framework efficiency was defined as $\eta = \frac{\#Points\ in\ F_{\ell+1}^{t,r-1}}{\#Points\ in\ B_{\ell+1}}$ where the set of all flagged points in level ℓ at time step t and solver iteration $r-1$ is represented as $F_{\ell}^{t,r-1}$ and the set of all points within blocks in level ℓ is represented by B_{ℓ}. To prolongate to a new level, η had to be lower than a pre-defined cutoff efficiency. In the new framework, the decision process is simplified to an all-or-nothing behavior where a single flagged point on ℓ will cause the solver to operate over the entirety of the domain on level $\ell + 1$ (i.e., $\Omega_{\ell+1}$). This behavior can be interpreted as creating a block $B_{\ell+1}$ whose size is determined by prolongating block $B_{\ell} = \Omega_{\ell}$ using the prolongation operator function $P_{\ell+1}^{\ell}(X_{\ell})$ for some set of points X on ℓ. This decision can be summarized as $F_{\ell}^{t,r-1} \neq \emptyset \Rightarrow B_{\ell+1} =$

$P_{\ell+1}^{\ell}(B_\ell) = \Omega_{\ell+1}$. Memory management is thus greatly simplified, since the solver either finishes at level ℓ or processes level ℓ for a given time step. Consequently, this decision also increases workload on levels where only a subset of Ω_ℓ requires smoothing.

While this method simplifies memory management, it can sacrifice solution accuracy. Residual error is calculated as:

$$\left\| R_\ell - L_\ell(\psi_\ell^{t,r}) \right\|_{B_\ell} = \sqrt{\frac{1}{|B_\ell|} \cdot \sum_{p \in B_\ell} \sum_{v \in V} (R_{p,v} - L_{p,v})^2} \qquad \text{Equation 2.2.1}$$

where RHS and LHS solutions are $R_{p,v}$ and $L_{p,v}$, respectively, for all points p in block $B_{\ell+1}$ and variables v in the set of all tumor model variables V. R_ℓ, L_ℓ, and $\psi_\ell^{t,r}$ are defined in **2.5 Supplementary Material**. When size of $B_{\ell+1}$ is not fit to the flagged points, sensitivity to local error is decreased. Thus, model error will be artificially high. This was corrected by redefining p to fit the set of all flagged point $F_\ell^{t,r-1}$:

$$\left\| R_\ell - L_\ell(\psi_\ell^{t,r}) \right\|_{F_\ell^{t,r-1}} = \sqrt{\frac{1}{|F_\ell^{t,r-1}|} \cdot \sum_{p \in F_\ell} \sum_{v \in V} (R_{p,v} - L_{p,v})^2} \qquad \text{Equation 2.2.2}$$

This method allows for easy memory transfers from CPU to GPU while retaining solution accuracy.

2.2.4 Model architecture

Flow of information during execution differs from the previous architecture. MPI implementation has two classes of processes:

1. Administrative process (AdP). Responsibilities include construction of model domain and decisions pertaining to solution convergence. There is only one process designated as AdP within MPI-CUDA runtime.

2. General Computation Process (GCP). GCPs take up a non-overlapping cubic region in Ω. Each can operate on more than one level as designated by AdP at start of model execution.

Algorithm 1 summarizes the process for any computation function X that is neither restriction nor prolongation. Before synchronization, each GCP must unload its corresponding GPU P_m containing unsynchronized data before executing X on GPU P_n. Preceding execution of function X on level ℓ, all data across GCPs is synchronized to avoid race conditions. Of note, in Algorithm 1 the binding rules for GPUs P_m and P_n are left to the implementer. Ideally, processes are bound in a non-overlapping fashion to a single GPU. That is, two GCPs g and h are the same if and only if $m_g = n_g = m_h = n_h$, but hardware limitations may require an overlapping allocation in which multiple MPI processes share GPU resources.

Algorithm 2.2.1– Run function X on GCP g on level ℓ.

RunFunction(X, g, ℓ, m, n)   {

Select GPU P_m

If GPU P_m contains unloaded data addressed to GCP g {
          Unload Ω_ℓ data from P_m
          Synchronize Ω_ℓ with all GCPs on level ℓ
     }

Select GPU P_n

Load level ℓ data associated with GCP g onto GPU P_n

Run X on P_n

}

Processes are applied to level ℓ sequentially filling a single region of the model in a manner depicted by **Figure 1**, in which level ℓ, level $\ell + 1$, and level $\ell + 2$ operate over the same domain object, represented by the triangle. Level ℓ contains a single process. Adapting a method of hierarchical process filling proposed by [140], on level $\ell + 1$ three additional processes are required to process level $\ell + 1$. All four processes, including region 1 on level $\ell + 1$, restrict to region 1. Same relationship exists between levels $\ell + 2$ and $\ell + 1$. One-eighth of domain covered by a single GCP unit in level ℓ is retained locally while other 7 parts of $\Omega_{\ell+1}$ are sent to seven other GCPs. Thus, amount of work increases linearly with number of levels, since processes on each level after and including level ℓ have same domain size [140]. This also means that each GCP on a previous level must operate on the final level ℓ_{max}. Scaling this approach for 3D, total amount of processes required is:

$$\text{Processes Required} = \begin{cases} 1, n_0 > m_0 \\ 8^{m_0 - n_0}, n_0 \leq m_0 \end{cases} \qquad \text{Equation 2.2.3}$$

where $n_0, m_0 \in \mathbb{N}$, the finest level ℓ_{max} has 2^{m_0} points on a side, and each process holds 2^{n_0} points per side per level with maximum RAM usage. Thus, for $n_0 = m_0 - 1 \Rightarrow \#\text{Processes} = 8^{m_0 - (m_0 - 1)} = 8$ processes. Because a portion of computational work remains on every finer level after a process is first introduced, processes are utilized to a greater degree over a non-hierarchical filling method.

16
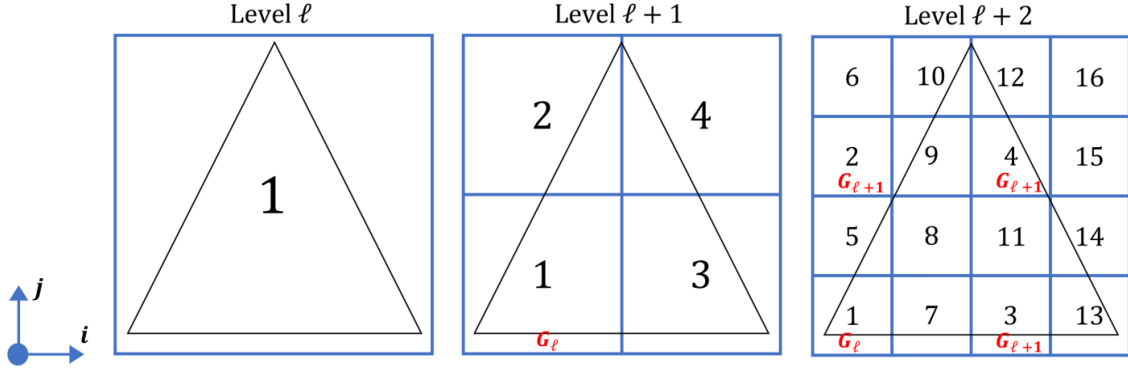
Figure 1 Multilevel Nodal Geometry on sequential levels ℓ, $\ell + 1$, and $\ell + 2$.

Processes on level ℓ, $\ell + 1$, and $\ell + 2$ operate over equally sized datasets regardless if operating on Ω_ℓ, $\Omega_{\ell+1}$, and $\Omega_{\ell+2}$, respectively. This is because the simulated distance between points is halved on level $\ell + 1$ and halved again on level $\ell + 2$, thus the density of information keeps pace with the addition of more GCPs. This approach is extended in this work to a three-dimensional simulation domain. During restriction, GCPs locally restrict their domain data and consolidate their information in the *-i* and *-j* direction to nodes marked with G_ℓ or $G_{\ell+1}$. Prolongation reverses this process by transferring G_ℓ data along the +*i* and +*j* direction.

At the beginning of model execution, a single AdP is designated. AdP starts by defining process boundaries determined by the maximum sized domain that each GCP can contain. To agree with domain Ω, cubic domain Ω_D for each GCP has side length 2^k, where $k \leq \ell_0 + \ell_{index}$. Value of k can be specified at runtime or be empirically derived by hardware availability. The resulting size is the fundamental size for each GCP. Consequently, coarsest level ℓ_0 may define a domain Ω_0 that is larger than a single GCP.

For process n operating over a subset of Ω_ℓ, denoted Ω_ℓ^n, a set of GPUs is paired with process n to process Ω_ℓ^n. For this study, we assume Ω_ℓ^n is cubic. If required by hardware constraints, Ω_ℓ^n is subdivided into subdomains ω_j^ℓ that are sufficiently reduced to fit in GPU RAM. Subdomains have following properties for m subdomains on level ℓ:

1. $\omega_j^\ell \subseteq \Omega_\ell^n, j \in \{1, \dots, m\}$

2. $\omega_1^\ell \cap \omega_2^\ell \cap \dots \cap \omega_m^\ell = \emptyset$

3. $\omega_1^\ell \cup \omega_2^\ell \cup \dots \cup \omega_m^\ell = \Omega_\ell^n$

4. $\omega_j^\ell \neq \emptyset, j \in \{1, \dots, m\}$

If a single GPU has enough RAM to hold Ω_ℓ^n, then $m = 1$. Because of stencil operations, a one-point shell layer around each subdomain is required. Next, GPUs receive relevant constant terms from the model, e.g., point spacing on level ℓ and domain dimensions. Finally, function X is called on all GPUs. After computation, data are unloaded as required to allow data to synchronize between all Ω_ℓ^n on Ω_ℓ. Due to memory transfers from GPU to CPU, this process constitutes the bulk of this method's overhead.

2.2.5 Data synchronization

When syncing data across GCPs, there are three vectors that must be defined: (1) a syncing vector, $\vec{S}$, (2) a process vector, $\vec{N}$, that points from self to an adjacent GCP, and (3) a data vector, $\vec{D}$, for directing synchronized information to the correct cubic feature (i.e., face, edge, or corner). Because processes are arranged as cubes in a Cartesian grid, there are 26 possible syncing directions for each GCP. Described by graph theory, each GCP forms a star graph S_{26} with its neighbors. Any MPI send-and-receive operation is a

two-step process, in which any link (u, v_m) for $m \in \{1,2,\dots,26\}$ from center node of star

graph u to vertex v_m must be traversed in both directions. For maximum performance,

perfect matching is desirable, meaning that on level ℓ, half of GCPs are sending data and

half of the GCPs are receiving data during the synchronization command. In addition, at

any given moment of synchronization, any chain of successive links on ℓ must be acyclic

to prevent hanging. Synchronization process in this model, therefore, has two objectives:

(1) creation of a unified timing structure that ensures synchronization across all nodes on

level ℓ without program hanging and (2) derivation of $\vec{D}$ and $\vec{N}$ at each link in star graph.

On each GCP every value in a 3x3x3 syncing stencil is cycled through in a preset

order. With the center process of the stencil as the center of a GCP's domain, each stencil

cell represents a cubic feature. A syncing vector $\vec{S}$ points from the origin to the cubic

feature represented by an index of the stencil, representing a link on the star graph. MPI

synchronization commands used in this framework do not resume execution until sending

and receiving operation is completed. Thus, by cycling through all possible syncing

vectors in a set order on all GCPs, every $\vec{S}$ at a given step of the syncing process will be

parallel, ensuring that the vector field of all syncing vectors has zero curl and, hence,

fulfilling objective 1. For a given $\vec{S}$, the GCPs send data in a checkerboard pattern, with

one half of the GCPs acting as senders and the other half as receivers. For a sending GCP

s operating in Ω_ℓ^s and a receiving GCP r operating in Ω_ℓ^r, s sends the cubic feature

indicated by $\vec{S} = \vec{D}_s = \vec{N}_s$ to the receiver whose $\vec{D}_r = \vec{N}_r = -\vec{S}$. Then, the

sending/receiving roles are reversed so that a cubic feature Ω_ℓ^r is sent to Ω_ℓ^s, giving both s

and r the data required to update their respective cubic feature. This process is repeated for all $\vec{S}$ such that any GCP n on ℓ can perform stencil operations anywhere in Ω_ℓ^n.

While $\vec{D}$ and $\vec{N}$ are parallel to $\vec{S}$ for interior synchronization events, syncing events on the border of Ω_ℓ involve cubic features that do not correspond to the syncing stencil. In these situations, vectors $\vec{N}$ and $\vec{D}$ are derived from projections of $\vec{S}$, thus linking objective 2 to objective 1. This allows the model to consistently synchronize information across all GCPs on ℓ without interaction from AdN and without forming cyclic subgraphs.

In the case of restriction, information must be consolidated from GCPs that exist on levels greater than or equal to $\ell + 1$ to GCPs that operate on both level ℓ and level $\ell + 1$. As represented in **Figure 1**, the filling method creates 2x2 squares of GCP domains. Each square contains a single GCP (G_ℓ) whose operating domain spans partitions of both ℓ and $\ell + 1$. G_ℓ's domain is at the minimum (i,j) corner of the 2x2 square. Restriction is performed locally on each GCP on $\ell + 1$, and the results are consolidated along the j-axis first followed by the i-axis at the corresponding G_ℓ. For each 2x2 square, this process moves all restriction information to each G_ℓ while parallelizing the restriction process. Likewise, prolongation involves distributing level ℓ data to all the corresponding GCPs on level $\ell + 1$. Distribution process reverses the consolidation process by distributing first from the G_ℓ along the i-axis and then the j-axis. Prolongation calculations are then done locally on all GCPs on level $\ell + 1$. On level $\ell + 2$ the restriction and prolongation processes scale to include nodes from both level ℓ (G_ℓ) and

nodes on level $\ell + 1$ ($G_{\ell+1}$). For this 3D model the preceding restriction and prolongation processes were scaled to a 2x2x2 cube region for each G_ℓ.

2.2.6 Performance timing

All timing results for openMP vs. CUDA test and MPI tests were obtained using time.h clock statements and operated on a reference homogenous tumor shape with heterogeneous vasculature created for this model runtime. Computer used for comparing openMP to MPI-CUDA framework has AMD 2990WX 32-core processor, two Titan RTX GPUs with computation load placed allocated to the non-display GPU, and 128GB of DDR4 RAM at 2666MHz. Both GPUs were set to WDDM mode. CUDA test case consists of two MPI processes: one AdP and one GCP. When running on a single PC, negligible overhead occurs from process communication thus a two process MPI-CUDA runtime is akin to a single process CUDA task, differing only in slight overhead due convergence decisions and process initialization steps. Furthermore, MPI-CUDA runtime was configured to run on a single, non-display Titan RTX GPU. Parameters other than time step size and tolerance were same as [119]. Time step size and tolerance for openMP and CUDA-only tests was $\theta = 5*10^{-3}$, and $\tau_{\ell_{max}} = 1*10^{-3}$, respectively. Lastly, each of the University of Kentucky's Lipscomb Compute Cluster (LCC) nodes used for MPI tests comprises two 20-core Intel Xeon 6230 processors, 192GB of RAM, and four Nvidia V100 32GB GPUs.

2.2.7 Simulation of cm-scale tumors with sub-mm resolution

Two large tumors were simulated: (1) ~1 cm tumor in a 256^3 domain, and (2) ~2 cm tumor in a 512^3 domain. The two simulated tumors are identical in shape to the performance tests, being homogeneously defined with an initial volume fraction $\tilde{\phi}_V =$

0.65. The shape was defined using a combination of sinusoidal functions and bivariate

normal distributions (as shown in Graphical Abstract). The initial conditions are included

in **2.5 Supplementary Material**. This domain size was derived from the diffusivity of

oxygen (10^{-5} cm^2/s [141, 142]). Both 256^3 and 512^3 simulations operated with resolution

of 50 µm lengths ($1.25 * 10^{-4}$ mm^3). Eight nodes on the LCC with eight CUDA-solving

processes per node were used for both simulations. Screenshots were taken for the initial

state, 167 time steps into the simulation (5 simulated days) and 267 time steps into the

simulation (8 simulated days). **Table 2** lists computational solver parameters used for

both domains.

Parameter	Description	Value Assigned for cm-Scale Runs	
		256^3	512^3
ℓ_{global}	Finest level that always spans Ω	2	
ℓ_{max}	Finest grid used for Ω	4	
σ	Tolerance reduction factor from level ℓ to $\ell + 1$	1.10	
θ	Time step size (days)	$3*10^{-2}$	
γ	Cycle Index (1 for V-cycle, 2 for W-cycle)	1	
$\tau_{\ell_{max}}$	Solution Tolerance for level ℓ_{max}	$2*10^{-3}$	
v_0, v_1, v_2, v_b	Preset number of smoothing steps	4,2,2,2	
r_{max}	Maximum number of Smoothing Steps before Divergence Exception is raised	15	45
C_ℓ	Maximum gradient difference allowed for Universal Gradient Test for the FLAG routine on ϕ_V.	0.05	
d_ℓ	Number of cells inward from the bound to include in near-boundary extra smoothing steps (for zero-indexed level ℓ)	2^ℓ	

Table 2 Computational parameters from [119] used for tumor simulations. Initial

values are set pre-model runtime. Values not listed are same as [119].

To increase model metabolite stability in the charge-balance equation, sodium concentrations were introduced throughout the model domain. A small increase in concentration of carbon dioxide, lactate, bicarbonate, and H^+ at the borders was applied to ensure convergence. As shown in **Figure 7,** the distance traveled by molecules before being absorbed by blood vasculature is significantly smaller than the distance between the tumor and the domain borders. This change, then, does not significantly affect the outcome by later points in the simulation. Before vasculature formation, the molecular species travel closer to the model borders, as noted in the smaller 256^3 case. To more accurately simulate a larger tumor mass and to provide sufficient oxygen and glucose to the model domain, more mature vascularization was created at the model borders and within the domain. Biological variables and parameters for long term 256^3 and 512^3 simulations are in **2.5 Supplementary Material**.

2.2.8 Statistics

All timing results were obtained for at least n = 3 simulation runs, with error bars representing 95% confidence interval (CI) of average value.

2.3 Results

2.3.1 Comparison of openMP and single MPI-CUDA process: CUDA contribution to model speedup

Tumor simulated for openMP vs. CUDA-only test was a 128^3 domain with initial condition in **Figure 9A**. Domain size was cubic with 4mm side length; thus, resolution of simulation was 31.25μm (from diffusivity of oxygen, 10^{-5} cm^2/s [141, 142]). Parameter values were unchanged from [118, 119]. Each coarser level $\ell - 1$ has twice the distance

between points as its corresponding finer level ℓ. From **Figure 2A**, a 14.7x performance increase of CUDA over openMP was seen for first-time step. In the second time step, our CUDA framework was 7.9x times faster than openMP. Due to corrections made in MPI-CUDA framework, this approach converged with fewer cycles than original openMP implementation. It is probable that convergence would be improved in openMP-based code if flux term changes were applied. However, we verified performance improvement by evaluating time per smoothing step. **Figure 2B** shows 10.7x improvement over original openMP implementation. Further, because of adaptive grid methods described in [119] that were used in openMP Multigrid algorithm, only a subset of the domain was solved over on the finest two levels of simulation; thus, openMP spends more time doing less computational work than our CUDA framework. Finally, because AMD 2990WX possess 32 cores, it is difficult to find current single socket computers capable of equivalent performance. Although it is possible that AMD 2990WX memory bandwidth may not fully utilize all CPU cores as effectively on a multi-die CPU system, the distinction is unlikely to close the performance gap. Consequently, it is reasonable to expect that performance improvements of CUDA over openMP will scale across other platforms.
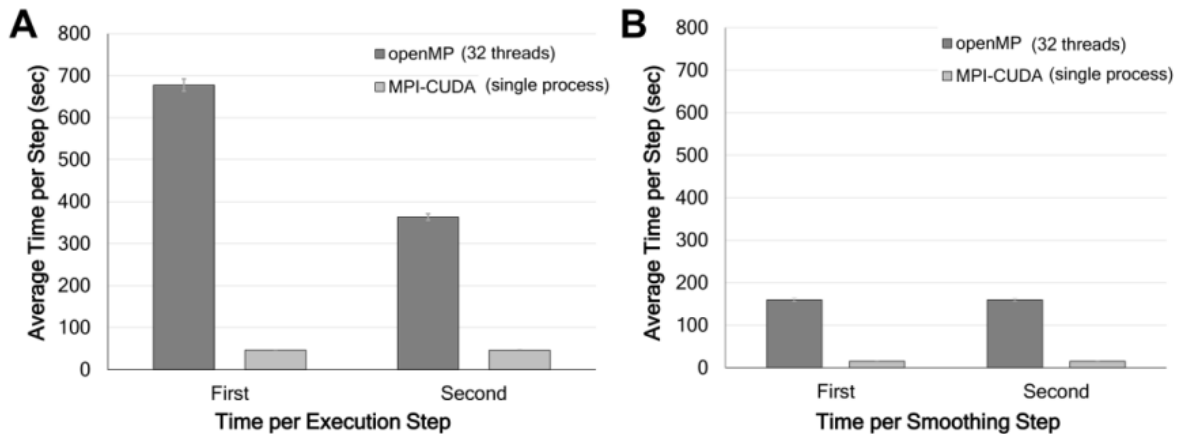
Figure 2 Performance comparison for first two time steps between openMP and single-process MPI-CUDA instance in 128^3 domain. (A) Execution time; (B) V-cycle solvers. Error bars are 95%.

Model accuracy was ensured by comparing model input to openMP numerical solutions in [118, 119]. To ensure model consistency across varying numbers of MPI thread counts, initial conditions and end-state after two time steps were compared between separate runs using SHA-256 hash. All algorithm behavior is represented in first two-time steps; thus, comparing first two time steps is sufficient to confirm solution integrity. This hash was created with printouts of volume fractions, pressures, metabolites, growth factors, and other model variables. Matching hashes implied that integrity of solving process was not impacted during development or by varying thread counts. This analysis also confirmed that MPI synchronization produced equivalent results for 1, 8, and 64 GCPs.

2.3.2 MPI Contribution to Model Speedup

To confirm that MPI increases performance over a single GCP MPI-CUDA instance, the LCC was used. Using same initial condition (**Figure 9B**) and resolution of 31.25µm, domain size was increased to a cube with 256^3 interior points (258^3 including border points). Thus, domain size was cubic with 8mm side length. All computational parameter values differing from [118, 119] are in **Table 3**.

Computational Parameter	Description	openMP vs. MPI-CUDA Single Process	MPI-CUDA LCC
$n_{\ell_{max}}$	Edge length of finest cubic domain $\Omega_{\ell_{max}}$	128	256
Domain Size	Side length of $\Omega_{\ell_{max}}$ (mm)	0.4	0.8

σ	Tolerance reduction factor from level ℓ to $\ell + 1$	4.0
$\tau_{\ell_{max}}$	Solution Tolerance for level ℓ_{max}	0.001

Table 3 Computational parameter values for CUDA-MPI tests. All other parameters were retained from [118, 119].

Triplicate tests were performed at three different numbers of MPI processes:

1.   Two process MPI-CUDA case: one AdP and one GCP. This test was akin to that used on AMD 2990WX test and baseline for cases 2 & 3.

2.   Nine process MPI-CUDA case: one AdP and eight GCPs. For an eight GCP setup the finest model domain was split into octants, with each process operating over a single octant. In this setup, each LCC Restriction operation from ℓ_{max} to $\ell_{max} - 1$ maps eight GCPs to a single GCP for processing. One LCC node was used with two MPI-CUDA processes assigned to two of the four available cluster GPUs.

3.   Sixty-five process MPI-CUDA case: one AdP and 64 GCPs. For this setup, an extra layer of 64 nodes is added at the finest level. Restricted information is sent to layer $\ell - 1$ containing eight of the 64 GCPs. Further restrictions to levels $\ell - 2$ and coarser behave identically to case 2. Four LCC nodes were used with four MPI-CUDA processes assigned to each of the 16 available GPUs.

Single process case used same test case in openMP vs. CUDA test but scaled to larger domain. Eight-GCP and 64-GCP cases were distributed to two and four nodes, respectively. To measure effect of process density of each GPU on performance, for two

groups, (1) 8 GCPs and one AdP and (2) 64 GCPs and one AdP, the number of nodes available was doubled; thus, 8-GCP-Low-Density test had two nodes with four GCPs per node while 64-GCP-Low-Density test had eight nodes with eight GCPs per node.

Averaging the ratios in timing results when moving from 8 GCPs to 64 GCPs for time steps 2 and 3 in **Figure 3**, a total improvement of 5.3x is observed. Multi-process allocation can bottleneck due to competition for memory bandwidth and simulation speeds. In eight-GCP case, four GPUs held two GCPs each; 16 GPUs held four processes each in the 64-GCPs case. To quantify performance lift by redistributing processes across more GPUs, two extra runs were performed with eight GPUs running one process apiece, increasing performance by 1.2x over the original case. This decreased the performance impact of switching to 64 processes from 2.8x in four GPU case to 2.4x in the eight GPU case. Similar to 8-process case, moving to 64 processes at 2 processes per GPU (for a total of 32 GPUs) increased performance 1.3x over 64-process runtime with 4 processes per GPU (16 GPUs). In total 64-GCP-Low-Density distribution outperforms CUDA-only distribution (1-GCP) by 6.7x. Combined with gains with CUDA over openMP, MPI-CUDA framework has capacity to simulate larger tumor masses in a distributed manner at speeds not possible under the previous framework. Furthermore, larger scale simulations benefit from increased resource availability, making 64 GCPs the selected distribution method for 256^3 domain and 512^3 domain simulations. However, there are diminished gains for scaling across more nodes, suggesting that this approach may weakly scale to project size.
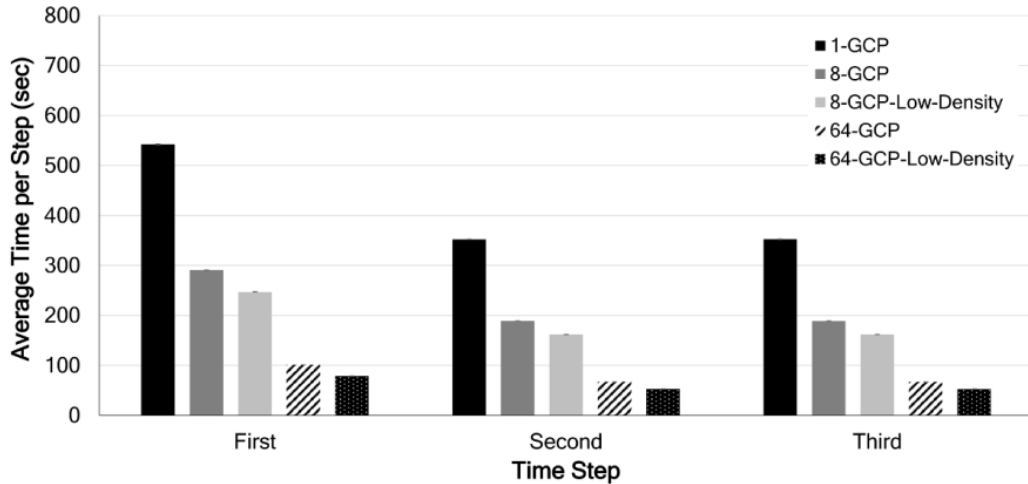
Figure 3 Mean performances per time step for MPI-CUDA processing a 256^3 domain. Error bars are 95%.

2.2.1 Simulation of cm-scale tumors

The 256^3 simulation that ran on 32 V100 GPUs took about 2 h real time to simulate 5 simulated days with an average time per time step of 43.2 s. An additional 93.8 min were required to reach 8 simulated days. For 512^3 simulation, same 32 V100 GPU setup took ~31.5 h to reach 5 simulated days at average rate of 11.3 min per time step. Additional 26.5 h were required to reach 8 simulated days. Here, average rate per time step increased to 15.9 min per time step.

Figure 4 shows 512^3 domain simulation of ~2cm diameter tumor at 5 and 8 simulated days. Viable and dead tissues are evident. Pronounced release of tumor angiogenic factors (TAF) is triggered by hypoxia, which leads to angiogenesis and growth of blood vasculature (**Figure 5**). However, both blood and lymphatic vasculature concentrations decreased overall. Cellular respiration leveraged increased oxygen supply, thereby raising carbon dioxide concentration. ECM concentration remained relatively

28

stable (**Figure 6**). As tumor mass compressed internally, matrix degrading enzymes (MDE) concentration shifted away from periphery, explaining local ECM loss at i=1.27 cm plane. Decline can also be attributed to lower concentration of myofibroblasts in inner tumor. Because myofibroblasts are created by the model within ECM and become necrotic at low oxygen levels, their concentration remained relatively stable from 5 to 8 simulated days. Meanwhile, a layer of higher viability tumor mass formed near vasculature in the peritumoral space. Negative pressure from tumor and ECM necrosis shifted the viable tumor layer towards interior regions, distancing this viable tissue from blood vasculature. This layer became necrotic and is present at both 5 simulated days and 8 simulated days. While tumor growth factor (TGF) concentration rose in peritumoral range over the 3 simulated day period, encouraging increased tumor proliferation at periphery, MDE concentration decreased locally at i=1.27 cm plane.
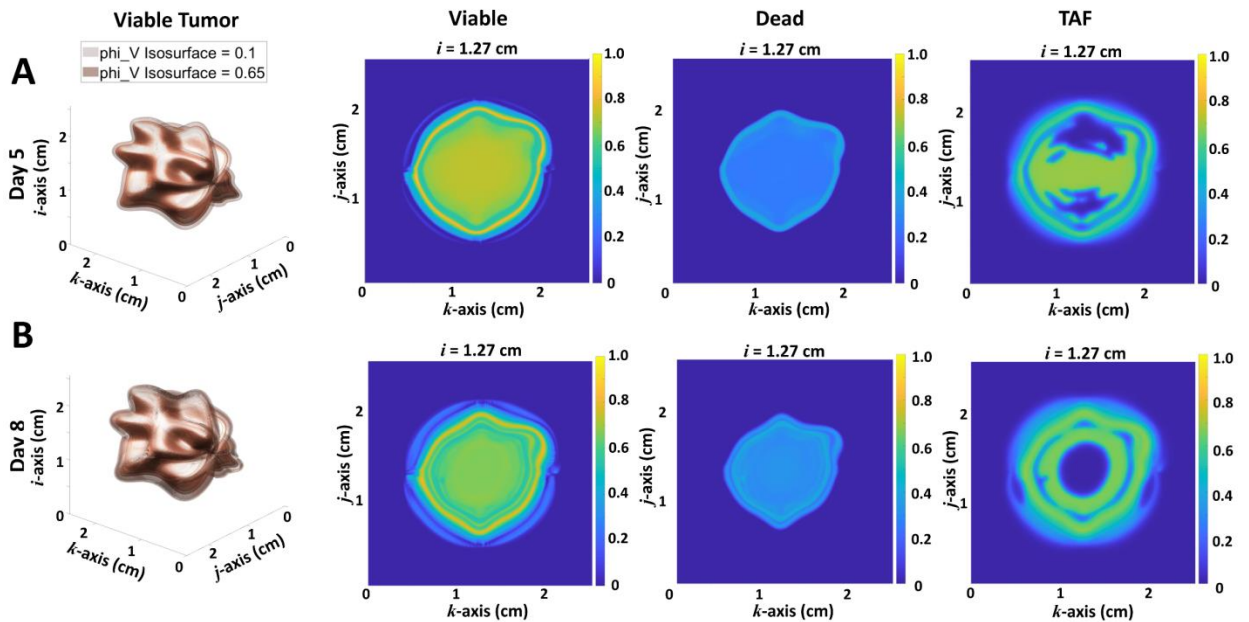
Figure 4 Evolution of ~2cm diameter tumor in 512³ domain at simulated (A) 5 days and (B) 8 days. Viable, dead, and tumor angiogenic factors (TAF) are shown (plane *jk*).
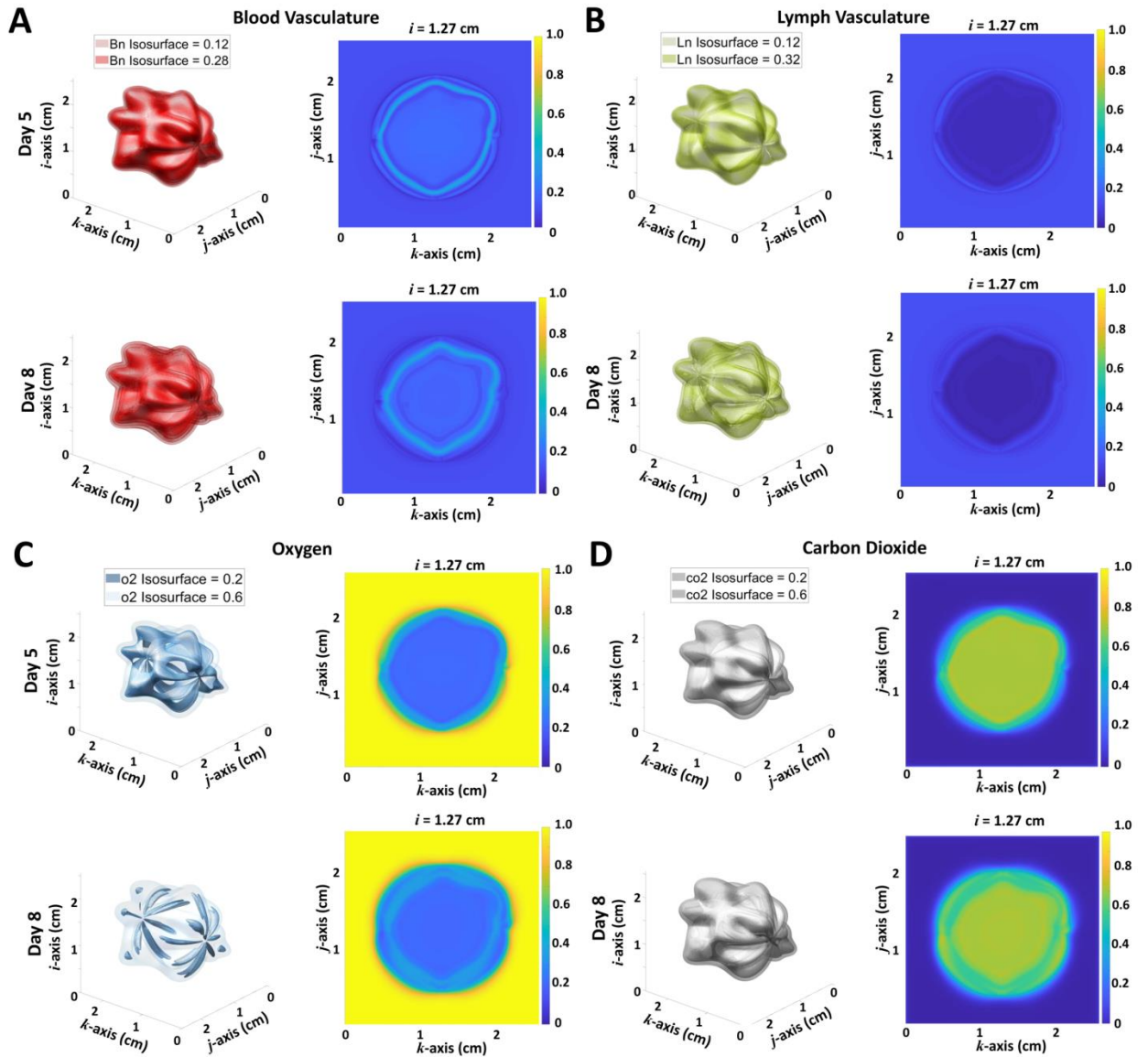
Figure 5 Tumor vessel evolution for ~2cm diameter tumor in 5123 domain. (A) Blood vasculature. (B) Lymphatic vasculature. (C) Oxygen. (D) Carbon dioxide.
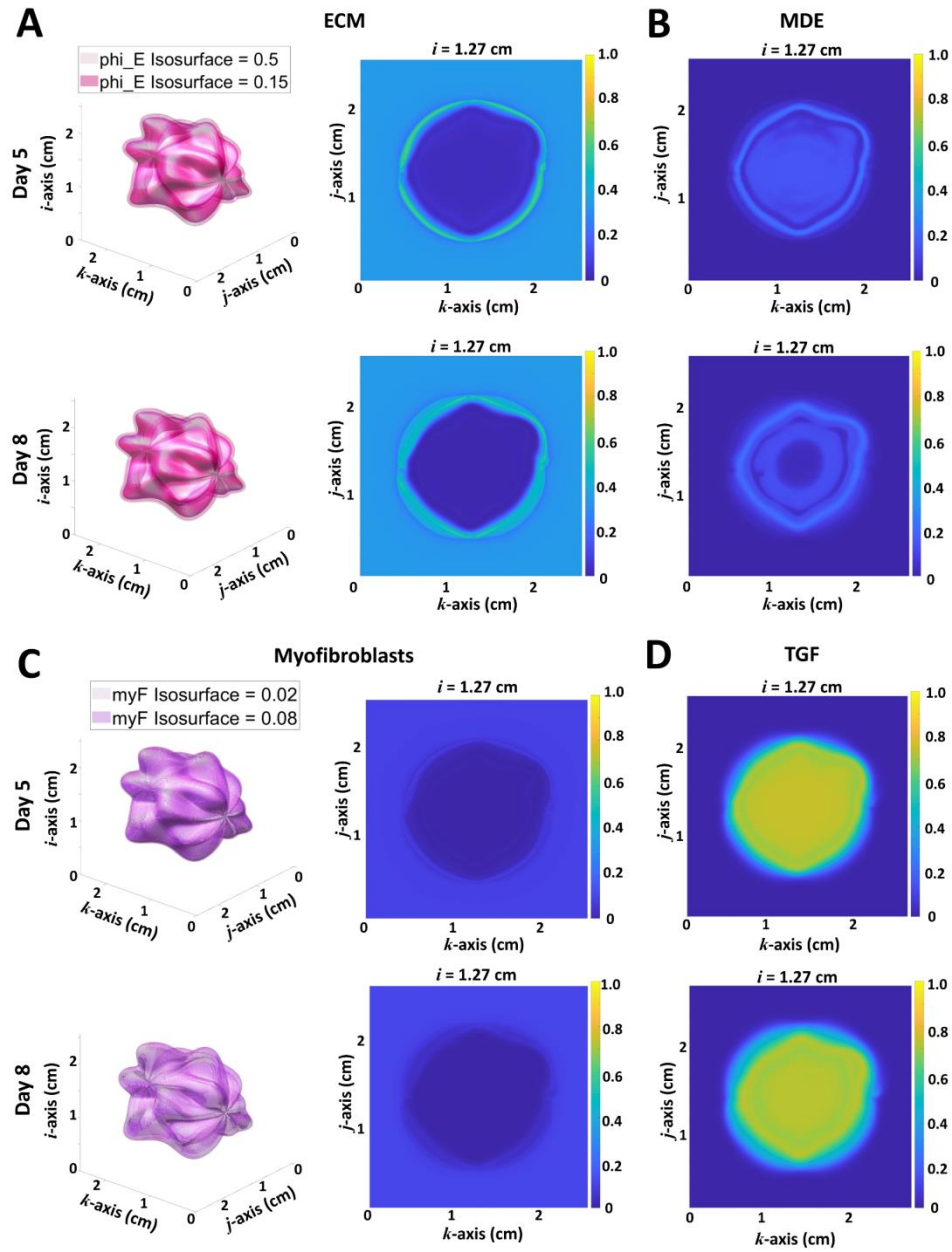
Figure 6 Tumor matrix evolution for ~2cm diameter tumor in 512³ domain. (A) Extracellular matrix (ECM). (B) Matrix degrading enzymes (MDE). (C) Myofibroblasts. (D) Tumor growth factors (TGF).

The highly hypoxic nature of the tumor resulted in a persistently high H^+ and lactic acid concentration from bicarbonate buffer and anaerobic glycolysis (**Figure 7**). Glucose, being necessary for both aerobic and anaerobic glycolysis, is scarcer in the internal tumor portions and continues to decrease in peritumoral region over time. Carbon dioxide, being formed by aerobic glycolysis, was consumed, in part, by the bicarbonate buffer, increasing bicarbonate prevalence.
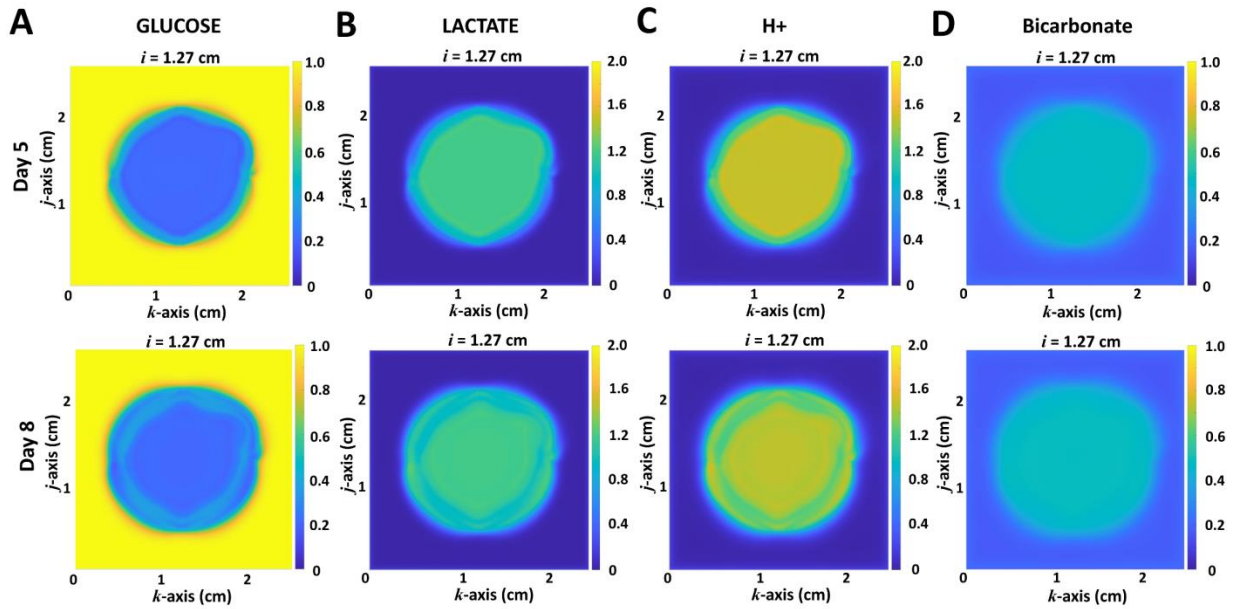
Figure 7 Evolution of metabolism-related variables for ~2cm diameter tumor in 512^3 domain. (A) Glucose. (B) Lactate. (C) Hydrogen ion (H^+). (D) Bicarbonate.

Simulations of ~1 cm tumor in 256^3 domain generally yielded similar results as the larger tumor in 512^3 domain using same parameter values (**Figure 8**). After an initial drop in mass due to lag in angiogenic response, both tumors assumed a growth pattern by 8 simulated days. Despite an overall decrease in density in the interior portions of the tumor, the 512^3 $\tilde{\phi}_V = 0.1$ isosurface exhibited a growth rate of 2.6% volume per day. The

more robust (blood and lymphatic) vascularization of the smaller tumor is evident at this timepoint earlier than in larger tumor, as are higher TAF and MDE concentrations.
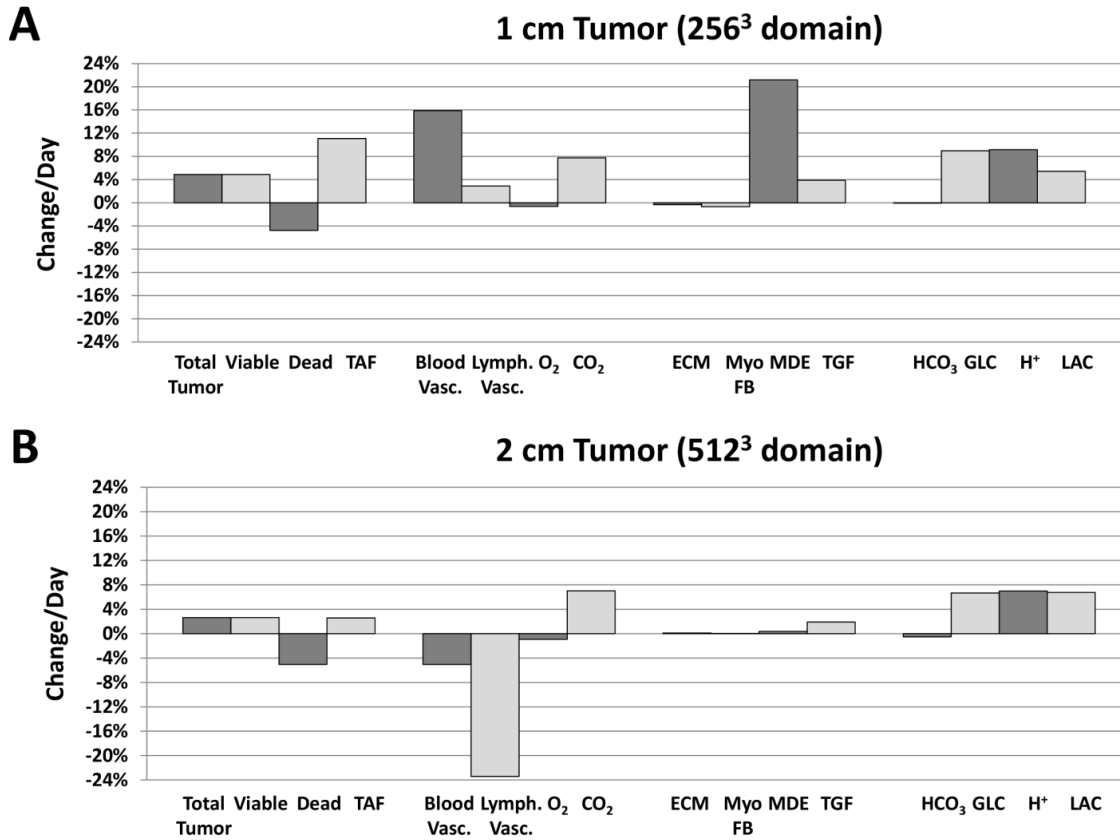
Figure 8 Rate of change of tumor variables (%change/day) at 8 simulated days for (A) 256^3 domain and (B) 512^3 domain. From left to right: total tumor; viable tumor; dead tumor; TAF (tumor angiogenic factors); blood vasculature; lymphatic vasculature; O2 (oxygen); CO2 (carbon dioxide); ECM (extracellular matrix); myoFB (myofibroblasts); MDE (matrix degrading enzymes); TGF (tumor growth factors); GLC (glucose); LAC (lactate); H+ (hydrogen ion); HCO3 (bicarbonate).

2.4 Discussion

This study implements a distributed computing (parallelized) implementation of the mixture model in [118, 119] to simulate 3D continuum tumor growth at cm-scale at sub-mm resolution. Compared to previous work, the model here accounts for a richer set of biological phenomena, simulating ECM-tumor interaction, blood and lymphatic vasculature evolution, metabolic consequences of anaerobic respiration, acidity induced via the bicarbonate buffer, and secretion of diffusible factors in response to hypoxic conditions. These results highlight how identical parameter sets perform at in different domain sizes, 256^3 and 512^3, suggesting future work required to fine-tune parameter sets best suited for large-scale growth.

The CUDA-MPI approach improves the model performance over the previous openMP approach [119] by ~50x. This value comes from accumulating the benefits seen across the smoothing test from openMP vs. CUDA (**Figure 2B**) and the step time duration between 1-GCP vs. 64-GCP test (**Figure 3**). Using the 1-GCP vs. 64-GCP-Low-Density increases total performance improvement to ~70x that of the previous openMP approach. Because of differing testing approaches and non-equivalent hardware, these performance improvements cannot be directly compared to other tumor modeling approaches. Nevertheless, cumulative improvements demonstrated here are in similar league to those in [127, 128, 132], demonstrating immediate benefits of using CUDA-MPI over openMP. To our knowledge, these results mark the first time a multigrid 3D continuum tumor model has been fully parallelized. Based on the performance metrics obtained, we anticipate future work to simulate tumor sizes as in [134]. These

improvements are also consistent with Navier-Stokes Multigrid simulations where CPU-side parallelization across 64 processors saw a 50x improvement in speed [143]. A different Navier-Stokes solver using an MPI-CUDA framework achieved a 21x performance uplift over an 8-core Intel Xeon baseline using 2 GPUs and a 130x performance uplift using 128 GPUs [144]. Huang et al. created an MPI-CUDA framework to implement a Sparse Equations and Least Squares method for use in seismic tomography. Their results report a 37x performance uplift using 60 CPU cores relative to a single core baseline; using 60 GPUs nearly doubled performance over their 60 CPU results [145]. These values suggest that our model's performance benefits are on the same order of magnitude as similarly parallelized problems.

Continuum tumor mixture models, due to the numerous interwoven phenomena simulated, have many guiding equations, leading to multiple variables and quantities to evaluate and compute. As such, the memory required per point in model domain at level ℓ (Ω_ℓ) may be significantly higher than the raw variable count suggested in the case of Navier-Stokes equations. RAM constraints on GPUs become increasingly difficult to navigate as biological precision and generalizability are pursued by more specialized model equations. While MPI can involve more GPUs and lower the per-GPU RAM requirements, we recognize that this study used Titan RTX and V100 GPUs, both of which possess over 20 GB of RAM. GPUs with lower RAM capacity individually and in aggregate would with current technology have difficulty running highly-detailed continuum tumor models, potentially relegating such models to high-end desktop PCs and, in the case of cm-scale modeling, to larger compute clusters.

While the parallelization performed on the tumor model is significant, further development is required before deployment in a clinical environment. First, a more finely-tuned parameter set could help achieve persistent intra-tumoral increasing concentrations, such as ECM, required to simulate large-scale particular cancer types. Second, this process structure has no fault tolerance. If a single GCP were to fail to respond, the program would exit without completing the model. Fault tolerance has already been implemented in Big Data cluster libraries, such as Hadoop and Apache Spark [136, 138]. Thus, future implementation may draw from techniques used by these Big Data frameworks.

With the addition of Multigrid technologies such as adaptive grid meshes, computational workload would be reduced and would increase model performance. For some problem sizes, a CUDA-MPI framework may not be optimal due to the overhead of passing data for processing to GPUs. Indeed, an openMP/MPI framework has outperformed CUDA-MPI tasks when operating on a smaller mathematical model [146]. It is suspected that a tradeoff point exists, which could be a subject for future research. Evaluation of openMP-MPI vs. CUDA-MPI at varied grid levels may lead to further optimizations of mixed grid sizes.

Additionally, because of parallel synchronization constraints, the adaptive grid mesh method previously used in [118, 119] was discarded in favor of a modified residual calculation procedure as detailed in **2.2 Materials and Methods**. An adaptive grid mesh

implementation would require adaptive process assignments to subsets of non-global domains and, if implemented at MPI level, may better utilize processing resources. In many cases only a single V-cycle was required to converge to selected tolerance. A minority of time steps, especially time steps directly after and including initial time step, required more smoothing iterations to achieve tolerance; it is likely that using a different multigrid cycle, such as the F-cycle, would improve convergence performance in those cases [147]. Some other minor performance improvements can be made, such as consolidating the AdP with a GCP to reduce thread count by one. From a GPU standpoint, with RAM counts on GPUs increasing significantly over the past half-decade, 256^3 currently and 512^3 in the future will likely become entirely GPU-side computations within a couple GPU generations. Further refinement could thus reduce MPI's contribution by removing most memory transfers.

Because of its low cost of failure and ideal reproducibility, *in silico* simulation of clinically-relevant tumor-sized growth could help to analyze patient treatment, especially when coupled to tumor-specific parameters. Flexibility afforded by parameters leveraged in this model may yield a platform for accommodating a wide range of characteristics, anticipating tumor evolution and forecasting on patient potential outcomes. Further, discovering which model parameters influence positive clinical outcome could posit opportunities for novel clinical approaches and provide a basis for further exploration. A faster turnaround would offer a more responsive methodology of engaging with oncological hypothesis testing and to focus *in vitro* and *in vivo* experimental effort.

With the complexity and scale of the model, the number of parameters makes assumptions inevitable. Akin to the reliance of machine learning on high data acquisition for training sets, determining patient-specific parameter values will require integrating *in silico* evaluation with relevant clinical data. This requirement is exacerbated as more detailed biological phenomena are considered. For example, introducing immunotherapies and immuno-onco interactions will require additional parameters, meaning that balancing performance with model complexity will continue to affect larger-scale continuum tumor modeling. Despite limitations, this study presents a first step in achieving centimeter-scale 3D continuum tumor simulations with sub-millimeter resolution, with future work envisioned to move this approach closer to clinical application.

2.5 Supplementary Material

2.5.1 Model Equations

Key equations from the continuum 3D tumor model presented in [118, 119] are summarized below. All scaling factors for non-dimensionalization are as in [118, 119]:

$$\frac{\partial \phi_V}{\partial t} + \nabla \cdot (\phi_V u_\alpha) = M \cdot \nabla \cdot (\phi_V \nabla \mu_T) + S_V \qquad \text{Equation 2.5.4}$$

$$\mu_E = \frac{\partial F_b}{\partial \phi_E} + \frac{\partial \mathcal{W}}{\partial \phi_E} - \epsilon_E^2 \cdot \nabla^2 \phi_E - \epsilon_{TE}^2 \cdot \nabla^2 \phi_E \qquad \text{Equation 2.5.5}$$

$$\frac{\partial \mathcal{W}}{\partial \phi_E} = \epsilon_e \cdot [6 \cdot \phi_E \cdot (1 - \phi_E)] \cdot \sum_{i,j=1}^{3} \left[\frac{1}{2} \cdot (\mathcal{E}_T)_{ij} \cdot \mathbb{T}_{ij}^* - (\mathcal{E}_T^*)_{ij} \cdot \mathbb{T}_{ij} \right] \qquad \text{Equation 2.5.6}$$

$$\mathbb{T}_{mn}^* = 2 \cdot (1 - L_2^C) \cdot (\mathcal{E}_T)_{mn} + (L_1^E - L_1^C) \cdot \delta_{mn} \cdot \sum_{k=1}^{3} (\mathcal{E}_T)_{kk} \qquad \text{Equation 2.5.7}$$

$$\mathbb{T}_{mn} = 2 \cdot L_2 \cdot (\mathcal{E}_T)_{mn} + L_1 \cdot \delta_{mn} \cdot \sum_{s=1}^{3} (\mathcal{E}_T)_{ss}$$

Equation 2.5.8

$$(\mathcal{E}_T)_{ij} = \mathcal{E}_{ij} - \mathcal{E}_{ij}^*$$

Equation 2.5.9

$$\mathcal{E}_{ij}^* = Q_3(\phi_E) \cdot (\mathcal{E}_T^*)_{ij} + (\mathcal{E}_C^*)_{ij}$$

Equation 2.5.10

$$(\mathcal{E}_T^*)_{ij} = (\mathcal{E}_E^*)_{ij} - (\mathcal{E}_C^*)_{ij}$$

Equation 2.5.11

$$\mathcal{E}_{mn} = \frac{1}{2} \cdot \left(\frac{\partial u_m^d}{\partial x_n} + \frac{\partial u_n^d}{\partial x_m} \right)$$

Equation 2.5.12

$$L_i = Q_3(\phi_E) \cdot \left(L_i^E - L_i^C \right) + L_i^C, i = 1,2$$

Equation 2.5.13

$$Q_3(x) = x^2 \cdot (3 - 2x)$$

Equation 2.5.14

$$\nabla \cdot \left[k_\alpha \cdot \left(\nabla p - \frac{\gamma_T}{\epsilon_T} \mu_T \nabla \phi_T - \frac{\gamma_E}{\epsilon_E} \mu_E \nabla \phi_E \right) \right] = -(S_V + S_D + S_E)$$

Equation 2.5.15

$$u_\alpha = -k_\alpha \cdot \left[\nabla p - \frac{\gamma_T}{\epsilon_T} \mu_T \nabla \phi_T - \frac{\gamma_E}{\epsilon_E} \mu_E \nabla \phi_E \right]$$

Equation 2.5.16

$$u_E = u_\alpha - M_E \cdot \nabla(\mu_E)$$

Equation 2.5.17

$$\nabla \cdot (D_n \nabla n) + k_{n1} n_C - (k_{n1} + k_{n2}) \cdot n = 0$$

Equation 2.5.18

$$\nabla \cdot \left(D_{tgf} \nabla(tgf) \right) + \lambda_{tgf} - \left(\lambda_{tgf} + \lambda_{de,tgf} + \lambda_{U,tgf} \right) \cdot tgf = 0$$

Equation 2.5.19

$$\nabla \cdot \left(D_{taf} \nabla(taf) \right) + \lambda_{taf} - \left(\lambda_{taf} + \lambda_{de,taf} + \lambda_{U,taf} \right) \cdot taf = 0$$

Equation 2.5.20

$$\frac{\partial m}{\partial t} = \nabla \cdot (D_m \cdot \nabla m) + S_m$$

Equation 2.5.21

$$\frac{\partial B_n^E}{\partial t} + \nabla \cdot (B_n^E u_E) = -\nabla \cdot \boldsymbol{J}_{BnE} + S_{BnE}$$

Equation 2.5.22

$$\frac{\partial L_n^E}{\partial t} + \nabla \cdot (L_n^E u_E) = -\nabla \cdot \boldsymbol{J}_{LnE} + S_{LnE}$$

Equation 2.5.23

where term values in equations 1 through 20 are given in **Table 4** and **Table 5**,

and

$$\delta_{mn} = \begin{cases} 0, m \neq n \\ 1, m = n \end{cases}.$$

Equation 2.5.24

Nondimensionalized Dependent Variable	Biological Representation	Scaling Factor
ϕ_V	Viable tumor cell volume fraction	$\tilde{\phi}_\alpha$ (fixed solid volume fraction)
ϕ_E	Extracellular Matrix (ECM) volume fraction	$\tilde{\phi}_\alpha$
ϕ_H	Healthy host cells volume fraction	$\tilde{\phi}_\alpha$
u_α	Solid cell velocity	$\dfrac{\mathcal{L}}{\mathcal{T}}$
u_E	ECM velocity	$\dfrac{\mathcal{L}}{\mathcal{T}}$
μ_T	Tumor cell potential	E_a^*
μ_E	Extracellular Matrix Potential	E_a^*
u^d	Displacement Vector	$\mathcal{L}$
p	Solid phase tumor cell Pressure	$\mathcal{P}$
n	Concentration of oxygen	$\tilde{n}_\infty$
tgf	Tumor growth factor (tgf) concentration	tgf_{sat}
taf	Tumor angiogenic factor (taf) concentration	taf_{sat}
m	Concentration of Matrix degrading enzymes (mdes)	m_{sat}
B_n^E	New blood vessels per ECM volume	$\tilde{B}_{max}$
L_n^E	New Lymphatic vessels per ECM volume	$\tilde{L}_{max}$

Table 4 List of dependent variables in Equations 1 through 20 for the model in [118].

Parameter	Biological Representation	Definition	Non-dimensionalization

M_i	Mobility of cell species i		$\mathcal{M}$
S_V	Viable Tumor Cell Source		
S_D	Dead/Necrotic Tumor Cell Source Term		$\tilde{\phi}_\alpha \cdot \mathcal{T}$
S_E	ECM Source Term		
S_{BnE}	Blood cell Source Term		$\tilde{B}_{max} \cdot \mathcal{T}$
$\mathcal{W}$	Elastic Energy		$\tilde{\phi}_\alpha \cdot E_a^*$
L_1^E & L_2^E	Lamé constants for ECM components		L_2^E & L_2^E
L_1^C & L_2^C	Lamé constants for cell components	[118]	L_2^E & L_2^E
ϵ_E	Interaction strength of ECM		$\bar{\bar{\epsilon}}$
ϵ_T	Interaction strength for tumor cells		$\bar{\bar{\epsilon}}$
ϵ_e	Strain energy coefficient		$\bar{\bar{\epsilon}}_e$
γ_T	Tumor cell adhesion parameter		$\gamma_T = \dfrac{\epsilon_T \cdot \tilde{\phi}_\alpha \cdot \sqrt{\tilde{\phi}_\alpha \cdot E_a^*}}{\mathcal{L} \cdot \mathcal{P}}$
γ_E	Extracellular matrix adhesion parameter		$\gamma_E = \dfrac{\epsilon_E \cdot \tilde{\phi}_\alpha \cdot \sqrt{\tilde{\phi}_\alpha \cdot E_a^*}}{\mathcal{L} \cdot \mathcal{P}}$
$\mathcal{E}$	Infinitesimal strain		$\bar{\bar{\mathcal{E}}}$
$\mathcal{E}_E^*$	Eigenstrain tensor for ECM		$\bar{\bar{\mathcal{E}}}$
$\mathcal{E}_C^*$	Eigenstrain tensor for cells	[119]	$\tilde{\bar{\bar{\mathcal{E}}}}$
k_{n1}	Oxygen Rate constants		$\lambda_{U,V,n}$
k_{n2}			$\lambda_{U,V,n}$
D_n	Diffusivity of oxygen in tumor		$D_{n,T}$
k_α	Motility of the solid phase	[118]	$\bar{\bar{k}}_\alpha$
D_{tgf}	Diffusivity of tumor growth factor		$D_{n,T}$

D_{tgf}	Diffusivity of tumor angiogenic factor		$D_{n,T}$
λ_{tgf}	Tumor growth factor rate constant		$\lambda_{U,V,n}$
$\lambda_{de,tgf}$	Degradation rate constant for tumor growth factor		$\lambda_{U,V,n}$
$\lambda_{U,tgf}$	Total uptake rate constant for tumor growth factor		$\lambda_{U,V,n}$
J_{BnE}	New blood vessel diffusive flux per ECM volume		$\tilde{B}_{max} \cdot \mathcal{T}$

Table 5 List of parameters in equations 1 through 20 for the model in [118, 119].

Values of parameters used in this study are given in [118].

Table 6 summarizes the non-dimensionalization parameters.

Nondimensionalization parameters	Description	Definition or Assigned Value
$\tilde{\phi}_\alpha$	Fixed Solid Volume Fraction	0.8
E_a^*	Energy Scale for Adhesion	0.001
E_e^*	Energy Scale for Elastic Effects	0.001
$\bar{\bar{k}}_\alpha$	Characteristic Solid Species Motility	1.0
$\mathcal{L}$	Characteristic Length	$\sqrt{\dfrac{D_{T,n}}{\lambda_{U,V,n}}}$
$\mathcal{P}$	Characteristic Pressure	$\dfrac{\mathcal{L}^2}{\bar{\bar{k}}_\alpha \cdot \mathcal{T}}$
$\mathcal{M}$	Characteristic Mobility	$\dfrac{\mathcal{L}^2}{\mathcal{T} E_a^*}$
$\bar{\bar{\epsilon}}$	Characteristic Interaction Strength	$\mathcal{L} \cdot \sqrt{\dfrac{E_a^*}{\tilde{\phi}_\alpha}}$

$\bar{\bar{\varepsilon}}$	Characteristic Strain	$\sqrt{\dfrac{E_a^* \cdot \tilde{\phi}_\alpha}{E_e^* \cdot \bar{\bar{\varepsilon}} \cdot L_2^E}}$	

Table 6 List of non-dimensionalization parameters used in Table 4 and Table 5 [118].

Dirichlet boundary conditions were kept the same as in [118], except for the conditions listed in **Table 7**. Neumann boundary conditions from [118] were unchanged.

Boundary Variable	Description	Value in [118]	Updated value used for 256^3 and 512^3 simulations	
$\tilde{w}$	CO_2 boundary condition	0.0	0.15	
$\tilde{l}$	Lactate boundary condition	0.0	0.15	
$\tilde{b}$	Bicarbonate boundary condition	0.0	0.15	
$\tilde{a}$	Hydroxide boundary condition	0.0	0.15	
$\tilde{s}$	Sodium boundary condition	0.0	0.5	
$\tilde{B}_\infty$	Vasculature boundary condition	0.2	0.4	
$\tilde{L}_\infty$	Lymphatic boundary condition	0.2	0.4	
Internal Initial Condition	**Description**	**Value in [118]**	**Updated value used for 256^3 and 512^3 simulations**	
			Extra-Tumoral	*Intra-Tumoral*
$\tilde{s}$	Sodium initial condition	0	0.5	
$\widetilde{B_n}$	Blood vasculature initial condition	0.2	0.14	0.28
$\widetilde{L_n}$	Lymphatic vasculature initial condition	0.2	0.14	
$\tilde{\phi}_V$	Viable tumor volume fraction initial condition	0.65	0	0.65
$\tilde{\phi}_E$	ECM volume fraction initial condition	0.35	0.35	0.35

Table 7 Boundary and initial condition updates for 256^3 and 512^3 model runs. All

others remain the same as in [118].

        Biological parameters changed for long term 256^3 and 512^3 simulations are in

Table 8.

Dimensionless Parameter	Biological Representation	Scaling Factor	Value Assigned in [119]	Value Assigned for 256^3 and 512^3 Long Runs
$\tilde{\lambda}_{N,V}$	Necrosis rate constant of viable tumor cells	$\lambda_{M,V}$	3.0	0.2
$\tilde{\lambda}_{L,D}$	Lysis rate constant of dead tumor cells	$\lambda_{M,V}$	1.0	0.18
$\tilde{\lambda}_{B,n,E}$	Transfer coefficient of O_2 via capillary network in ECM regions	$\lambda_{U,V,n}$	0.1	0.90
$\tilde{\lambda}_{B,n,T}$	Transfer coefficient of O_2 via capillary network in tumor regions	$\lambda_{U,V,n}$	0.001	0.90
$\tilde{\lambda}_{B,n,H}$	Transfer coefficient of O_2 via capillary network in host regions	$\lambda_{U,V,n}$	0.01	0.90
$\tilde{\lambda}_{B,g,E}$	Transfer coefficient of glucose via capillary network in ECM regions	$\lambda_{U,V,n}$	0.1	0.90
$\tilde{\lambda}_{B,g,T}$	Transfer coefficient of glucose via capillary network in tumor regions	$\lambda_{U,V,n}$	0.001	0.90
$\tilde{\lambda}_{B,g,H}$	Transfer coefficient of glucose via capillary network in host regions	$\lambda_{U,V,n}$	0.01	0.90

$\tilde{\lambda}_{B,l,E}$	Transfer coefficient of lactate via capillary network in ECM regions	$\lambda_{U,V,n}$	1.0	1.0
$\tilde{\lambda}_{B,l,T}$	Transfer coefficient of lactate via capillary network in tumor regions	$\lambda_{U,V,n}$	0.1	1.0
$\tilde{\lambda}_{B,l,H}$	Transfer coefficient of lactate via capillary network in host regions	$\lambda_{U,V,n}$	0.5	1.0
$\tilde{\lambda}_{V,tgf}$	Production rate constant of tgfs by viable tumor cells	$\lambda_{U,V,n}$	0.2	0.4
$\tilde{\lambda}_{de,tgf}$	Degradation rate constant of tgfs	$\lambda_{U,V,n}$	0.05	0.1
$\tilde{\lambda}_{V,taf}$	Production rate constant of tafs by viable tumor cells	$\lambda_{U,V,n}$	0.2	0.4
$\tilde{\lambda}_{de,taf}$	Degradation rate constant of tafs	$\lambda_{U,V,n}$	0.05	0.15
$\tilde{\lambda}_{U,L,taf}$	Uptake rate constant of tafs by proliferating lymphatic endothelial cells	$\lambda_{U,V,n}$	0.0011574	0.0021574
$\tilde{\lambda}_{de,m}$	Decay rate constant of mdes	$\lambda_{M,V}$	5.0	10.0
$\tilde{\lambda}_{M,FE}$	Mitosis rate constant of myofibroblast cells	$\lambda_{M,V}$	0.1	0.21875
$\tilde{\lambda}_{N,FE}$	Necrosis rate constant of myofibroblast cells	$\lambda_{M,V}$	0.3	0.2
$\mathcal{F}_{Bn}$	Fraction of new blood vessels sprouting	-	0.01	0.90
$\lambda_{crush,BnE}$	Maximum degradation rate constant of new blood vessels due to cell pressure	$\lambda_{M,V}$	1.0	0.33
$\lambda_{re,BnE}$	Remodeling rate constant of new	$\dfrac{\lambda_{M,V}}{m_{sat}}$	1.0	0.33

	blood vessels by mdes			
$\mathcal{F}_{Ln}$	Fraction of new lymphatic vessels sprouting	-	0.01	0.2
$\lambda_{crush,LnE}$	Maximum degradation rate constant of new lymphatic vessels due to cell pressure	$\lambda_{M,V}$	1.0	0.33
$\lambda_{re,LnE}$	Remodeling rate constant of new lymphatic vessels by mdes	$\dfrac{\lambda_{M,V}}{m_{sat}}$	1.0	0.33
$\tilde{p}_{t,L}$	Threshold pressure corresponding to the onset of lymphatic vessel loss	$\mathcal{P}$	0.6	1.0
$\tilde{p}_{c,Bn}$	Threshold pressure corresponding to the maximum rate of neo-blood vessel loss	$\mathcal{P}$	0.8	1.2
$\tilde{p}_{c,Ln}$	Threshold pressure corresponding to the maximum rate of neo-lymphatic vessel loss	$\mathcal{P}$	0.8	1.2
$\tilde{k}_T$	Motility of the tumor cell phase	$\bar{\bar{k}}_\alpha$	10.0	20.0
$\tilde{k}_E$	Motility of the ECM phase	$\bar{\bar{k}}_\alpha$	10.0	20.0
$\tilde{k}_H$	Motility of the healthy host cell phase	$\bar{\bar{k}}_\alpha$	10.0	20.0
$\mathcal{F}_{V,l,tgf}$	Effective Factor of lactate level in upregulating the production rate of tgf by viable tumor cells	-	1.0	0.0
$\mathcal{F}_{F,l,tgf}$	Effective Factor of lactate level in	-	1.0	0.0

	upregulating the production rate of tgf by myofibroblast cells			
$\mathcal{F}_{B,l,tgf}$	Effective Factor of lactate level in upregulating the production rate of tgf by endothelial cells	-	1.0	0.0
$\mathcal{F}_{L,l,tgf}$	Effective Factor of lactate level in upregulating the production rate of tgf by lymphatic Endothelial cells	-	1.0	0.0
$\mathcal{F}_{V,l,taf}$	Effective Factor of lactate level in upregulating the production rate of taf by viable tumor cells	-	1.0	0.0
$\mathcal{F}_{F,l,taf}$	Effective Factor of lactate level in upregulating the production rate of taf by myofibroblast cells	-	1.0	0.0
$\mathcal{F}_{B,l,taf}$	Effective Factor of lactate level in upregulating the production rate of taf by endothelial cells	-	1.0	0.0
$\mathcal{F}_{L,l,taf}$	Effective Factor of lactate level in upregulating the production rate of taf by lymphatic endothelial cells	-	1.0	0.0

Table 8 List of biological parameters changed for long term 256^3 and 512^3 simulations.

2.5.2 Numerical Solution

The coupled nature of mixture models has led to development of numerical solution frameworks [148-151], as described in [119] for the model in [118], and as summarized by the Adaptive Multigrid Solver:

For each level $\ell = \ell_{min}$ to ℓ_{max}
    If $\ell = \ell_{min}$
        $\overline{\psi}_{\ell_{min}}^{t,0,v_0} = \text{SMOOTH}\left(v_0, \psi_{\ell_{min}}^{t,r=0}, L_\ell, R_\ell\right)$
    Else
        If $\ell < \ell_{global}$
$r = r + 1$
$\psi_\ell^{t,r} = \text{ADAPTFAS}\left(K, \gamma, \tau_\ell, v_0, v_1, v_2, v_b, \psi_\ell^{t,r-1}, \psi_{\ell-1}^{t,r-1}, L_\ell, R_\ell\right)$
        Else
            Do
$r = r + 1$
$\psi_\ell^{t,r} = \text{ADAPTFAS}\left(L, \gamma, \tau_\ell, v_0, v_1, v_2, v_b, \psi_\ell^{t,r-1}, \psi_{\ell-1}^{t,r-1}, L_\ell, R_\ell\right)$
            While $\left(\left\| R_\ell - L_\ell\left(\psi_\ell^{t,r}\right)\right\| > \tau_\ell\right)$
        End If
    End If
    If $\ell < \ell_{global}$
        Find prolongate solution $\psi_{\ell+1}^{t,r-1} = \text{PROLONGATE}\left(\psi_\ell^{t,r-1}\right)$
    Else If $\ell_{global} \leq \ell < \ell_{max}$
$F_\ell^{t,r-1} = \text{FLAG}(\psi_\ell^{t,r-1})$
If $F_\ell^{t,r-1} \neq \emptyset$
        Create block $B_{\ell+1} \subseteq \Omega_{\ell+1}$:
        $B_{\ell+1} =$
$\text{BLOCKGEN}\left(F_\ell^{t,r-1}, \eta_{threshold}, threshold_{size}, \eta_{min}\right)$
        Find prolongate solution $\psi_{\ell+1}^{t,r-1} = \text{PROLONGATE}\left(\psi_\ell^{t,r-1}\right)$
    Else
        Break
    End If
    End If
End For

where ADAPTFAS, PROLONGATE, BLOCKGEN, and SMOOTH are defined in [119] and the variables and parameters are respectively defined in **Table 9** and **Table 10**.

In each section, openMP improved algorithm performance by parallelizing operations performed on Ω_ℓ.

Computational Variable	Description
Ω_ℓ	Model domain at level ℓ
ℓ	Level index (zero-indexed)
γ_ℓ	Cycle Index for Level ℓ
r	Multigrid iteration number
t	Time step index
$\psi_\ell^{t,r}$	Solution on level ℓ at time step t and iteration r
$\bar{\psi}_{\ell_{min}}^{t,0,v_0}$	Initial solution estimate for time step t at level $\ell = \ell_{min}$ and Multigrid iteration $r = 0$ using v_0 smoothing steps
L_ℓ	Left-hand side equation terms for level ℓ
R_ℓ	Right-hand side equation terms for level ℓ

Table 9 Computational Variables from [119].

Computational Parameter	Description	Value
ℓ_{global}	Finest level that always spans Ω_ℓ (zero-indexed)	2
ℓ_{max}	Finest grid level used on Ω (zero-indexed)	4
θ	Time step size (days)	$1*10^{-2}$
γ	Cycle Index (1 for V-cycle, 2 for W-cycle)	1
σ	Tolerance reduction factor from level ℓ to $\ell + 1$	4.0
$\tau_{\ell_{max}}$	Solution Tolerance for level ℓ_{max}	$5*10^{-4}$
v_0, v_1, v_2, v_b	Preset number of smoothing steps	4,2,2,2

$\eta_{min}, \eta_{threshold}$	Minimum and threshold efficiencies, respectively	0.5, 0.9
$threshold_{size}$	Minimum block size requirement for block generation	10^3

Table 10 Computational Parameters from [119].

2.5.3 Supplementary Figure
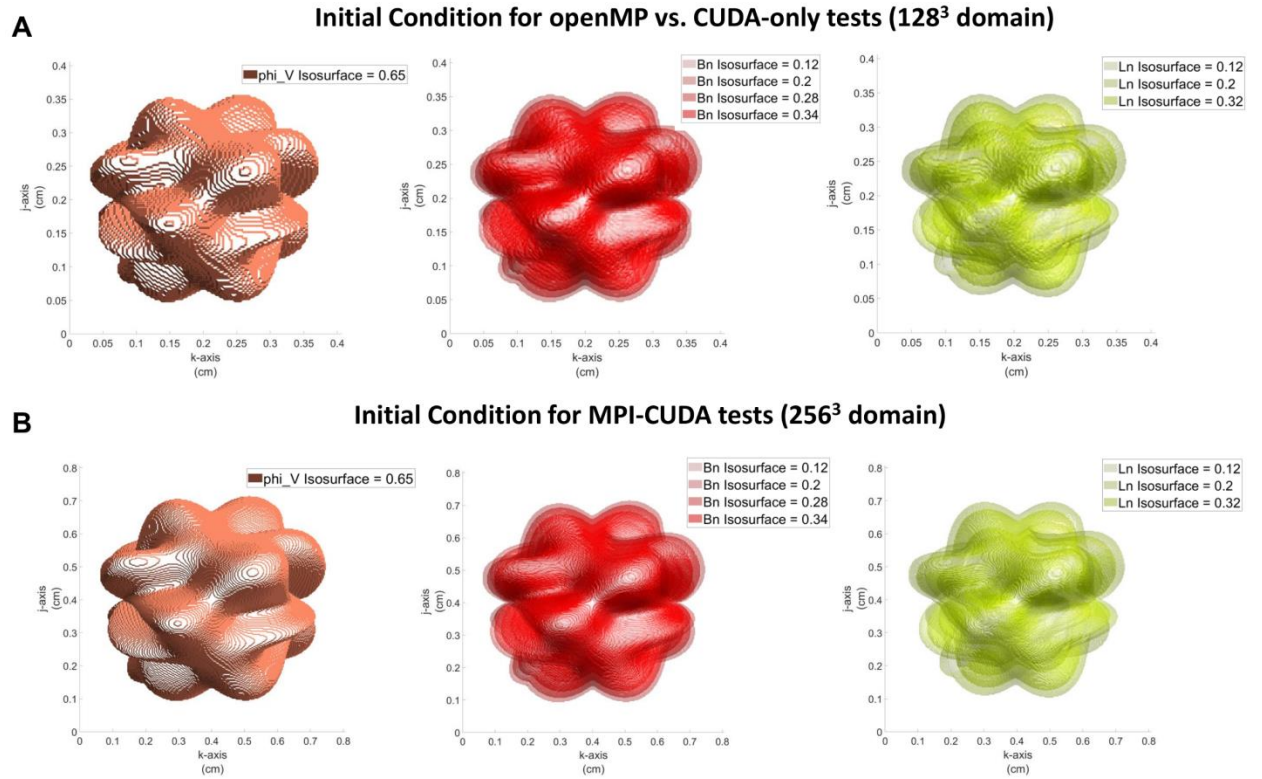
Figure 9 Initial conditions for performance tests showing plane *jk* view for nondimensionalized tumor viable fraction $\widetilde{\phi}_V$ (phi_V), blood vasculature (Bn), and lymphatic vasculature (Ln). (A) openMP vs. CUDA only (128^3 domain); (B) MPI-CUDA (256^3 domain). Tumor non-symmetric shape was generated using a superposition of a spherical tumor mass, bivariate normal distributions, and periodic functions.

CHAPTER 3: EVALUATION OF INNATE AND ADAPTIVE IMMUNE SYSTEM
INTERACTIONS IN THE TUMOR MICROENVIRONMENT VIA A 3D
CONTINUUM MODEL[2]

3.1 Introduction

The immune system has the capability to exert both pro-tumor and anti-tumor stimuli in
the tumor microenvironment (TME), the net effect of which may lead to either tumor
control or tumor escape. It is difficult, however, to evaluate whether particular patient
tumor conditions favor an anti- or pro-tumor response, as elucidation of tumor-immune
interactions during cancer progression and treatment remains an ongoing challenge.
Recent reviews of the immune system's involvement in the TME have highlighted both
innate and adaptive immune species [18-20]. Neutrophils (NE), Natural Killer (NK) cells,
Dendritic (DC) cells, and Monocytes (Mo) provide a quickly mounted innate immune
response [152-156]. Monocytes differentiate into monocyte derived DC or macrophages
[157]. Anti-tumor macrophage Type 1 (M1) are cytotoxic via nitric oxide synthase 2
expression [158]. Pro-tumor macrophage Type 2 (M2) release transforming growth factor
β (TGF-β) and induce higher tumor release of Vascular Endothelial Growth Factor A
(VEGF-A), respectively promoting tumor growth and angiogenesis [159-161]. DC

initiate tumor apoptosis using contact-dependent death receptor ligands expressed on the tumor membrane [162]. NK are cytotoxic on contact against tumor cells [163, 164]. NE can eliminate cancer cells using contact-dependent hydrogen peroxide release [165]. Myeloid-derived suppressor cells (MDSC) promote tumor growth by inhibiting anti-tumor immune species, especially via stymieing $CD4^+$ and $CD8^+$ T-cell proliferation [166, 167].

In contrast, the slower reacting but longer lasting adaptive immune system comprises lymphocyte B-cells, including resting effector (BeR), active effector (BeA), and regulatory (Breg) cell lines and lymphocyte T-cells, including CD4+ helper T cells type 1 (Th1) and type 2 (Th2), CD8+ cytotoxic T lymphocytes (CTL), and regulatory T-cells (Treg). DC bridge the innate and adaptive immune responses by presenting antigens to adaptive immune cells and mediating their polarization into effector cells [168]. B-cells generally encourage angiogenesis [169, 170]. BeR transition into BeA to produce antibodies that cause tumor lysis [171]. Breg regulate immune response and pro-inflammatory immune species, including Mo, NK, CTL, Th1, and Th2, while promoting select immune species including Treg and DC [170, 172]. CTL benefit from signaling from helper T-cells and are a common target in cancer immunotherapy [173, 174]. Regulatory T-cells modulate immune responses, having been found to regulate Th1, Th2, CTL, Mo, and NK immune populations [175-179].

The intricate interactions of innate and adaptive immune systems in the TME present a complex system that would benefit from a systems-level analysis. This need is especially

52

apparent when facing the reality that these interactions remain inadequately understood.

Mathematical modeling applied to elucidate tumor-immune system interactions was

recently reviewed [64]. Due to computational cost, these models are typically constrained

to simulating a handful of immune species or interactions, yielding relevant predictions

but incapable of providing a more complete picture of these interactions [64]. For

example, tumors and immune species were abstracted into a predator-prey model in [74].

While not delineating between immune species, equilibria were categorized based on

tumor quantity, fitting the model to a B-cell lymphoma murine model to predict a

transient, dormant tumor state, followed by either successful immune-based tumor

response or continued tumor proliferation. This conclusion was further supported by a

model presented in [75]. In [180] the immune response of NK and CTL with metastatic

melanoma was evaluated using a temporal model that incorporated NK to CTL

interactions. Model parameters were calibrated with patient-specific data and used to

explore the effects of NKG2D ligand-based stimulation of NK and CTL. A hybrid

mathematical model was derived in [65] to simulate macrophage interactions with tumor

associated macrophages (TAMs), including M1, M2, and Tie2-expressing macrophages.

This approach was built upon in [57, 59, 60] to evaluate the targeting of macrophages as

vehicles to deliver drug-loaded nanovectors into hypo-vascularized tumor lesions. A

hybrid mathematical model in [77] was used to simulate an adaptive immune response

against lymph node metastases that suppressed immune response via the PD-1/PD-L1

pathway by considering T-cell differentiation into either helper-T-cells (CD4+) or CTL,

maturation of T-cells, and intracellular responses to cell signaling. In addition, the

interactions of T lymphocytes with the TME have been explored via mathematical

modeling [67, 78]. Although these models demonstrate a wide range of interactions and

immune species, each individual application specializes model derivation, potentially

neglecting particular immune species and their interactions in the TME [64, 79].

Recently, a quantitative systems pharmacology model was coupled with a 3D agent-based

model to bridge from the tissue to the cell scale, simulating tumor growth, multiple

immune species, including CTL, Treg, and MDSC, as well as select local tumor-immune

interactions [71].

Here, a distributed computing implementation is leveraged to simulate a wide

variety of tumor-immune interactions in 3D, building upon the continuum mixture

representation of desmoplastic tumor growth presented in [82, 83, 181]. Continuum

mixture models represent tumors as multiple phases within a single domain, enabling the

simulation of large tissue without the need for tracking individual cells. Early work [92-

96, 98-106, 108-110, 112, 182-184] has led to the development of various diffuse-

interface models [84, 85, 185, 186]. A continuum mixture model that simulates

desmoplastic tumor tissue, extracellular matrix (ECM), nutrient uptake, vasculature

formation, and tumorigenic species in a 3D domain was recently presented [82]. Here, the

scope of the model in [82] is increased to include immune cell species and their

interactions, as well as chemokine production promoting leukocyte and lymphocyte

extravasation and directing chemotaxis [187, 188]. Immune species modeled include Mo,

M1, M2, NK, DC, MDSC, NE, BeR, BeA, Breg, CTL, Treg, Th1, and Th2. This system

enables representing intricate biological interactions of innate and adaptive immune

responses in the TME. Longer term, the goal is to establish a framework that can evaluate patient tumor-specific immunotherapeutic interventions.

3.2 Mathematical Model

3.2.1 3D Model Summary

The 3D model of desmoplastic vascularized tumor growth in [82] presents key equations in their non-dimensionalized form, as follows [82, 83]:

$$\frac{\partial \phi_V}{\partial t} + \nabla \cdot (\phi_V u_\alpha) = M \nabla \cdot (\phi_V \nabla \mu_T) + S_V \qquad \text{Equation 3.2.1}$$

$$\mu_T = \frac{\partial F_b}{\partial \phi_T} - \epsilon_T^2 \cdot \nabla^2 \phi_T - \epsilon_{TE}^2 \cdot \nabla^2 \phi_E \qquad \text{Equation 3.2.2}$$

$$\mu_E = \frac{\partial F_b}{\partial \phi_E} + \frac{\partial \mathcal{W}}{\partial \phi_E} - \epsilon_E^2 \cdot \nabla^2 \phi_E - \epsilon_{TE}^2 \cdot \nabla^2 \phi_T \qquad \text{Equation 3.2.3}$$

$$\frac{\partial \mathcal{W}}{\partial \phi_E} = \epsilon_e \cdot [6 \cdot \phi_E (1 - \phi_E)] \cdot \sum_{i,j=1}^{3} \left[\frac{1}{2} \cdot (\mathcal{E}_T)_{ij} \cdot \mathbb{T}_{ij}^* - (\mathcal{E}_T^*)_{ij} \cdot \mathbb{T}_{ij} \right] \qquad \text{Equation 3.2.4}$$

$$\mathbb{T}_{mn}^* = 2 \cdot (1 - L_2^C) \cdot (\mathcal{E}_T)_{mn} + (L_1^E - L_1^C) \cdot \delta_{mn} \cdot \sum_{k=1}^{3} (\mathcal{E}_T)_{kk} \qquad \text{Equation 3.2.5}$$

$$\mathbb{T}_{mn} = 2 \cdot L_2 \cdot (\mathcal{E}_T)_{mn} + L_1 \cdot \delta_{mn} \cdot \sum_{s=1}^{3} (\mathcal{E}_T)_{ss} \qquad \text{Equation 3.2.6}$$

$$(\mathcal{E}_T)_{ij} = \mathcal{E}_{ij} - \mathcal{E}_{ij}^* \qquad \text{Equation 3.2.7}$$

$$\mathcal{E}_{ij}^* = Q_3(\phi_E) \cdot (\mathcal{E}_T^*)_{ij} + (\mathcal{E}_C^*)_{ij} \qquad \text{Equation 3.2.8}$$

$$(\mathcal{E}_T^*)_{ij} = (\mathcal{E}_E^*)_{ij} - (\mathcal{E}_C^*)_{ij} \qquad \text{Equation 3.2.9}$$

$$\mathcal{E}_{mn} = \frac{1}{2} \cdot \left(\frac{\partial u_m^d}{\partial x_n} + \frac{\partial u_n^d}{\partial x_m} \right) \qquad \text{Equation 3.2.10}$$

$$L_i = Q_3(\phi_E) \cdot (L_i^E - L_i^C) + L_i^C, i = 1,2 \qquad \text{Equation 3.2.11}$$

$$Q_3(x) = x^2 \cdot (3 - 2x) \qquad \text{Equation 3.2.12}$$

$$\nabla \cdot \left[k_\alpha \cdot \left(\nabla p - \frac{\gamma_T}{\epsilon_T} \mu_T \nabla \phi_T - \frac{\gamma_E}{\epsilon_E} \mu_E \nabla \phi_E \right) \right] = -(S_V + S_D + S_E)$$

<div align="right">Equation 3.2.13</div>

$$u_\alpha = -k_\alpha \cdot \left[\nabla p - \frac{\gamma_T}{\epsilon_T} \mu_T \nabla \phi_T - \frac{\gamma_E}{\epsilon_E} \mu_E \nabla \phi_E \right]$$

<div align="right">Equation 3.2.14</div>

$$\nabla \cdot (D_n \nabla n) + k_{n1} n_C - (k_{n1} + k_{n2}) \cdot n = 0$$

<div align="right">Equation 3.2.15</div>

$$\nabla \cdot \left(D_{tgf} \nabla(tgf) \right) + \lambda_{tgf} - \left(\lambda_{tgf} + \lambda_{de,tgf} + \lambda_{U,tgf} \right) \cdot tgf = 0$$

<div align="right">Equation 3.2.16</div>

$$\nabla \cdot \left(D_{taf} \nabla(taf) \right) + \lambda_{taf} - \left(\lambda_{taf} + \lambda_{de,taf} + \lambda_{U,taf} \right) \cdot taf = 0$$

<div align="right">Equation 3.2.17</div>

$$\frac{\partial m}{\partial t} = \nabla \cdot (D_m \cdot \nabla m) + S_m$$

<div align="right">Equation 3.2.18</div>

$$\frac{\partial B_n^E}{\partial t} + \nabla \cdot (B_n^E u_E) = -\nabla \cdot \boldsymbol{J}_{BnE} + S_{BnE}$$

<div align="right">Equation 3.2.19</div>

$$\frac{\partial L_n^E}{\partial t} + \nabla \cdot (L_n^E u_E) = -\nabla \cdot \boldsymbol{J}_{LnE} + S_{LnE}$$

<div align="right">Equation 3.2.20</div>

where subscripts and term values in Equation 3.2.1 through Equation 3.2.20 are in

Tables 11 through **13**, and

$$\delta_{mn} = \begin{cases} 0, m \neq n \\ 1, m = n \end{cases}.$$

<div align="right">Equation 3.2.21</div>

Table 14 summarizes the non-dimensionalization parameters from **Tables 11** and

13.

General Subscript	Description
T	Tumor tissue
V	Viable tumor tissue
D	Dead tumor tissue
E	ECM
H	Host tissue

Table 11 General Subscripts.

Dependent Variable	Biological Representation	Scaling Factor
ϕ_σ	Volume fraction of species σ	$\tilde{\phi}_\alpha$ (fixed solid volume fraction)
ϕ_E	Extracellular matrix volume fraction	$\tilde{\phi}_\alpha$
ϕ_H	Healthy host tissue volume fraction	$\tilde{\phi}_\alpha$
u_α	Solid tissue velocity	$\dfrac{\mathcal{L}}{\mathcal{T}}$
u_E	Extracellular Matrix velocity	$\dfrac{\mathcal{L}}{\mathcal{T}}$
μ_σ	Chemical potential species σ	E_a^*
u^d	Displacement vector	$\mathcal{L}$
p	Solid phase tumor tissue pressure	$\mathcal{P}$
n	Concentration of oxygen	$\tilde{n}_\infty$
tgf or TGF	Concentration of tumor growth factors	tgf_{sat}
taf or TAF	Net concentration of tumor pro-angiogenic factors	taf_{sat}
m	Concentration of Matrix Degrading Enzymes	m_{sat}
B_n^E	New blood vasculature	$\tilde{B}_{max}$
L_n^E	New Lymphatic vasculature	$\tilde{L}_{max}$

Table 12 Non-dimensionalized Variables from Equation 3.2.1 through Equation

3.2.20. Here, species refers to subscripts in **Table 11**.

Parameter	Biological Representation	Parameter Definition	Non-dimensionalization
M	Cell mobility	[82]	$\mathcal{M}$

S_V	Viable tumor tissue source		
S_D	Dead/necrotic rumor tissue source		$\tilde{\phi}_\alpha \cdot \mathcal{T}$
S_E	Extracellular matrix source		
S_{BnE}	Blood vasculature source		$\tilde{B}_{max} \cdot \mathcal{T}$
S_{LnE}	Lymphatic vasculature source		$\tilde{L}_{max} \cdot \mathcal{T}$
$\mathcal{W}$	Elastic energy		$\tilde{\phi}_\alpha \cdot E_a^*$
F_b	Bulk free energy		$\tilde{\phi}_\alpha \cdot E_a^*$
L_1^E & L_2^E	Lamé constants for ECM components		L_2^E & L_2^E
L_1^C & L_2^C	Lamé constants for cell components		L_2^E & L_2^E
ϵ_σ	Interaction strength within species σ		$\bar{\bar{\epsilon}}$
$\epsilon_{\sigma\tau}$	Interaction strength between different species σ and τ		$\bar{\bar{\epsilon}}$
ϵ_e	Strain energy coefficient		$\bar{\bar{\epsilon}}_e$
γ_σ	Adhesion parameter for species σ		$\gamma_\sigma = \dfrac{\epsilon_\sigma \cdot \tilde{\phi}_\alpha \cdot \sqrt{\tilde{\phi}_\alpha \cdot E_a^*}}{\mathcal{L} \cdot \mathcal{P}}$
$\mathcal{E}$	Infinitesimal strain		$\bar{\bar{\mathcal{E}}}$
$\mathcal{E}_E^*$	Eigenstrain tensor for ECM		$\bar{\bar{\mathcal{E}}}$
$\mathcal{E}_C^*$	Eigenstrain tensor for cells	[83]	$\bar{\bar{\mathcal{E}}}$
k_{n1}	Oxygen Rate constants		$\lambda_{U,V,n}$
k_{n2}			$\lambda_{U,V,n}$
k_α	Motility of the solid phase	[82]	$\bar{\bar{k}}_\alpha$

D_σ	Diffusivity of species $\sigma \in \{n, tgf, taf\}$		$D_{n,T}$
λ_σ	Production rate of $\sigma \in \{tgf, taf\}$		$\lambda_{U,V,n}$
$\lambda_{de,\sigma}$	Degradation rate for $\sigma \in \{tgf, taf\}$		$\lambda_{U,V,n}$
$\lambda_{U,\sigma}$	Total uptake rate for $\sigma \in \{tgf, taf\}$		$\lambda_{U,V,n}$
$\boldsymbol{J}_{BnE}$	Blood vasculature diffusive flux		$\tilde{B}_{max} \cdot \mathcal{T}$
$\boldsymbol{J}_{LnE}$	Lymphatic vasculature diffusive flux		$\tilde{L}_{max} \cdot \mathcal{T}$

Table 13 Parameters in Equation 3.2.1 through Equation 3.2.20.

Non-dimensionalization parameters	Description	Definition or Assigned Value
$\tilde{\phi}_\alpha$	Fixed Solid Volume Fraction	0.8
E_a^*	Energy Scale for Adhesion	0.001
E_e^*	Energy Scale for Elastic Effects	0.001
$\bar{\bar{k}}_\alpha$	Characteristic Solid Species Motility	1.0
$\mathcal{L}$	Characteristic Length	$\sqrt{\dfrac{D_{T,n}}{\lambda_{U,V,n}}}$
$\mathcal{P}$	Characteristic Pressure	$\dfrac{\mathcal{L}^2}{\bar{\bar{k}}_\alpha \cdot \mathcal{T}}$
$\mathcal{M}$	Characteristic Mobility	$\dfrac{\mathcal{L}^2}{\mathcal{T} \cdot E_a^*}$
$\bar{\bar{\epsilon}}$	Characteristic Interaction Strength	$\mathcal{L} \cdot \sqrt{\dfrac{E_a^*}{\tilde{\phi}_\alpha}}$

$\bar{\bar{\varepsilon}}$	Characteristic Strain	$\sqrt{\dfrac{E_a^* \cdot \tilde{\phi}_\alpha}{E_e^* \cdot \bar{\bar{\epsilon}} \cdot L_2^E}}$

Table 14 Non-dimensionalization parameters. Assigned values were obtained from [181].

3.2.2 Immune Species Definitions and Interactions

The 3D tumor model summarized in **Section 3.2.1** is expanded in this study by adding key immune cell species, described in **Table 15**.

Immune Cell Species	Abbreviation	Model Variable
Monocytes	Mo	M_0
M1 macrophages	M1	M_1
M2 macrophages	M2	M_2
Natural killer cells	NK	NK
Neutrophils	NE	Ne
Dendritic Cells	DC	Den
Myeloid-Derived Suppressor Cells	MDSC	$MDSC$
B-effector cells in resting state	BeA	$B_E R$
B-effector cells in active state	BeR	$B_E A$
Regulatory B-cells	Breg	B_{reg}
Cytotoxic T Lymphocytes (CD8+)	CTL	T_C
Regulatory T-cells	Treg	T_R
Helper T-Cells	Th1	T_{H1}
	Th2	T_{H2}

Table 15 Immune cell species simulated in the model.

Table 16 summarizes the classifications for each immune species as a pro- or anti- tumor species. The list of immune-immune interactions incorporated in the model is in **Table 17**. **Table 18** lists immune interactions with non-immune species. As the existence and net effect of macrophage interactions with Treg are not fully elucidated [189], these interactions are left for future work. It has been hypothesized that Treg could inhibit DC through an IL-10 mechanism [190]. Having not found evidence proving this connection directly, this study refrains from modeling this inhibitory pathway. Neutrophils have multifaceted heterogeneous interactions with cancer, whose implementation through immune interactions is reserved for future work [191]. It has been shown *in vivo* that Breg can regulate DC antigen presentation [192]. However, this model does not include T-cell differentiation or DC antigen presentation in lymphatic tissues [193].

Immune Species	Classification (Pro- or Anti- tumor)	Biological Justification
M1	Anti-	[194]
M2	Pro-	[195]
NK	Anti-	[164]
NE	Anti-	[165]
DC	Anti-	[162, 196]
MDSC	Pro-	[167]
BeR	Pro-	[169, 170]
BeA	Anti-	[171]
Breg	Pro-	[170]
CTL	Anti-	[173]
Treg	Pro-	[175]
Th1	Anti-	[197, 198]
Th2	Pro-	[174]

Table 16 Immune cell species categorized as pro- or anti-tumor, respectively promoting or abating tumor growth.

Type	Positive Active Influence	Negative Active Influence	Differentiated /Activated From	Notes	References
Mo	Th1,Th2			Th2 contributes to M2-biased Mo differentiation via Interleukin-4 (IL-4). Th1 increase M1-biased Mo differentiation by IFN-γ.	[154, 195, 199, 200]
M1	Th1		Mo	Th1 increases activity of M1 by IFN-γ.	[195, 200]
M2	Th2		Mo	Th2 increases M2 activity by IL-4.	[195]
NK	Th1	MDSC, Treg, Breg		Upregulated by Th1. Downregulated by Breg. MDSC inhibit NK function. Treg regulate NK tumor response.	[170, 174, 178, 179, 201]
DC	Th1	MDSC		Antigen presentation upregulated by Th1. MDSC inhibit dendritic cell function through IL-10 and nitric oxide (NO).	[174, 202, 203]
MDSC	BeR, BeA, Breg			Cancer-induced B-Cells and regulatory B-cells promote MDSC activity.	[166]
BeR	Th1,Th2			CD4$^+$ T-cells activate B-cells using CD40 ligand.	[204]
BeA	Th1,Th2	MDSC	BeR	CD4$^+$ T-cells activate B-cells using CD40 ligand. Activated form of BeR. MDSC inhibit B cell response via IL-7 and STAT5.	[171, 204, 205]
Breg	Th1,Th2			CD4$^+$ T-cells activate B-cells using CD40 ligand.	[204]
CTL	Th1	MDSC, Breg, Treg, Th2		Th1 enhances CTL response through IFN-γ expression. Th2 inhibits CTL through IL-10 expression. Downregulated by Breg IL-10 expression. Inhibited by MDSC.	[170, 176, 198, 201, 206-210]

				Treg leads to T-cell exhaustion.	
Treg	MDSC, Breg			Upregulated by Breg.	[170]
Th1	M1, DC, BeA	MDSC, Breg, Treg		Treg regulates Th1 and Th2 activity. M1 encourages polarization to Th1 by IL-12. Dendritic cells present antigens to increase differentiation of T_{H0} (not modeled) to Th1 and Th2. Downregulated by Breg. Downregulated by MDSC. Co-stimulated by BeA.	[167, 170, 171, 175, 177, 194, 195, 211]
Th2	M2, DC, BeA	MDSC, Breg, Treg		Treg regulates Th1 and Th2 activity. Downregulated by Breg. M2 increases Th2 response. Downregulated by MDSC. Co-stimulated by BeA.	[167, 170, 171, 175, 177, 195, 200]

Table 17 Immune-immune species interactions implemented in the model.

Type	Noted Interactions	References
M1	Kills tumor cells using Interleukin 12 (IL-12).	[194]
M2	Promotes tumor growth via secretion of TGF-β. Promotes angiogenesis through VEGF-A expression.	[159-161]
NK	Contact Dependent perforin and granzymes release.	[164]
NE	Contact Dependent hydrogen-peroxide release.	[165]
DC	Cytotoxic via contact-dependent peroxynitrite mechanism and cytokine release.	[162, 196]
BeR	Activates angiogenesis when cells are filled with STAT3.	[169, 170]
BeA	Activates angiogenesis when cells are filled with STAT3.	[169-171]

	Kills tumor cells on contact.	
Breg	Activates angiogenesis when cells are filled with STAT3.	[169, 170]
CTL	Cytotoxic via granule exocytosis and Fas ligand-mediated apoptosis induction.	[173]
Th1	Contact-based cytotoxicity.	[212]
Th2	Activates fibroblasts and myofibroblasts via IL-4 and IL-13.	[213, 214]

Table 18 Immune species interactions with tumor system components.

3.2.3 Immune Model Formation

In this section the 3D model in **3.2.1 3D Model Summary** is extended by adding the immune species described in **3.2.2 Immune Species Definitions and Interactions** into the diffuse interface method (**3.2.3.1 Diffuse Interface Model**). This model accounts for immune-immune interactions using the equations derived in **3.2.3.2 Immune-Immune Species Interactions**. Source and sink terms for all immune species are described in **3.2.3.3 Source Terms**. Chemical potentials defined in **3.2.3.1 Diffuse Interface Model** are presented in **3.2.3.4 Immune Cell Species Chemical Potentials**. Immune interactions with the tumor and with the TME are accounted for in **3.2.3.5 Immune-Tumor Interactions** and **3.2.3.6 Immune Cell Species and the Tumor Microenvironment**, respectively. Finally, an expanded form for solid cell motility and an equation for CHE are derived in **3.2.3.7 Solid Cell Phase Motility** and **3.2.3.8 Chemokines**, respectively.

3.2.3.1 Diffuse Interface Model

Akin to [82], it is assumed there are no voids in the tumoral tissue such that solid phase α and liquid phase β constitute a saturated mixture:

$$\phi_\alpha + \phi_\beta = 1 \qquad\qquad \text{Equation 3.2.22}$$

This study redefines the collection of solid volume fractions ϕ_α to include new immune species G, along with the previously defined four dominant volume fraction types: viable (V) and dead (D) tumor mass, ECM (E), and healthy host tissue (H). Assuming further that the solid mixture lacks voids:

$$\sum_{i=1}^{N} \phi_{\alpha,i} = 1 \qquad\qquad \text{Equation 3.2.23}$$

where $\phi_{\alpha,i}$ is phase component i in the solid phase α. Here, $0 = \beta$, $1 = V$, $2 = D$, $3 = E$, all immune species $G = \{4, \dots N - 1\}$, and $N = H$. From the mixture model derivation in [82], for each $\phi_i = \phi_\alpha \cdot \phi_{\alpha,i}$:

$$\frac{\partial \phi_i}{\partial t} + \nabla \cdot \left(\phi_i \cdot \boldsymbol{u}_\alpha + \frac{1}{\rho_i} \cdot \boldsymbol{J}_{\alpha,i} \right) = \frac{1}{\rho_i} \cdot S_{\alpha,i}, 1 \le i \le N \qquad \text{Equation 3.2.24}$$

where the density and source (both positive and negative) terms of phase component i is ρ_i and S_i, respectively, the velocity of phase α is $\boldsymbol{u}_\alpha$, and $\boldsymbol{J}_{\alpha,i}$ is the diffusive flux of phase component i. Using the same approach as in [84], the total general Helmholtz free energy is

$$E = \sum_{i=0}^{N} E_i = \sum_{i=0}^{N} \int \bar{E}_i \, d\boldsymbol{x} \qquad\qquad \text{Equation 3.2.25}$$

It is assumed that the free energy of the aqueous interstitial phase is constant, thus $\phi_\beta = \tilde{\phi}_\beta$ and $\phi_\alpha = \sum_{i=1}^{N} \phi_i = 1 - \tilde{\phi}_\beta = \tilde{\phi}_\alpha$. With Lagrange multipliers p^* and q, representing the solid and liquid pressures respectively, adapting the energy form from [82]:

$$\frac{dE}{dt} = \int \left\{ \tilde{\phi}_\beta \cdot \nabla \left(\frac{\delta E}{\delta \phi_\beta} + q \right) \cdot \boldsymbol{u}_\beta + \left(\nabla p - \sum_{i=1}^{N} \frac{\delta E}{\delta \phi_i} \nabla \phi_i \right) \cdot \boldsymbol{u}_\alpha \right.$$

$$+ \sum_{i=1}^{N-1} \nabla \left[\frac{1}{\rho_i} \cdot \frac{\delta E}{\delta \phi_i} - \frac{1}{\rho_N} \cdot \frac{\delta E}{\delta \phi_N} + \frac{1}{\tilde{\phi}_\alpha} \cdot \left(\frac{1}{\rho_i} - \frac{1}{\rho_N} \right) \right.$$

$$\left. \left. \cdot \left(p - \sum_{j=1}^{N} \phi_j \cdot \frac{\delta E}{\delta \phi_j} \right) \right] \cdot \boldsymbol{J}_{\alpha,i} \right\} d\boldsymbol{x}$$

Equation 3.2.26

where $p = \tilde{\phi}_\alpha \cdot p^* + \sum_{i=1}^{N} \phi_i \cdot \frac{\delta E}{\delta \phi_i}$. Like in [82] the terms in Equation 3.2.26 are

assumed to be separately dissipative, constitutive relations that are thermodynamically

consistent. Thus:

$$\boldsymbol{u}_\beta = -k_\beta \nabla \left(\frac{\delta E}{\delta \phi_\beta} + q \right)$$

Equation 3.2.27

$$\boldsymbol{u}_\alpha = -k_\alpha \cdot \left[\nabla p - \sum_{i=1}^{N} \frac{\delta E}{\delta \phi_i} \cdot \nabla \phi_i \right]$$

Equation 3.2.28

$$\boldsymbol{J}_{\alpha,i} = -M_i \cdot \nabla \left[\frac{1}{\rho_i} \cdot \frac{\delta E}{\delta \phi_i} - \frac{1}{\rho_N} \cdot \frac{\delta E}{\delta \phi_N} + \frac{1}{\tilde{\phi}_\alpha} \cdot \left(\frac{1}{\rho_i} - \frac{1}{\rho_N} \right) \right.$$

$$\left. \cdot \left(p - \sum_{j=1}^{N} \phi_j \cdot \frac{\delta E}{\delta \phi_j} \right) \right], 1 \leq i \leq N-1$$

Equation 3.2.29

where k_α and k_β represent the motilities of the solid and liquid phases,

respectively. The generalized Helmholtz free energy equation as [82] is applied:

$$\bar{E}(\boldsymbol{\phi}, \nabla \boldsymbol{\phi}, \boldsymbol{\varepsilon}) = F_b(\boldsymbol{\phi}) + \mathcal{W}(\boldsymbol{\phi}, \boldsymbol{\varepsilon}) + \sum_{i=0}^{N} \left(\phi_i \cdot \sum_{i=1}^{L} \chi_{il}^* \cdot \sigma_l \right)$$

$$+ \sum_{i,j=0}^{N} \frac{\kappa_{ij}}{2} \cdot (\nabla \phi_i \cdot \nabla \phi_j)$$

Equation 3.2.30

where the first term represents the bulk free energy F_b (defined in Equation

3.2.31), the second term represents the elastic energy $\mathcal{W}$ as derived in [82], the third term,

as posed by [86], represents chemotaxis of cell species i with L potential CHE of concentration σ_l at strength $\chi_{il}^* > 0$ for $l \in \{1, \dots, L\}$, and the fourth term, like in [84] and [82], represents the interaction strengths $\kappa_{ij} > 0$ between cell species i and j.

From [215] the total bulk free energy of the system is:

$$F_b(\phi_0, \dots, \phi_N) = \tilde{\phi}_\beta \cdot F_\beta(\tilde{\phi}_\beta) + \tilde{\phi}_\alpha F_\alpha(\phi_1, \dots, \phi_N) \qquad \text{Equation 3.2.31}$$

where $\tilde{f}_\beta = \tilde{\phi}_\beta \cdot F_\beta(\tilde{\phi}_\beta)$ and $F_\alpha(\phi_1, \dots, \phi_N) = E_a^* \cdot f(\phi_1, \dots, \phi_N)$ where E_a^* is the positive energy scale for adhesion. Because $\tilde{f}_\beta$ is constant, $\frac{\partial F_b}{\partial \phi_\beta} = 0$. The following is defined:

$$\phi_G = \sum_{\psi \in G} \phi_\psi \qquad \qquad \text{Equation 3.2.32}$$

for all immune species $\psi \in G =$

$\{M_0, M_1, M_2, NK, Ne, Den, MDSC, B_E R, B_E A, B_{reg}, T_C, T_R, T_{H1}, T_{H2}\}$.

Without chemotactic gradients to prompt immune species migration and penetration into tumors, immune species are assumed to reside in host tissue. As such ϕ_G and ϕ_H comprise a single combined host mixture phase $\phi_{\mathbb{H}} = \phi_H + \phi_G$. Thus, the free energy describes a ternary system around the collective tumor species $\phi_T = \phi_V + \phi_D$, ϕ_E, and $\phi_{\mathbb{H}}$ where ϕ_T and $\phi_{\mathbb{H}}$ are immiscible and ϕ_E is partially miscible with $\phi_{\mathbb{H}}$ using the free energy form adapted from [151]:

$$f_\alpha(\phi_T, \phi_E, \phi_\mathbb{H})$$

$$= A_1 \cdot \left(\frac{\phi_T}{\tilde{\phi}_\alpha}\right)^2 \cdot \left(\frac{\phi_\mathbb{H}}{\tilde{\phi}_\alpha}\right)^2 + \left(\frac{\phi_T}{\tilde{\phi}_\alpha} + A_2\right) \cdot \left(\frac{\phi_E}{\tilde{\phi}_\alpha} - A_3\right)^2$$

$$+ \left(\frac{\phi_\mathbb{H}}{\tilde{\phi}_\alpha} + A_4\right) \cdot \left(\frac{\phi_E}{\tilde{\phi}_\alpha} - A_5\right)^2$$

Equation 3.2.33

Substituting $\phi_\mathbb{H} = \tilde{\phi}_\alpha - \phi_E - \phi_T$ into Equation 3.2.33 obtains:

$$\frac{\partial F_b}{\partial \phi_\mathbb{H}} = \frac{\partial F_b}{\partial \phi_\mathbb{H}} = \frac{\partial F_b}{\partial \phi_H} = \frac{\partial F_b}{\partial \phi_\psi} = 0, \psi \in G$$

Equation 3.2.34

As in [82], it is assumed that cell types have the same, constant misfit tensor for

the elastic energy $\mathcal{W}$. Thus, $\frac{\partial w}{\partial \phi_j} = 0$ for all $j \neq E$ and the form for $\frac{\partial w}{\partial \phi_E}$ remains as shown

in Equation 3.2.4 through Equation 3.2.10.

Because the liquid phase has no chemotaxis, $\chi_{0l} = 0$ for $l \in \{1, \dots, L\}$. In this

model, immune species chemotaxis occurs from high free energy regions to low free

energy regions across the modeling domain Ω. Thus, $\chi_{\tau l}^* < 0$ implies σ_l has an attractive

effect on cell species τ and $\chi_{\tau l}^* > 0$ implies τ is repulsed by σ_l. Because this study

simulates chemoattractants only, $\chi_{\tau l} = -\chi_{\tau l}^*$ for clarity. Thus, $\chi_{\tau l} > 0$ and $\chi_{\tau l} < 0$ imply

attraction and repulsion, respectively, of cell species τ with respect to σ_l.

It is assumed that all immune species have the same interaction strengths, i.e.,

$\kappa_{ij} = \kappa_{ji} = \kappa_{ii} = \kappa_{GG}$ for all $i, j \in G$. The total interaction strength between immune

species can then be represented as:

$$\frac{\kappa_{GG}}{2} \cdot \left[\left(\sum_{k \in G} [\nabla\phi_k \cdot \nabla\phi_k] \right) + \sum_{i,j \in G, i \neq j} [\nabla\phi_i \cdot \nabla\phi_j] \right] = \frac{\kappa_{GG}}{2} \cdot \left[\left(\nabla \sum_{k \in G} \phi_k \right)^2 \right]$$

$$= \frac{\kappa_{GG}}{2} \cdot |\nabla\phi_G|^2$$

<div style="text-align:right">Equation 3.2.35</div>

Assuming that immune species can travel unhindered through the solid cell phase, $\kappa_{\psi i} = 0$ for $i \in \{V, D, E, H\}$. The liquid phase is assumed to have negligible interactions; thus, $\kappa_{0\xi} = \kappa_{\xi 0} = 0$ for $\xi \in \{V, D, E, H, G\}$. Eliminating ϕ_H through the relation $\nabla\phi_H = -\nabla\phi_E - \nabla\phi_T - \nabla\phi_G$ results in:

$$\sum_{i,j=0}^{N} \frac{\kappa_{ij}}{2} \cdot \left(\nabla\phi_i \cdot \nabla\phi_j \right)$$

$$= \frac{\epsilon_E^2}{2} \cdot |\nabla\phi_E|^2 + \frac{\epsilon_T^2}{2} \cdot |\nabla\phi_T|^2 + \frac{\epsilon_G^2}{2} \cdot |\nabla\phi_G|^2 + \epsilon_{TE}^2$$
$$\cdot (\nabla\phi_T \cdot \nabla\phi_E) + \epsilon_{EG}^2 \cdot (\nabla\phi_E \cdot \nabla\phi_G) + \epsilon_{TG}^2 \cdot (\nabla\phi_T \cdot \nabla\phi_G)$$

<div style="text-align:right">Equation 3.2.36</div>

where

$$\epsilon_E^2 = \kappa_{EE} - 2\kappa_{EH} + \kappa_{HH}$$
$$\epsilon_T^2 = \kappa_{TT} - 2\kappa_{TH} + \kappa_{HH}$$
$$\epsilon_{TE}^2 = \kappa_{HH} + \kappa_{TE} - \kappa_{TH} - \kappa_{EH}$$
$$\epsilon_G^2 = \kappa_{GG} + \kappa_{HH}$$
$$\epsilon_{EG}^2 = \kappa_{HH} - \kappa_{EH}$$
$$\epsilon_{TG}^2 = \kappa_{HH} - \kappa_{TH}$$

<div style="text-align:right">Equation 3.2.37</div>

Combining Equations Equation 3.2.30 and Equation 3.2.36 into the Euler-Lagrange equation $\frac{\delta E}{\delta \phi_j} = \frac{\partial E}{\partial \phi_j} - \nabla \cdot \frac{\partial E}{\partial \nabla\phi_j}$ gives:

$$\frac{\delta E}{\delta \phi_j} = \frac{\partial F_b}{\partial \phi_j} + \frac{\partial \mathcal{W}}{\partial \phi_j} - \sum_{l=1}^{L} \chi_{jl} \cdot \sigma_l - \sum_{i \in \{T,E,G\}} \left[\epsilon_i^2 \cdot \nabla^2\phi_i \cdot \frac{\partial \nabla\phi_i}{\partial \nabla\phi_j} \right]$$

$$- \sum_{mn \in \{TE, EG, TG\}} \epsilon_{mn}^2$$
$$\cdot \left(\nabla^2\phi_m \cdot \frac{\partial \nabla\phi_n}{\partial \nabla\phi_j} + \nabla^2\phi_n \cdot \frac{\partial \nabla\phi_m}{\partial \nabla\phi_j} \right)$$

<div style="text-align:right">Equation 3.2.38</div>

Recognizing that $\frac{\partial \nabla \phi_G}{\partial \nabla \phi_\psi} = 1$ for all $\psi \in G$, $\frac{\partial W}{\partial \phi_\tau} = 0$ for $\tau \neq E$, and $\chi_{il} = 0$ where

$i \in \{T, E\}$, combining Equation 3.2.33, Equation 3.2.34, and Equation 3.2.38 obtains:

$$\frac{\delta E}{\delta \phi_\beta} = \frac{\partial F_b}{\partial \phi_\beta} = 0 \qquad \text{Equation 3.2.39}$$

$$\frac{\delta E}{\delta \phi_E} = \mu_E = \frac{\partial F_b}{\partial \phi_E} + \frac{\partial W}{\partial \phi_E} - \epsilon_E^2 \cdot \nabla^2 \phi_E - \epsilon_{TE}^2 \cdot \nabla^2 \phi_T - \epsilon_{EG}^2 \cdot \nabla^2 \phi_G \qquad \text{Equation 3.2.40}$$

$$\frac{\delta E}{\delta \phi_T} = \frac{\delta E}{\delta \phi_V} = \frac{\delta E}{\delta \phi_D} = \mu_T$$

$$= \frac{\partial F_b}{\partial \phi_T} - \epsilon_T^2 \cdot \nabla^2 \phi_T - \epsilon_{TE}^2 \cdot \nabla^2 \phi_E - \epsilon_{TG}^2 \cdot \nabla^2 \phi_G \qquad \text{Equation 3.2.41}$$

$$\frac{\delta E}{\delta \phi_\psi} = \mu_\psi = -\sum_{l=1}^{L} \chi_{\psi l} \cdot \sigma_l - \epsilon_G^2 \cdot \nabla^2 \phi_G - \epsilon_{EG}^2 \cdot \nabla^2 \phi_E - \epsilon_{TG}^2$$

$$\cdot \nabla^2 \phi_T, \psi \in G \qquad \text{Equation 3.2.42}$$

$$\frac{\delta E}{\delta \phi_H} = \mu_H = \frac{\partial F_b}{\partial \phi_H} = 0 \qquad \text{Equation 3.2.43}$$

where $\frac{\partial W}{\partial \phi_E}$ remains as derived in [82]. Substituting into Equation 3.2.27 and

Equation 3.2.28 obtains:

$$\boldsymbol{u}_\beta = -k_\beta \nabla q \qquad \text{Equation 3.2.44}$$

$$\boldsymbol{u}_\alpha = -k_\alpha \cdot \left(\nabla p - \mu_T \nabla \phi_T - \mu_E \nabla \phi_E - \sum_{i \in G} \mu_i \nabla \phi_i \right) \qquad \text{Equation 3.2.45}$$

Keeping the assumption of cell species densities matching such that $\rho_i = \rho$, for

each flux term with the relation $\sum_{i=1}^{N} \boldsymbol{J}_{\alpha,i} = 0$, yields:

$$\boldsymbol{J}_{\alpha,1} = \boldsymbol{J}_{\alpha,V} = -M \phi_V \rho \nabla \mu_T$$

$$\boldsymbol{J}_{\alpha,2} = \boldsymbol{J}_{\alpha,D} = -M \phi_D \rho \nabla \mu_T$$

$$\boldsymbol{J}_{\alpha,3} = \boldsymbol{J}_{\alpha,E} = -M \phi_E \rho \nabla \mu_E \qquad \text{Equation 3.2.46}$$

$$\boldsymbol{J}_{\alpha,\sigma} = -M \phi_\sigma \rho \nabla \mu_\sigma, \sigma = 4,5,\dots,N-1$$

$$J_{\alpha,N} = J_{\alpha,H} = -\sum_{k=1}^{N-1} J_{\alpha,k} = M\rho\left(\phi_T\nabla\mu_T + \phi_E\nabla\mu_E + \sum_{\sigma\in G}\phi_\sigma\nabla\mu_\sigma\right)$$

Substituting into Equation 3.2.24 yields:

$$\frac{\partial\phi_V}{\partial t} + \nabla\cdot(\phi_V\cdot\boldsymbol{u}_\alpha) = M\nabla\cdot(\phi_V\cdot\nabla\mu_T) + S_V$$

$$\frac{\partial\phi_D}{\partial t} + \nabla\cdot(\phi_D\cdot\boldsymbol{u}_\alpha) = M\nabla\cdot(\phi_D\cdot\nabla\mu_T) + S_D$$

$$\frac{\partial\phi_E}{\partial t} + \nabla\cdot(\phi_E\cdot\boldsymbol{u}_\alpha) = M\nabla\cdot(\phi_E\cdot\nabla\mu_E) + S_E$$

$$\frac{\partial\phi_\sigma}{\partial t} + \nabla\cdot(\phi_\sigma\cdot\boldsymbol{u}_\alpha) = M\nabla\cdot(\phi_\sigma\cdot\nabla\mu_\sigma) + S_\sigma, \sigma\in G$$

Equation 3.2.47

$$\frac{\partial\phi_H}{\partial t} + \nabla\cdot(\phi_H\cdot\boldsymbol{u}_\alpha)$$

$$= -M\nabla\cdot\left(\phi_T\cdot\nabla\mu_T + \phi_E\cdot\nabla\mu_E + \sum_{\sigma\in G}\phi_\sigma\nabla\mu_\sigma\right)$$

$$+ S_H$$

where $S_i = S_{\alpha,i}/\rho$. From mass exchange, it is assumed that homeostatic healthy host tissue remains in equilibrium with any changes negligible compared to tumor and immune cells. Thus, $S_H = 0$. Because mass is conserved, the mass exchange between solid and liquid phases is:

$$S_\beta = -S_\alpha = -\left(S_V + S_D + S_E + \sum_{i\in G}S_i\right)$$

Equation 3.2.48

This relation implies that immune species penetration is accompanied by an equivalent displacement of aqueous interstitial components from the system. Also, extending the source assumption in [82], it is assumed that immune species death is instantly processed and converted to fluid into the interstitial space, and that immune species departure through the lymphatic vasculature occurs concomitantly with an equivalent addition of aqueous interstitial components.

3.2.3.2 Immune-Immune Species Interactions

Interactions between any two particular immune species are governed by their density in the model domain, represented by volume fractions, and the relative activation level of each species. The overall activation level of an immune species σ is labeled as a unit-less adjustment factor $\mathcal{A}_{I|\sigma}$ with a range from 0 to 1. Each interaction between two species has an associated unit-less constant $\lambda_{\varphi|\sigma} \in \mathbb{R}^+$ where the interaction consists of species φ influencing species σ. The immune-species interactions depend on the volume fractions of both φ and σ, as well as the activation levels of each species. Thus, a system of equations is required to solve for all the adjustment factors. The solution of the system creates activation levels that influence immune-tumor interactions and immune promotion of tumor growth factors (TGF) and tumor angiogenic factors (TAF) release, ECM formation, and angiogenesis.

Each dual-species interaction can contribute either positively or negatively to the activity level of species σ. For any immune species σ, positive interactions with species τ_1 through τ_n fall in a positive (i.e. stimulatory) contribution set $T_\sigma^+ = \{\tau_1, \tau_2, ..., \tau_n\}^+$. Likewise, negative (i.e. suppressive or inhibitory) influences with species ζ_1 through ζ_m fall in a negative contribution set $Z_\sigma^- = \{\zeta_1, \zeta_2, ..., \zeta_m\}^-$. Together they form the set $I_\sigma = \{T_\sigma^+, Z_\sigma^-\}$. For any species $\tau \in T_\sigma^+$, the contribution to $\mathcal{A}_{I|\sigma}$ is:

$$F(\tau) = \mathcal{A}_{I|\tau} \cdot Q_3\left(\frac{\phi_\tau}{\phi_{GG}}\right)$$

<div align="right">Equation 3.2.49</div>

where Q_3 is a cubic interpolation function $Q_3(x) = \begin{cases} 0, x \leq 0 \\ x^2 \cdot (3 - 2x), 0 < x \leq 1 \\ 1, \ x > 1 \end{cases}$ and

ϕ_{GG} is the saturation volume fraction for immune species interactions. Incorporation of

species-specific saturation volume fractions, assumed to be equal in this study, is left to future work. For any species $\zeta \in Z_\sigma^-$, the contribution to $\mathcal{A}_{I|\sigma}$ is:

$$G(\zeta) = 1 - \mathcal{A}_{I|\zeta} \cdot Q_3\left(\frac{\phi_\zeta}{\phi_{GG}}\right)$$

<div align="right">Equation 3.2.50</div>

As shorthand, $\{\tau_1, \tau_2, \ldots, \tau_n\}_\sigma^+$ in subsequent equations represents the sum of all $F(\tau_i)$ terms for all immune species τ_i where $i \in T_\sigma^+$. Likewise, $\{\zeta_1, \zeta_2, \ldots, \zeta_m\}_\sigma^-$ represents the sum of all $G(\zeta_j)$ terms for all immune species ζ_j where $j \in Z_\sigma^-$.

Because $Q_3(x) \in [0,1]$ each interaction can be represented as a weighted average of interaction contributions, with weights $\lambda_{i|\sigma}$ for $i \in I_\sigma$:

$$\mathcal{A}_{I|\sigma} = \frac{\sum_{\tau \in T_\sigma^+} \lambda_{\tau|\sigma} F(\tau) + \sum_{\zeta \in Z_\sigma^-} \lambda_{\zeta|\sigma} G(\zeta)}{\sum_{i \in I_\sigma} \lambda_{i|\sigma}}$$

<div align="right">Equation 3.2.51</div>

Before applying the activity levels to each equation, the activation levels are solved by using the following set of equations:

$$\mathcal{A}_{I|M_1} = \lambda_{Base|M_1} + \left(1 - \lambda_{Base|M_1}\right) \cdot \frac{\{T_{H1}\}_{M_1}^+}{\lambda_{T_{H1}|M_1}}$$

$$= \lambda_{Base|M_1} + \left(1 - \lambda_{Base|M_1}\right) \cdot \mathcal{A}_{I|T_{H1}} \cdot Q_3\left(\frac{\phi_{T_{H1}}}{\phi_{GG}}\right)$$

<div align="right">Equation 3.2.52</div>

$$\mathcal{A}_{I|M_2} = \lambda_{Base|M_2} + \left(1 - \lambda_{Base|M_2}\right) \cdot \frac{\{T_{H2}\}_{M_2}^+}{\lambda_{T_{H1}|M_2}}$$

$$= \lambda_{Base|M_2} + \left(1 - \lambda_{Base|M_2}\right) \cdot \mathcal{A}_{I|T_{H2}} \cdot Q_3\left(\frac{\phi_{T_{H2}}}{\phi_{GG}}\right)$$

<div align="right">Equation 3.2.53</div>

$$\mathcal{A}_{I|NK} = \lambda_{Base|NK} + \left(1 - \lambda_{Base|NK}\right) \cdot \frac{\{T_{H1}\}_{NK}^+ + \{B_{reg}, MDSC, T_R\}_{NK}^-}{\sum \lambda_{I_{NK}|NK}}$$

<div align="right">Equation 3.2.54</div>

$$\mathcal{A}_{I|Ne} = \lambda_{Base|Ne}$$

<div align="right">Equation 3.2.55</div>

$$\mathcal{A}_{I|Den} = \lambda_{Base|Den} + \left(1 - \lambda_{Base|Den}\right) \cdot \frac{\{T_{H1}\}_{Den}^+ + \{MDSC\}_{Den}^-}{\sum \lambda_{I_{Den}|Den}}$$

<div align="right">Equation 3.2.56</div>

$$\mathcal{A}_{I|MDSC} = \lambda_{Base|MDSC} + \left(1 - \lambda_{Base|MDSC}\right) \cdot \frac{\{B_E R, B_E A, B_{reg}\}_{MDSC}^+}{\sum \lambda_{I_{MDSC}|MDSC}}$$

<div align="right">Equation 3.2.57</div>

$$\mathcal{A}_{I|B_ER} = \lambda_{Base|B_ER} + \left(1 - \lambda_{Base|B_ER}\right) \cdot \frac{\{T_{H1}, T_{H2}\}^+_{B_ER}}{\sum \lambda_{I_{B_ER}|B_ER}}$$

Equation 3.2.58

$$\mathcal{A}_{I|B_EA} = \lambda_{Base|B_EA} + \left(1 - \lambda_{Base|B_EA}\right) \cdot \frac{\{T_{H1}, T_{H2}\}^+_{B_EA} + \{MDSC\}^-_{B_EA}}{\sum \lambda_{I_{B_EA}|B_EA}}$$

Equation 3.2.59

$$\mathcal{A}_{I|B_{reg}} = \lambda_{Base|B_{reg}} + \left(1 - \lambda_{Base|B_{reg}}\right) \cdot \frac{\{T_{H1}, T_{H2}\}^+_{B_{reg}}}{\sum \lambda_{I_{B_{reg}}|B_{reg}}}$$

Equation 3.2.60

$$\mathcal{A}_{I|T_C} = \lambda_{Base|T_C} + \left(1 - \lambda_{Base|T_C}\right) \cdot \frac{\{T_{H1}\}^+_{T_C} + \{MDSC, B_{reg}, T_R, T_{H2}\}^-_{T_C}}{\sum \lambda_{I_{T_C}|T_C}}$$

Equation 3.2.61

$$\mathcal{A}_{I|T_R} = \lambda_{Base|T_R} + \left(1 - \lambda_{Base|T_R}\right) \cdot \frac{\{MDSC, B_{reg}\}^+_{T_R}}{\sum \lambda_{I_{T_R}|T_R}}$$

Equation 3.2.62

$$\mathcal{A}_{I|T_{H1}} = \lambda_{Base|T_{H1}} + \left(1 - \lambda_{Base|T_{H1}}\right)$$
$$\cdot \frac{\left[\{M_1, Den, B_EA\}^+_{T_{H1}} + \{B_{reg}, T_R, MDSC\}^-_{T_{H1}}\right]}{\sum \lambda_{I_{T_{H1}}|T_{H1}}}$$

Equation 3.2.63

$$\mathcal{A}_{I|T_{H2}} = \lambda_{Base|T_{H2}} + \left(1 - \lambda_{Base|T_{H2}}\right)$$
$$\cdot \frac{\{M_2, Den, B_EA\}^+_{T_{H2}} + \{B_{reg}, T_R, MDSC\}^-_{T_{H2}}}{\sum \lambda_{I_{T_{H2}}|T_{H2}}}$$

Equation 3.2.64

For each equation, $\lambda_{Base|\sigma} \in [0,1]$ represents the minimum activation level for each immune species σ. With regards to model implementation, all interaction adjustment factors are updated on a per-iteration basis using the Multigrid approach detailed in [83].

This model does not include interactions with NE, thus NE activation is assumed to be saturated. Therefore, $\lambda_{Base|Ne} = 1$.

3.2.3.3 Source Terms

3.2.3.3.1 General Definition

Most of the source terms (both positive and negative contributions) are equivalent to $S_{fund|\tau}$, species τ's general actions in the model domain Ω. In general, immune species can enter into the domain by blood vasculature [216], exit through lymphatic vasculature

[217], and die by either necrosis or apoptosis. All four phenomena are reflected in the following equation for $\sigma \in G$:

$$S_{fund|\sigma} \equiv r_{enter|\sigma} - r_{exit|\sigma} + r_{mitosis|\sigma} - r_{death|\sigma}$$

$$r_{mitosis|\sigma} = \lambda_{mitosis|\sigma} \cdot \mathcal{A}_{mitosis|\sigma} \cdot \phi_\sigma$$

Immune species enter the tumor domain via extravasation from the blood vasculature and are assumed to not be subject to mitosis [168, 218]. It is acknowledged that immune cells could proliferate in response to tumor exposure, as has been observed with effector T-cells [219, 220] and potentially with macrophages [157]; here, the mitotic activity is assumed to be negligible in order to evaluate immune interactions in a controlled manner. Thus, for this study, $\lambda_{\sigma|mitosis} = 0$. It is assumed by this model that all immune species can leave the domain via lymphatic vasculature. From this the source terms for immune species are defined:

$$r_{exit|\sigma} = \lambda_{exit|\sigma} \cdot \mathcal{A}_{exit|\sigma} \cdot \phi_\sigma$$

$$\lambda_{exit|\sigma} = \lambda_{exit|G} \cdot \left(\frac{\mathcal{F}_\sigma^{L_p} L_p + \mathcal{F}_\sigma^{L_n} L_n}{L_{max}} \right)$$

$$r_{enter|\sigma} = \lambda_{enter|\sigma} \cdot \mathcal{A}_{enter|\sigma} \cdot \tilde{\phi}_\alpha$$

$$\lambda_{enter|\sigma} = \lambda_{enter|G} \cdot \left(\frac{\mathcal{F}_\sigma^{B_p} B_p + \mathcal{F}_\sigma^{B_n} B_n}{B_{max}} \right)$$

$$r_{death|\sigma} = r_{apoptosis|\sigma} + r_{necrosis|\sigma}$$

$$r_{apoptosis|\sigma} = \lambda_{apoptosis|\sigma} \cdot \mathcal{A}_{apoptosis|\sigma} \cdot \phi_\sigma$$

$$r_{necrosis|\sigma} = \lambda_{necrosis|\sigma} \cdot \mathcal{A}_{necrosis|\sigma} \cdot \phi_\sigma$$

where immune species σ enter the domain, exit from the domain, and undergo apoptosis or necrosis with rates $\lambda_{enter|\sigma}$, $\lambda_{exit|\sigma}$, $\lambda_{apoptosis|\sigma}$ and $\lambda_{necrosis|\sigma}$,

respectively. Species σ extravasates and exits into the domain from neo- (υ_p) and pre-existing (υ_n) vasculature at a rate determined by the product of tissue-specific extravasation and exit rates $\lambda_{enter|G}$ and $\lambda_{exit|G}$, respectively, in addition to species-specific dimensionless factors $\mathcal{F}_\sigma^{\upsilon_p}$ and $\mathcal{F}_\sigma^{\upsilon_n}$ for $\upsilon = \{B, L\}$. The tissue-specific extravasation and exit rates are assumed to differ across ECM $(\lambda_{\psi,E|G})$ and cell $(\lambda_{\psi,C|G})$ domains for $\psi = \{enter, exit\}$:

$$\lambda_{\psi|G} = \lambda_{\psi,E|G} \cdot Q_3\left(\frac{\phi_E}{\tilde{\phi}_\alpha}\right) + \lambda_{\psi,C|G} \cdot \left(1 - Q_3\left(\frac{\phi_E}{\tilde{\phi}_\alpha}\right)\right)$$

Equation 3.2.74

$$\lambda_{\psi,C|G} = \left(\lambda_{\psi,T|G} \cdot Q_3\left(\frac{\phi_T}{\phi_C}\right) + \lambda_{\psi,H|G} \cdot \left(1 - Q_3\left(\frac{\phi_T}{\phi_C}\right)\right)\right)$$

Equation 3.2.75

where $\phi_C = \phi_T + \phi_{\mathbb{H}}$ represents the sum of all cell-based volume fractions. Assuming the entrance and exit rates in the combined host tissue phase $\phi_{\mathbb{H}}$ is homogeneous across species in the host tissue, the rate of entrance and exit through tumor, ECM, and combined host tissue phases is $\lambda_{\psi,T|G}$, $\lambda_{\psi,E|G}$, and $\lambda_{\psi,\mathbb{H}|G} = \lambda_{\psi,H|G} = \lambda_{\psi,G|G}$, respectively. Immune cell extravasation occurs when chemokines attract immune species [187]. In this model, chemokines are represented by che. These interactions are included in $\mathcal{A}_{enter|\sigma}$:

$$\mathcal{A}_{enter|\sigma} = \left(1 + \mathcal{F}_B^{che} \cdot \frac{che}{che_{sat}}\right) \cdot \left(1 - \frac{\phi_\sigma}{\tilde{\phi}_\alpha}\right) \cdot \left(1 - \frac{n}{n_\infty}\right) \cdot Q_3\left(1 - \frac{p_\alpha}{p_{t,B}}\right)$$

Equation 3.2.76

where n_∞ is the concentration of oxygen at the model domain's borders, $p_{t,B}$ is the threshold pressure corresponding to the onset of blood vasculature loss, che_{sat} is the saturating concentration for chemokines (CHE), and $\mathcal{F}_B^{che}$ is the effective factor of CHE on the entrance rate of species σ.

It is assumed that all immune species exit the tumor domain through lymph vasculature [217] and that apoptosis occurs at a constant rate for all species. Thus, $\mathcal{A}_{apoptosis|\sigma}$, $\mathcal{A}_{necrosis|\sigma}$, and $\mathcal{A}_{exit|\sigma}$ are defined using the following equations:

$$\mathcal{A}_{apoptosis|\sigma} = 1$$
<div align="right">Equation 3.2.77</div>

$$\mathcal{A}_{necrosis|\sigma} = 1 - \mathcal{H}\left(\frac{n}{n_{v,G}} - 1\right) \cdot \mathcal{H}\left(\frac{g}{g_{v,G}} - 1\right)$$
<div align="right">Equation 3.2.78</div>

$$\mathcal{A}_{exit|\sigma} = Q_3\left(1 - \frac{p}{p_{t,L}}\right)$$
<div align="right">Equation 3.2.79</div>

where $\mathcal{H}(x)$ is the Heaviside function of x, $n_{v,G}$ and $g_{v,G}$ are the viability limits of oxygen and glucose, respectively, for immune species, and $p_{t,L}$ is the threshold solid phase pressure corresponding to the onset of lymphatic vasculature loss due to compression (crushing).

3.2.3.3.2 Monocyte Differentiation

Monocytes differentiate into macrophage species with predominantly M1 or M2 phenotypes [154], which for simplicity are assumed to be mutually exclusive binary states. Their differentiation can occur without stimulation by T-cells; however, the process is amplified by Th2 through Interleukin-4 (IL-4) for M2 [154, 199]. Th1 cells increase M1 differentiation via IFN-γ [195, 200]. Furthermore, as in [65], this model simulates tumor cytokine release that promotes M1 or M2 phenotypes. The tgf term used in this model from [82] includes cytokines that encourage differentiation of Mo into either M1 or M2 [221]. Consequently, this model upregulates the total differentiation rate in the presence of higher tgf concentration. While it has been reported that Breg releasing IL-10 can reduce Mo activation, this model does not incorporate this interaction

[170, 222]. Further, although monocytes can differentiate into monocyte-derived DC

[157], it is assumed for simplicity that monocytes only differentiate into macrophages

and that polarization is set at differentiation. Thus, for monocytes and macrophages an

additional rate term is added: $r_{diff|M_0}$:

$$S_{M_0} = S_{fund|M_0} - r_{diff|M_0}$$

Equation 3.2.80

$$r_{diff|M_0} = \lambda_{diff|M_0} \cdot \mathcal{A}_{diff|M_0} \cdot \phi_{M_0}$$

Equation 3.2.81

$$\mathcal{A}_{diff|M_0} = 1 + \mathcal{F}_{tgf}^{Diff|M_0} \cdot \frac{tgf}{tgf_{sat}}$$

Equation 3.2.82

where $\mathcal{F}_{tgf}^{Diff|M_0}$ is the effective factor of TGF on the differentiation of Mo and

tgf_{sat} is the saturating concentration of tgf. M1 and M2 have similar derivations:

$$S_{M_1} = S_{fund|M_1} + r_{diff|M_1}$$

Equation 3.2.83

$$S_{M_2} = S_{fund|M_2} + r_{diff|M_2}$$

Equation 3.2.84

$$r_{diff|M_1} + r_{diff|M_2} = r_{diff|M_0}$$

Equation 3.2.85

The values of $r_{diff|M_1}$ and $r_{diff|M_2}$ depend on $\mathcal{A}_{diff|M_1}$ and $\mathcal{A}_{diff|M_2}$,

respectively. The former adjustment factor can be interpreted as the probability of $M_0 \rightarrow$

M_1 and the latter as the probability of the $M_0 \rightarrow M_2$ differentiation event:

$$r_{diff|M_1} = \lambda_{diff|M_0} \cdot \mathcal{A}_{diff|M_1} \cdot \mathcal{A}_{diff|M_0} \cdot \phi_{M_0}$$

Equation 3.2.86

$$r_{diff|M_2} = \lambda_{diff|M_0} \cdot \mathcal{A}_{diff|M_2} \cdot \mathcal{A}_{diff|M_0} \cdot \phi_{M_0}$$

Equation 3.2.87

$$\mathcal{A}_{diff|M_1} = 1 - F_P$$

Equation 3.2.88

$$\mathcal{A}_{diff|M_2} = F_P$$

Equation 3.2.89

where F_P is the probability of the $M_0 \rightarrow M_2$ differentiation event bounded in the

closed interval [0,1] and defined by Equation 3.2.90:

$$F_P = \left(\mathcal{F}_{T_{H2}|M_2 \, diff} \cdot \mathcal{A}_{I|T_{H2}} \cdot Q_3 \left(\frac{\phi_{T_{H2}}}{\phi_{GG}} \right) \right.$$

$$\left. + \mathcal{F}_{T_{H1}|M_1 \, diff} \cdot \left(1 - \mathcal{A}_{I|T_{H1}} \cdot Q_3 \left(\frac{\phi_{T_{H1}}}{\phi_{GG}} \right) \right) \right)$$

$$\cdot \frac{1}{\mathcal{F}_{T_{H2}|M_2,diff} + \mathcal{F}_{T_{H1}|M_1,diff}} + \mathcal{F}_{F_{bias}} \qquad \text{Equation } 3.2.90$$

where $\mathcal{F}_{F_{bias}}$ is a dimensionless biasing parameter that shifts the equilibrium

macrophage ratio as dictated by $\mathcal{F}_{T_{H1}|M_1,diff}$, and $\mathcal{F}_{T_{H2}|M_2,diff}$. By adjusting the

parameters in F_P, the differentiation outlook can be adjusted.

3.2.3.3.3 B-Cell Activation

B-effector cells transition from a resting B-cell state to an active B-cell state [171, 223]. This is accounted for by the rate term r_{act}, which represents the conversion to the active state:

$$S_{B_ER} = S_{fund|B_ER} - r_{act|B_ER} \qquad \text{Equation } 3.2.91$$

$$S_{B_EA} = S_{fund|B_EA} + r_{act|B_ER} \qquad \text{Equation } 3.2.92$$

where each rate term is defined using a lambda rate constant with adjustment

factor $\mathcal{A}_{act|B_ER}$:

$$r_{act|B_ER} = \lambda_{act|B_ER} \cdot \mathcal{A}_{act|B_ER} \cdot \phi_{B_ER} \qquad \text{Equation } 3.2.93$$

where $\lambda_{act|B_ER}$ represents the rate of BeR activation to BeA. The change between

resting and active states for B-effector cells is assumed to be proportional to both viable

(ϕ_V) and dead (ϕ_D) tumor tissue. Therefore:

$$\mathcal{A}_{act|B_ER} = \begin{cases} \dfrac{\phi_T}{\phi_{TSat}}, \phi_T \leq \phi_{TSat} \\ 1, \phi_T > \phi_{TSat} \end{cases} \qquad \text{Equation } 3.2.94$$

where ϕ_{TSat} is the concentration that saturates the effect of ϕ_T to cause BeR to transition to BeA.

3.2.3.3.4 Source Terms for Other Immune Species

For $\tau \in \{NK, Ne, Den, MDSC, B_{reg}, T_C, T_R, T_{H1}, T_{H2}\}$, it is assumed that mitosis, apoptosis, necrosis, entrance, and exit rates constitute the source terms of each species τ. Thus:

$$S_\tau = S_{fund|\tau}$$

3.2.3.4 Immune Cell Species Chemical Potentials

The underlying mechanism for leukocyte chemotaxis involves actin rearrangement in the direction of higher concentrations of chemokines [224]. For simplicity, this model assumes that chemotaxis movement of all immune species is proportional to chemokine concentrations and that immune species follow higher concentration gradients. In making this assumption, it is acknowledged that chemotaxis behavior differs across leukocyte species [225-228]. Chemotaxis in this model is associated with three different cytokines: che, tgf, and taf. It is also assumed that immune species tend to migrate toward hypoxic regions [229, 230]. Therefore, from Equation 3.2.42, for each immune species σ:

$$\begin{aligned}
\mu_\sigma + \epsilon_{TG}^2 \cdot \nabla^2 \phi_T + \epsilon_G^2 \cdot \nabla^2 \phi_G + \epsilon_{EG}^2 \cdot \nabla^2 \phi_E \\
= -\chi_{\sigma,che} \cdot \mathcal{A}_{X_{G,che}} \cdot che - \chi_{\sigma,tgf} \cdot \mathcal{A}_{X_{G,tgf}} \cdot tgf \\
- \chi_{\sigma,taf} \cdot \mathcal{A}_{X_{G,taf}} \cdot taf
\end{aligned}$$

$$\mathcal{A}_{X_{G,\varsigma}} = Q_3 \left(\frac{n - n_{v,G}}{n_\infty - n_{v,G}} \right)$$

where $\varsigma \in \{che, tgf, taf\}$.

3.2.3.5 Immune-Tumor Interactions

This section covers immune species-mediated killing of viable tumor, removal of dead tumor, and promotion of tumor proliferation.

3.2.3.5.1 Viable Tumor Removal

Viable tumor tissue either converts into dead tumor volume fraction by a constant apoptosis rate ($r_{A,V}$), becomes necrotic due to hypoxic conditions ($r_{N,V}$), or is eliminated by immune species ($r_{G,V}$), as represented by the term:

$$S_{death|V} = r_{N,V} + r_{A,V} + r_{G,V}$$

<div align="right">Equation 3.2.98</div>

The immune interactions leading to tumor death are contingent not only on the presence of a tumor volume fraction but also on the volume fractions of immune species that contribute to the promotion and inhibition of these interactions. All immune-tumor interactions contribute to $r_{G,V}$:

$$r_{G,V} = -\lambda_{InduceDeath|V} \cdot \mathcal{A}_{InduceDeath|V} \cdot \phi_V$$

<div align="right">Equation 3.2.99</div>

where $\mathcal{A}_{InduceDeath|V}$ is the adjustment factor for the death rate $\lambda_{InduceDeath|V}$. Neutrophils induce death via contact-dependent interaction using hydrogen peroxide, leading to apoptosis [165]. M1 cells can kill tumor cells using Interleukin 12 (IL-12) [194]. It is assumed that the cytotoxic effect of IL-12 is localized such that the M1-tumor interaction can be considered contact-based. Natural killer cells induce cell death with contact-based release of perforin and granzymes [164]. DC can kill tumor cells both with a contact-dependent peroxynitrite mechanism and a cytokine mechanism via Tumor Necrosis Factor-Related Apoptosis-Inducing Ligand (TRAIL) [162, 196]. CTL cells attack tumor cells via granule exocytosis and Fas ligand-mediated apoptosis induction [173]. BeA can kill tumor cells on contact [171]. It has been recently shown that T-cells

can exhibit a CD4$^+$ cytotoxic phenotype that can kill cancer on contact via a major histocompatibility complex (MHC) class II molecule-dependent mechanism [212]. In this model, this cytotoxic behavior is associated with the anti-tumor Th1 immune species. Therefore, death induced locally by tumor-immune interactions is represented by $\mathcal{A}_{InduceDeath|V}$:

$$\mathcal{A}_{InduceDeath|V} = \frac{\sum_{i \in ID} \left[\mathcal{F}_{InduceDeath,i} \cdot \mathcal{A}_{I|i} \cdot Q_3 \left(\frac{\phi_i}{\phi_{GG}} \right) \right]}{\sum_{i \in ID} \mathcal{F}_{InduceDeath,i}} \qquad \text{Equation 3.2.100}$$

where $ID = \{Ne, M_1, NK, Den, B_E A, T_C, T_{H1}\}$ and $\mathcal{F}_{InduceDeath,i}$ is the effective factor of immune species $i \in ID$ on $\mathcal{A}_{InduceDeath|V}$.

3.2.3.5.2 Dead Tumor Removal

Dead tumor tissue either lyses over time or is phagocytosed by immune species. In this model, it is assumed that death induced in ϕ_V by immune species contributes to the ϕ_D volume fraction. Neutrophils can perform efferocytosis on tumor cells (phagocytosis on apoptotic cells), effectively removing tumor volume from the model [231, 232]. Efferocytosis is also performed by macrophages and dendritic cells [233]. Hence, $r_{G,D}$ represents the rate at which immune cells remove dead tumor tissue from the model via phagocytosis and the rate at which dead tissue is created in ϕ_V:

$$\begin{aligned} r_{G,D} = &-\lambda_{efferocytosis|D} \cdot \mathcal{A}_{efferocytosis|D} \cdot \phi_D \\ &+ \lambda_{InduceDeath|V} \cdot \mathcal{A}_{InduceDeath|V} \cdot \phi_V \end{aligned} \qquad \text{Equation 3.2.101}$$

$$\mathcal{A}_{efferocytosis|D} = \frac{\sum_{i \in EF} \mathcal{F}_i^D \cdot \mathcal{A}_{I|i} \cdot Q_3 \left(\frac{\phi_i}{\phi_{GG}} \right)}{\sum_{i \in EF} \mathcal{F}_i^D} \qquad \text{Equation 3.2.102}$$

where $EF = \{M_1, M_2, Den, Ne\}$ and $\mathcal{F}_i^D$ is a dimensionless factor accounting for immune species i's contribution to dead cell efferocytosis for $i \in EF$. Immune cells are assumed to not directly affect the ϕ_D lysing rate.

3.2.3.5.3 Tumor Promotion

M2 macrophages release TGF-β, which encourages tumor proliferation [159, 160]. While it is known that TGF-β has an immunosuppressive effect [159], this particular interaction is currently neglected. TGF-β release is incorporated into the general TGF equation from [82]:

$$0 = \nabla \cdot \left(D_{tgf} \cdot \nabla tgf \right) + S_{tgf}$$

Equation 3.2.103

$$S_{tgf} = tgf_{sat} \cdot \lambda_{tgf} - \left(\lambda_{tgf} + \lambda_{de,tgf} + \lambda_{U,tgf} \right) \cdot tgf$$

Equation 3.2.104

$$\lambda_{tgf} = \sum_{i \in \{V,B,L,F,M_2\}} \lambda_{i,tgf} \cdot \mathcal{A}_{i,tgf}$$

Equation 3.2.105

$$\lambda_{U,tgf} = \lambda_{U,V,tgf} \cdot \mathcal{A}_{U,V,tgf}$$

Equation 3.2.106

Where λ_{tgf}, $\lambda_{U,tgf}$, and $\lambda_{de,tgf}$ are the production, uptake, and extracellular decay rates of tgf, respectively, and the production and uptake rates of tgf by species i are $\lambda_{i,tgf}$ and $\lambda_{U,i,tgf}$, respectively. M_2's adjustment factor for λ_{tgf} is defined as:

$$\mathcal{A}_{M_2,tgf} = \mathcal{A}_{I|M_2} \cdot Q_3 \left(\frac{\phi_{M_2}}{\phi_{GG}} \right)$$

Equation 3.2.107

Adjustment factors for all other species in Equation 3.2.105 and Equation 3.2.106 are unchanged from [82].

3.2.3.6 Immune Cell Species and the Tumor Microenvironment

3.2.3.6.1 Diffusivity

Like [82], the following nutrient and waste products are included: oxygen (n), glucose (g), carbon dioxide (w), lactate ion (ℓ), bicarbonate ion (b), hydrogen ion (a),

83

and sodium (s) and chloride (r) ions. Here, it is assumed that for any diffusive species in the model σ, $D_{\sigma,H} = D_{\sigma,G} = D_{\sigma,\mathbb{H}}$. Thus, the effective diffusivity, D_σ, of all nutrients, waste products, TAF (taf), TGF (tgf), matrix degrading enzymes (m), as well as the motility of blood (B_n^E) and lymphatic (L_n^E) neo-vasculature remains the same as in [82]:

$$D_\sigma = D_{\sigma,E} \cdot Q_3\left(\frac{\phi_E}{\tilde{\phi}_\alpha}\right) + D_{\sigma,C} \cdot \left[1 - Q_3\left(\frac{\phi_E}{\tilde{\phi}_\alpha}\right)\right] \qquad \text{Equation 3.2.108}$$

$$D_{\sigma,C} = D_{\sigma,T} \cdot Q_3\left(\frac{\phi_T}{\phi_C}\right) + D_{\sigma,H} \cdot \left[1 - Q_3\left(\frac{\phi_T}{\phi_C}\right)\right] \qquad \text{Equation 3.2.109}$$

3.2.3.6.2 Angiogenesis

B-cells containing STAT3 have been reported to promote angiogenesis [169, 170, 234]. Also, M2 macrophages encourage angiogenesis through VEGF-A expression [161]. In this model, M2-induced upregulation of VEGF-A and VEGF-C tumor expression [235, 236] are neglected. For B-cells, it is assumed that the angiogenesis interaction is localized. Thus, this interaction is incorporated in the blood neo-vasculature source term from [82]:

$$S_{BnE} = r_{m,BnE} - r_{de,BnE} - r_{crush,BnE} \qquad \text{Equation 3.2.110}$$

Inside the mitosis rate term, the B-lymphocyte is introduced through the adjustment factor $\mathcal{A}_{m,BnE}$:

$$r_{m,BnE} = \lambda_{m,BnE} \cdot \mathcal{A}_{m,BnE} \cdot B_n^E \qquad \text{Equation 3.2.111}$$

$$\begin{aligned}\mathcal{A}_{m,BnE} = \mathcal{F}_{Bn} \cdot \left(1 - \mathcal{F}_{lg|Bn} \cdot \frac{B_n^E}{B_{max}}\right) \cdot Q_3\left(\frac{taf - taf_{Bn}}{taf_{sat} - taf_{Bn}}\right) \\ \cdot \left(1 + \mathcal{F}_{BnE,G} \cdot \mathcal{A}_{mitosis,G|BnE}\right)\end{aligned} \qquad \text{Equation 3.2.112}$$

$$\mathcal{A}_{mitosis,G|BnE} = \left[\sum_{i \in BL}\left(\mathcal{F}_{i|BnE} \cdot Q_3\left(\frac{\phi_i}{\phi_{GG}}\right) \cdot \mathcal{A}_{I|i}\right)\right] \Bigg/ \left[\sum_{i \in BL}(\mathcal{F}_{i|BnE})\right] \qquad \text{Equation 3.2.113}$$

where $\mathcal{F}_{Bn}$ is the fraction of sprouting blood neo-vasculature, taf_{sat} is the saturating concentration of TAF, taf_{Bn} is the minimum TAF concentration required to engage endothelial mitosis, B_{max} is the maximum density of blood vasculature, $BL = \{B_E R, B_E A, B_{reg}\}$, and the effective factor $\mathcal{F}_{i|BnE}$ (for $i \in BL$) represents the strength of the interaction between B-cells with the endothelium. For logistic growth, $\mathcal{F}_{lg|Bn} = 1$. Otherwise, $\mathcal{F}_{lg|Bn} = 0$. Potential contribution to the lymphatic vasculature proliferation is neglected in this model.

For M2-induced angiogenesis, VEGF-A and VEGF-C expression is accounted through the general TAF equation from [82]:

$$0 = \nabla \cdot \left(D_{taf} \cdot \nabla taf \right) + S_{taf} \qquad \text{Equation 3.2.114}$$

$$S_{taf} = taf_{sat} \cdot \lambda_{taf} - \left(\lambda_{taf} + \lambda_{de,taf} + \lambda_{U,taf} \right) \cdot taf \qquad \text{Equation 3.2.115}$$

$$\lambda_{taf} = \sum_{i \in \{V,B,L,F,M_2\}} \lambda_{i,taf} \cdot \mathcal{A}_{i,taf} \qquad \text{Equation 3.2.116}$$

$$\lambda_{U,taf} = \lambda_{U,V,taf} \cdot \mathcal{A}_{U,V,taf} \qquad \text{Equation 3.2.117}$$

$$\mathcal{A}_{M_2,taf} = \mathcal{A}_{I|M_2} \cdot Q_3 \left(\frac{\phi_{M_2}}{\phi_{GG}} \right) \qquad \text{Equation 3.2.118}$$

where each lambda term is analogously defined to the TGF equation in **3.2.3.5.3 Tumor Promotion**.

3.2.3.6.3 ECM Formation

ECM formation increases with heightened activity of T_{H2} through stimulation of fibroblasts to produce collagen via IL-13 and IL-4 [213, 214]. Noting that this model does not distinguish between the origins and differentiation stages of myofibroblast cells, yields the following expansion of the ECM source term from [82]:

$$S_E = \sum_{\tau \in T} r_{\tau,E} - r_{de,E}$$

$$r_{\tau,E} = \lambda_{i,E} \cdot \mathcal{A}_{i,E} \cdot \tau, \{i, \tau\} \in \{\{V, \phi_V\}, \{B, B\}, \{L, L\}, \{F, F\}\}$$

$$\mathcal{A}_{i,E} = \left(1 - \frac{\phi_E}{\tilde{\phi}_\alpha}\right) \cdot \left(1 + \frac{tgf}{tgf_{sat}}\right) \cdot \left(1 + \mathcal{F}_{n,E}^i \cdot \frac{n_h - n}{n_h - n_{v,F}} \cdot \mathcal{H}(n_h - n)\right)$$
$$\cdot \mathcal{H}(n - n_{v,F}), i \in T \,\&\, i \neq F$$

$$\mathcal{A}_{F,E} = \left(1 - \frac{\phi_E}{\tilde{\phi}_\alpha}\right) \cdot \left(1 + \frac{tgf}{tgf_{sat}}\right) \cdot \left(1 + \mathcal{F}_{n,E}^F \cdot \frac{n_h - n}{n_h - n_{v,F}} \cdot \mathcal{H}(n_h - n)\right)$$
$$\cdot \left(1 + \mathcal{F}_{F_E}^{T_{H2}} \cdot \mathcal{A}_{I|T_{H2}} \cdot Q_3\left(\frac{\phi_{T_{H2}}}{\phi_{GG}}\right)\right) \cdot \mathcal{H}(n - n_{v,F})$$
$$\cdot \mathcal{H}(tgf - tgf_{FE,E})$$

where $T = \{V, B, L, F\}$, $B \equiv B_p + B_n$, $L \equiv L_p + L_n$, n_h is the hypoxic threshold of

oxygen, $n_{v,i}$ is the oxygen viability threshold for species i, $\mathcal{F}_{n,E}^\tau$ is the effective constant

for the increase in ECM secretion by species τ in response to hypoxia, $\mathcal{F}_{F_E}^{T_{H2}}$ is the

effective factor of ECM secretion upregulation in myofibroblasts due to T_{H2}, $r_{de,E}$ is the

rate of ECM degradation as given in [82], $tgf_{FE,E}$ is the minimum tgf concentration

required to initiate ECM secretion by myofibroblasts, and F represents the reduced

weighted myofibroblast concentration per unit volume of tissue as defined in [82] as $F = $

$\phi_E F_E$ where F_E is the ECM-component concentration of myofibroblast cells, defined per

volume of ECM.

3.2.3.6.4 Nutrients and Waste Products

Nutrient and waste transfer rates are adjusted akin to [237] such that blood pre-

and neo-vasculature release nutrients and uptake waste products at a rate $\lambda_{Bp,\sigma}$ and $\lambda_{Bn,\sigma}$,

respectively for $\sigma \in \{n, g, w, \ell\}$. Further, immune and host phases are assumed to have

similar transfer rates. Thus for $\psi \in \{Bp, Bn\}$, the forms for nutrient transfer remain the same as in [82] but are applied separately to pre- and neo-vasculature:

$$\lambda_{\psi,\sigma} = \lambda_{\psi,\sigma,E} \cdot Q_3 \left(\frac{\phi_E}{\tilde{\phi}_\alpha}\right) + \lambda_{\psi,\sigma,C} \cdot \left[1 - Q_3 \left(\frac{\phi_E}{\tilde{\phi}_\alpha}\right)\right] \qquad \text{Equation 3.2.123}$$

$$\lambda_{\psi,\sigma,C} = \lambda_{\psi,\sigma,T} \cdot Q_3 \left(\frac{\phi_T}{\phi_C}\right) + \lambda_{\psi,\sigma,H} \cdot \left[1 - Q_3 \left(\frac{\phi_T}{\phi_C}\right)\right] \qquad \text{Equation 3.2.124}$$

where ECM, cell, tumor, and host tissue nutrient transfer rates are $\lambda_{\psi,\sigma,E}$, $\lambda_{\psi,\sigma,C}$, $\lambda_{\psi,\sigma,T}$, and $\lambda_{\psi,\sigma,H} = \lambda_{\psi,\sigma,G} = \lambda_{\psi,\sigma,\mathbb{H}}$, respectively. Using Equation 3.2.123 and Equation 3.2.124, the rate of nutrient and waste product transfer from [82] is expanded:

$$r_{B,\sigma} = \begin{cases} \left(\lambda_{Bp,\sigma} \cdot \dfrac{B_p}{B_{max}} + \lambda_{Bn,\sigma} \cdot \dfrac{B_n}{B_{max}}\right) \cdot \mathcal{A}_{B,\sigma} \cdot (\sigma_C - \sigma), \sigma = \{n, g\} \\[4mm] -\left(\lambda_{Bp,\sigma} \cdot \dfrac{B_p}{B_{max}} + \lambda_{Bn,\sigma} \cdot \dfrac{B_n}{B_{max}}\right) \cdot \mathcal{A}_{B,\sigma} \cdot (\sigma - \sigma_C), \sigma = \{w, l\} \end{cases} \qquad \text{Equation 3.2.125}$$

$$\mathcal{A}_{B,\sigma} = Q_3 \left(1 - \frac{p}{p_{t,B}}\right) \cdot \mathcal{H}(p_{t,B} - p) \qquad \text{Equation 3.2.126}$$

where blood pre- and neo-vasculature per unit volume of tissue are B_P and B_n, respectively, σ_C represents the concentration of σ in the blood capillaries, and $p_{t,B}$ is the threshold pressure corresponding to the onset of blood vasculature loss. The source terms for hydrogen, bicarbonate, sodium, and chloride ions remain as defined in [82], with $r_{B,a} = r_{B,\ell}$.

3.2.3.7 Solid Cell Phase Motility

The definition of solid cell phase motility from [83], $k_\alpha = f(\phi_T, \phi_E)$, is expanded to include $k_\alpha = g(\phi_T, \phi_E, \phi_G)$. In this study, the following function is used:

$$k_\alpha = g(\phi_T, \phi_E, \phi_G)$$

$$= Q_3\left(\frac{\phi_E}{\tilde{\phi}_\alpha}\right) \cdot (k_\alpha)_E + \left(1 - Q_3\left(\frac{\phi_E}{\tilde{\phi}_\alpha}\right)\right)$$

$$\cdot \left[Q_3\left(\frac{\phi_T}{\phi_C}\right) \cdot (k_\alpha)_T + \left(1 - Q_3\left(\frac{\phi_T}{\phi_C}\right)\right)\right.$$

$$\left. \cdot \left(Q_3\left(\frac{\phi_G}{\phi_\mathbb{H}}\right) \cdot (k_\alpha)_G + \left(1 - Q_3\left(\frac{\phi_G}{\phi_\mathbb{H}}\right)\right) \cdot (k_\alpha)_H\right)\right]$$

Equation 3.2.127

where the solid cell phase motility of species $\sigma \in \{T, E, G, H\}$ is $(k_\alpha)_\sigma$.

3.2.3.8 Chemokines

Similar to TGF and TAF, CHE are classified as cytokines. Here, CHE released by tumor tissue and uptaken by immune species are included [238]. As in **3.2.3.4 Immune Cell Species Chemical Potentials**, it is assumed that immune cell species are attracted in a macrophage-like manner to hypoxic regions of tissue [229, 230], in which CHE production is upregulated. Because the time scales for cell mitosis are significantly larger than the diffusion of CHE (day or longer vs seconds), the quasi-steady state equation for TGF is adapted for CHE:

$$\nabla \cdot (D_{che} \cdot \nabla che) + \lambda_{che} \cdot che_{sat} - (\lambda_{che} + \lambda_{de,che} + \lambda_{U,che}) \cdot che = 0$$

Equation 3.2.128

$$\lambda_{che} = \lambda_{V,che} \cdot \mathcal{A}_{V,che}$$

Equation 3.2.129

$$\mathcal{A}_{V,che} = \left(1 + \mathcal{F}_{che,n}^V \cdot \left(\frac{n_h - n}{n_h - n_{v,V}}\right) \cdot \mathcal{H}(n_h - n)\right) \cdot \frac{\phi_V}{\tilde{\phi}_\alpha}$$

Equation 3.2.130

$$\lambda_{U,che} = \lambda_{U,G,che} \cdot Q_3\left(\frac{n - n_{v,G}}{n_\infty - n_{v,G}}\right) \cdot \frac{\phi_G}{\tilde{\phi}_\alpha}$$

Equation 3.2.131

where lambda constants and adjustment factors are defined analogously to the TGF equation in [82], $\lambda_{U,G,che}$ represents the rate of CHE uptake by immune species, $n_{v,\tau}$ represents the oxygen viability limit for species $\tau \in \{V, G\}$, the saturation concentration for che is che_{sat}, and the degradation is assumed to occur at a constant rate $\lambda_{de,che}$. The

effective diffusivity of CHE, D_{che}, is calculated using Equation 3.2.108 and Equation 3.2.109 Hypoxia upregulates CHE production by tumor tissue via the effective factor parameter $\mathcal{F}^V_{che,n}$.

3.2.3.9 Model Non-Dimensionalization

Volume fraction and chemical potential non-dimensionalization follows the same approach given in [82], where the scaling parameters used for non-dimensionalization are listed across **Table 12**, **Table 13**, **and Table 14**. The che non-dimensionalization for Equation 3.2.128 through Equation 3.2.131 is identical to tgf in [82] using non-dimensionalized factor che_{sat}. Non-dimensionalization of Equation 3.2.51 through Equation 3.2.64 fits the following general form:

$$\mathcal{A}_{I|\sigma} = \lambda_{Base|\sigma} + \left(1 - \lambda_{Base|\sigma}\right) \cdot \frac{\sum_{\tau \in T_\sigma^+} \lambda_{\tau|\sigma} \tilde{F}(\tau) + \sum_{\zeta \in Z_\sigma^-} \lambda_{\zeta|\sigma} \tilde{G}(\zeta)}{\sum_{i \in I_\sigma} \lambda_{i|\sigma}}$$

Equation 3.2.132

$$\tilde{F}(\tau) = \mathcal{A}_{I|\tau} \cdot Q_3\left(\frac{\tilde{\phi}_\tau}{\tilde{\phi}_{GG}}\right)$$

Equation 3.2.133

$$\tilde{G}(\zeta) = 1 - \mathcal{A}_{I|\zeta} \cdot Q_3\left(\frac{\tilde{\phi}_\zeta}{\tilde{\phi}_{GG}}\right)$$

Equation 3.2.134

where the non-dimensionalized form of any variable V is $\tilde{V}$ and the interaction lambda constants and $\mathcal{A}_{I|\sigma}$ are dimensionless. Equation 3.2.135 denotes the non-dimensionalization of solid cell phase motility using scaling factor $\bar{\bar{k}}_\alpha$ for k_α:

$$\widetilde{k_\alpha} = Q_3(\tilde{\phi}_E) \cdot \widetilde{(k_\alpha)}_E + \left(1 - Q_3(\tilde{\phi}_E)\right)$$
$$\cdot \left(Q_3\left(\frac{\tilde{\phi}_T}{\tilde{\phi}_C}\right) \cdot \widetilde{(k_\alpha)}_T + \left(1 - Q_3\left(\frac{\tilde{\phi}_T}{\tilde{\phi}_C}\right)\right)\right.$$
$$\cdot \left(Q_3\left(\frac{\tilde{\phi}_G}{\tilde{\phi}_N}\right) \cdot \widetilde{(k_\alpha)}_G + \left.\left(1 - Q_3\left(\frac{\tilde{\phi}_G}{\tilde{\phi}_N}\right)\right) \cdot \widetilde{(k_\alpha)}_H\right)\right)$$

Equation 3.2.135

where $\tilde{\phi}_N = \tilde{\phi}_{\mathbb{H}} = \tilde{\phi}_G + \tilde{\phi}_H$ and $\tilde{\phi}_C = \tilde{\phi}_T + \tilde{\phi}_N$. The non-dimensionalized form

for $\boldsymbol{u}_\alpha$ is derived as in [82]:

$$\tilde{\boldsymbol{u}}_\alpha = -\tilde{k}_\alpha \cdot \left(\nabla\tilde{p} - \frac{\tilde{\gamma}_T}{\tilde{\epsilon}_T} \cdot \tilde{\mu}_T \nabla\tilde{\phi}_T - \frac{\tilde{\gamma}_E}{\tilde{\epsilon}_E} \cdot \mu_E \nabla\tilde{\phi}_E - \frac{\tilde{\gamma}_G}{\tilde{\epsilon}_G} \cdot \sum_{i \in G} \tilde{\mu}_i \nabla\tilde{\phi}_i \right) \qquad \text{Equation 3.2.136}$$

where the dimensionless cell adhesion parameter $\tilde{\gamma}_i = \epsilon_i \cdot \tilde{\phi}_\alpha \sqrt{\tilde{\phi}_\alpha \cdot E_a^*} / (\mathcal{L} \cdot \mathcal{P})$

for $i \in \{T, E, G\}$. Also adapted from [82], Equation 3.2.136 is substituted into $\nabla \cdot \tilde{\boldsymbol{u}}_\alpha =$

$\tilde{S}_\alpha = \sum_{i=1}^N \tilde{S}_i$ to obtain:

$$\nabla \cdot \left[\tilde{k}_\alpha \cdot \left(\nabla\tilde{p} - \frac{\tilde{\gamma}_T}{\tilde{\epsilon}_T} \cdot \tilde{\mu}_T \nabla\tilde{\phi}_T - \frac{\tilde{\gamma}_E}{\tilde{\epsilon}_E} \cdot \mu_E \nabla\tilde{\phi}_E - \frac{\tilde{\gamma}_G}{\tilde{\epsilon}_G} \cdot \sum_{i \in G} \tilde{\mu}_i \nabla\tilde{\phi}_i \right) \right] \qquad \text{Equation 3.2.137}$$
$$= -\sum_{i=1}^N \tilde{S}_i$$

The non-dimensionalized form for $\boldsymbol{u}_\beta$ is expanded to include immune source

terms (both positive and negative rates):

$$-\nabla \cdot \tilde{\boldsymbol{u}}_\beta = \nabla \cdot \left(\tilde{k}_\beta \cdot \nabla\tilde{q} \right) = R_{\alpha,\beta} \cdot \sum_{i=1}^N \tilde{S}_i \qquad \text{Equation 3.2.138}$$

where $R_{\alpha,\beta} = \tilde{\phi}_\alpha / \tilde{\phi}_\beta$. Noting that $\mu_H = 0$ from Equation 3.2.43, the definition

for the ECM-component velocity $\tilde{\boldsymbol{u}}_E$ remains the same as in [82, 83]:

$$\tilde{\boldsymbol{u}}_E = \tilde{\boldsymbol{u}}_\alpha - \tilde{M}\nabla(\tilde{\mu}_E) \qquad \text{Equation 3.2.139}$$

3.2.3.10 Numerical Implementation

Immune species volume fractions (Equation 3.2.47) and chemical potentials

(Equation 3.2.96) are solved simultaneously with tumor and ECM volume fractions using

the Multigrid solver detailed in [83] and [181]. Having an identical form to TGF

(Equation 3.2.103), Equation 3.2.128 discretization for CHE was performed analogously

to [83]. That is, at each point P with Cartesian coordinates (i, j, k) in domain Ω at time

step a, iteration r of the Multigrid solver, and smoothing step n, the following set of equations are used to solve for $\widetilde{che}$ at P using points orthogonally adjacent to P (discretized here using the lexicographical Gauss-Seidel method for simplicity):

$$-\left[\left(\tilde{\lambda}_{che} + \tilde{\lambda}_{de,che} + \tilde{\lambda}_{U,che}\right)_{i,j,k}^{a,r-1} + \frac{1}{2\eta^2} \cdot (\tilde{\varphi}_{che}^D)^{a,r-1}\right]\left(\widetilde{che}\right)_{i,j,k}^{a,r,n}$$
$$= \left(\tilde{\lambda}_{che}\right)_{i,j,k}^{a,r-1} - \frac{1}{2\eta^2}\left[\left(\tilde{\varphi}_1^{D,che}\right)^{a,r,n-1} + \left(\tilde{\varphi}_2^{D,che}\right)^{a,r,n}\right]$$
$$(2.6.1)$$

$$(\tilde{\varphi}_\sigma^D)^{a,r-1} = \left(\widetilde{D}_\sigma\right)_{i-1,j,k}^{a,r-1} + \left(\widetilde{D}_\sigma\right)_{i,j-1,k}^{a,r-1} + \left(\widetilde{D}_\sigma\right)_{i,j,k-1}^{a,r-1} + 6\left(\widetilde{D}_\sigma\right)_{i,j,k}^{a,r-1}$$
$$+ \left(\widetilde{D}_\sigma\right)_{i+1,j,k}^{a,r-1} + \left(\widetilde{D}_\sigma\right)_{i,j+1,k}^{a,r-1} + \left(\widetilde{D}_\sigma\right)_{i,j,k+1}^{a,r-1}$$
$$(2.6.2)$$

$$(\tilde{\varphi}_1^{D,\sigma})^{a,r,n-1} = (\tilde{\sigma})_{i+1,j,k}^{a,r,n-1}\left[\left(\widetilde{D}_\sigma\right)_{i,j,k}^{a,r-1} + \left(\widetilde{D}_\sigma\right)_{i+1,j,k}^{a,r-1}\right]$$
$$+ (\tilde{\sigma})_{i,j+1,k}^{a,r,n-1}\left[\left(\widetilde{D}_\sigma\right)_{i,j,k}^{a,r-1} + \left(\widetilde{D}_\sigma\right)_{i,j+1,k}^{a,r-1}\right]$$
$$+ (\tilde{\sigma})_{i,j,k+1}^{a,r,n-1}\left[\left(\widetilde{D}_\sigma\right)_{i,j,k}^{a,r-1} + \left(\widetilde{D}_\sigma\right)_{i,j,k+1}^{a,r-1}\right]$$
$$(2.6.3)$$

$$(\tilde{\varphi}_2^{D,\sigma})^{a,r,n} = (\tilde{\sigma})_{i-1,j,k}^{a,r,n}\left[\left(\widetilde{D}_\sigma\right)_{i,j,k}^{a,r-1} + \left(\widetilde{D}_\sigma\right)_{i-1,j,k}^{a,r-1}\right]$$
$$+ (\tilde{\sigma})_{i,j-1,k}^{a,r,n}\left[\left(\widetilde{D}_\sigma\right)_{i,j,k}^{a,r-1} + \left(\widetilde{D}_\sigma\right)_{i,j-1,k}^{a,r-1}\right]$$
$$+ (\tilde{\sigma})_{i,j,k-1}^{a,r,n}\left[\left(\widetilde{D}_\sigma\right)_{i,j,k}^{a,r-1} + \left(\widetilde{D}_\sigma\right)_{i,j,k-1}^{a,r-1}\right]$$
$$(2.6.4)$$

where smoothing is performed using a Gauss-Seidel smoother with red-black ordering as in [83] and [181].

Discretization for immune species volume fractions and chemical potentials was performed analogously to [83], discretizing volume fraction equations and chemical potentials in time using the Crank-Nicholson method as described in [113]. Numerical solutions were computed using the distributed computing approach in [181], in which the Multigrid solver from [83] is parallelized across multiple CPU threads using Message Passing Interface (MPI) and operates on GPUs using CUDA. All Multigrid tasks (e.g., Gauss-Seidel smoother, restriction, prolongation, etc.) are computed by multiple CUDA-

enabled GPUs concurrently, with one GPU per CPU thread. GPUs operate within

mutually exclusive cubic regions of the domain (i.e., subdomain). After each numerical

process concludes, points adjacent to multiple subdomains are synchronized across CPU

threads such that each thread has an updated copy of data surrounding its sub-domain.

3.3 Results

This section assumes that any immune species σ that interacts with any other

immune species, the set of which is denoted as I_σ, contributes equally through

stimulatory or inhibitory events to the overall level of activation of σ (denoted $\mathcal{A}_{I|\sigma}$).

Consequently, the weight of any given interaction on σ, represented by the lambda

constants $\lambda_{i|\sigma}$ for all $i \in I_\sigma$, are equally weighted. Hence, for n stimulatory and m

inhibitory interactions on σ, $\lambda_{i|\sigma} = 1/(n + m)$. This model does not include interactions

with NE; thus, NE activation is assumed to be saturated ($\lambda_{Base|Ne} = 1$). Our initial

analysis concerns immune species $\psi \in G$ whose activation levels are coupled through

Equations 2.3.2.4 through 2.3.2.16. The base activation level is set uniformly across all

immune species. Hence, $\lambda_{Base|\psi} = \lambda_{Base}$ where $\lambda_{Base} \in [0,1]$.

The range of solutions for $\mathcal{A}_{I|\psi}$ provided by Equation 3.2.52 through Equation

3.2.64 was explored using three case studies summarized in **Table 19**: creation of an (1)

upper and (2) lower bound for each $\mathcal{A}_{I|\psi}$ and (3) saturation of all stimulatory and

inhibitory interactions, for which higher immune species concentrations will not affect

these interactions. For cases 1 and 2, immune volume fractions are uncoupled from the

stimulatory interaction term $\tilde{F}(\tau)$ and inhibitory interaction term $\tilde{G}(\zeta)$, representing

immune dysregulation. For case 1, immune species are desensitized to inhibitory

interactions ($\tilde{G}(\zeta) = 1$) and are over-sensitized to stimulatory interactions ($\tilde{F}(\tau) = \mathcal{A}_{I|\tau}$).

For case 2, immune species are desensitized to stimulatory interactions ($\tilde{F}(\tau) = 0$) and

are over-sensitized to inhibitory interactions ($\tilde{G}(\zeta) = 0$). Case 3 represents local

saturation of all immune species ($\tilde{\phi}_\psi \geq \tilde{\phi}_{GG}$). Thus, $\tilde{F}(\tau) = \mathcal{A}_{I|\tau}$, and $\tilde{G}(\zeta) = 1 - \mathcal{A}_{I|\zeta}$.

Solving cases 1 and 2 produces the solutions $\mathcal{A}_\psi = 1$ and $\mathcal{A}_{I|\psi} = \lambda_{Base}$,

respectively, for all ψ. Because immune species in this model cannot selectively

participate in stimulatory and inhibitory interactions and must, therefore, regress $\mathcal{A}_{I|\psi}$

away from its minimum and maximum values, case 1 is unattainable. Therefore,

considering that $\lambda_{Base} \in [0,1]$, cases 1 and 2 confirm that $\mathcal{A}_{I|\psi}$ will be bounded from 0

to 1.

In case 3 all $\mathcal{A}_{I|\psi}$ reduce to functions of λ_{Base}. **Figure 10** shows the effect of

varying λ_{Base} 0 to 1 under the conditions of case 3.

Case #	Value for Stimulatory Interactions ($\tilde{F}(\tau)$)	Value for Inhibitory Interactions ($\tilde{G}(\zeta)$)	Solution value for $\mathcal{A}_{I|\psi}$
1	$\mathcal{A}_{I|\tau}$	1	1
2	0	0	λ_{Base}
3	$\mathcal{A}_{I|\tau}$	$1 - \mathcal{A}_{I|\zeta}$	Function of λ_{Base}

Table 19 Cases used for immune-immune interaction analysis. For all immune

species $\psi \in G$ and $\psi \neq NE$, Cases 1 and 2 describe upper and lower bounds,

respectively, to model activation levels. Case 3 reduces activation levels to a function of a

parameter that specifies the minimum level of immune species activation (λ_{Base}).
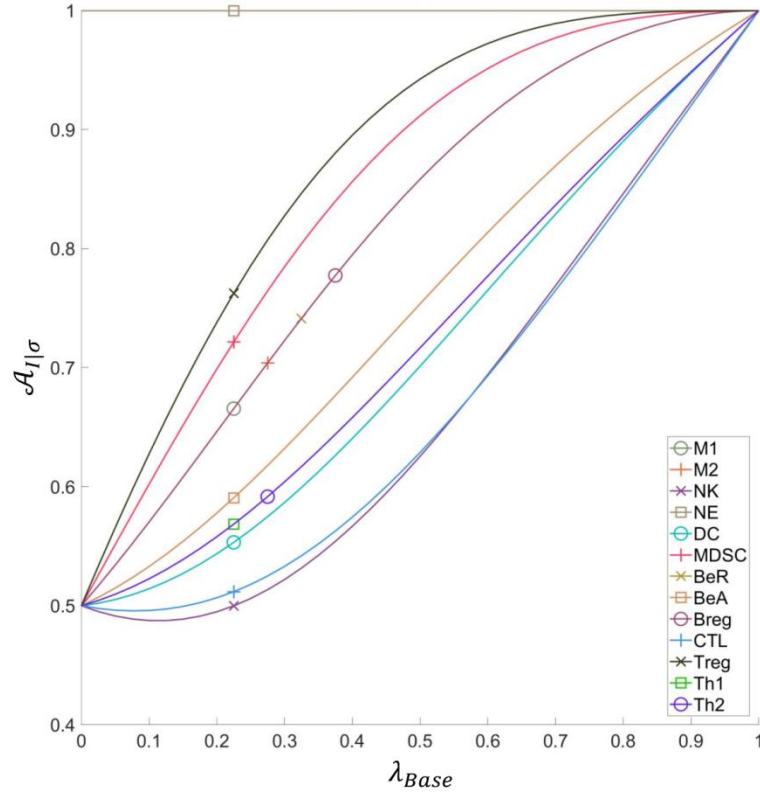
Figure 10 Values of the activation level $\mathcal{A}_{I|\sigma}$ of a given immune species σ in regions where immune response is saturated (that is, $Q_3\left(\frac{\bar{\phi}_\sigma}{\bar{\phi}_{GG}}\right) = 1$) as a function of the minimum level of immune species activation λ_{Base}. Saturation in this context implies that higher immune species concentrations will not further affect immune-immune interactions. In general activation levels increase with raised λ_{Base}. Activation levels are stratified due to two phenomena: (1) increased quantity of inhibitory interactions and (2) reduced activation levels of stimulatory immune species. NK and CTL's activation levels, having three and four inhibitory interactions, respectively, initially decline with increasing λ_{Base} due to significant stimulation of NK- and CTL-inhibitory immune species. Superimposed activation level curves are distinguished with unique symbol markers.

94

In **Figure 10** for $\lambda_{Base} = 0$, in the system of interaction equations resolves to $\mathcal{A}_{I|\psi} = \frac{1}{2}$. Interestingly, this indicates the stimulatory and inhibitory effects in Equation 3.2.52 through Equation 3.2.64 offset each other in saturated conditions. Increasing λ_{Base} raises inhibitory immune species activation primarily, including MDSC and Treg. Species M1, M2, BeR, and Breg depend on Th1 and/or Th2, both of which possess the same response curve, responding equally, therefore, to changes in λ_{Base}. Treg benefits from high MDSC response to changes and rising Breg activation, having the highest activation level out of the non-neutrophil activation levels. The dependence of MDSC activation on BeA and BeA's inhibition by MDSC pulls both BeA and MDSC lower than BeR and Treg activations, respectively. DC is balanced by Th1 activation and MDSC inhibition and remains qualitatively linear from roughly $\lambda_{Base} = 0.45$ and onwards. NK and CTL have a high proportion of inhibitory interactions that greatly inhibits their activation levels from rising above 0.5 until $\lambda_{Base} = 0.16$ and $\lambda_{Base} = 0.23$, respectively. Superimposed curves in **Figure 10** imply that under saturated immune conditions, some immune species activation levels respond identically to the base activation level parameter λ_{Base}. This implies that a single function with λ_{Base} as its input could be used to describe the behavior of multiple immune species in case 3. NE activation level stays at 1.0 throughout and is plotted for completeness.

3.3.1 Immune-Tumor Microenvironment Interactions

To evaluate the immune model's interactions with the TME, parameter sets defined in **Table 20** through **Table 26 (Part 3.3.1.1)** were used to conduct 4 *in silico* experiments: (I) simulation of a growing tumor mass with tumor-dependent immune

differentiation (**Part 3.3.1.2**), (II) quantification of immune species interactions between pro-tumor and anti-tumor states (**Part 3.3.1.3**), (III) evaluation of immune species effect on a seed-grown tumor based on $\tilde{\phi}_G$ composition (**Part 3.3.1.4**), and (IV) simulation of varying MDSC activation and entrance rates on immune species influence on the tumor grown from Part III (**Part 3.3.1.5**). Parameters not specified were unchanged from [82, 83, 181]. **Table 20** through **Table 24** describe mathematical parameters and **Table 25** describes changes to the boundary conditions. All scaling factors for introduced parameters are listed in **Table 20** through **Table 23**. Because simulated nutrient and waste product diffusion length is large compared to the simulation size, it is assumed that lactic acid, bicarbonate, carbon dioxide, and H^+ boundary concentrations are negligible compared to their concentrations within the model domain. An oxygen initial condition is also established based on the uptake of oxygen by host tissue. To simulate desmoplastic conditions, the initial viable volume fraction of the tumor seed is chosen so that ECM initially constitutes the majority of tissue throughout the model domain [15, 239]. In these simulations, the Mo apoptotic rate is assumed to be negligible compared to the rate of monocyte differentiation into macrophages. Thus, $\lambda_{apoptosis|M_0} = 0$.

Table 26 describes the computational parameters used. To distinguish the interior and exterior of a continuum model tumorous mass (assuming only living tumor tissue is relevant), tumor tissue is defined by $\tilde{\phi}_V \geq 0.05$.

3.3.1.1 Tables of Parameters and Initial Conditions

Parameter	Description	Scaling Factor	Non-dimensional Value Assigned	
			Part I	Parts III & IV
ϵ_G	Interaction strength for immune species	$\bar{\bar{\epsilon}}$	0.01	
ϵ_{TG}	Interaction strength between tumor and immune species	$\bar{\bar{\epsilon}}$	0.01	
ϵ_{EG}	Interaction strength between immune species and ECM	$\bar{\bar{\epsilon}}$	0.01	
$\tilde{\gamma}_G$	Cell adhesion for immune species	$\tilde{\gamma}_G = \dfrac{\epsilon_G \cdot \tilde{\phi}_\alpha \cdot \sqrt{\tilde{\phi}_\alpha \cdot E_a^*}}{\mathcal{L} \cdot \mathcal{P}}$	0.0	
ϕ_{GG}	Saturation volume fraction for immune species interactions	$\tilde{\phi}_\alpha$	0.0025	
$\lambda_{enter|\sigma}$	Entrance rate of species σ from model vasculature	$\lambda_{M,V}$	Computed	
$\lambda_{exit|\sigma}$	Exit rate of species σ from model vasculature	$\lambda_{M,V}$	Computed	
$\lambda_{enter|G}$	Entrance rate of species G from model vasculature	$\lambda_{M,V}$	Computed	
$\lambda_{enter,E|G}$	Entrance rate of immune species within ECM	$\lambda_{M,V}$	0.03	
$\lambda_{enter,T|G}$	Entrance rate of immune species within tumor tissue	$\lambda_{M,V}$	0.03	
$\lambda_{enter,H|G}$	Entrance rate of immune species within host tissue	$\lambda_{M,V}$	0.03	
$\lambda_{exit|G}$	Exit rate of species G from model vasculature	$\lambda_{M,V}$	Computed	
$\lambda_{exit,E|G}$	Exit rate of immune species within ECM	$\lambda_{M,V}$	0.03	
$\lambda_{exit,T|G}$	Exit rate of immune species within tumor tissue	$\lambda_{M,V}$	0.03	
$\lambda_{exit,H|G}$	Exit rate of immune species within host tissue	$\lambda_{M,V}$	0.03	
$\lambda_{mitosis|\sigma}$	Mitotic rate for each species $\sigma \in G$	$\lambda_{M,V}$	0.0	
$\lambda_{apoptosis|M_0}$	Apoptotic rate for Mo	$\lambda_{M,V}$	0.0	
$\lambda_{apoptosis|\sigma}$	Apoptotic rate for each species $\sigma \in G$ except Mo	$\lambda_{M,V}$	0.1	
$\lambda_{necrosis|\sigma}$	Necrotic rate for each species $\sigma \in G$	$\lambda_{M,V}$	0.0	

$\lambda_{exit\|\sigma}$	Exit rate for species $\sigma \in G$	$\lambda_{M,V}$	0.0
$\mathcal{F}_B^{che}$	Effective factor of CHE on immune species extravasation	Dimensionless	1.0
$\lambda_{Bp,n,E}$	Transfer coefficient of O2 via pre-existing blood vasculature in ECM regions	$\lambda_{U,V,n}$	0.50
$\lambda_{Bp,n,T}$	Transfer coefficient of O2 via pre-existing blood vasculature in tumor regions	$\lambda_{U,V,n}$	0.50
$\lambda_{Bp,n,H}$	Transfer coefficient of O2 via pre-existing blood vasculature in healthy regions	$\lambda_{U,V,n}$	0.50
$\lambda_{Bn,n,E}$	Transfer coefficient of O2 via blood neo-vasculature in ECM regions	$\lambda_{U,V,n}$	8.0
$\lambda_{Bn,n,T}$	Transfer coefficient of O2 via blood neo-vasculature in tumor regions	$\lambda_{U,V,n}$	8.0
$\lambda_{Bn,n,H}$	Transfer coefficient of O2 via blood neo-vasculature in healthy regions	$\lambda_{U,V,n}$	8.0
$\lambda_{Bp,g,E}$	Transfer coefficient of glucose via pre-existing blood vasculature in ECM regions	$\lambda_{U,V,n}$	0.1
$\lambda_{Bp,g,T}$	Transfer coefficient of glucose via pre-existing blood vasculature in tumor regions	$\lambda_{U,V,n}$	0.1
$\lambda_{Bp,g,H}$	Transfer coefficient of glucose via pre-existing blood vasculature in healthy regions	$\lambda_{U,V,n}$	0.1
$\lambda_{Bn,g,E}$	Transfer coefficient of glucose via blood neo-vasculature in ECM regions	$\lambda_{U,V,n}$	1.0
$\lambda_{Bn,g,T}$	Transfer coefficient of glucose via blood neo-vasculature in tumor regions	$\lambda_{U,V,n}$	1.0
$\lambda_{Bn,g,H}$	Transfer coefficient of glucose via blood neo-	$\lambda_{U,V,n}$	1.0

	vasculature in healthy regions		
$\lambda_{Bp,w,E}$	Transfer coefficient of carbon dioxide via pre-existing blood vasculature in ECM regions	$\lambda_{U,V,n}$	1.0
$\lambda_{Bp,w,T}$	Transfer coefficient of carbon dioxide via pre-existing blood vasculature in tumor regions	$\lambda_{U,V,n}$	1.0
$\lambda_{Bp,w,H}$	Transfer coefficient of carbon dioxide via pre-existing blood vasculature in healthy regions	$\lambda_{U,V,n}$	1.0
$\lambda_{Bn,w,E}$	Transfer coefficient of carbon dioxide via blood neo-vasculature in ECM regions	$\lambda_{U,V,n}$	1.0
$\lambda_{Bn,w,T}$	Transfer coefficient of carbon dioxide via blood neo-vasculature in tumor regions	$\lambda_{U,V,n}$	1.0
$\lambda_{Bn,w,H}$	Transfer coefficient of carbon dioxide via blood neo-vasculature in healthy regions	$\lambda_{U,V,n}$	1.0
$\lambda_{Bp,\ell,E}$	Transfer coefficient of lactate ion via pre-existing blood vasculature in ECM regions	$\lambda_{U,V,n}$	1.0
$\lambda_{Bp,\ell,T}$	Transfer coefficient of lactate ion via pre-existing blood vasculature in tumor regions	$\lambda_{U,V,n}$	0.1
$\lambda_{Bp,\ell,H}$	Transfer coefficient of lactate ion via pre-existing blood vasculature in healthy regions	$\lambda_{U,V,n}$	0.5
$\lambda_{Bn,\ell,E}$	Transfer coefficient of lactate ion via blood neo-vasculature in ECM regions	$\lambda_{U,V,n}$	1.0
$\lambda_{Bn,\ell,T}$	Transfer coefficient of lactate ion via blood neo-vasculature in tumor regions	$\lambda_{U,V,n}$	1.0

Symbol	Description	Units/Param	Value	Value
$\lambda_{Bn,\ell,H}$	Transfer coefficient of lactate ion via blood neo-vasculature in healthy regions	$\lambda_{U,V,n}$	1.0	
$\mathcal{F}_{\sigma}^{B_p}$	Effective extravasation factor for species $\sigma \in G$ via pre-existing blood vasculature	Dimensionless	See **Table 23**	
$\mathcal{F}_{\sigma}^{B_n}$	Effective extravasation factor for species $\sigma \in G$ via blood neo-vasculature	Dimensionless	See **Table 23**	
$\mathcal{F}_{\sigma}^{L_p}$	Effective exit factor for species $\sigma \in G$ via pre-existing lymphatic vasculature	Dimensionless	0.0	
$\mathcal{F}_{\sigma}^{L_n}$	Effective exit factor for species $\sigma \in G$ via lymphatic neo-vasculature	Dimensionless	0.0	
$n_{v,G}$	O2 viability limit for immune species	n_{∞}	0.05	
$g_{v,G}$	Glucose viability limit for immune species	g_{∞}	0.005	
$\lambda_{diff|M_0}$	Rate of monocyte differentiation	$\lambda_{M,V}$	70.0	0.0
$\lambda_{act|B_E R}$	Rate of activation of effector B-cells	$\lambda_{M,V}$	6.0	0.0
$\lambda_{efferocytosis|D}$	Efferocytotic uptake of dead cells by immune species	$\lambda_{M,V}$	0.0	2.0
$\mathcal{F}_{InduceDeath,Ne}$	Effective factor of NE tumor cytotoxicity	Dimensionless	1.0	
$\mathcal{F}_{InduceDeath,M_1}$	Effective factor of M1 tumor cytotoxicity	Dimensionless	1.0	
$\mathcal{F}_{InduceDeath,NK}$	Effective factor of NK tumor cytotoxicity	Dimensionless	1.0	
$\mathcal{F}_{InduceDeath,Den}$	Effective factor of DC tumor cytotoxicity	Dimensionless	1.0	
$\mathcal{F}_{InduceDeath,B_E A}$	Effective factor of BeA tumor cytotoxicity	Dimensionless	1.0	
$\mathcal{F}_{InduceDeath,T_C}$	Effective factor of CTL tumor cytotoxicity	Dimensionless	1.0	
$\mathcal{F}_{InduceDeath,T_{H1}}$	Effective factor of Th1 tumor cytotoxicity	Dimensionless	1.0	
$\lambda_{InduceDeath|V}$	Tumor death rate in response to cytotoxic immune species	$\lambda_{M,V}$	0.0	1.0

$\mathcal{F}_\sigma^D$	Effective factor of immune species $\sigma \in \{Ne, M_1, M_2, Den\}$ on efferocytosis of dead tumor cells	Dimensionless	0.25	
$\mathcal{F}_{tgf}^{Diff\|M_0}$	Effective factor of TGF on monocyte differentiation	Dimensionless	1.0	0.0
$\mathcal{F}_{F_{bias}}$	Bias for steady-state M1:M2 ratio	Dimensionless	0.14286	
$\mathcal{F}_{T_{H2}\|M_2,diff}$	Effect of Th2 on monocyte differentiation	Dimensionless	0.5	
$\mathcal{F}_{T_{H1}\|M_1,diff}$	Effect of Th1 on monocyte differentiation	Dimensionless	0.5	
$\lambda_{M_2,tgf}$	Release rate of TGF by M2	$\lambda_{U,V,n}$	0.0	0.2
$\lambda_{M_2,taf}$	Release rate of TAF by M2	$\lambda_{U,V,n}$	0.0	0.2
ϕ_{TSat}	Saturation tumor volume fraction affecting BeR activation	$\tilde{\phi}_\alpha$	0.05	
$\chi_{\sigma,che}$	Chemotaxis coefficient of CHE on immune species $\sigma \in G$	E_a^*/che_{sat}	See **Table 21**	
$\chi_{\sigma,tgf}$	Chemotaxis coefficient of TGF on immune species $\sigma \in G$	E_a^*/tgf_{sat}	0.0	
$\chi_{\sigma,taf}$	Chemotaxis coefficient of TAF on immune species $\sigma \in G$	E_a^*/taf_{sat}	0.0	
$\mathcal{F}_{F_E}^{T_{H2}}$	Effective factor of Th2 on ECM production by myofibroblasts	Dimensionless	0.0	0.15
$(k_\alpha)_\sigma$	Motility of species $\sigma \in \{T, E, G, H\}$	$\bar{\bar{k}}_\alpha$	10.0	
$\lambda_{Base\|\sigma}$	Base activation level for immune species $\sigma \in G$	Dimensionless	0.333	
D_{che}	Diffusivity of chemokines	$D_{n,T}$	Computed	
$D_{che,E}$	Diffusivity of chemokines in ECM regions	$D_{n,T}$	1.0	
$D_{che,H}$	Diffusivity of chemokines in healthy regions	$D_{n,T}$	1.0	
$D_{che,T}$	Diffusivity of chemokines in tumor regions	$D_{n,T}$	1.0	

$\lambda_{V,che}$	Release rate of chemokines by the tumor	$\lambda_{U,V,n}$	1.25	
$\lambda_{U,G,che}$	Uptake rate of CHE by immune species	$\lambda_{U,V,n}$	0.25	
$\lambda_{de,che}$	Degradation rate of CHE	$\lambda_{U,V,n}$	0.05	
$\mathcal{F}_{che,n}^{V}$	Effective factor of hypoxia upregulation of CHE production by tumor tissue	Dimensionless	1.0	
$\mathcal{F}_{BnE,G}$	Maximum effect of immune species on blood neo-vasculature formation	Dimensionless	0.0	1.0
$\mathcal{F}_{i|BnE}$	Effective factor of immune species $i \in \{B_E R, B_E A, B_{reg}\}$ on blood neo-vasculature formation	Dimensionless	0.0	0.333

Table 20 Summary of model immune parameters. Computed parameters are defined

as functions of model variables or constant-valued model parameters. Set $G = \{M_0, M_1, M_2, NK, Ne, Den, MDSC, B_E R, B_E A, B_{reg}, T_C, T_R, T_{H1}, T_{H2}\}$.

Chemotaxis coefficient	Non-dimensionalized Value Assigned in Part I
$\chi_{M_0,che}$	0.5
$\chi_{M_1,che}$	0.6
$\chi_{M_2,che}$	0.7
$\chi_{NK,che}$	0.8
$\chi_{Ne,che}$	0.9
$\chi_{Den,che}$	1.0
$\chi_{MDSC,che}$	1.1
$\chi_{B_E R,che}$	1.2
$\chi_{B_E A,che}$	1.3

$\chi_{B_{reg},che}$	1.4
$\chi_{T_C,che}$	1.5
$\chi_{T_R,che}$	1.6
$\chi_{T_{H1},che}$	1.7
$\chi_{T_{H2},che}$	1.8

Table 21 Chemotaxis parameter values by immune species. All values are non-dimensionalized using $\frac{E_a^*}{che_{sat}}$. For Parts III and IV, all chemotaxis coefficients were chosen to be 40.0.

Parameter	Non-dimensionalized Value Assigned		Parameter	Non-dimensionalized Value Assigned	
	Parts I-III	Part IV		Parts I-III	Part IV
$\lambda_{M_1|T_{H1}}$	0.167	0.06	$\lambda_{B_EA|MDSC}$	0.333	
$\lambda_{Den|T_{H1}}$	0.167	0.06	$\lambda_{B_{reg}|MDSC}$	0.333	
$\lambda_{B_EA|T_{H1}}$	0.167	0.06	$\lambda_{T_{H1}|B_ER}$	0.5	
$\lambda_{B_{reg}|T_{H1}}$	0.167	0.06	$\lambda_{T_{H2}|B_ER}$	0.5	
$\lambda_{T_R|T_{H1}}$	0.167	0.06	$\lambda_{T_{H1}|B_EA}$	0.333	0.1
$\lambda_{MDSC|T_{H1}}$	0.167	0.7	$\lambda_{T_{H2}|B_EA}$	0.333	0.1
$\lambda_{M_2|T_{H2}}$	0.167	0.04	$\lambda_{MDSC|B_EA}$	0.333	0.8
$\lambda_{Den|T_{H2}}$	0.167	0.04	$\lambda_{T_{H1}|B_{reg}}$	0.5	
$\lambda_{B_EA|T_{H2}}$	0.167	0.04	$\lambda_{T_{H2}|B_{reg}}$	0.5	
$\lambda_{B_{reg}|T_{H2}}$	0.167	0.04	$\lambda_{T_{H1}|T_C}$	0.2	0.05
$\lambda_{T_R|T_{H2}}$	0.167	0.04	$\lambda_{T_{H2}|T_C}$	0.2	0.05

$\lambda_{MDSC|T_{H2}}$	0.167	0.8	$\lambda_{Breg|T_C}$	0.2	0.05
$\lambda_{T_{H1}|NK}$	0.25	0.067	$\lambda_{MDSC|T_C}$	0.2	0.8
$\lambda_{T_R|NK}$	0.25	0.067	$\lambda_{T_R|T_C}$	0.2	0.05
$\lambda_{MDSC|NK}$	0.25	0.8	$\lambda_{MDSC|T_R}$	0.5	
$\lambda_{Breg|NK}$	0.25	0.067	$\lambda_{Breg|T_R}$	0.5	
$\lambda_{B_ER|MDSC}$	0.333		$\lambda_{T_{H1}|Den}$	0.5	0.3
$\lambda_{MDSC|Den}$	0.5	0.7			

Table 22 Activation term parameters for Equation 3.2.52 through Equation 3.2.64.

For species α and β and $\alpha, \beta \in$

$\{M_1, M_2, NK, Ne, Den, MDSC, B_ER, B_EA, B_{reg}, T_C, T_R, T_{H1}, T_{H2}\}$, the effective interaction

of α on species β is $\lambda_{\alpha|\beta}$. All λ parameters are dimensionless.

Parameter	Description	Value Assigned		
		Part I	Part III Pro-tumor	Part III Anti-tumor
$\mathcal{F}_{M_0}^{Bp}$		2.0	0	0
$\mathcal{F}_{M_1}^{Bp}$		0.0	0.5	2.25
$\mathcal{F}_{M_2}^{Bp}$	For immune species $\sigma \in G$, extravasation factor for pre-existing blood vasculature	0.0	2.25	0.5
$\mathcal{F}_{NK}^{Bp}$		2.1	0.5	2.25
$\mathcal{F}_{Ne}^{Bp}$		2.2	0.5	2.25
$\mathcal{F}_{Den}^{Bp}$		2.3	0.5	2.25
$\mathcal{F}_{MDSC}^{Bp}$		2.4	2.25	0.5
$\mathcal{F}_{B_ER}^{Bp}$		2.5	2.25	0.5

$\mathcal{F}_{B_E A}^{Bp}$		0.0	0.5	2.25
$\mathcal{F}_{B_{reg}}^{Bp}$		2.6	2.25	0.5
$\mathcal{F}_{T_C}^{Bp}$		2.7	0.5	2.25
$\mathcal{F}_{T_R}^{Bp}$		2.8	2.25	0.5
$\mathcal{F}_{T_{H1}}^{Bp}$		2.9	0.5	2.25
$\mathcal{F}_{T_{H2}}^{Bp}$		3.0	2.25	0.5
$\mathcal{F}_\sigma^{Bn}$	Extravasation rate of species $\sigma \in G$ fromblood neo-vasculature	$1.2 \cdot \mathcal{F}_\sigma^{Bp}$	$\mathcal{F}_\sigma^{Bp}$	

Table 23 Entrance factors (dimensionless units). Set $G =$

$\{M_0, M_1, M_2, NK, Ne, Den, MDSC, B_E R, B_E A, B_{reg}, T_C, T_R, T_{H1}, T_{H2}\}.$

Parameter	Description	Previous Value from [82]	New Value
$\tilde{n}_h$	Hypoxic Threshold	0.3	0.489
$\tilde{n}_{v,V}$	O2 viability limit of viable tumor tissue	0.21	0.10
$\tilde{p}_{t,B}$	Threshold pressure corresponding on the onset of blood vasculature loss	0.6	0.15
$\tilde{p}_{t,L}$	Threshold pressure corresponding on the onset of lymphatic vasculature loss	0.6	0.15
$\tilde{p}_{c,Bp}$	Threshold pressure corresponding to the maximum rate of pre-existing blood vasculature loss	0.8	0.9
$\tilde{p}_{c,Lp}$	Threshold pressure corresponding to the maximum rate of pre-existing lymphatic vasculature loss	0.8	0.9
$\tilde{p}_{c,Bn}$	Threshold pressure corresponding to the maximum rate of pre-existing blood vasculature loss	0.8	0.2

$\tilde{p}_{c,Ln}$	Threshold pressure corresponding to the maximum rate of pre-existing lymphatic vasculature loss	0.8	0.2
$\tilde{\lambda}_{N,V}$	Necrotic rate for viable tumor tissue	3.0	1.0
$\tilde{\lambda}_{L,D}$	Lysis rate of dead tumor tissue	1.0	9.0
$\tilde{\lambda}_{F,E}$	ECM rate of secretion by myofibroblasts	5.0	2.0
$\tilde{\lambda}_{de,E}$	Degradation rate of ECM	1.0	0.0
$\tilde{\lambda}_{de,C}$	Degradation of ECM in reaction to matrix degrading enzymes	5.0	0.7
$\tilde{\lambda}_{U,V,n}$	Uptake rate of oxygen by viable tumor tissue	1.0	1.85
$\tilde{\lambda}_{U,H,n}$	Uptake rate of oxygen by host tissue	0.0001	0.036
$\tilde{\lambda}_{V,tgf}$	Production rate of tumor growth factors by ϕ_V	0.2	0.37115
$\tilde{\lambda}_{V,taf}$	Production rate constant of tumor angiogenic factors by ϕ_V	0.2	3.0
$\tilde{\lambda}_{de,taf}$	Degradation rate constant of tumor angiogenic factors	0.05	1.0
$\widetilde{\lambda}_{V,m}$	Production rate constant of matrix degrading enzymes by ϕ_V	0.2	3.0
$\tilde{\lambda}_{de,m}$	Decay rate of matrix degrading enzymes	5.0	10.0
$\tilde{\lambda}_{M,FE}$	Mitosis rate constant for myofibroblasts	0.1	0.75
$\tilde{\lambda}_{N,FE}$	Necrosis rate constant of myofibroblasts	0.3	0.1
$\tilde{\lambda}_{m,BnE}$	Maximum mitosis rate of blood neo-vasculature	1.0	18.0
$\tilde{\lambda}_{crush,BnE}$	Maximum degradation rate constant of blood neo-vasculature due to solid tissue pressure	1.0	5.0
$\tilde{\lambda}_{de,BnE}$	Remodeling rate constant of blood neo-vasculature due to matrix degrading enzymes	1.0	5.0
$\tilde{\lambda}_{m,LnE}$	Maximum mitosis rate of lymphatic neo-vasculature	1.0	2.0
$\tilde{\lambda}_{crush,LnE}$	Maximum degradation rate constant of lymphatic neo-vasculature due to tissue pressure	1.0	4.0
$\widetilde{tgf}_{FE,E}$	Minimum threshold for tgf required to initiate ECM secretion by myofibroblasts	0.2	0.2 (*)

	Remodeling rate constant of new lymphatic vasculature due to matrix degrading enzymes	1.0	4.0
$\tilde{\lambda}_{de,LnE}$			
$\mathcal{F}_{lg|Bn}$	Vasculature (with logistic growth) (0 = Disabled, 1 = Enabled)	0	1

Table 24 Parameter values different from [82]. (*) Value was not given in [82] and is included here for completeness.

Variable	Condition Type	Value from [181]	New Value
Sodium ($\tilde{s}$)	Boundary & Internal	0.5	1.0
Oxygen ($\tilde{n}$)		1.0	0.844
Pre-existing Blood Vasculature ($\tilde{B}_E^p$)		0.0	0.13
Blood Neo-Vasculature ($\tilde{B}_E^n$)		0.4	0.0
Pre-existing Lymphatic Vasculature ($\tilde{L}_E^p$)		0.0	0.025
Lymphatic Neo-Vasculature ($\tilde{L}_E^n$)		0.4	0.0
ECM ($\tilde{\phi}_E$)		0.35	0.75
Seeded Viable Tumor ($\tilde{\phi}_V$)	Internal Only	0.65	0.1875
Lactic Acid ($\tilde{\ell}$)	Boundary Only	0.15	0.0
Bicarbonate ($\tilde{b}$)		0.15	0.0
Carbon Dioxide ($\tilde{w}$)		0.15	0.0
H$^+$ ($\tilde{a}$)		0.15	0.0

Table 25 Model internal and boundary initial condition values. All other conditions and values are as in [181].

		Value Assigned	
Parameter	Description	Figure 11 through Figure 13	Figure 14 through Figure 18
#Simulated Points	Number of points within the cubic simulated domain	643	323

#Levels used	Number of levels used in the Multigrid solver	4	3
ℓ_{global}	Finest level that always spans Ω	4	3
ℓ_{max}	Finest grid used for Ω	4	3
η	Point spacing (Simulation Resolution)	33.3 µm	
σ	Tolerance reduction factor from level ℓ to $\ell + 1$	1.10	
θ	Time step size (days)	1.25*10-2	
$\tau_{\ell_{max}}$	Solution Tolerance for level ℓ_{max}	1.5*10-3	
v_0, v_1, v_2, v_b	Preset number of smoothing steps	12,6,6,0	
r_{max}	Maximum number of smoothing steps before divergence exception is raised	45	

Table 26 Computed parameters from [83] used for immune simulations. Initial values are set pre-model runtime. Values not listed were set as in [83].

3.3.1.2 Part I – Evaluation of Immune Species Distribution

To establish immune species distributions interacting with a growing tumor, Part I simulates the growth of a tumor from a 66 µm diameter avascular tumor seed over the course of 10 simulated days in a 64^3 domain. Using MATLAB, differing isosurfaces for each immune species, CHE, and living tumor mass ($\tilde{\phi}_V$) were plotted. Entrance and chemotaxis rates were chosen to slightly differ across immune species to promote output variability. **Figure 11** and **Figure 12** visualize the immune species in 3D surrounding a single tumor mass after 10 simulated days. Distribution of immune species both inside and outside the tumor mass after 10 simulated days was quantified with results in **Figure 13**.
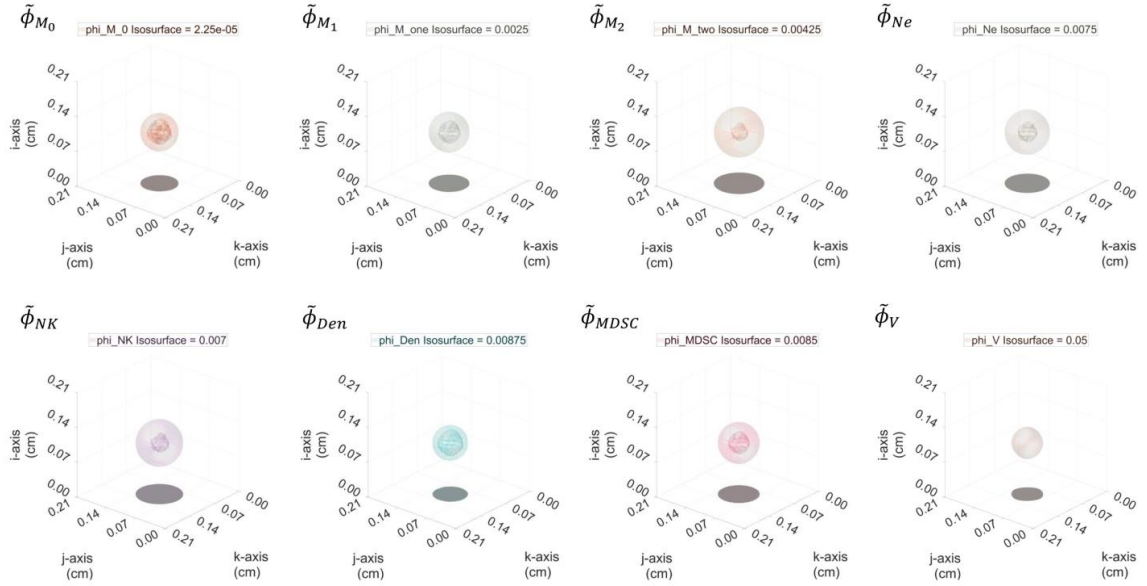
Figure 11 3D representation of innate immune species and tumor mass after 10 simulated days in a 2.1x2.1x2.1 mm³ domain.
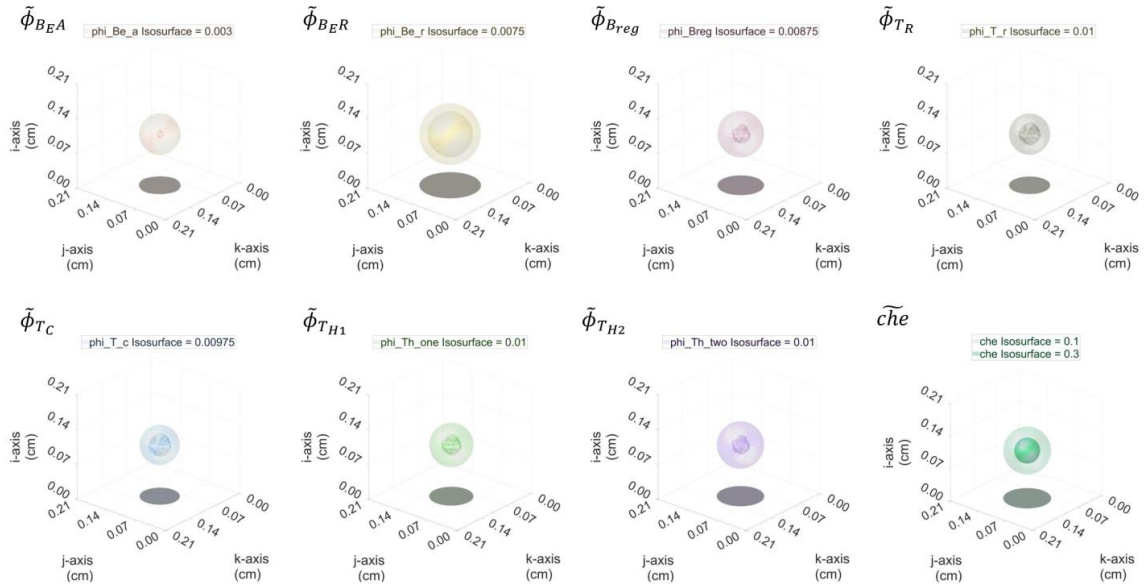
Figure 12 3D representation of adaptive immune species and chemokine densities after 10 simulated days in a 2.1x2.1x2.1 mm³ domain.
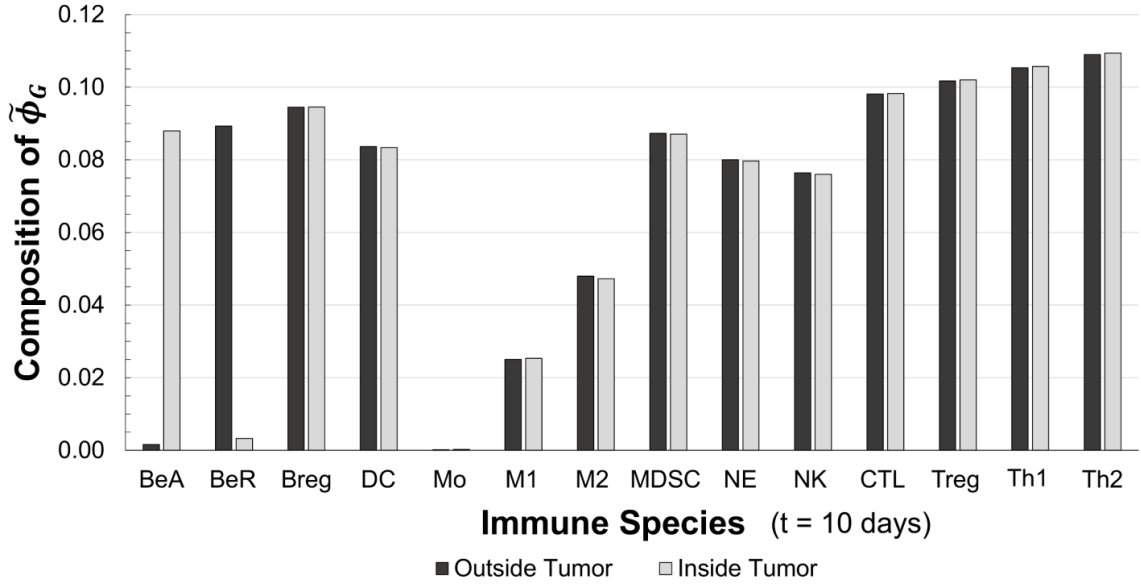
Figure 13 Composition of $\widetilde{\phi}_G$ inside and outside a spherical tumor mass after 10 simulated days. Interior tumor points are defined by $\tilde{\phi}_V \geq 0.05$. Interior tumor points are defined by $\tilde{\phi}_V \geq 0.05$.

In **Figure 11** and **Figure 12**, immune species penetrated the tumor after 10 simulated days. This was driven by two phenomena: (1) raised local extravasation due to neovascularization and local CHE expression and (2) chemotaxis up the CHE gradient. **Figure 11** depicts isosurfaces surrounding the viable tumor and innate immune species, whereas **Figure 12** illustrates adaptive immune species and chemotaxis concentration. Species-specific extravasation and chemotaxis rates lead to heterogeneous $\tilde{\phi}_G$ composition, as seen qualitatively in **Figure 11** and **Figure 12** and quantitatively in **Figure 13**. For all immune species, except B-effector cells whose activation depends on local tumor presence, contribution to $\tilde{\phi}_G$ was homogenous in the tumor domain. Steady,

rapid differentiation of Mo into M1 and M2 left a negligible population of Mo. Our

model used a baseline M1:M2 ratio of 1.0:1.8 in keeping with *in vivo* data from breast

cancer liver metastases [59]. However, higher Th2 concentration over Th1 shifted the

M1:M2 ratio of the domain to 1.0:1.9 overall. Tumor-localized B-effector cell activation

dramatically increases BeA contribution from <0.2% outside to 8.8% of $\tilde{\phi}_G$ inside the

tumor.

3.3.1.3 Part II – Evaluation of Immune Species Interactions

To explore the model's ability to balance immune interactions using adjustment

factors, the effect of shifting immune volume fractions was quantified. In a tumor-free

domain with 32^3 points containing a homogenous field of immune volume fractions, a

single immune species' volume fraction was increased from a background volume

fraction ($\tilde{\phi}_{GG}/4$) to a near-saturation concentration ($7 \cdot \tilde{\phi}_{GG}/8$), perturbing the

adjustment factor equilibrium. **Figure 14** documents the results from these perturbations.

In order to examine potential interaction values found in Equation 3.2.52 through

Equation 3.2.64, two representative initial conditions were created, one pro-tumor and

one anti-tumor. Pro-tumor and anti-tumor cases differed only in the immune

concentrations chosen for each immune species. Starting with the homogenously defined

initial condition used in **Figure 14**, the volume fractions of either pro- or anti- tumor

species were increased. As mentioned in **Table 16**, pro-tumor species, including M2,

MDSC, Breg, Treg, and Th2, and anti-tumor species, consisting of M1, NK, NE, DC,

BeR, BeA, CTL, and Th1, were increased in their respective cases from a background to

near-saturation concentration. A non-immune baseline case was also simulated.

Monocytes, having no simulated interactions, were excluded from Part II. Interaction strengths were calculated all scenarios. The volume fraction and the activation levels were recorded, from which the Influence term for each immune species σ ($\mathcal{A}_{I|\sigma} \cdot Q_3\left(\tilde{\phi}_\sigma / \tilde{\phi}_{GG}\right)$) was calculated. **Figure 15** reports σ activation levels ($\mathcal{A}_{I|\sigma}$), normalized volume fraction ($\tilde{\phi}_\sigma / \tilde{\phi}_{GG}$), and influence.
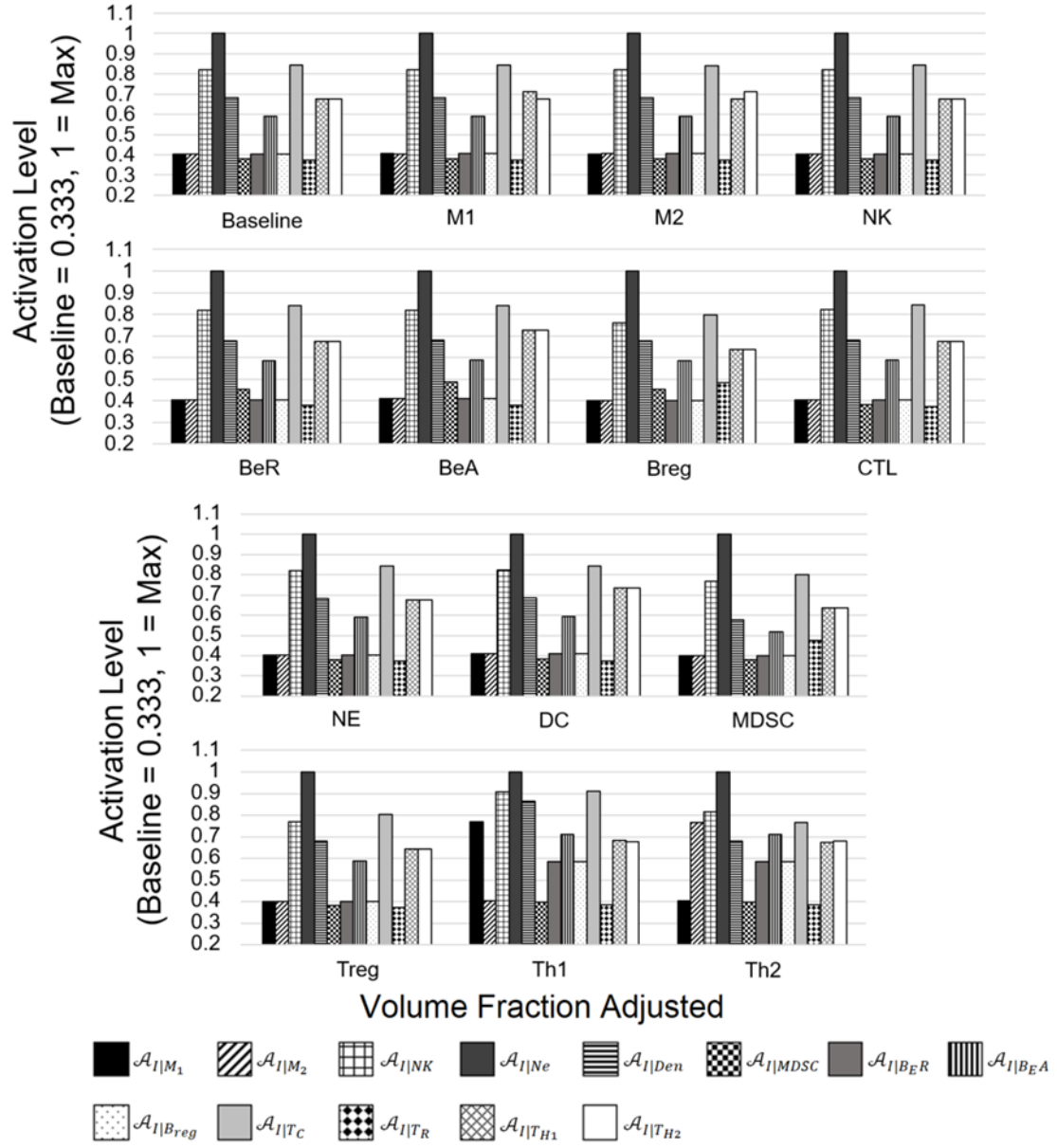
Figure 14 Effect on immune activation levels due to shifting individual volume fractions from background to near-saturation concentration within the tumor domain. Immune species can affect immune activation levels either directly or indirectly by stimulating or inhibiting specific immune species. For each case an individual volume fraction was shifted from $(\tilde{\phi}_{GG}/4)$ to $(7 \cdot \tilde{\phi}_{GG}/8)$. Excluding $\mathcal{A}_{I|Ne} = 1.0$, $\mathcal{A}_{I|\sigma}$ values ranged from a minimum of 0.375 (observed with MDSC in a high-MDSC environment or

high-Treg environment) and a maximum of 0.870 (observed with NK in a high-Th1 environment). Baseline activation was set to 0.333.

Figure 14 shows the effects of shifting individual volume fraction concentrations for immune-immune interactions in a tumor-free simulation. Neutrophils, being independent from other immune species concentrations, remained at maximum activation (1.0). Higher activation levels for each immune species are only realized under concomitant aggregation of corresponding multiple T-term immune species. This is evidenced in comparing M1 reaction, a species only dependent on Th1 concentration, to raised Th1 prevalence in which M1 activation nearly doubles from 0.40 to 0.77. Reduced activation is seen in MDSC activation levels due to co-dependence on three T-term immune species: Breg, BeA, and BeR. Increasing Breg or BeR, each with activation level 0.40, raises MDSC activation from 0.38 to 0.45, an 18% increase over baseline. Due to an inhibitory interaction with MDSC, the BeA activation baseline (0.59) is raised relative to baseline Breg and BeR activation (both 0.40). Consequently, MDSC activation is slightly raised in the BeA case to 0.49, an 8.9% increase over the Breg or BeR case.
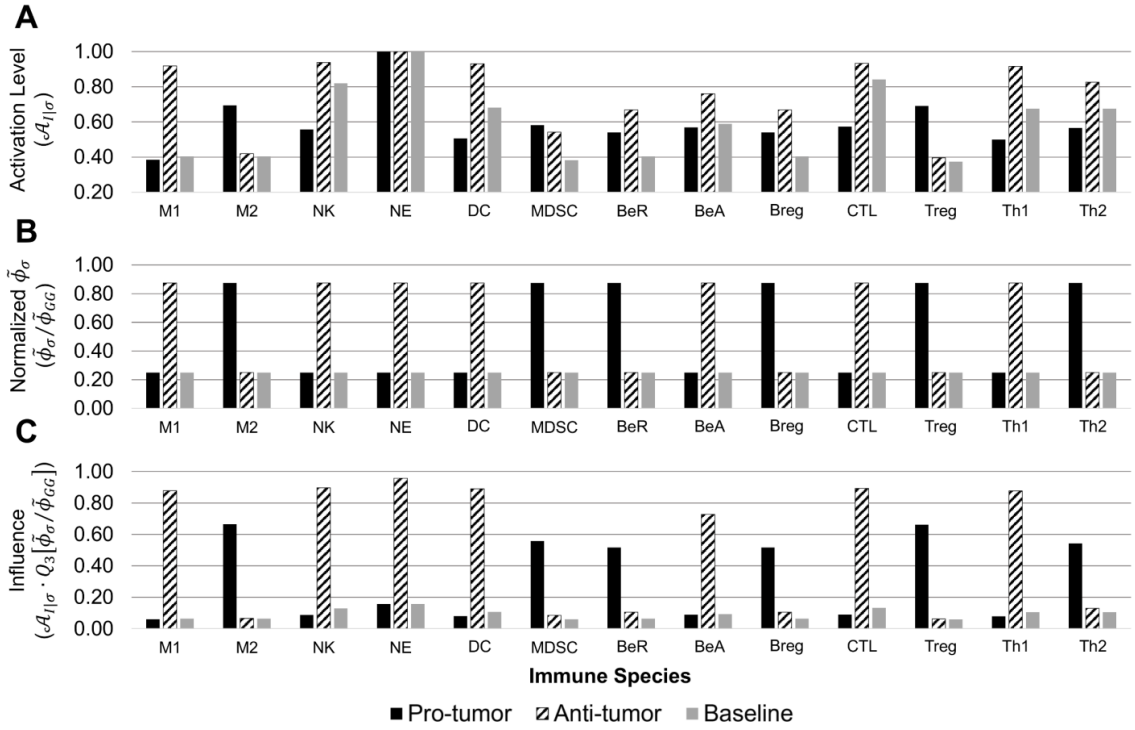
Figure 15 Summary of (A) activation levels ($\mathcal{A}_{I|i}$), (B) normalized volume fraction ($\widetilde{\phi}_i/\widetilde{\phi}_{GG}$), and (C) Influence on the TME ($\mathcal{A}_{I|i} \cdot Q_3(\widetilde{\phi}_i/\widetilde{\phi}_{GG})$) for each immune species $i \in G$ under either pro-tumor, anti-tumor, or baseline conditions.

3.3.1.3.1 Pro-Tumor Case

Figure 15 quantifies the co-dependence of immune species activation levels upon one another when immune volume fractions are varied in pro-tumor and anti-tumor scenarios (**Figure 15A** & **Figure 15B**). Pro-tumor environments have higher concentrations of M2, MDSC, BeR, Breg, Treg, and Th2 species. M1 species, depending only on Th1 concentration, see minimal change over baseline. M2, BeR, and Breg species are activated in this model by Th2, thus increased Th2 concentration permits higher activation of all three species over baseline. BeA lacks regulation in the baseline case and is only slightly downregulated by MDSC due to helper T-cell activation. NK are

115

hampered by higher MDSC, Breg, and Treg presence, reducing its activation level. Low Th1 and high MDSC concentrations lower DC activation. MDSC exhibit a similar phenomenon: Both BeR and Breg contribute higher volume fractions, but mediocre B-cell activation blunts B-cell effect. MDSC activation level rises due to marginal B-cell influence. CTL, being upregulated by Th1 but inhibited by Th2, Breg, MDSC, and Treg, are significantly inhibited. Treg activation level is elevated due to higher Breg and MDSC presence. Helper T-cells in this simulation have the most immune interactions, with Th1 being stimulated by M1, Th2 stimulated by M2, both species stimulated by DC and BeA, and both species inhibited by Breg, Treg, and MDSC. Breg, Treg, and MDSC have increased volume fractions and increased activation levels and DC has a significantly lowered activation state, leading to a strong inhibitory effect. Th2 has reduced inhibition relative to Th1 due to increased M2 activation and M2 concentration. Finally, neutrophils lack interactions in this model, maintaining their interaction strength at maximum (1.0).

3.3.1.3.2 Anti-Tumor Case

Dominating the set of anti-tumor interactions in **Figure 15** is the mutually stimulatory effect of M1, DC, BeA, and Th1. Depending only on Th1 for stimulation, M1 and DC activation levels are allowed to climb significantly with Th1 activations. Meanwhile Th1 relies on M1, DC, and BeA for stimulatory interactions. Activation rises for M1, DC, and Th1. Consequently, without the inhibition found in the pro-tumor case, Th1 raises CTL and NK activation, but BeA, depending on both helper T-cell species, experiences a more modest gain in activation level. BeR, BeA, and Breg, being stimulated by Th1, have raised stimulation above both baseline and pro-tumor conditions. Mirroring M1 in the pro-tumor case, M2 activation is largely unchanged in the anti-tumor case.

3.3.1.3.3 Influence on the TME of Pro-Tumor and Anti-Tumor Cases

Finally, observations in both pro-tumor and anti-tumor cases are combined together in **Figure 15C** to obtain the influence of immune species σ on the TME, including differentiation of macrophages (Equation 3.2.90), tumor removal (and Equation 3.2.99), TGF and TAF production (Equation 3.2.100 and Equation 3.2.102, respectively), angiogenesis (Equation 3.2.113), and production of ECM by myofibroblasts (Equation 3.2.122). Higher concentrations of NE in the anti-tumor case increases NE influence dramatically from 0.16 to 0.96, demonstrating that activation is necessary but not sufficient for strong influence. For B-cell species, dependence on anti-tumor species drives anti-tumor case activation levels beyond both baseline and pro-tumor scenarios, but limited volume fractions dampen the influence that B-cells can exert on the outcome. Thus, changes to the value of $\tilde{\phi}_\sigma$ in the domain between pro-tumor and anti-tumor cases significantly affect σ to change the TME. **Table 27** summarizes the activation levels across all three cases.

Immune Species		Pro-tumor	Anti-tumor	Baseline
Abbreviated Name	Volume Fraction			
M1	$\tilde{\phi}_{M1}$	0.39	0.92	0.40
M2	$\tilde{\phi}_{M2}$	0.69	0.42	0.40
NK	$\tilde{\phi}_{NK}$	0.56	0.94	0.82
NE	$\tilde{\phi}_{Ne}$	1.00	1.00	1.00
DC	$\tilde{\phi}_{Den}$	0.51	0.93	0.68
MDSC	$\tilde{\phi}_{MDSC}$	0.58	0.54	0.38

BeR	$\tilde{\phi}_{B_E R}$	0.54	0.67	0.40
BeA	$\tilde{\phi}_{B_E A}$	0.57	0.76	0.59
Breg	$\tilde{\phi}_{B_{reg}}$	0.54	0.67	0.40
CTL	$\tilde{\phi}_{T_C}$	0.57	0.93	0.84
Treg	$\tilde{\phi}_{T_R}$	0.69	0.40	0.37
Th1	$\tilde{\phi}_{T_{H1}}$	0.50	0.92	0.68
Th2	$\tilde{\phi}_{T_{H2}}$	0.57	0.83	0.68

Table 27 Activation levels for pro-tumor, anti-tumor and baseline cases.

3.3.1.4 Part III – Quantification of Immune Species Effect on the TME

The effects of simulations dominated by either pro- or anti-tumor immune species were quantified. **Figure 16** and **Figure 17** compare the effects of pro- and anti- immune environments on a single tumor relative to an immune-species-free baseline case. The tumor grew from a 66 μm avascular seed for a period of 5 simulated days (at which time the diameter reached 267 μm), after which immune species extravasated into the domain over 4 additional simulated days. By 5 days, the tumor exhibited steady growth. Because tumors grown from a seed (akin to the tumor shown in **Figure 11**) were essentially spherical, the tumor radius was computed assuming a spherical tumor. To ensure a stable and reliable comparison of M1, M2 and BeA for pro-tumor and anti-tumor conditions, differentiation was disabled, monocytes were excluded from this simulation, and all species entered into the tumor domain by extravasation out of blood vasculature.
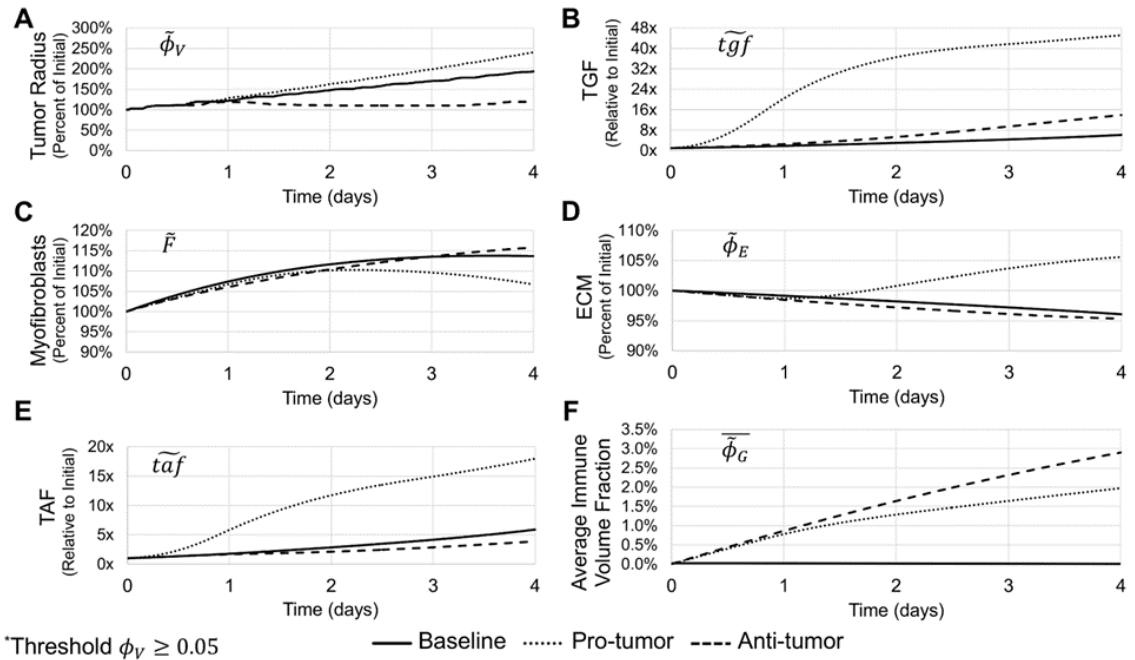
Figure 16 Graph of non-dimensionalized (A) viable tumor volume fraction ($\tilde{\phi}_V$) with threshold $\tilde{\phi}_V \geq 0.05$, (B) Tumor growth factor ($\widetilde{tgf}$), (C) myofibroblast concentration per unit volume of tissue ($\tilde{F}$), (D) ECM volume fraction ($\tilde{\phi}_E$), (E) Tumor angiogenic factor ($\widetilde{taf}$), and (F) average total volume fraction of immune species ($\overline{\tilde{\phi}_G}$), within a 1.1x1.1x1.1 mm3 domain. At t = 4 days the pro-tumor case had higher tumor proliferation, ECM density, greater TGF and TAF production over baseline and maintained similar overall neovascularization compared to baseline. The anti-tumor case produced a smaller tumor with reduced TAF and overall neovascularization and increased TGF production. Overall myofibroblast presence was controlled significantly by hypoxic regions. Time t = 0 marks initial immune species extravasation time step after an initial 5 days of tumor growth. An increasing immune species presence is evident in the anti-tumor case compared to the pro-tumor case.
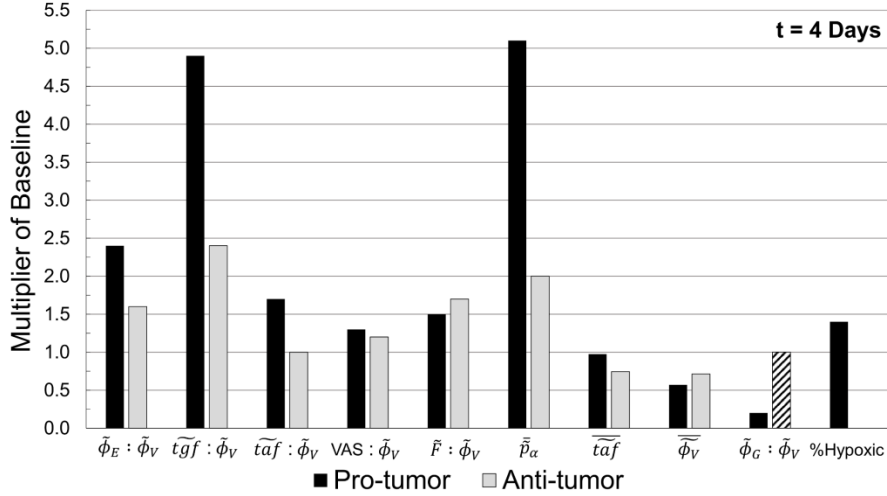
Figure 17 Measurements within the tumor mass for 4 simulated days after an initial 5 days of growth. Metrics include ratio of $\tilde{\phi}_E$ to $\tilde{\phi}_V$, $\widetilde{tgf}$ to $\tilde{\phi}_V$, $\widetilde{taf}$ to $\tilde{\phi}_V$, ratio of non-dimensionalized vasculature, both blood and lymphatic, to $\tilde{\phi}_V$, ratio of myofibroblast concentration per unit volume of tissue ($\tilde{F}$) to $\tilde{\phi}_V$ [82], mean solid-state pressure ($\bar{\tilde{p}}_\alpha$), mean TAF ($\overline{\widetilde{taf}}$), mean volume fraction of viable tumor tissue ($\overline{\tilde{\phi}_V}$), ratio of $\tilde{\phi}_G$ to $\tilde{\phi}_V$, and the percentage of tumor tissue that was hypoxic (%Hypoxic). Here, tumor tissue is defined by points containing $\tilde{\phi}_V \geq 0.05$. Anti-tumor case is $\tilde{\phi}_G : \tilde{\phi}_V$ reference value (striped bar). All other metrics are relative to the baseline case. VAS = Vasculature (both blood and lymphatic).

Tumor radius (**Figure 16A**) grew 2.4x over initial size in the pro-tumor case, improving on the 1.9x increase observed in the baseline case. The immune population in the anti-tumor case effectively regulated tumor growth, with only 1.2x growth occurring after 4 simulated days compared to the initial tumor radius. Tumor growth in the pro-tumor case was promoted by M2 release of TGF (Equation 3.2.103 through Equation 3.2.107) (**Figure 16B**), with overall pro-tumor TGF presence rising to 7.3x over baseline

and, per **Figure 17**, a 4.9x baseline intra-tumor $\widetilde{tgf} : \tilde{\phi}_V$ ratio after 4 simulated days. Local anti-tumor case M2 TGF release raised overall TGF concentration to 2.3x baseline and $\widetilde{tgf} : \tilde{\phi}_V$ to 2.4x baseline. Heightened local TGF expression raised the ratio of myofibroblast concentration ($\tilde{F}$) to $\tilde{\phi}_V$ ($\tilde{F} : \tilde{\phi}_V$) to 1.5x and 1.7x baseline for pro-tumor and anti-tumor cases, respectively, by promoting myofibroblast mitosis. However, tumor growth caused %Hypoxia to rise to 1.4x baseline and hindered myofibroblast mitosis, causing overall $\tilde{F}$ to fall to 94% baseline in the pro-tumor case (**Figure 16C**). With reduced oxygen uptake due to stunted tumor growth, the anti-tumor case overall had 1.9% higher $\tilde{F}$ over baseline. Myofibroblasts, stimulated by Th2 (Equation 3.2.119 through Equation 3.2.122), raised $\tilde{\phi}_E : \tilde{\phi}_V$ ratio in the pro-tumor case to 2.4x baseline and increased overall ECM in conjunction with M2-derived TGF production by 5.6% over initial ECM volume fraction at t = 0 (**Figure 16D**). With the parameter values used, the contribution to the change in overall ECM and $\tilde{\phi}_E : \tilde{\phi}_V$ from baseline due to Th2 stimulation was ~2% and ~3%, respectively. In both anti-tumor and baseline cases matrix degrading enzymes reduced ECM to 95% and 96% of its amount at t = 0 days, respectively. Raised TGF production elevated $\tilde{\phi}_E : \tilde{\phi}_V$ to 1.6x baseline. Consequently, the solid-state pressure within tumor tissue ($\bar{\tilde{p}}_\alpha$) in the anti-tumor case increased to 2.0x baseline, where tumor tissue is defined as $\tilde{\phi}_V \geq 0.05$.

M2 TAF release (Equation 3.2.114 through Equation 3.2.118) in the pro-tumor case raised $\widetilde{taf} : \tilde{\phi}_V$ to 1.7x baseline and led to 3.1x baseline TAF expression in the domain overall (**Figure 16E**). $\bar{\tilde{p}}_\alpha$ increased to 5.1x baseline, thus distributing tumor tissue over a greater volume. This is evidenced by the decline of mean tumor volume

fraction ($\overline{\tilde{\phi}_V}$) within tumor tissue to 0.6x baseline. Reduced $\overline{\tilde{\phi}_V}$ offset raised TAF

production thus keeping average intra-tumor TAF ($\overline{\widetilde{taf}}$) at baseline. Elevated ECM

expression raised the ratio of (blood and lymphatic) vasculature to $\tilde{\phi}_V$ (VAS : $\tilde{\phi}_V$) to 1.3x

baseline, offsetting pressure-induced displacement of pre-existing blood vasculature.

The smaller tumor in the anti-tumor case consumed insufficient oxygen to

generate hypoxic conditions and reached only 66% baseline TAF expression after 4

simulated days. Deterred by anti-tumor immune response, $\overline{\tilde{\phi}_V}$ only reached 0.7x baseline,

contributing to the decrease to 0.7x baseline in $\overline{\widetilde{taf}}$. Consequently, $\tilde{B}_n$ growth was

diminished to 4.5% of overall baseline vascularization. Controlling for the mass of the

tumor, M2 TAF release kept $\widetilde{taf}$: $\tilde{\phi}_V$ at baseline. Like the pro-tumor case, elevated ECM

production raised VAS : $\tilde{\phi}_V$ to 1.2x baseline.

Finally, the tumor tissue $\tilde{\phi}_G$: $\tilde{\phi}_V$ ratio in **Figure 17** decreased in the pro-tumor

case to 0.2x of the anti-tumor case. Because this model simulates seven anti-tumor

species compared to six pro-tumor species, the anti-tumor case has a higher number of

immune species than the pro-tumor case; however, this difference is insufficient to

account for the change in $\tilde{\phi}_G$: $\tilde{\phi}_V$ because the species all share the same extravasation

values as shown in **Table 23**. Rather, this difference can be accounted for by the change

in $\bar{\tilde{p}}_\alpha$ between the cases. The pro-tumor case had a 2.6x higher $\bar{\tilde{p}}_\alpha$ value over the anti-

tumor case from tumor proliferation and ECM secretion. Higher pressure reduced

immune species extravasation (Equation 3.2.76) and discouraged immune species

chemotaxis (Equation 3.2.47, Equation 3.2.96, Equation 3.2.97, and Equation 3.2.136).

Therefore, due to raised intratumor pressure primarily and a higher number of anti-tumor

species secondarily, the average total volume fraction of immune species ($\overline{\tilde{\phi}_G}$) was higher

in the anti-tumor case than the pro-tumor case, by 4 simulated days, reaching 2.9% and

2.0%, respectively (**Figure 16F**). This pro-tumor domain, then, reduced intra-tumor

immune species presence and increased ECM formation, both of which are characteristic

of pro-tumor desmoplastic tumor microenvironments [15, 57, 239]. **Table 28** summarizes

the results of **Figure 17**.

Metric	Pro-tumor	Anti-tumor
$\tilde{\phi}_E : \tilde{\phi}_V$	2.4	1.6
$\widetilde{tgf} : \tilde{\phi}_V$	4.9	2.4
$\widetilde{taf} : \tilde{\phi}_V$	1.7	1.0
$VAS : \tilde{\phi}_V$	1.3	1.2
$\tilde{F} : \tilde{\phi}_V$	1.5	1.7
$\bar{\tilde{p}}_\alpha$	5.1	2.0
$\overline{\widetilde{taf}}$	1.0	0.7
$\overline{\widetilde{\phi_V}}$	0.6	0.7
$\tilde{\phi}_G : \tilde{\phi}_V$	0.2	1.0
%Hypoxic	1.4	0.0

Table 28 Resulting metrics from Part III simulation cases displayed in Figure 17.

Baseline case was 0.0 for $\tilde{\phi}_G : \tilde{\phi}_V$ since the baseline case did not contain immune species

and was 1.0 for all other metrics. VAS = Vasculature (both blood and lymphatic).

3.3.1.5 Part IV – MDSC Inhibitory Effect on the TME

MDSC are notable in inhibiting CTL and NK [166, 201] and thus promoting

tumor escape. Heightened interest in immunotherapeutics targeting CTL has spurred

interest into mitigating MDSC-mediated inhibition of immune-checkpoint blockade

(ICB) therapies [47-49]. Because of the diverse immune species interactions in the TME,

it has been difficult to tease out MDSC-specific effects. Here, the model is employed to

evaluate the potential effects of MDSC activation on immune species in the TME. For

this purpose, an initial evaluation on the effect of MDSC on immune species populations

for 4 days was performed using the *in silico* tumor grown in Part III. Three representative

pairs of MDSC entrance rates and base activations levels were chosen (respectively

defining low, medium and high inhibitory MDSC effects on the TME, as in **Table 29**).

The average immune volume fraction across all immune species at 4 days within the

tumor was calibrated in all cases to fit within the range of CTL densities observed in

colorectal cancer in [240]. A T-cell diameter of 6 μm was assumed based on the naïve T-

cell diameter reported in [241]. For this study, it is acknowledged that immune species

distributions can vary significantly across differing tumor types and immune species [57,

242, 243]. **Figure 18** graphs the activation level, volume fraction, and influence

parameter of each immune species.

Parameter		MDSC Effect on the TME		
		Low	Medium	High
ϕ_{GG}			0.004	
$\lambda_{Base\|\tau}$			0.05	
$\mathcal{F}_{B_{reg}}^{Bp}$	$\mathcal{F}_{B_{reg}}^{Bn}$		0.5	

$\mathcal{F}_{T_R}^{Bp}$	$\mathcal{F}_{T_R}^{Bn}$	0.5		
$\mathcal{F}_{T_{H2}}^{Bp}$	$\mathcal{F}_{T_{H2}}^{Bn}$	0.5		
$\mathcal{F}_{\psi}^{Bp}$	$\mathcal{F}_{\psi}^{Bn}$	3.0		
$\lambda_{Base|MDSC}$		0.10	0.45	0.90
$\mathcal{F}_{MDSC}^{Bp}$		0.25	0.80	0.90
$\mathcal{F}_{MDSC}^{Bn}$		0.25	0.80	0.90

Table 29 Parameter settings for Part IV. Any parameters not listed were set to values from Part III. Here $\tau \in G \;\&\; \tau \neq MDSC$ and $\psi \in G \;\&\; \psi \notin \{MDSC, B_{reg}, T_R, T_{H2}\}$. All parameters are assigned non-dimensional values.

MDSC Effect on TME

Low	Medium	High
$\lambda_{Base\|MDSC} = 0.10$	$\lambda_{Base\|MDSC} = 0.45$	$\lambda_{Base\|MDSC} = 0.9$
$\mathcal{F}^{Bp}_{MDSC} = \mathcal{F}^{Bn}_{MDSC} = 0.25$	$\mathcal{F}^{Bp}_{MDSC} = \mathcal{F}^{Bn}_{MDSC} = 0.8$	$\mathcal{F}^{Bp}_{MDSC} = \mathcal{F}^{Bn}_{MDSC} = 0.9$

Immune Species: M1, NK, DC, BeR, Breg, Treg, Th2, M2, NE, MDSC, BeA, CTL, Th1
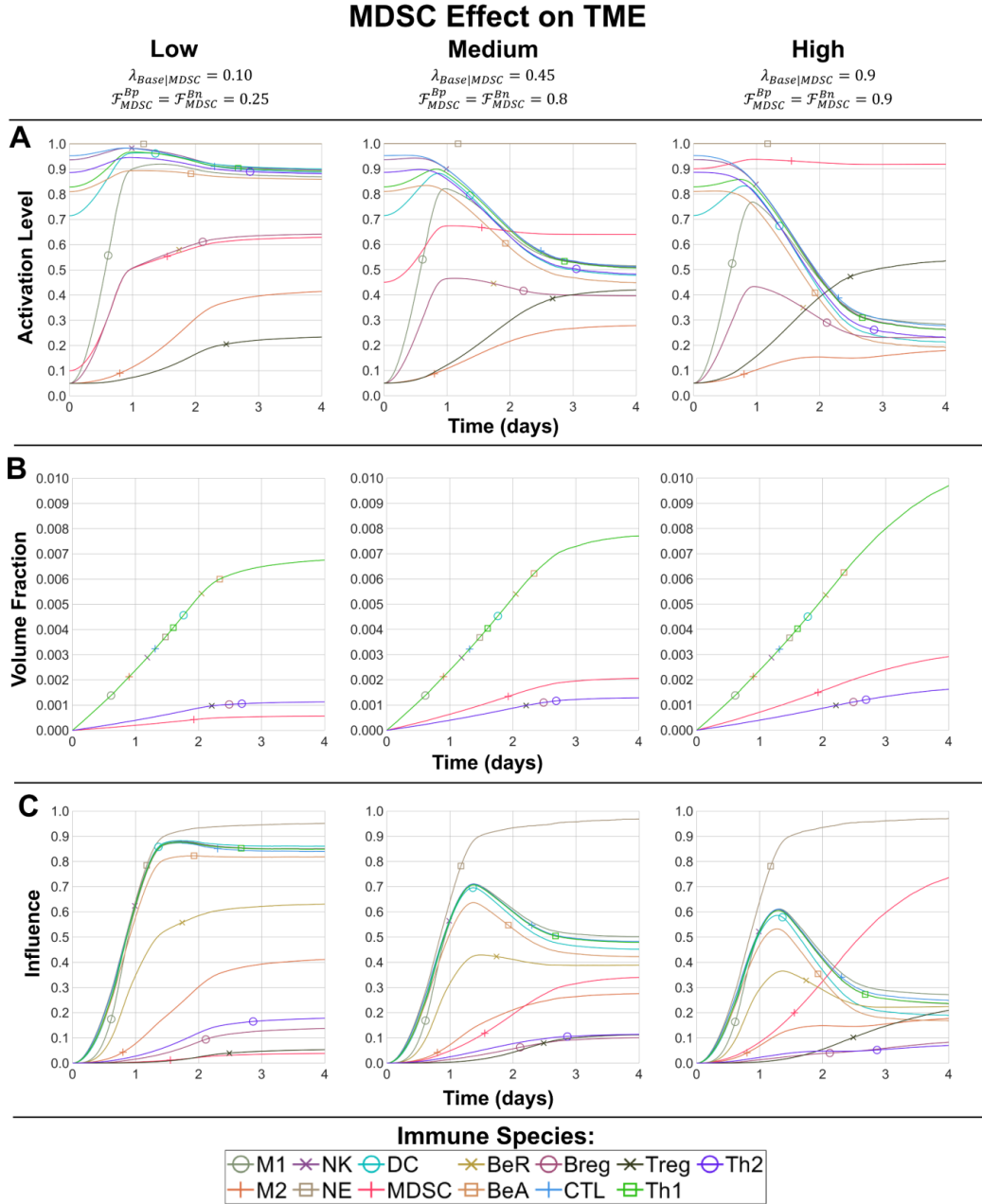
Figure 18 Measurements of intra-tumoral MDSC effects on immune species based on low, medium or high MDSC effect on the TME (as defined in Table 19). (**A**) Immune species activation levels, (**B**) average immune volume fractions, and (**C**) influence ($\mathcal{A}_{I|i} \cdot Q_3(\tilde{\phi}_i / \tilde{\phi}_{GG})$) for each immune species $i \in G$ on the TME.

The average MDSC intra-tumor activation level (**Figure 18A**) increased from 0.63 to 0.92 by 4 days across low to high cases of MDSC effect on the TME. Correspondingly, the average intra-tumor volume fraction for MDSC (**Figure 18B**) increased 5.2x from 5.7E-4 to 2.9E-3, remaining below the saturation volume fraction ($\tilde{\phi}_{GG} = 0.004$) for all cases. Consequently, average intra-tumor influence on the TME for most of the individual immune species was significantly affected as the MDSC effect increased (**Figure 18C**).

The consequences of increasing MDSC influence from low to high were particularly evident for multiple anti-tumor species. Low MDSC effect on the TME prevented MDSC activation from deterring CTL and NK activation. In this case, intra-tumor CTL and NK influence remained strong at 0.84 and 0.85, respectively, by 4 days. However, with medium MDSC effect, continued MDSC extravasation caused the intra-tumor activation levels of CTL and NK to fall monotonically from 0.5 days onward from 0.95 and 0.94 to 0.51 and 0.51, respectively. As CTL and NK continued to infiltrate the TME, influence correspondingly climbed to 0.71 for both CTL and NK by 1.4 days. At this point, increase in CTL and NK volume fractions was insufficient to buffer decline in CTL and NK activation levels. As MDSC continued to accumulate, average influence of CTL and NK fell to 0.48 for both species by 4 days. These trends were exacerbated in the case of high MDSC effect, where peak influence fell from 0.61 for CTL and NK at 1.3 days to 0.25 and 0.24, respectively, by 4 days. The general trend exhibited in NK and CTL occurred across all anti-tumor immune species. Thus, the anti-tumor immune response was effectively thwarted by accumulating MDSC.

The collective anti-tumor influence in the MDSC low case was sufficient to limit

tumor radius growth to 20% of initial value up to 0.8 days. However, rising MDSC

influence combined with declining anti-tumor influence caused tumor radius growth to

transition from being constant in time to growing at a linear rate at 2.2 and 1.7 simulated

days for medium and high cases, respectively. Thus, tumor radius in medium and high

cases reached 46% and 58% of initial value, respectively, by 4 simulated days. The ratio

of intra-tumoral vasculature to tumor volume increased for medium and high MDSC

effects to 26% and 28% above the low case, respectively. Anti-tumor immune species

presence in medium and high cases was increased by 14% and 44% over the low case,

respectively. Interestingly, as MDSC effect increased, myofibroblasts were less displaced

by the tumor mass and produced less ECM in the immediate vicinity of the tumor. Intra-

tumor pressure, therefore, decreased, displacing less vasculature and, by extension,

permitting increased local immune species extravasation. This is consistent with

observations that MDSC can directly promote TME remodeling during tumor growth

[244].

3.4 Discussion

This study presents a novel 3D continuum mixture model implementation of

tumor-immune system interactions implemented via a distributed computing solution.

The results illustrate immune-immune species interactions using localized activation

levels of immune species and independent chemotactic response. Variation in simulated

immune response affects simulated tissue composition, influencing tumor

vascularization, ECM secretion, and tumor growth and cytokine release rates. In

aggregate, the model displays a promising range of calibration capable of simulating tumor-immune interactions conducive to tumor supportive or tumor suppressive environments.

Prospectively, this model offers a first step toward a framework for *in silico* evaluation of cancer immunotherapeutic strategies. Because it can be difficult to account for the effects of particular immune species simultaneously *in vivo*, such a framework could serve as a tool to evaluate the consequences of perturbing the balance between immune species as a result of therapeutic intervention. To reach clinical applicability, model equations are required to simulate differing delivery approaches, such as macrophage-mediated delivery of chemotherapeutics [57, 59, 60] or blood-borne therapeutics that improve immune response in the TME [245]. By simulating multiple immune species simultaneously, therapeutics could be evaluated within heterogeneous immune conditions that may inhibit or promote efficacy. Multiple CPU threads operating concurrently with multiple GPUs could potentially be leveraged to run the model computations in a clinically relevant period of time.

While this model documents numerous immune interactions, it is far from comprehensive. Unlike [71], which uses ODEs to simulate lymph node, blood, and peripheral compartments, events and locations outside the TME are excluded in this study, such as lymphopoiesis and presentation of antigens to naïve T-cells by dendritic cells [168]. Some TME interactions are also not included, such as memory T-cell function [246]. Future work could incorporate additional immune species types (e.g. plasma cells,

Th17), MDSC promotion of angiogenesis, and the complement system [243, 247-249]. Neutrophil types, including anti-tumor and pro-tumor tumor-associated neutrophils, are ignored [250]. The model also simplifies the continuum of tumor-associated macrophages polarization into a M1-M2 dichotomy [251]. Some known drivers of macrophage polarization, such as M2 polarization induced by tumor cell apoptosis, are neglected [252]. The model further ignores species-specific responses to hypoxia-inducible factor signaling [253].

Constant parameters implicitly assume consistent sensitivity to underlying chemokines and pathways, ignoring homeostatic variations. Additionally, the model as presented uses deterministic chemotaxis on continuum fields to represent movement of discrete objects. In comparison, the tumor-immune hybrid model in [65] used semi-stochastic chemotaxis for discrete tumor-associated macrophages, simulating observed migratory behavior [254]. The effect of this mitotic activity, assumed negligible in this study to evaluate immune interactions in a controlled manner, will be considered in future work. This work could also introduce semi-stochasticity into the continuum model framework to permit emergent domain heterogeneity, e.g., for the movement of individual immune cell species [65]. It is further noted that values for some of the parameters, such as blood neo-vascularization rate, do not necessarily correspond to experimental observations, as they were calibrated to achieve biologically-relevant tumor growth rates.

Calibration of model parameters for particular tumors, e.g., using immunohistochemical staining [60, 255-258] requires further exploration. Calibrating vasculature, ECM growth rate, and oxygen uptake in tandem could more realistically simulate formation of tumor proliferative layers [142]. Experimental assays could provide relative densities of different immune species populations, which could be reflected in the model volume fractions. This, in turn, could inform immune entrance and exit rates. In particular, immune species prevalence and distribution could be ascertained by flow cytometry to calibrate immune volume fractions more precisely than presented in Part IV. For example, flow cytometry was used in [259] to confirm T-cell penetration into breast cancer spheroids and in [260] to quantify the prevalence of B-cells, T-cells, NK cells, and monocytes in melanoma, breast cancer, and brain cancer. This model could also be calibrated using histology and imaging as has been done with prior continuum models [142, 261-265]. Future work could leverage these methods to calibrate model parameters to accurately represent *in vivo* immune responses *in silico*. Further, a comprehensive sensitivity analysis is reserved for future investigation.

Imaging could potentially be used for informing model initial conditions. For example, the vascular mathematical model from [266] simulated drug delivery using angiogram data to explore the effects of the blood-brain barrier on glioblastoma drug delivery. Diffusion tensor imaging was used by [267] to initialize a macroscopic tumor model to simulate 2D anisotropic glioblastoma growth along neural fiber tracts. Metabolomic analysis could provide molecular-level insight that could inform model parameter values. In [268] metabolites were ascribed to each of the well-known

hallmarks of cancer [269], inviting the possibility of using metabolomic data to calibrate tumor phenomena. Recently, a continuum tumor model was calibrated in [270] using metabolomic data to simulate lung cancer chemotherapeutic outcomes. Immune cells can also be characterized by differing metabolomic profiles [271]. Effector T-cell activity has been linked to changing from a catabolic metabolism to an anabolic metabolism [272]. In [273] potential T-cell metabolic pathway targets were presented for therapeutic intervention to boost T-cell based immunotherapeutic efficacy. Macrophage polarization has also been studied metabolically: relative to M2, M1 have a higher glycolytic metabolism, raised iNOS-mediated nitric oxide (NO) production, and, due to higher NO concentration, reduced oxidative phosphorylation [274]. Future work could build upon these insights to inform model parameter calibration and thus move towards personalized patient tumor evaluation.

CHAPTER 4: MULTIPLE BREAST CANCER LIVER METASTASES RESPONSE TO

MACROPHAGE-DELIVERED NANOTHERAPY EVALUATED VIA A 3D

CONTINUUM MODEL[3]

4.1 Introduction

It is projected that in 2022, half of all breast cancer patients will develop liver

metastases over the duration of the disease [275-278]. Breast cancer liver metastases

(BCLM) are characterized by poor prognosis, with median survival less than 18 months

and a 16% 5-year survival rate when diagnosed with primary in the breast [279, 280]. As

such, BCLM represent a significant therapeutic challenge. Recent clinical

recommendation discourages hepatectomy for the majority of patients [12], while the

most frequently used systemic chemotherapy regimens are ineffective and considered to

be palliative care [12, 13]. BCLM mainly rely on the liver vasculature for access to

oxygen and nutrients, and usually appear as hypo-attenuating lesions when imaged with

contrast agents [17]. The low vascularization of BCLM, consisting of small nodules

mainly receiving oxygen and nutrients from the surrounding hepatic capillaries, presents

a challenge to efficiently target tumor cells with intravenously administered

chemotherapy, thereby presenting physiological resistance to the treatment [281].

Previous *in vitro* and *in vivo* studies have found that nanocarriers with intrinsic affinity to macrophages can significantly enhance drug therapeutic efficacy in BCLM. Tumor-associated macrophages (TAM) are known to surround BCLM [10-13], thus offering an attractive target to transport therapeutics into BCLM, including drug-loaded nanovectors [14, 15]. In particular, encapsulation of nanoalbumin-bound paclitaxel (nab-PTX) in a porous silicon multistage nanovector (MSV) taken up by macrophages surrounding BCLM lesions has been proposed to overcome transport barriers and physiological resistance in BCLM, thereby increasing cytotoxicity [57]. An *in silico* 2D model enabled systematic evaluation of response of single metastatic lesions to these MSV-nab-PTX targeting macrophages [57, 59]. The model included the interactions of pro-tumorigenic (M1) and anti-tumorigenic (M2) macrophage subtypes in the tumor microenvironment (TME) to predict the overall response [59, 60].

BCLM patients usually present with multiple metastases, with 30% of 54 patients observed to have three or more liver metastases [282], and a group of over 500 systemically treated BCLM patients having on average of two or more metastases per subject [7]. Simulating response for multiple lesions has remained an unmet need for thorough evaluation of clinically relevant therapies. To address this need, a 3D model of multiple BCLM is developed in this study. The model simulates therapeutic response based on the interaction of the delivery vehicle, MSV-nab-PTX, with macrophages in the TME, building upon a 3D continuum mixture model developed in [82] and solved numerically in [83]. To enable computational feasibility of representing multiple metastases interacting with macrophages, we leverage a novel MPI-CUDA framework

[181], in contrast to the CPU-bound framework of the 3D mixture model in [82, 83] that simulated desmoplastic tumors. Tumor burden is evaluated as a function of treatment regimen and metastases number by simulating multiple BCLM of varying sizes in a liver lobe, calibrated to an experimental mouse model of BCLM.

4.2 Materials and Methods

4.2.1 Cell Culture

4T1 cells (ATCC) were cultured in RPMI1640 medium supplemented with 10% fetal bovine serum in humidified (37 °C, 5% CO_2) incubators. Cells were trypsinized and resuspended with RPMI 1640 medium. Cells were pelleted at a concentration of 100,000 cells/0.1mL in PBS (phosphate buffered saline).

4.2.2 Animals

Female BALB/C mice (6-8-week-old) were purchased from the Jackson Laboratory. All experimental protocols were approved by the Institutional Animal Care and Use Committee of Houston Methodist Research Institute (HMRI) and conform to the National Institutes of Health (NIH) guidelines of the care and use of laboratory animals.

4.2.3 Experimental Model of BCLM

To establish the experimental model of BCLM, splenic injection of breast cancer 4T1 cells was performed in BALB/C mice. Briefly, mice were injected with 4T1 cells (100,000 cells/0.1ml PBS) into the spleen to enable hematologic dissemination through the portal vein as described previously and spleen (the primary tumor site) was removed afterwards. Animals injected with PBS served as control. All injections were performed on the same day. Allocation of experimental groups (each n=3) was based on a simple

135

randomization. Animals were sacrificed at D7-10 and liver tissues were harvested and fixed in 10% neutral buffered formalin for paraffin processing or in OCT (optimal cutting temperature) for cryo-sectioning.

To visualize BCLM, tissue slides were stained with Hematoxylin & Eosin (H&E) using standard histological protocols. OCT block tissue was initially fixed with 4% paraformaldehyde in PBS for 15 min before being frozen in OCT for cryosectioning. For immunofluorescence staining of macrophages, sections were incubated with anti-mouse F4/80 monoclonal antibody (41-4801-82, Invitrogen, Waltham, MA) at 4˚C overnight followed by incubation with goat anti-mouse AF568 secondary antibody (A-21124, Invitrogen, Waltham, MA) for 1h at room temperature and counterstained with 4′,6-Diamidine-2′-phenylindole dihydrochloride (DAPI). For modeling of the therapy experiments with albumin bound paclitaxel (nab-PTX) and MSV, with the affinity to accumulate into macrophages, encapsulated nab-PTX (MSV-nab-PTX) was used from [58] and [57].

4.2.4 Clinical BCLM

De-identified human BCLM paraffin embedded tissue slides were purchased from a commercial biorepository (BiocoreUSA) and stained with H&E using standard protocols.

4.2.5 Mathematical Model

The 3D continuum mixture model that serves as a basis for the BCLM model simulates viable tumor tissue, represented as ϕ_V, as a volume fraction that interacts with ϕ_H and ϕ_E, respectively representing host tissue and extracellular matrix (ECM) volume

fractions. Tumor growth is promoted with sufficient oxygen and glucose levels delivered through the blood vasculature and is hindered distal to the vasculature by hypoxia. Tumor tissue death contributes to the dead volume fraction (ϕ_D). Tumor aerobic and anaerobic respiration affects local concentrations of bicarbonate, lactic acid, and H^+. Viable tumor tissue, ECM, and host tissue volume fractions vie for limited space, an interaction characterized by both pressure and chemical potentials. Pressure from continuing tumor proliferation creates velocities that drive motion of tumor tissue and ECM. Neo-vasculature formed in response to a net balance of pro-angiogenic factors released by the tumor tissue promotes tumor proliferation. Myofibroblasts are simulated to excrete ECM. Immune species (ϕ_G) extravasate into the TME, follow chemotactic gradients, and interact with the tumor tissue and the vasculature. In particular, monocytes (ϕ_{M_0}) extravasate from blood vasculature and differentiate into M1 (ϕ_{M1}) or M2 (ϕ_{M2}), for simplicity assuming a binary state. M1 are anti-tumorigenic and cytotoxic to tumor cells, converting ϕ_V into ϕ_D, while M2 promote tumor proliferation by releasing tumor growth and angiogenic factors. Further details on the model are in **4.5 Supplementary Material**.

4.3 Results

4.3.1 Simulation of Single BCLM

The 3D model parameters were first calibrated to the experimental data previously obtained to calibrate the 2D model of single BCLM [57, 59]. A single lesion was then simulated with the 3D model, starting with a ~66 μm diameter seed and growing to a 400 μm diameter after ~6.8 days. The tumor diameter was obtained by assuming an essentially spherical mass and defining tumor tissue as $\phi_V \geq 0.05$. The tumor was grown in a cubic domain containing 32^3 points with a 33.3 μm point spacing,

creating a 1.1x1.1x1.1 mm^3 domain. Half-life of the simulated drug was calibrated to

match the 20-hour half-life of nab-PTX [283]. Hypoxic threshold, and oxygen production

and uptake parameters were tuned to yield the typical 100 μm-deep proliferative layer of

tumor tissue in the vicinity of blood vasculature, as observed experimentally [142].

Macrophage chemotaxis was calibrated to achieve penetration of BCLM as observed *in*

vitro in [59]. Parameters for the proliferative layer tuning and macrophage chemotaxis are

summarized in **4.5 Supplementary Material**. It is assumed that drug in the interstitium

does not reenter the vasculature at significant concentrations and that drug uptake by host

tissue is negligible (i.e., $\lambda_{D_p,uptake,H} = 0$). Ratios of 1.0:1.8 and 1.2:1.0 M1:M2 were

established as initial conditions for untreated and MSV-nab-PTX-treated treatment cases,

respectively, to match the *in vivo* results reported in [59]. The boundary conditions are

listed in **4.5 Supplementary Material**.

After an initial 6.8-day growth phase the simulated tumor was subjected to

different MSV-nab-PTX treatment regimens. Macrophages were present but did not

actively interact with the TME until the growth phase had elapsed, after which

macrophage functionality was either enabled (represented as M1+ or M2+) or disabled

(M1- or M2-). Total and localized drug concentrations for MSV-nab-PTX and nab-PTX

for the (M1- M2-) case are compared in **Figure 19**, highlighting the therapeutic effect of

the drug transport and delivery by macrophages into the tumor tissue.
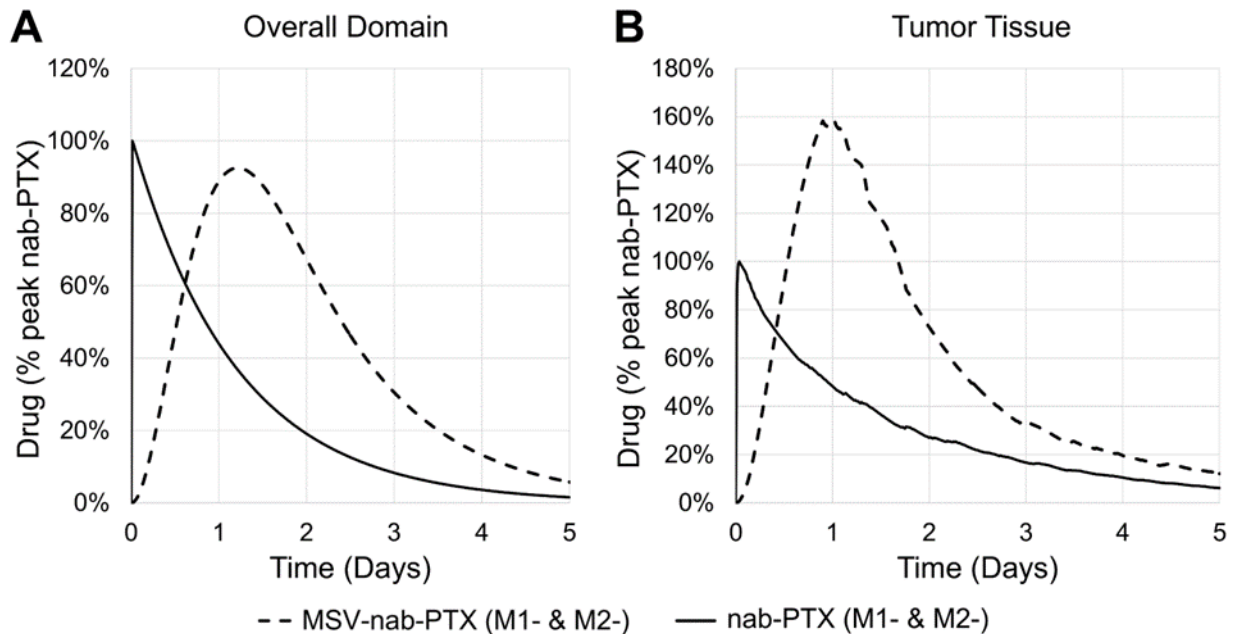
Figure 19 Simulated drug delivery to a single BCLM with the 3D model. Delivery was compared between free nab-PTX and release from macrophages following MSV-nab-PTX administration. (**A**) Concentrations in total domain (tumor and surroundings). (**B**) Concentrations within tumor (tissue is defined by $\phi_V \geq 0.05$). For easier comparison, the concentrations are normalized to the peak concentration of nab-PTX. While less at peak compared to free nab-PTX, release of drug from macrophages encapsulating MSV-nab-PTX maintained a concentration >50% for >1.5 days longer. Slight perturbations in curves in (**B**) reflect tumor size changes during the drug exposure.

In **Figure 19A**, the drug released from M1 and M2 macrophages following simulated intravenously administered MSV-nab-PTX administration peaked at 92.5% compared to that of free nab-PTX. While the nab-PTX peaked immediately after intravenous injection, the drug released from macrophages-encapsulated MSV-nab-PTX peaked at 1.2 days. In this case, the drug reached half concentration in 2.5 days after

initial administration, which occurred 1.7 days after the drug's half-life had been reached via nab-PTX injection. The delay induced by the macrophages acting as the drug source increases the drug exposure by extending the overall therapeutic window. The results are consistent with drug release profiles previously obtained by the 2D model in [57], where macrophage-encapsulated MSV-nab-PTX significantly prolonged the drug release compared to bolus nab-PTX. Within the tumor, drug release associated with macrophages yielded 58% higher concentration relative to free nab-PTX (**Figure 19B**). As shown in [57], uptake of MSV-nab-PTX by macrophages maintains a higher localized intra-tumoral concentration of drug for a longer duration than free drug.

Next, different combinations of activated macrophages were simulated *in silico* in combination with treatment. As reported in [59], simulations without treatment ("control") were calibrated to a 1.0:1.8 M1:M2 ratio to match untreated BCLM macrophage distribution and to a 1.2:1.0 M1:M2 ratio when treated with MSV-nab-PTX. As expected, untreated cases grew unbounded (**Figure 20**). By 40 hours, the (M1- M2-) baseline case reached 122% initial radius, while M1 by itself (M1+) attenuated, but did not eliminate, tumor growth, leading to 115% initial radius within this timeframe. Tumor radius is defined as the radius of a spherical tumor whose volume is the sum of ϕ_V across the domain. Release of growth factors F_{M2} by M2 in the M2-only (M2+) case increased tumor radius to 146% by 40 hours. The effect of F_{M2} outweighed the cytotoxic effect of M1 in the M1+ M2+ case, with the tumor reaching 137% initial radius during this time.
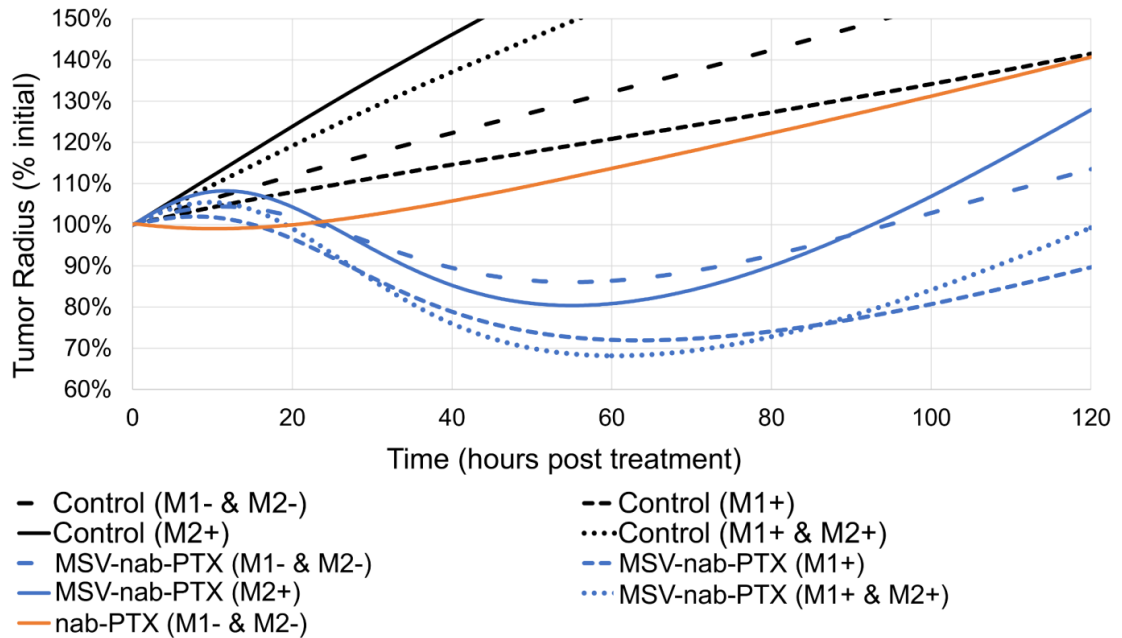
Figure 20 Simulations of treatment for a single BCLM lesion with the 3D model.

Tumor radius is shown as percent of initial size at start of treatment (t=0), as a

function of macrophage (functionality (M1 and M2, either anti-tumorigenic or pro-

tumorigenic, respectively). "Control" cases are untreated, highlighting the macrophage

effects. Treatment with free nab-PTX (red line) was insufficiently localized at the tumor

to achieve a significant response compared to drug delivery by macrophages

encapsulating MSV-nab-PTX.

All cases with MSV-nab-PTX treatment showed a decrease in tumor radius

(**Figure 20**). MSV-nab-PTX without effects from macrophages (M1- & M2-) decreased

tumor radius by 14% after 55 hours. Activation of M1 (M1+) decreased tumor radius by

an additional 14% after 62 hours. By favoring tumor proliferation and growth, thereby

increasing its susceptibility to cell-cycling drugs such as PTX, M2 activation (M2+)

lowered tumor radius to 20% of initial by 53 hours. The combination of M1 and M2

effects (M1+ & M2+) in tandem with MSV-nab-PTX achieved the smallest tumor radius (68% of initial after 60 hours). These results are consistent with the previous 2D model results [59], as confirmed *in vivo* [60]. **Figure 20** further shows that there is minimal effect from free nab-PTX.

4.3.2 Simulation of Multiple BCLM

To explore tumor burden with the clinically-relevant scenario of multiple BCLM, we evaluated BCLM in mouse liver lobes (**Figure 21A-C**). It can be seen that macrophages distribute evenly in the unaffected mouse livers (**Figure 21E**), while concentrating in the periphery of the tumor lesions (**Figure 21D**). The mouse model is consistent with human BCLM, as shown by the multiple lesions clearly visible in patient liver core biopsies (**Figure 21F**). The mouse experimental samples were used to measure diameters for simulations of multiple BCLM, as described in **4.5 Supplementary Material**. To establish a range of possible tumor densities for the simulations, tumor sizes observed experimentally were quantified across three mouse liver lobe slides and aggregated to represent the distribution of sizes found therein. It was assumed that the liver is isotropic; hence, the frequencies of tumor diameters and mean tumor density measured from liver lobe slices were considered representative of the entire mouse liver lobe.
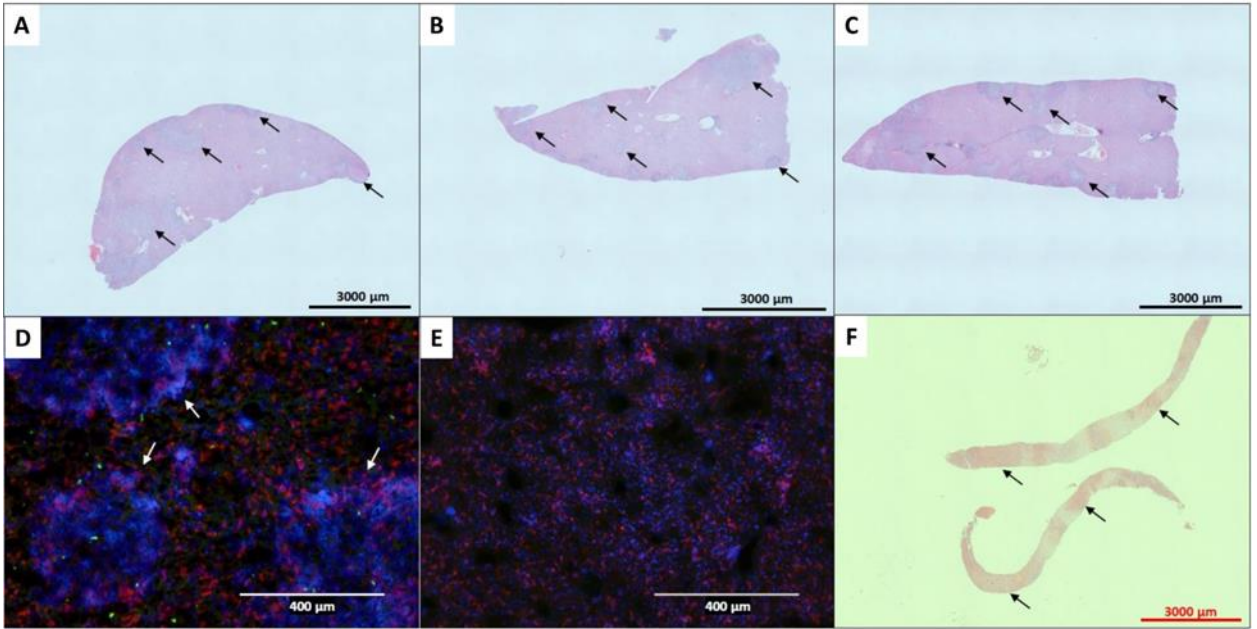
Figure 21 BCLM observations in vivo. (A-C) H&E stained mouse liver lobes with multiple BCLM lesions (black arrows) used for *in silico* model calibration. (D) Fluorescently stained mouse liver lobes with BCLM (white arrows) at D10 and (E) control/healthy liver; blue – DAPI (cellular nuclei); red – F4/80 (macrophage). (F) Representative human BCLM metastasis biopsy cores stained with H&E, showing multiple lesions (black arrows).

In the 3D model, the multiple BCLM were simulated to grow within a $3.8 \times 3.8 \times 3.8$ mm³ region of mouse liver lobe tissue centered within a $4.3 \times 4.3 \times 4.3$ mm³ domain. Tumors were first grown from "seeds" of varying sizes (**Figure 25**) for 6.8 simulated days, with the results in **Figure 22**. MSV-nab-PTX treatment was then simulated immediately following the growth phase. **Figure 23** shows the treatment response after 24 and 48 hours, showing a noticeable effect on all metastases by 24 hours, and eliminating regions with lower tumor tissue density. However, by 48 hours, deeper

and denser portions of the metastases had survived the single therapeutic administration (**Figure 23B**).
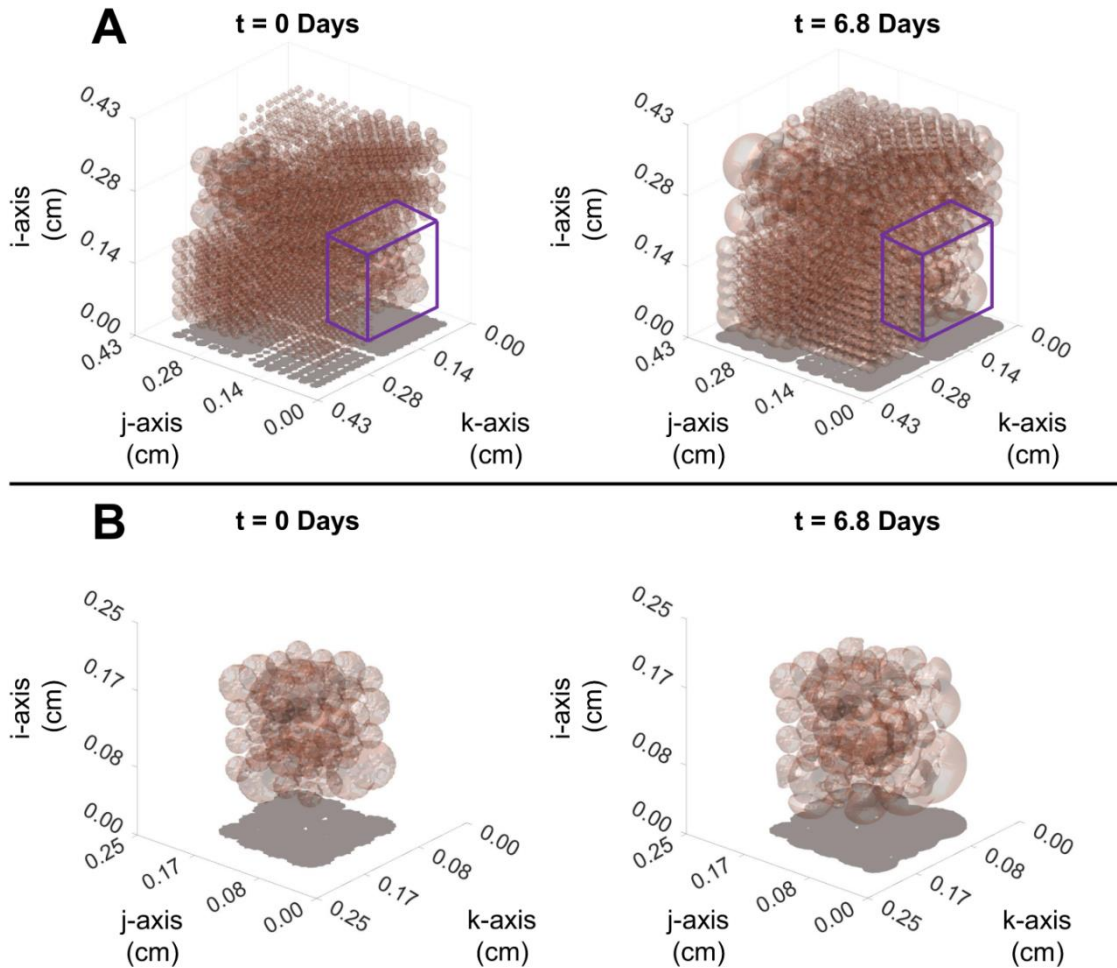
Figure 22 Simulation of multiple BCLM growth with the 3D model. (A) In silico mouse liver lobe with multiple metastases and (B) octant containing 64 metastases of assorted diameters at initial seeding and after6.8 days of growth. Cubed region highlighted in A is magnified in B. Tumor tissue is defined as $\phi_V \geq 0.05$.
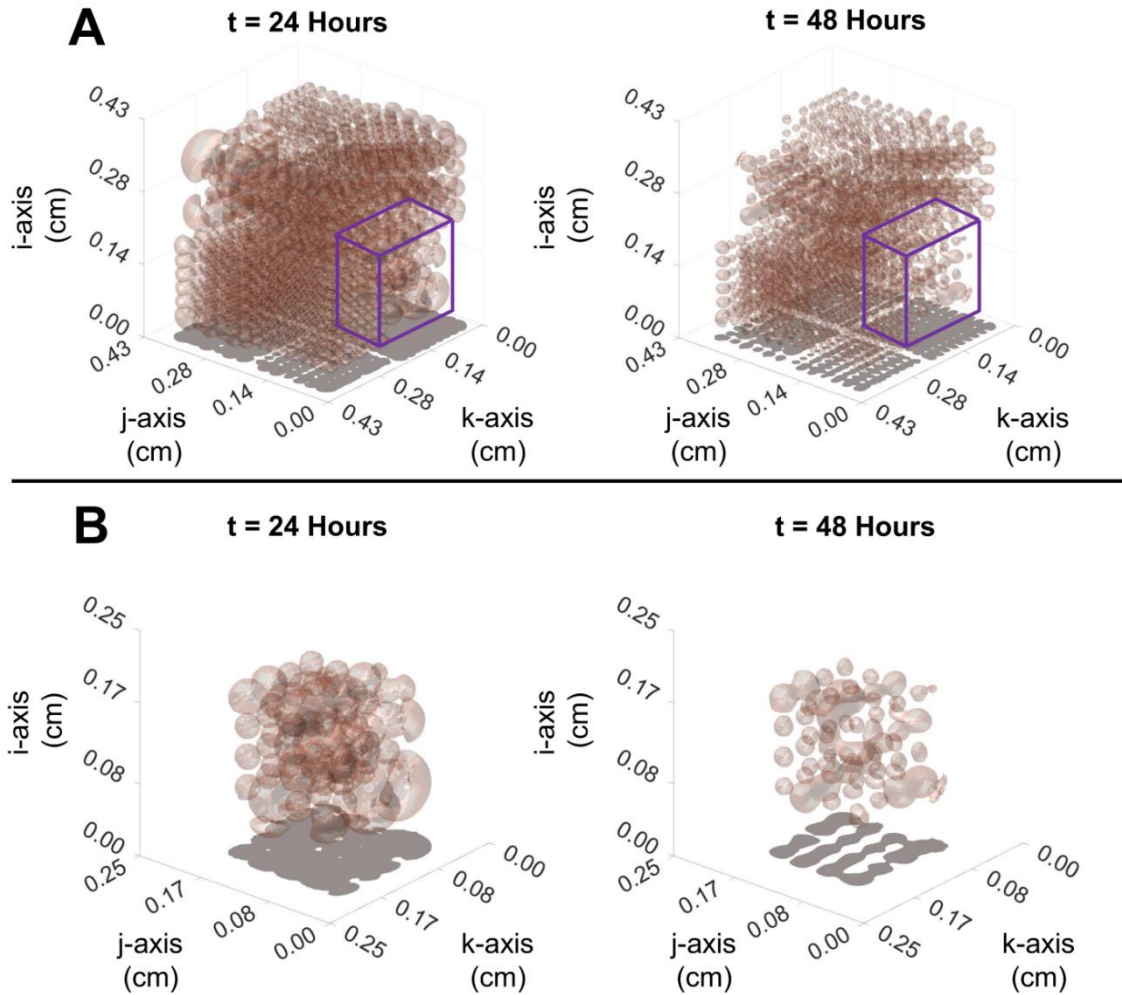
Figure 23 Treatment response of multiple BCLM to macrophage-delivered MSV-nab-PTX simulated by the 3D model. (A) *In silico* mouse liver lobe with multiple metastases and (B) octant containing 64 metastases of assorted diameters 24 hours and 48 hours after simulated administration of MSV-nab-PTX. Cubed region highlighted in A is magnified in B, showing viable tumor tissue surviving the single treatment. Tumor tissue is defined as $\phi_V \geq 0.05$.

4.3.3 Simulation of Repeated Treatment for Multiple BCLM

To evaluate whether repeated MSV-nab-PTX administration could eradicate multiple BCLM, treatments were simulated in 1- through 7-day intervals. Peak %tumor burden after each treatment is shown in **Figure 24**. Tumor burden was defined as the mass of all tumor tissue where $\phi_V \geq 0.05$. Treatment at 1-, 2-, 3-, and 4-day intervals effectively eradicated the tumor burden by 14 days after start of therapy. In contrast, 5-day intervals decreased tumor burden to <20% of initial burden by 11 days. This is consistent with the response of multiple BCLM previously observed in mice with MSV-nab-PTX administered in 5-day intervals [58]. A 6-day interval was less effective at controlling tumor growth, peaking at 79% of initial burden by 12 days, and falling to 11% of initial burden by 14 days. In comparison, a 7-day interval proved ineffective, with tumor burden fully recovering within the treatment interval. This indicates that with the given parameter set based on the multiple BCLM mouse model, MSV-nab-PTX treatment intervals exceeding 6 days would be ineffective in controlling the overall BCLM burden.
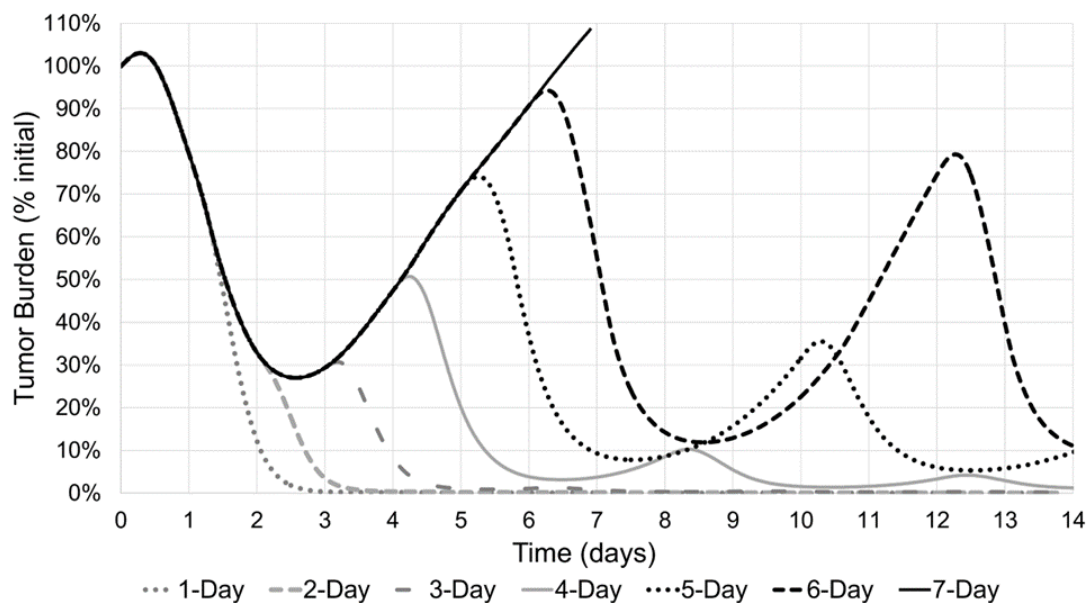
Figure 24 Response of multiple BCLM to repeated treatments with macrophage-delivered MSV-nab-PTX simulated by the 3D model. Effect on tumor burden is shown with differing schedules of MSV-nab-PTX therapy based on 1st treatment at Day 0 followed by additional treatments every 1, 2, 3, 4, 5, 6, or 7 days. Increasing the time duration between treatments reduces overall BCLM response, with 1-day, 2-day, 3-day, 4-day, intervals effectively eradicating tumor growth, a 5-day interval eliciting strong tumor response, a 6-day interval curtailing growth, and a 7-day interval failing to control growth. All treatments were simulated with the same initial condition.

4.4 Discussion

The liver is a common destination for metastatic spread of tumors from various origins. Liver cancers represent the second leading cause of global cancer-related mortality [284] with more than 700,000 annual deaths. Secondary liver cancers are much more frequent than primary, and breast cancer represents one of the most frequent malignancies that metastasize to the liver, especially for young women [279]. The main

reasons for the high mortality are the presence of multiple liver lesions that are unresectable and the lack of therapeutic efficacy of agents commonly used for targeting primary tumors [239]. In previous work [58], we have found that hypo-vascularization of BCLM [26] plays a major role in the inefficiency of systemically administered therapeutic agents. We also proposed a strategy to overcome this obstacle by targeting macrophages surrounding BCLM with mesoporous silicon nanovector associated nanoalbumin paclitaxel (MSV-nab-PTX) to retain drug in the TME [58], and evaluated the therapeutic responses *in silico* considering a single lesion in the liver [57, 59, 60].

To more realistically evaluate multiple BCLM progression and therapeutic response, this study evaluates macrophage-delivered MSV-nab-PTX with a 3D continuum mixture model solved via distributed computing to enable simulation of multiple BCLM. Single metastasis results were consistent with our previous *in silico* [59] and *in vivo* [60] findings. The 3D computational model was calibrated to multiple BCLM sizes and distribution experimentally observed in mouse liver lobes *in vivo* and consistent with human BCLM metastasis biopsy cores. The results provide an upper bound for intervals between repeated treatments to eradicate overall tumor burden. The results demonstrate successful *in silico* replication of multiple BCLM found *in vivo* and illustrate the potential of the model as a platform to investigate the effectiveness of therapeutics and dosing regimens targeting macrophage-associated BCLM.

The tumor simulations in this study used a homogenous parameter set that describes a replacement growth pattern, which is hallmarked by low neovascularization,

absence of a desmoplastic rim surrounding the tumor, and resistance to angiogenic drug delivery [285, 286]. This is consistent with clinical BCLM histology: 43 out of 45 (96%) BCLM samples in [26] and 16 out of 17 (94%) BCLM in [285] were shown to have a replacement growth pattern, including in samples collected from autopsies, highlighting the importance of evaluating targeted therapeutic approaches in BCLM in order to maximize positive outcomes. Further, the simulated solid phase pressures perturb the growth of the multiple metastases, causing particular BCLM to diverge from a spherical shape and potentially affecting their treatment response. These deviations in the local tumor microenvironment reflect potential conditions *in vivo*, in which tumors grow by displacing normal tissue due to locally raised anisotropic solid stresses [287, 288].

The model presented here has several limitations, including a simplified representation of tumor biology and associated cellular-stroma interactions. In particular, the model calibration was performed using data from BCLM in mice; although a mouse model of BCLM is considered to adequately represent the human disease [58], it presents characteristics that may not translate to the human condition. Further, measuring sizes and distinguishing individual tumors in a multi-metastases continuum simulation remains an ongoing challenge due to interactions of different tumors in the domain and the parallelization employed to compute simulation results. Moreover, the area calculations assumed each mouse lobe metastasis was circular and that metastatic distribution was isotropic. Because tumor shapes are amorphous [288], a deeper analysis of metastasis density across a broader BCLM cohort is required.

Because macrophages migrate along chemokine concentration gradients, future work could explore the effects on therapeutic efficacy of gradient variation due to ECM and other TME conditions [224]. Additional factors that affect therapeutic resistance (e.g., the immune environment) could also be introduced into the model. Transitioning the model to calibrate with clinical data will require parameter tuning and reevaluation of BCLM sizes and distributions relevant to human patients. For example, the model could be calibrated to clinical BCLM based on the number and size of lesions obtained with standard imaging analysis techniques. Future work will also require calibrating the model drug effect to clinical results.

In summary, the multiple metastasis 3D model presented in this study provides a proof-of-concept for the evaluation of therapy for multiple BCLM. The study focuses on the physiological resistance of chemotherapeutics in BCLM, based on the transport impairment in liver tumor lesions, and how this resistance can be overcome by targeting macrophages in the tumor microenvironment. This work moves further towards realistic representation of BCLM, with the ultimate goal of personalized evaluation of metastatic cancer. We envision that the proposed approach will longer term enable design of efficient therapy regimens to eradicate BCLM.

4.5 Supplementary Material

4.5.1 Mathematical Model

Equation 4.5.1 through Equation 4.5.20 represent the key equations in non-dimensionalized form of the tumor model, based upon the formulation in [82, 83, 289]:

$$\frac{\partial \phi_V}{\partial t} + \nabla \cdot (\phi_V \boldsymbol{u}_\alpha) = M \nabla \cdot (\phi_V \nabla \mu_T) + S_V$$

<div style="text-align:right">Equation 4.5.1</div>

$$\mu_T = \frac{\partial F_b}{\partial \phi_T} - \epsilon_T^2 \cdot \nabla^2 \phi_T - \epsilon_{TE}^2 \cdot \nabla^2 \phi_E - \epsilon_{TG}^2 \cdot \nabla^2 \phi_G$$

<div style="text-align:right">Equation 4.5.2</div>

$$\mu_E = \frac{\partial F_b}{\partial \phi_E} + \frac{\partial \mathcal{W}}{\partial \phi_E} - \epsilon_E^2 \cdot \nabla^2 \phi_E - \epsilon_{TE}^2 \cdot \nabla^2 \phi_E - \epsilon_{EG}^2 \cdot \nabla^2 \phi_G$$

<div style="text-align:right">Equation 4.5.3</div>

$$\frac{\partial \mathcal{W}}{\partial \phi_E} = \epsilon_e \cdot [6\phi_E(1 - \phi_E)] \cdot \sum_{i,j=1}^{3} \left[\frac{1}{2} \cdot (\mathcal{E}_T)_{ij} \cdot \mathbb{T}_{ij}^* - (\mathcal{E}_T^*)_{ij} \cdot \mathbb{T}_{ij} \right]$$

<div style="text-align:right">Equation 4.5.4</div>

$$\mathbb{T}_{ij}^* = 2 \cdot (1 - L_2^C) \cdot (\mathcal{E}_T)_{ij} + (L_1^E - L_1^C) \cdot \delta_{ij} \cdot \sum_{k=1}^{3} (\mathcal{E}_T)_{kk}$$

<div style="text-align:right">Equation 4.5.5</div>

$$\mathbb{T}_{ij} = 2 \cdot L_2 \cdot (\mathcal{E}_T)_{ij} + L_1 \cdot \delta_{ij} \cdot \sum_{s=1}^{3} (\mathcal{E}_T)_{ss}$$

<div style="text-align:right">Equation 4.5.6</div>

$$(\mathcal{E}_T)_{ij} = \mathcal{E}_{ij} - \mathcal{E}_{ij}^*$$

<div style="text-align:right">Equation 4.5.7</div>

$$\mathcal{E}_{ij}^* = Q_3(\phi_E) \cdot (\mathcal{E}_T^*)_{ij} + (\mathcal{E}_C^*)_{ij}$$

<div style="text-align:right">Equation 4.5.8</div>

$$(\mathcal{E}_T^*)_{ij} = (\mathcal{E}_E^*)_{ij} - (\mathcal{E}_C^*)_{ij}$$

<div style="text-align:right">Equation 4.5.9</div>

$$\mathcal{E}_{ij} = \frac{1}{2} \cdot \left(\frac{\partial u_i^d}{\partial x_j} + \frac{\partial u_j^d}{\partial x_i} \right)$$

<div style="text-align:right">Equation 4.5.10</div>

$$L_i = Q_3(\phi_E) \cdot (L_i^E - L_i^C) + L_i^C, i = 1,2$$

<div style="text-align:right">Equation 4.5.11</div>

$$Q_3(x) = x^2 \cdot (3 - 2x)$$

<div style="text-align:right">Equation 4.5.12</div>

$$\nabla \cdot \left[k_\alpha \cdot \left(\nabla p - \frac{\gamma_T}{\epsilon_T} \mu_T \nabla \phi_T - \frac{\gamma_E}{\epsilon_E} \mu_E \nabla \phi_E - \frac{\gamma_G}{\epsilon_G} \cdot \sum_{i \in G} \tilde{\mu}_i \nabla \tilde{\phi}_i \right] = \right.$$
$$- \left(S_V + S_D + S_E + \sum_{i \in G} S_i \right)$$

<div style="text-align:right">Equation 4.5.13</div>

$$\tilde{\boldsymbol{u}}_\alpha = \tilde{k}_\alpha \cdot \left(\nabla \tilde{p} - \frac{\tilde{\gamma}_T}{\tilde{\epsilon}_T} \cdot \tilde{\mu}_T \nabla \tilde{\phi}_T - \frac{\tilde{\gamma}_E}{\tilde{\epsilon}_E} \cdot \mu_E \nabla \tilde{\phi}_E - \frac{\tilde{\gamma}_G}{\tilde{\epsilon}_G} \cdot \sum_{i \in G} \tilde{\mu}_i \nabla \tilde{\phi}_i \right)$$

<div style="text-align:right">Equation 4.5.14</div>

$$\nabla \cdot (D_n \nabla n) + k_{n1} n_C - (k_{n1} + k_{n2}) \cdot n = 0$$

<div style="text-align:right">Equation 4.5.15</div>

$$\nabla \cdot \left(D_{tgf} \nabla (tgf) \right) + \lambda_{tgf} - \left(\lambda_{tgf} + \lambda_{de,tgf} + \lambda_{U,tgf} \right) \cdot tgf = 0$$

Equation 4.5.16

$$\nabla \cdot \left(D_{taf} \nabla (taf) \right) + \lambda_{taf} - \left(\lambda_{taf} + \lambda_{de,taf} + \lambda_{U,taf} \right) \cdot taf = 0$$

Equation 4.5.17

$$\frac{\partial m}{\partial t} = \nabla \cdot (D_m \nabla m) + S_m$$

Equation 4.5.18

$$\frac{\partial B_n^E}{\partial t} + \nabla \cdot (B_n^E u_E) = -\nabla \cdot \boldsymbol{J}_{BnE} + S_{BnE}$$

Equation 4.5.19

$$\frac{\partial L_n^E}{\partial t} + \nabla \cdot (L_n^E u_E) = -\nabla \cdot \boldsymbol{J}_{LnE} + S_{LnE}$$

Equation 4.5.20

Values of the terms in Equation 4.5.1 through Equation 4.5.20 are given in **Table 30** and **Table 31**.

Dependent Variable	Biological Representation	Scaling Factor
ϕ_V	Viable tumor volume fraction	$\tilde{\phi}_\alpha$ (fixed solid volume fraction)
ϕ_E	ECM volume fraction	$\tilde{\phi}_\alpha$
ϕ_H	Healthy host cells volume fraction	$\tilde{\phi}_\alpha$
u_α	Solid mass velocity	$\dfrac{\mathcal{L}}{\mathcal{T}}$
u_E	ECM Velocity within ECM	$\dfrac{\mathcal{L}}{\mathcal{T}}$
μ_T	Tumor cell potential	E_a^*
μ_E	ECM potential	E_a^*
u^d	Displacement vector	$\mathcal{L}$
p	Solid phase tumor cell pressure	$\mathcal{P}$
n	Concentration of oxygen	$\tilde{n}_\infty$
tgf	Tumor growth factors concentration	tgf_{sat}

taf	Tumor angiogenic factors concentration		taf_{sat}
m	Concentration of matrix degrading enzymes		m_{sat}
B_n^E	New blood vessels		$\tilde{B}_{max}$
L_n^E	New lymphatic vessels		$\tilde{L}_{max}$

Table 30 Dependent variables in Equation 4.5.1 through Equation 4.5.20, following the model in [82].

Parameter	Biological Representation	Parameter Definition	Non-dimensionalization
M_i	Mobility of cell species i		$\mathcal{M}$
S_V	Viable tumor cell source		
S_D	Dead/necrotic tumor cell source		$\tilde{\phi}_\alpha \cdot \mathcal{T}$
S_E	ECM source term		
S_{BnE}	Blood cell source term		$\tilde{B}_{max} \cdot \mathcal{T}$
$\mathcal{W}$	Elastic energy of ECM		$\tilde{\phi}_\alpha \cdot E_a^*$
L_1^E & L_2^E	Lamé constants for ECM components		L_2^E & L_2^E
L_1^C & L_2^C	Lamé constants for cell components	[82]	L_2^E & L_2^E
ϵ_E	Interaction strength of ECM with itself		$\bar{\bar{\epsilon}}$
ϵ_T	Interaction strength of tumor mass with itself		$\bar{\bar{\epsilon}}$
ϵ_e	Strain energy coefficient		$\bar{\bar{\epsilon}}_e$
γ_T	Tumor cell self-adhesion parameter		$\gamma_T = \dfrac{\epsilon_T \cdot \tilde{\phi}_\alpha \cdot \sqrt{\tilde{\phi}_\alpha \cdot E_a^*}}{\mathcal{L} \cdot \mathcal{P}}$
γ_E	ECM self-adhesion parameter		$\gamma_E = \dfrac{\epsilon_E \cdot \tilde{\phi}_\alpha \cdot \sqrt{\tilde{\phi}_\alpha \cdot E_a^*}}{\mathcal{L} \cdot \mathcal{P}}$

ϵ_G	Interaction strength for immune species		$\bar{\bar{\epsilon}}$
γ_G	Cell adhesion for immune species	[289]	$\gamma_G = \dfrac{\epsilon_G \cdot \tilde{\phi}_\alpha \cdot \sqrt{\tilde{\phi}_\alpha \cdot E_a^*}}{\mathcal{L} \cdot \mathcal{P}}$
$\epsilon_{\sigma\tau}$	Interaction strength between species σ and τ	[82, 289]	$\bar{\bar{\epsilon}}$
$\mathcal{E}$	Infinitesimal strain		$\bar{\bar{\bar{\mathcal{E}}}}$
$\mathcal{E}_E^*$	Eigenstrain tensor for ECM		$\bar{\bar{\bar{\mathcal{E}}}}$
$\mathcal{E}_C^*$	Eigenstrain tensor for cells	[83]	$\bar{\bar{\bar{\mathcal{E}}}}$
k_{n1}	Oxygen rate constants		$\lambda_{U,V,n}$
k_{n2}			$\lambda_{U,V,n}$
D_n	Diffusivity of oxygen in tumor		$D_{n,T}$
k_α	Motility of the solid phase		$\bar{\bar{k}}_\alpha$
D_{tgf}	Diffusivity of tumor growth factors		$D_{n,T}$
D_{tgf}	Diffusivity of tumor angiogenic factors	[82]	$D_{n,T}$
λ_{tgf}	Tumor growth factor rate constant		$\lambda_{U,V,n}$
$\lambda_{de,tgf}$	Degradation rate constant for tumor growth factors		$\lambda_{U,V,n}$
$\lambda_{U,tgf}$	Total uptake rate constant for tumor growth factors by tumor		$\lambda_{U,V,n}$
$J_{\sigma nE}$	Vasculature diffusive flux for $\sigma \in \{B, L\}$		$\tilde{\sigma}_{max} \cdot \mathcal{T}$

Table 31 Parameters in Equation 4.5.1 through Equation 4.5.20, following the model in [82, 83, 289]. Parameters values for this study are as in [82] and [289].

Table 32 summarizes the non-dimensionalization parameters.

Non-dimensionalization parameter	Description	Definition or Assigned Value
$\tilde{\phi}_\alpha$	Fixed solid volume fraction	0.8
E_a^*	Energy scale for adhesion	0.001
E_e^*	Energy scale for ECM elastic effects	0.001
$\bar{\bar{k}}_\alpha$	Characteristic motility of the solid phase (cells)	1.0
$\mathcal{L}$	Characteristic length	$\sqrt{\dfrac{D_{T,n}}{\lambda_{U,V,n}}}$
$\mathcal{T}$	Characteristic time	$\dfrac{1}{\lambda_{M,V}}$
$\mathcal{P}$	Characteristic pressure	$\dfrac{\mathcal{L}^2}{\bar{\bar{k}}_\alpha \cdot \mathcal{T}}$
$\mathcal{M}$	Characteristic mobility	$\dfrac{\mathcal{L}^2}{\mathcal{T} E_a^*}$
$\bar{\bar{\epsilon}}$	Characteristic interaction strength	$\mathcal{L} \cdot \sqrt{\dfrac{E_a^*}{\tilde{\phi}_\alpha}}$
$\bar{\bar{\mathcal{E}}}$	Characteristic strain	$\sqrt{\dfrac{E_a^* \cdot \tilde{\phi}_\alpha}{E_e^* \cdot \bar{\bar{\epsilon}} \cdot L_2^E}}$

Table 32 List of non-dimensionalization parameters used in Table 30 and Table 31, following the model in [82].

G denotes the set of all simulated immune species in Equation 4.5.2 and Equation 4.5.3, while δ_{mn} in Equation 4.5.5 and Equation 4.5.6 is defined as:

$$\delta_{mn} = \begin{cases} 0, m \neq n \\ 1, m = n \end{cases}.$$

In this study, only monocytes and macrophages are simulated. Hence, it is assumed that other immune species negligibly contribute to the TME. Thus, $G = \{M_0, M_1, M_2\}$.

Differentiation of monocytes is accounted for in the rate terms $r_{diff|M_1}$ and

$r_{diff|M_2}$ for M1 and M2, respectively:

$$r_{diff|M_1} = \lambda_{diff|M_0} \cdot \mathcal{A}_{diff|M_1} \cdot \mathcal{A}_{diff|M_0} \cdot \phi_{M_0}$$
<div align="right">Equation 4.5.21</div>

$$r_{diff|M_2} = \lambda_{diff|M_0} \cdot \mathcal{A}_{diff|M_2} \cdot \mathcal{A}_{diff|M_0} \cdot \phi_{M_0}$$
<div align="right">Equation 4.5.22</div>

$$\mathcal{A}_{diff|M_1} = 1 - F_P$$
<div align="right">Equation 4.5.23</div>

$$\mathcal{A}_{diff|M_2} = F_P$$
<div align="right">Equation 4.5.24</div>

where differentiation occurs at a rate $\lambda_{diff|M_0}$, and F_P is the probability of the

$M_0 \to M_2$ differentiation event bounded in the closed interval [0,1] defined as:

$$
F_P = \left(\mathcal{F}_{TH2|M_2\ diff} \cdot \mathcal{A}_{I|TH2} \cdot Q_3\left(\frac{\phi_{TH2}}{\phi_{GG}}\right) \right.
$$

$$
+ \mathcal{F}_{TH1|M_1\ diff} \cdot \left(1 - \mathcal{A}_{I|TH1} \cdot Q_3\left(\frac{\phi_{TH1}}{\phi_{GG}}\right)\right) \bigg)
$$
<div align="right">Equation 4.5.25</div>

$$
\cdot \frac{1}{\mathcal{F}_{TH2|M_2\ diff} + \mathcal{F}_{TH1|M_1\ diff}} + \mathcal{F}_{F_{bias}}
$$

where ϕ_{GG} is the saturation volume fraction for immune species interactions.

Interactions between macrophages and helper T-cells are neglected in this study. Thus,

$\phi_{TH1} = \phi_{TH2} = 0$. Therefore, Equation 4.5.25 simplifies to $F_P = \mathcal{F}_{F_{bias}}$, where $\mathcal{F}_{F_{bias}}$ is

a constant dimensionless parameter representing the probability of the $M_0 \to M_2$ event.

4.5.2 Formulation for BCLM

We expand the 3D model described above with the capability to simulate a

chemotherapeutic regimen as well as the release of growth factors by M2 macrophages.

Pertinent model variables are summarized in **Table 33**.

Variable	Description	Non-dimensionalization Factor

ϕ_{M1}	Volume fraction of M1	$\tilde{\phi}_\alpha$
ϕ_{M2}	Volume fraction of M2	$\tilde{\phi}_\alpha$
D_P	Simulated drug concentration	$\overline{D}_p$
F_{M2}	Tumor growth factors released by M2	$(F_{M2})_{sat}$

Table 33 Model variables pertinent to BCLM in this study.

As in [65], tumor hypoxia is adjusted by shifting the hypoxic threshold n_h using M2-released growth factors, denoted as F_{M2}. Factor F_{M2} is assumed to represent proteins, following diffusion gradients in a manner akin to tumor growth factors (TGF) using a quasi-steady state equation as described in Equation 4.5.16:

$$\nabla \cdot \left(D_{F_{M2}} \cdot \nabla F_{M2}\right) + (F_{M2})_{sat} \cdot \lambda_{F_{M2}} - \left(\lambda_{F_{M2}} + \lambda_{de,F_{M2}} + \lambda_{U,F_{M2}}\right) \cdot F_{M2} = 0 \qquad \text{Equation 4.5.26}$$

$$\lambda_{F_{M2}} = \lambda_{M_2,F_{M2}} \cdot \mathcal{A}_{M_2,F_{M2}} \qquad \text{Equation 4.5.27}$$

$$\mathcal{A}_{M_2,F_{M2}} = \mathcal{A}_{I|M_2} \cdot Q_3\left(\frac{\phi_{M2}}{\phi_{GG}}\right) \qquad \text{Equation 4.5.28}$$

$$\lambda_{U,F_{M2}} = \lambda_{U,F_{M2},V} \cdot \frac{\phi_V}{\tilde{\phi}_\alpha} \qquad \text{Equation 4.5.29}$$

where the effective diffusivity and rate of production, degradation, and uptake of F_{M2} are $D_{F_{M2}}, \lambda_{F_{M2}}, \lambda_{de,F_{M2}}$, and $\lambda_{U,F_{M2}}$, respectively. The saturation concentration of F_{M2} is $(F_{M2})_{sat}$, $\mathcal{A}_{I|M_2}$ is the interaction strength of M_2, and ϕ_{GG} is the saturation volume fraction for immune model interactions. M2 produce F_{M2} at a rate $\lambda_{M_2,F_{M2}}$, and tumors uptake F_{M2} at a rate $\lambda_{U,F_{M2},V}$. Adjusting ϕ_{GG} allows for M2 to produce F_{M2} with discrete-like behavior akin to [57]; a full continuum effect can be achieved using ϕ_{GG} to the total solid volume fraction $\tilde{\phi}_\alpha$ as defined in [289]. $D_{F_{M2}}$ is computed using the effective diffusivity formula from [82]:

$$D_{F_{M2}} = D_{F_{M2},E} \cdot Q_3\left(\frac{\phi_E}{\tilde{\phi}_\alpha}\right) + D_{F_{M2},C} \cdot \left[1 - Q_3\left(\frac{\phi_E}{\tilde{\phi}_\alpha}\right)\right]$$

<div align="right">Equation 4.5.30</div>

$$D_{F_{M2},C} = D_{F_{M2},T} \cdot Q_3\left(\frac{\phi_T}{\phi_C}\right) + D_{F_{M2},H} \cdot \left(1 - Q_3\left(\frac{\phi_T}{\phi_C}\right)\right)$$

<div align="right">Equation 4.5.31</div>

where the diffusivity of F_{M2} in ECM, tumor, and host regions is $D_{F_{M2},E}$, $D_{F_{M2},T}$, and $D_{F_{M2},H}$, respectively. Like the model in [65], F_{M2} affects the tumor by adjusting the mitotic rate of proliferative tissue via adjustment factor $\mathcal{A}_{M,V}$:

$$\mathcal{A}_{M,V} = \begin{cases} \frac{n}{n_\infty} \cdot \left(1 + \mathcal{F}_{tgf,V}^M \cdot \frac{tgf}{tgf_{sat}} + \mathcal{F}_{F_{M2},V}^M \cdot \frac{F_{M2}}{(F_{M2})_{sat}}\right), & \frac{n}{n_\infty} \geq \left(\frac{n_h}{n_\infty} - n_{F_{M2},V}\right) \\ 0, & \frac{n_{v,V}}{n_\infty} \leq \frac{n}{n_\infty} < \frac{n}{n_\infty} - \left(\frac{n_h}{n_\infty} - n_{F_{M2},V}\right) \\ 0, & \frac{n}{n_\infty} < \frac{n_{v,V}}{n_\infty} \end{cases}$$

<div align="right">Equation 4.5.32</div>

$$n_{F_{M2},V} = \begin{cases} \mathcal{F}_{F_{M2},V}^{n_h} \cdot \frac{F_{M2}}{(F_{M2})_{sat}}, & F_{M2} < (F_{M2})_{sat} \\ \mathcal{F}_{F_{M2},V}^{n_h}, & F_{M2} \geq (F_{M2})_{sat} \end{cases}$$

<div align="right">Equation 4.5.33</div>

where F_{M2} saturates at a concentration $(F_{M2})_{sat}$, n_∞ is the far-field concentration of oxygen, $n_{n,V}$ is the oxygen viability threshold for ϕ_V, and $\mathcal{F}_{F_{M2},V}^{n_h}$ and $\mathcal{F}_{F_{M2},V}^M$ are the effective factors for F_{M2}'s effect on n_h and the mitotic rate of ϕ_V, respectively [65].

Macrophages have been shown to penetrate breast cancer spheroids and congregate within deeper portions of the tumor mass while stopping short of spheroid centers [59]. This behavior is replicated in this model by adjusting macrophage chemotaxis in proportion to tumor volume fraction ϕ_V:

$$\mu_\sigma + \epsilon_{TG}^2 \cdot \nabla^2 \phi_T + \epsilon_G^2 \cdot \nabla^2 \phi_G + \epsilon_{EG}^2 \cdot \nabla^2 \phi_E$$
$$= -\chi_{\sigma,che} \cdot \mathcal{A}_{X_G,che} \cdot che - \chi_{\sigma,tgf} \cdot \mathcal{A}_{X_G,tgf} \cdot tgf - \chi_{\sigma,taf}$$
$$\cdot \mathcal{A}_{X_G,taf} \cdot taf$$

Equation 4.5.34

$$\mathcal{A}_{X_G,\varsigma} = Q_3 \left(1 - \mathcal{F}_{Halt_G|V,\varsigma} \cdot \frac{\phi_V}{\tilde{\phi}_\alpha} \right)$$

Equation 4.5.35

where $\sigma \in G$, $\mathcal{F}_{Halt_G|V,\varsigma}$ is a dimensionless factor representing the effect of ϕ_V to mitigate macrophage chemotaxis, and $\varsigma = \{che, tgf, taf\}$.

Here, a generic cytotoxic drug D_P is introduced. This drug simulates the nab-PTX mechanism of action by selectively affecting proliferating tumor tissue [290]. For MSV-nab-PTX this model simulates drug release from both M1 and M2 that differentiate in the tumor domain from monocytes Mo. Equation 4.5.37 through Equation 5.2.39, adapted from [237, 291], simulate both extravasation of nab-PTX and release of MSV-nab-PTX by macrophages while accounting for a transition time in the TME between non-drug to drug-releasing macrophages:

$$\frac{\partial D_P}{\partial t} = \nabla \cdot \left(D_{D_P} \cdot \nabla D_P \right)$$
$$+ \left(\lambda_{extravasate,D_P} \cdot \mathcal{A}_{extravasate,D_P} - \lambda_{decay,D_P} \right.$$
$$\left. - \lambda_{uptake,D_P} \right) \cdot D_P$$
$$+ \left(\lambda_{D_P,M_1} \cdot \left(1 - e^{-\lambda_{M1,D_P,Turnover} \cdot t_i} \right) \cdot \frac{\phi_{M1}}{\tilde{\phi}_\alpha} + \lambda_{D_P,M_2} \right.$$
$$\left. \cdot \left(1 - e^{-\lambda_{M2,D_P,Turnover} \cdot t_i} \right) \cdot \frac{\phi_{M2}}{\tilde{\phi}_\alpha} \right) \cdot \left(\overline{D}_P \cdot e^{-\beta t} - D_P \right)$$

Equation 4.5.36

$$\lambda_{uptake,D_P}$$
$$= \begin{cases} \lambda_{D_P,uptake,H} \cdot \frac{\phi_H}{\tilde{\phi}_\alpha} + \lambda_{D_P,uptake,V} \cdot \frac{\phi_V}{\tilde{\phi}_\alpha}, \frac{n}{n_\infty} \geq \frac{n_h}{n_\infty} + \mathcal{F}_{nh,V}^{F_{M2}} \cdot \frac{F_{M2}}{(F_{M2})_{sat}} \geq \frac{n_V}{n_\infty} \\ \lambda_{D_P,uptake,H} \cdot \frac{\phi_H}{\tilde{\phi}_\alpha}, \text{otherwise} \end{cases}$$

Equation 4.5.37

$$\mathcal{A}_{extravasate,D_P} = \frac{B_n + B_p}{B_{max}} \cdot \left(1 - \frac{p_\alpha}{p_{t,B}}\right) \cdot \left(C_{D_P,t} - \frac{D_P}{\overline{D}_P}\right) \qquad \text{Equation 4.5.38}$$

$$C_{D_P,t} = \begin{cases} \left(1 - e^{-\alpha_1 \cdot (t-t_i)}\right), t_i \leq t < t_f \\ \left(1 - e^{-\alpha_1(t_f - t_i)}\right) \cdot e^{-\alpha_2(t-t_f)}, t \geq t_f \end{cases} \qquad \text{Equation 4.5.39}$$

where drug D_P extravasates at a rate $\lambda_{extravasate,D_P}$, diffuses with effective diffusivity D_{D_P}, decays at a rate λ_{decay,D_P}, is released by species $\sigma \in \{M_1, M_2\}$ at a rate of $\lambda_{D_P,\sigma}$, and is taken up by ϕ_H and proliferating tumor ϕ_V at a rate of $\lambda_{uptake,H}$ and $\lambda_{uptake,V}$, respectively. Like $D_{F_{M2}}$, D_{D_P} is computed using Equation 4.5.30 and Equation 4.5.31 where the diffusivities of D_P in tumor, ECM, and healthy regions are $D_{D_P,T}$, $D_{D_P,E}$, and $D_{D_P,H}$, respectively. For bolus administration, D_P extravasates from blood pre-existing (B_p) and neo- (B_n) vasculature when two conditions are locally met: solid cell pressure p_α is overcome by intravascular pressure $p_{t,B}$, above which vasculature is considered crushed and no longer functional, and intravascular concentration of the drug, $C_{D,t}$, exceeds the drug's extravascular concentration, D_P. The release concentration profile in vasculature can be tuned through rate constants α_1 and α_2, and start and finish times of drug administration, defined as t_i and t_f, respectively [291]. For bolus administration, $\alpha_1 \gg 0$. The quantity of PTX inside the macrophages is assumed to decay from a nominal concentration $\overline{D}_P$ at decay rate β. This model assumes that the proportion of drug-releasing macrophages to total macrophage population converges to 1 at an exponentially decaying rate defined by $\lambda_{M1,D_P,Turnover}$ and $\lambda_{M2,D_P,Turnover}$ for M1 and M2, respectively.

D_P affects the tumor through rate term $r_{D_P,V}$ affecting source term S_V from [82] and [289], is coupled to the mitotic rate, and, to maintain balance between the mitotic rate and the drug's effect, is proportional to the tumor volume fraction:

$$S_V = r_{M,V} - r_{A,V} - r_{N,V} - r_{G,V} - r_{B,V} - r_{L,V} - r_{de,V} - r_{D_P,V}$$

Equation 4.5.40

$$r_{D_P,V} = \lambda_{D_P,V} \cdot \mathcal{A}_{D_P,V} \cdot \phi_V$$

Equation 4.5.41

$$\mathcal{A}_{D_P,V} = \frac{D_P}{\overline{D_P}} \cdot \mathcal{A}_{M,V}$$

Equation 4.5.42

$$r_{M,V} = \lambda_{M,V} \cdot \mathcal{A}_{M,V} \cdot \phi_V$$

Equation 4.5.43

where $\lambda_{D_P,V}$ is the rate constant describing the effect of D_P on ϕ_V and $r_{M,V}$, $r_{A,V}$, $r_{N,V}$, $r_{G,V}$, $r_{B,V}$, $r_{L,V}$, and $r_{de,V}$ are the rates of mitosis, apoptosis, necrosis, elimination by macrophages, metastatic dissemination through blood and lymph, and autophagic degradation, respectively. The mitotic rate $r_{M,V}$ is proportional to a constant mitotic rate $\lambda_{M,V}$ and $\mathcal{A}_{M,V}$. Tumor cells killed by D_P are assumed to contribute to S_D via $r_{D_P,V}$:

$$S_D = r_{A,V} + r_{N,V} - r_{L,D} + r_{G,D} + r_{D_P,V}$$

Equation 4.5.44

where $r_{L,D}$ is the rate of dead tumor cell lysis and $r_{G,D}$ from [289] represents the rate at which viable tumor tissue is eliminated by macrophages and the rate at which macrophages phagocytize dead tumor tissue. Drug distribution, tumor growth, vascularization, nutrient and metabolite production, and macrophage presence and effects were simulated in parallel using coupled differential equations and solved using a Multigrid algorithm as described in [83, 147, 181].

4.5.3 BCLM Model Non-Dimensionalization

For each model equation, dependent variables and model parameters were non-dimensionalized. Non-dimensionalization of Equation 4.5.26 through Equation 4.5.29 proceeds similarly to non-dimensionalization of TGF given in [82]:

$$\nabla \cdot \left(\widetilde{D_{F_{M2}}} \cdot \nabla \widetilde{F_{M2}}\right) + \widetilde{\lambda_{F_{M2}}} - \left(\widetilde{\lambda_{F_{M2}}} + \lambda \widetilde{de,F_{M2}} + \widetilde{\lambda_{U,F_{M2}}}\right) \cdot \widetilde{F_{M2}} = 0$$

<div align="right">Equation 4.5.45</div>

$$\widetilde{\lambda_{F_{M2}}} = \widetilde{\lambda_{M2,F_{M2}}} \cdot \widetilde{\mathcal{A}_{M2,F_{M2}}}$$

<div align="right">Equation 4.5.46</div>

$$\widetilde{\mathcal{A}_{M2,F_{M2}}} = \mathcal{A}_{I|M_2} \cdot Q_3\left(\frac{\widehat{\phi_{M2}}}{\widehat{\phi_{GG}}}\right)$$

<div align="right">Equation 4.5.47</div>

$$\widetilde{\lambda_{U,F_{M2}}} = \widetilde{\lambda_{U,F_{M2},V}} \cdot \widetilde{\phi_V}$$

<div align="right">Equation 4.5.48</div>

Equation 4.5.30 and Equation 4.5.31 are non-dimensionalized as D_F in [82]. Non-dimensionalized forms of Equation 4.5.32 and Equation 4.5.33 are shown as Equation 4.5.49 and Equation 4.5.50, respectively:

$$\widetilde{\mathcal{A}_{M,V}} = \begin{cases} \tilde{n} \cdot \left(1 + \mathcal{F}_{tgf,V}^{M} \cdot \widetilde{tgf} + \mathcal{F}_{F_{M2},V}^{M} \cdot \widetilde{F_{M2}}\right), \tilde{n} \geq \left(\widetilde{n_h} - \widetilde{n_{F_{M2},V}}\right) \\ 0, \widetilde{n_{v,V}} \leq \tilde{n} < \tilde{n} - \left(\widetilde{n_h} - \widetilde{n_{F_{M2},V}}\right) \\ 0, \tilde{n} < \widetilde{n_{v,V}} \end{cases}$$

<div align="right">Equation 4.5.49</div>

$$\widetilde{n_{F_{M2},V}} = \begin{cases} \mathcal{F}_{F_{M2},V}^{n_h} \cdot \widetilde{F_{M2}}, \widetilde{F_{M2}} < 1 \\ \mathcal{F}_{F_{M2},V}^{n_h}, \widetilde{F_{M2}} \geq 1 \end{cases}$$

<div align="right">Equation 4.5.50</div>

Equation 4.5.34 and Equation 4.5.35 are non-dimensionalized as described across [82] and [289] to form Equation 4.5.51 and Equation 4.5.52, respectively:

$$\begin{aligned} \tilde{\mu}_\sigma + \tilde{\epsilon}_{TG}^2 \cdot \nabla^2 \tilde{\phi}_T + \tilde{\epsilon}_G^2 \cdot \nabla^2 \tilde{\phi}_G + \tilde{\epsilon}_{EG}^2 \cdot \nabla^2 \tilde{\phi}_E \\ = -\tilde{\chi}_{\sigma,che} \cdot \tilde{\mathcal{A}}_{X_{G,che}} \cdot che - \tilde{\chi}_{\sigma,tgf} \cdot \tilde{\mathcal{A}}_{X_{G,tgf}} \cdot \widetilde{tgf} \\ - \tilde{\chi}_{\sigma,taf} \cdot \tilde{\mathcal{A}}_{X_{G,taf}} \cdot \widetilde{taf} \end{aligned}$$

<div align="right">Equation 4.5.51</div>

$$\tilde{\mathcal{A}}_{X_G,\varsigma} = Q_3\left(1 - \mathcal{F}_{Halt_G|V,\varsigma} \cdot \widetilde{\phi_V}\right)$$

<div align="right">Equation 4.5.52</div>

where $\sigma \in \{M_0, M_1, M_2\}$ and $\varsigma = \{che, tgf, taf\}$.

Non-dimensionalization of Equation 4.5.36 through Equation 4.5.39 is presented

in Equation 4.5.53 through Equation 4.5.56:

$$\frac{\partial \widetilde{D_P}}{\partial \tilde{t}} = \nabla \cdot \left(\widetilde{D_P} \cdot \nabla \widetilde{D_P}\right) + \left(\widetilde{\lambda_{extravasate,D_P}} \cdot \widetilde{\mathcal{A}_{extravasate,D_P}}\right.$$
$$- \widetilde{\lambda_{decay,D_P}} - \widetilde{\lambda_{uptake,D_P}}\left.\right) \cdot \widetilde{D_{D_P}}$$
$$+ \left(\widetilde{\lambda_{D_P,M_1}} \cdot \left(1 - e^{-\lambda_{M1,D_P,Turnover} \cdot t_i}\right) \cdot \widetilde{\phi_{M1}}\right.$$
$$+ \widetilde{\lambda_{D_P,M_2}} \cdot \left(1 - e^{-\lambda_{M2,D_P,Turnover} \cdot t_i}\right) \cdot \widetilde{\phi_{M2}}\left.\right) \cdot \left(e^{-\tilde{\beta}\tilde{t}} - \widetilde{D_{D_P}}\right)$$

Equation 4.5.53

$$\widetilde{\lambda_{uptake,D_P}}$$
$$= \begin{cases} \widetilde{\lambda_{D_P,uptake,H}} \cdot \widetilde{\phi_H} + \widetilde{\lambda_{D_P,uptake,V}} \cdot \widetilde{\phi_V}, \tilde{n} \geq \widetilde{n_h} + \mathcal{F}_{nh,V}^{FM2} \cdot \widetilde{F_{M2}} \geq \widetilde{n_V} \\ \widetilde{\lambda_{D_P,uptake,H}} \cdot \widetilde{\phi_H}, \text{otherwise} \end{cases}$$

Equation 4.5.54

$$\widetilde{\mathcal{A}_{extravasate,D_P}} = \left(\widetilde{B_n} + \widetilde{B_p}\right) \cdot \left(1 - \frac{\widetilde{p_\alpha}}{\widetilde{p_{t,B}}}\right) \cdot \left(\widetilde{C_{D_P}}(t) - \widetilde{D_P}\right)$$

Equation 4.5.55

$$\widetilde{C_{D_P}}(t) = \begin{cases} \left(1 - e^{-\widetilde{\alpha_1} \cdot (\tilde{t} - \tilde{t}_i)}\right), \tilde{t}_i \leq \tilde{t} < \tilde{t}_f \\ \left(1 - e^{-\widetilde{\alpha_1}(\tilde{t}_f - \tilde{t}_i)}\right) \cdot e^{-\widetilde{\alpha_2}(\tilde{t} - \tilde{t}_f)}, \tilde{t} \geq \tilde{t}_f \end{cases}$$

Equation 4.5.56

where $p_{t,B}$ has non-dimensionalization factor $\mathcal{P}$ from **Table 32**. S_V non-

dimensionalization in Equation 4.5.38 is extended from [82] and [289], with the novel

rate term $r_{D_P,V}$ from Equation 4.5.41 and Equation 4.5.42 non-dimensionalized as

Equation 4.5.57 and Equation 4.5.58, respectively:

$$\widetilde{r_{D_P,V}} = \widetilde{\lambda_{D_P,V}} \cdot \widetilde{\mathcal{A}_{D_P,V}} \cdot \tilde{\phi}_V$$

Equation 4.5.57

$$\widetilde{\mathcal{A}_{D_P,V}} = \widetilde{D_P} \cdot \widetilde{\mathcal{A}_{M,V}}$$

Equation 4.5.58

Equation 4.5.43 is non-dimensionalized as in [82] using Equation 4.5.49 and

Equation 4.5.50 for $\widetilde{\mathcal{A}_{M,V}}$. Non-dimensionalization of Equation 4.5.44 is trivially

extended from [82] and [289] using Equation 4.5.57 and Equation 4.5.58.

4.5.4 Boundary Conditions

Neumann and Dirichlet boundary conditions were established for D_P and F_{M_2}, respectively:

$$\mathbf{n} \cdot \nabla \widetilde{D_P} = \widetilde{F_{M_2}} = 0 \qquad \text{Equation 4.5.59}$$

where $\mathbf{n}$ is the outward normal from the boundary. Neumann and Dirichlet boundary conditions hold for the non-dimensionalized volume fractions and chemical potentials, respectively, of all $\sigma \in G$:

$$\mathbf{n} \cdot \nabla \tilde{\phi}_\sigma = \tilde{\mu}_\sigma = 0 \qquad \text{Equation 4.5.60}$$

Like tgf and taf in [82], a Dirichlet boundary condition is specified for the non-dimensionalized chemotaxis concentration $\widetilde{che}$:

$$\widetilde{che} = 0 \qquad \text{Equation 4.5.61}$$

All other boundary conditions are as in [289].

4.5.5 Model Discretization

Discretization of Equation 4.5.26 follows the discretization of TGF given in [83]. Drug discretization in time was performed using the Crank-Nicholson method and in space using the operators defined in [83].

4.5.6 Model Parameter Values and Initial Conditions

Table 34 summarizes BCLM-specific model parameters. **Table 35** lists additional model parameters. Initial monocyte and macrophage volume fractions were chosen to be: $\phi_{M_0} = 9.8 \cdot 10^{-3}$, $\phi_{M_1} = 4.891 \cdot 10^{-2}$, and $\phi_{M_2} = 4.076 \cdot 10^{-2}$ for 1.2:1.0 M1:M2, and $\phi_{M_0} = 9.8 \cdot 10^{-3}$, $\phi_{M_1} = 3.185 \cdot 10^{-2}$, and $\phi_{M_2} = 5.782 \cdot 10^{-2}$ for 1.0:1.8 M1:M2. These fractions were set homogenously in the model domain. Tumor seeds, however, were assumed to be avascular and initially free of immune cells. To study the effects of

vascularity and macrophages, this model separates the chemoattractant term *che* to dictate macrophage chemotaxis and tumor angiogenic factors (TAF) to promote angiogenesis. Ratios of 1.2:1.0 M1:M2 and 1.0:1.8 M1:M2 were enforced by setting $\mathcal{F}_{F_{bias}}$ to -0.045455 and 0.14286, respectively. To preserve an average macrophage volume fraction within tumors at ~10% as reported in [57], the monocyte extravasation factors for previous- and neo- blood vasculature ($\mathcal{F}_{M_0}^{Bp}$ and $\mathcal{F}_{M_0}^{Bn}$) were adjusted in multiple metastasis simulations to 13.615 and 3.402, respectively.

Parameter	Description	Non-dimensionalization Factor	Value	Reference
$D_{F_{M2},E}$	Diffusivity of F_{M2} in ECM regions	$D_{n,T}$	0.01	Calibrated
$D_{F_{M2},T}$	Diffusivity of F_{M2} in tumor regions	$D_{n,T}$	0.01	Calibrated
$D_{F_{M2},H}$	Diffusivity of F_{M2} in host regions	$D_{n,T}$	0.01	Calibrated
$\lambda_{F_{M2}}$	Production rate of F_{M2}	$\lambda_{U,V,n}$	Computed	Calibrated
$\lambda_{M_2,F_{M2}}$	Rate of release of F_{M2} by M2	$\lambda_{U,V,n}$	0.20	Calibrated
$\lambda_{de,F_{M2}}$	Degradation rate of F_{M2}	$\lambda_{U,V,n}$	0.20	Calibrated
$\lambda_{U,F_{M2}}$	Uptake rate of F_{M2}	$\lambda_{U,V,n}$	Computed	Calibrated
$\lambda_{U,F_{M2},V}$	Uptake rate of F_{M2} by tumor cells	$\lambda_{U,V,n}$	0.0	Calibrated
$\mathcal{F}_{F_{M2},V}^{M}$	Effect of F_{M2} on tumor mitotic rate	Dimensionless	0.95	Calibrated
$\mathcal{F}_{F_{M2},V}^{n_h}$	Effect of F_{M2} on tumor hypoxic threshold	Dimensionless	0.30	Calibrated
$\mathcal{F}_{Halt_G|V,che}$	Effect of ϕ_V to mitigate chemokine-mediated macrophage chemotaxis	Dimensionless	0.40	Calibrated
$\mathcal{F}_{Halt_G|V,tgf}$	Effect of ϕ_V to mitigate TGF-mediated macrophage chemotaxis	Dimensionless	0.0	Calibrated

$\mathcal{F}_{Halt_G|V,taf}$	Effect of ϕ_V to mitigate TAF-mediated macrophage chemotaxis	Dimensionless	0.0	Calibrated
D_{D_P}	Effective diffusivity of D_P	$\dfrac{\mathcal{L}^2}{\mathcal{T}}$	Computed	Calibrated
$D_{D_P,H}$	Diffusivity of D_P in healthy regions	$\dfrac{\mathcal{L}^2}{\mathcal{T}}$	0.25	Calibrated to results in [57]
$D_{D_P,E}$	Diffusivity of D_P in ECM regions	$\dfrac{\mathcal{L}^2}{\mathcal{T}}$	0.25	Calibrated to results in [57]
$D_{D_P,T}$	Diffusivity of D_P in tumor regions	$\dfrac{\mathcal{L}^2}{\mathcal{T}}$	0.25	Calibrated to results in [57]
$\lambda_{extravasate,D_P}$	Rate of extravasation of drug D_P	$\lambda_{M,V}$	4600	Calibrated
λ_{decay,D_P}	Rate of decay of drug D_P	$\lambda_{M,V}$	0.833	Calibrated to half-life in [283]
λ_{uptake,D_P}	Rate of uptake of drug D_P	$\lambda_{M,V}$	Computed	Calibrated
$\lambda_{D_P,uptake,H}$	Rate of uptake of drug D_P by healthy host tissue (H)	$\lambda_{M,V}$	0.0	Calibrated
$\lambda_{D_P,uptake,V}$	Rate of uptake of drug D_P by viable tumor tissue (V)	$\lambda_{M,V}$	0.16	Calibrated
$\lambda_{D_P,V}$	Death rate of viable tumor tissue (V) due to drug D_P	$\lambda_{M,V}$	7.95	Calibrated
λ_{D_P,M_1}	Rate of drug D_P release by M1	$\lambda_{M,V}$	46.9	Calibrated
λ_{D_P,M_2}	Rate of drug D_P release by M2	$\lambda_{M,V}$	46.9	Calibrated
α_1	Rate of drug concentration saturation in the vasculature	$\mathcal{T}^{-1}$	7.0	Calibrated
α_2	Rate of drug clearance in the vasculature	$\mathcal{T}^{-1}$	7.0	Calibrated
β	Rate of drug decay in macrophages	$\mathcal{T}^{-1}$	0.9	Calibrated
$\lambda_{M1,D_P,Turnover}$	Rate of M1 turnover from non-drug carrying to drug-carrying versions	$\mathcal{T}^{-1}$	0.50	Calibrated
$\lambda_{M2,D_P,Turnover}$	Rate of M2 turnover from non-drug carrying to drug-carrying versions	$\mathcal{T}^{-1}$	0.50	Calibrated

Table 34 BCLM-specific model parameters. Computed parameters are defined as functions of model variables or constant-valued model parameters.

Parameter	Description	Non-dimensionalization Factor	Value	Reference
$\lambda_{Base\|\sigma}$	Base activation level for immune species $\sigma \in \{M_1, M_2\}$	Dimensionless	1.0	Calibrated
ϕ_{GG}	Saturation volume fraction for immune species interactions	$\tilde{\phi}_\alpha$	0.04	Calibrated
$n_{v,B}$	O2 viability limit of endothelial cells	n_∞	0.4	Calibrated
$n_{v,L}$	O2 viability of lymphatic cells	n_∞	0.4	Calibrated
$n_{v,F}$	O2 viability of myofibroblastic cells	n_∞	0.4	Calibrated
$\lambda_{diff\|M_0}$	Rate of monocyte differentiation	$\lambda_{M,V}$	1.2	Calibrated
$\mathcal{F}_{M_0}^{Bp}$	Monocyte extravasation factor for pre-existing blood vasculature	Dimensionless	7.0	Calibrated to match [57]
$\mathcal{F}_{M_0}^{Bn}$	Monocyte extravasation factor for neo-blood vasculature	Dimensionless	1.75	Calibrated to match [57]
$\lambda_{InduceDeath\|V}$	Tumor death rate in response to cytotoxic immune species	$\lambda_{M,V}$	0.200	Calibrated
$\lambda_{Bn,n,H}$	Transfer coefficient of O2 via neo-vasculature in healthy regions	$\lambda_{U,V,n}$	0.60	Calibrated to match [142]
$\lambda_{Bn,n,E}$	Transfer coefficient of O2 via neo-vasculature in ECM regions	$\lambda_{U,V,n}$	0.60	Calibrated to match [142]
$\lambda_{Bn,n,T}$	Transfer coefficient of O2 via neo-vasculature in tumor regions	$\lambda_{U,V,n}$	0.60	Calibrated to match [142]
$\lambda_{Bp,w,H}$	Transfer coefficient of carbon dioxide via preexisting vasculature in healthy regions	$\lambda_{U,V,n}$	3.0	Calibrated

$\lambda_{Bp,w,E}$	Transfer coefficient of carbon dioxide via preexisting vasculature in ECM regions	$\lambda_{U,V,n}$	3.0	Calibrated
$\lambda_{Bp,w,T}$	Transfer coefficient of carbon dioxide via preexisting vasculature in tumor regions	$\lambda_{U,V,n}$	3.0	Calibrated
$\lambda_{U,V,g}$	Uptake rate constant of glucose by viable tumor cells	$\lambda_{U,V,n}$	0.09	Calibrated
$\lambda_{Bp,\ell,T}$	Transfer coefficient of lactic ion via preexisting blood vasculature in tumor regions	$\lambda_{U,V,n}$	3.0	Calibrated
$\lambda_{Bp,\ell,E}$	Transfer coefficient of lactic ion via preexisting blood vasculature in ECM regions	$\lambda_{U,V,n}$	3.0	Calibrated
$\lambda_{Bp,\ell,H}$	Transfer coefficient of lactic ion via preexisting blood vasculature in host regions	$\lambda_{U,V,n}$	3.0	Calibrated
$\chi_{M_0,c}$	Chemotaxis parameter for monocytes	$\dfrac{E_a^*}{che_{sat}}$	5.0	Calibrated
$\chi_{M_1,c}$	Chemotaxis parameter for M1	$\dfrac{E_a^*}{che_{sat}}$	15.0	Calibrated
$\chi_{M_2,c}$	Chemotaxis parameter for M2	$\dfrac{E_a^*}{che_{sat}}$	15.0	Calibrated
k_f	Forward reaction rate of the dissolution of CO2 and H2O	$\lambda_{U,V,n}$	3.0	Calibrated
k_r	Reverse reaction rate of the dissolution of CO2 and H2O	$\dfrac{\lambda_{U,V,n}}{n_\infty}$	3.0	Calibrated
k_β	Motility of the fluid phase	$\bar{\bar{k}}_\beta$	3.0	Calibrated
$\lambda_{M2,tgf}$	Release rate of TGF by M2	$\lambda_{U,V,n}$	0.0	Calibrated

Table 35 Additional model parameter values used in this study. All other model

parameters are set as in [289].

4.5.7 Calibration of Multiple Metastases Size and Number

To quantify the theoretical maximum size of simulated tumors, each seed size was centered in a 2.1x2.1x2.1 mm^3 domain (64^3 points with 33.3 μm point spacing) and grown for 6.8 simulated days. Mitotic rates for each tumor were varied to change tumor sizes from each seed type. Sizes of each tumor were then estimated by deriving a radial measurement from a total volume measurement, assuming each tumor was approximately spherical. Tumor tissue for radial measurements is defined as $\phi_V \geq 0.05$. Because metastatic growth can be negatively affected by adjacent metastases through nutrient deprivation and formation of impeding solid-state pressure gradients, radii obtained from simulations of individual tumors represent an ideal condition for growth and, by extension, the (theoretical) maximum attainable radius for that particular tumor. The seed diameter, mitotic rates, and theoretical maximum tumor volumes are plotted in **Figure 25**, with red points indicating selected tumor initial conditions. Selected seed diameter, mitotic rates, and theoretical maximum tumor volumes are given in **Table 36**.
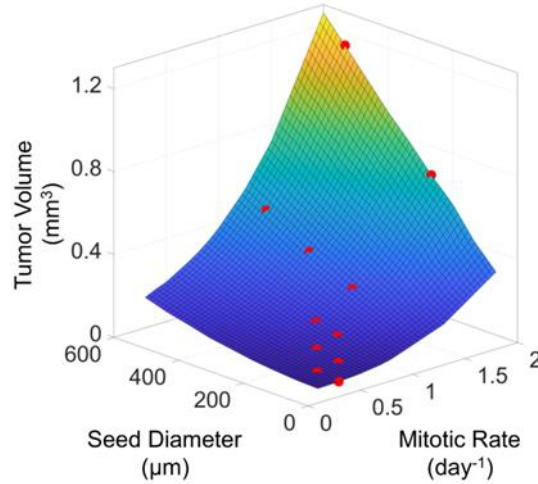
Figure 25 Plot of Seed Diameter vs. Mitotic Rate vs. Theoretical Maximum Tumor Volume. Red points are selected combinations used to generate the initial in silico multiple metastatic condition. Values for selected conditions are given in **Table 36**. Color varies from minimum = 0.0012 mm^3 (blue) to maximum = 1.26 mm^3 (yellow).

Mitotic Rate	Seed Diameter (μm)	Theoretical Maximum Tumor Volume (mm^3)	Theoretical Maximum Diameter (μm)
0.50	66.7	0.0037	192
0.50	133.3	0.0121	285
0.70	133.3	0.0276	375
0.70	200.0	0.0558	474
0.90	200.0	0.0895	555
0.90	266.7	0.1194	611
1.25	266.7	0.2262	756
1.25	400.0	0.333	860
1.25	533.3	0.4589	957
2.00	266.7	0.6614	1081
2.00	533.3	1.1398	1296

Table 36 List of BCLM seeds and mitotic rates used to simulate multiple BCLM *in silico*. Diameters were calculated assuming spherical tumor growth and represent the theoretical maximum tumor volumes attainable without growth-adverse pressure gradients and nutrient deprivation.

The 3D initial condition was calibrated such that differences between comparable tumor sizes were within one standard deviation of the *in vivo* data. Maximum spatial resolution in these simulations is 33.3 μm and, hence, this study focuses on tumors >100 μm diameter (of note, no tumors <100 μm were observed *in vivo*). **Figure 26** compares the distribution of tumor sizes observed in the histological liver lobe slides vs the model simulated tumors.
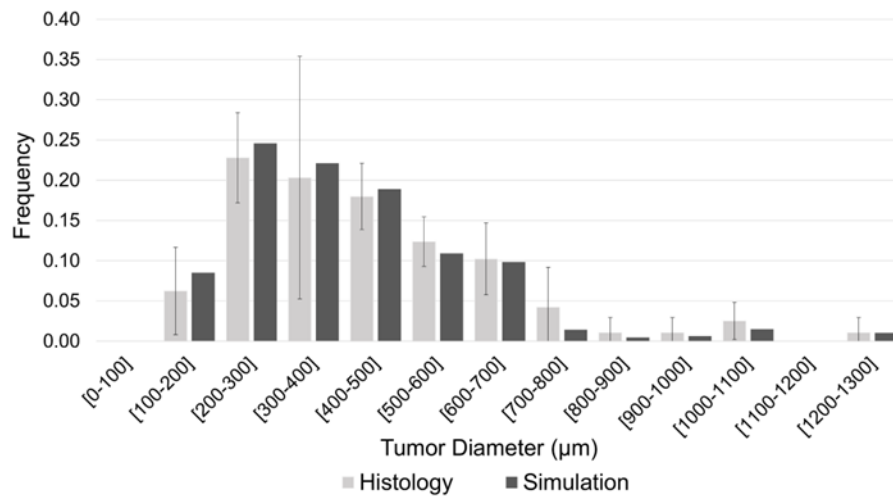
Figure 26 Histogram of tumor sizes observed in mouse liver histology compared to the simulated distribution achieved by varying seed size and mitotic rates. Simulated seed sizes were determined based on *in silico* measurements of single-BCLM simulations with varying mitotic rates. Error bars on histology measurements represent one standard deviation. Simulation counts are exact (no variability).

The frequencies of tumor sizes *in silico* were fit to match those *in vivo*. Because a 3D model was used to replicate densities found in 2D histology slides, a significantly

higher number of tumors were required *in silico* to match the tumor density seen *in vivo*. Thus, for example, 214 metastases with a theoretical maximum diameter of 192 μm (**Table 36**) were required to generate a density in line with the 6 lesions of 100-200 μm BCLM measured *in vivo*. Average tumor density *in vivo* was measured as 26.5%±1.9%, while tumor density *in silico* was 28.3%. The simulated tumor density fell within a single standard deviation of the average *in vivo* tumor density, having an absolute error and absolute relative error of 1.8% and 6.7%, respectively. The number of tumors categorized by diameter ranges is tabulated in **Table 37**.

Diameter Range (μm)	*In vivo*		Simulated	
	# Tumors	Average Fraction of Overall Tumor Burden ± σ	# Tumors	Fraction of Overall Tumor Burden
100 to 200	6	0.063±0.054	214	0.085
200 to 300	20	0.228±0.056	618	0.246
300 to 400	16	0.203±0.151	556	0.221
400 to 500	15	0.180±0.041	475	0.189
500 to 600	11	0.124±0.031	274	0.109
600 to 700	9	0.102±0.045	247	0.098
700 to 800	4	0.042±0.050	36	0.014
800 to 900	1	0.011±0.019	12	0.005
900 to 1000	1	0.011±0.019	16	0.006
1000 to 1100	2	0.025±0.023	38	0.015
1200 to 1300	1	0.011±0.019	26	0.010

Table 37 Comparison of tumor diameter ranges, number, and fraction of overall tumor burden observed in mouse liver BCLM vs simulated 3D multiple BCLM. No tumors were observed *in vivo* in the 1100-1200 μm range. σ = standard deviation.

CHAPTER 5: SYNERGISTIC EFFECT OF ANTI-PDL1 AND CYTOTOXIC T-CELL-ACTIVATING NANOTHERAPY IN PRIMARY AND LIVER METASTATIC PANCREATIC DUCTAL ADENOCARCINOMA EVALUATED VIA 3D MATHEMATICAL MODELING

5.1 Introduction

Pancreatic ductal adenocarcinoma (PDAC) is projected to become the second-most lethal cancer type by 2030 and is estimated to be responsible for over 50,000 US deaths in 2024 [5, 292, 293]. PDAC comprises 90% of diagnosed pancreatic cancers, with only 12% of patients living 5 years after diagnosis [294-296]. PDAC is hallmarked by a pronounced stromal compartment (desmoplasia) that surrounds the tumor cells and reduce the tumor microenvironment (TME) permeability to distinct immune cell populations [14-16]. Additionally, high interstitial fluid pressure contributes to sparse vascularization, rendering intravenously administered chemotherapeutics largely ineffective [16, 21-25]. Contributing further to the high PDAC mortality is a prevalent metastatic burden: patients diagnosed at stage IV constitute 47% of PDAC diagnoses and have a 5-year survival rate of <5% [5]. Liver metastases of PDAC (PDAC-LM) are present in nearly 80% of PDAC patient autopsies [10]. Thus, PDAC-LM represents a significant portion of advanced-stage PDAC burden.

In contrast to primary PDAC, PDAC-LM primarily exhibit a replacement growth type, which is characterized by hypovascularization with normal stromal deposition [26, 297, 298]. However, both PDAC and PDAC-LM TME exhibit elevated expression of Programmed Cell Death Ligand 1 (PD-L1), a transmembrane protein expressed by PDAC cells but also stromal cells including macrophages, myeloid derived suppressor cells (MDSC), and myofibroblasts. By binding to the corresponding Programmed Cell Death Protein 1 (PD-1) receptor expressed by T cells, PD-L1 expressing cells promote cytotoxic T cell (CTL) exhaustion via the PD-1 pathway [15, 51-53, 299, 300]. Exhausted CTL exert reduced cytotoxicity that contributes to lower immunotherapeutic efficacy [54-56]. In general, immune checkpoint blockade (ICB) has become a potent therapeutic strategy against cancers such as from lung or breast [27, 28]. However, ICB has revealed little to no effect in preclinical studies and clinical trials of PDAC patients [301]. In line with these observations, durvalumab did not lead to reduction of PDAC burden *in vitro* [53] and in metastatic PDAC patients [24], supporting the view that targeting the PD-L1/PD-1 axis alone is insufficient for treating PDAC.

Several preclinical studies have tested combinatorial approaches involving different ICB strategies or ICB with other therapeutic approaches demonstrating improved tumor responses in TME-enriched PDAC [302-304]. In particular, combinatorial nanomedicine-based approaches have shown promise [305], including for PDAC [306]. Recently, chitosan nanoparticles (CNP) loaded with a model antigen SIINFEKL (SIINFEKL-CNP), an ovalbumin-derived peptide (OVA-257-264), showed promising anti-PDAC effects via murine dendritic cell (DC) mediated CTL activation

[307], as stimulation of DC with SIINFEKL-CNP elicited potent antigen-specific CTL

responses against Panc-OVA cells [307]. Despite this progress, it remains to be elucidated

whether the combination of nanotherapy (antigen-CNP) targeting DC-mediated CTL

activation and anti-PD-L1 blockade would be effective in reducing tumor burden of

primary PDAC and liver metastases.

Mathematical modelling has provided an avenue to simulate immune interactions

in primary and metastatic microenvironments [57, 59, 60, 67, 308-313]. Such

mathematical tumor models have been successfully applied to evaluate macrophage and

CTL interactions in the PDAC-LM microenvironment [67], therapeutic response of

primary and metastatic colorectal cancer [314], and macrophage-mediated administration

of paclitaxel to breast cancer liver metastases (BCLM) [57]. In Leonard et al. [59], the

mathematical model hypothesized potential improvements to BCLM nanotherapy-

mediated nab-PTX treatment in the presence of a mix of M1 and M2 macrophage types.

This prediction was later confirmed *in vitro* [60]. Furthermore, targeting the PD-1/PD-L1

axis has been modeled using ordinary differential equations (ODE) [69, 310]. The ODE

applied in Butner et al. [310] was fitted to aggregated clinical trial data and was validated

using a non-small cell lung cancer patient cohort. A system of ODE was used in Wang et

al. [69] to identify the fraction of a virtual cohort of mice that are susceptible to PD-

1/PD-L1 immune checkpoint inhibition. The model in Yamamoto et al. [313] evaluated

FOLFIRINOX, gemcitabine (GEM), and GEM+nab-paclitaxel against primary and

metastatic PDAC. However, because clinical PDAC often measures ≥ 1 cm [72, 73],

modelling a three-dimensional clinically sized primary PDAC has remained a

computational challenge, making *in silico* evaluation of therapeutics within the PDAC TME elusive.

A mathematical tumor model developed in Ng & Frieboes [82] simulated tumor in a three-dimensional environment that was capable of growth at centimeter-scales [181]. Further biological details in Goodin & Frieboes [289] included various immune species and associated microenvironment phenomena, including M1/M2 macrophages, and CTL extravasation and chemotaxis, as well as local CTL and M1 mediated cytotoxicity against tumor tissue [308]. This model has recently been used to evaluate macrophage-mediated drug delivery [57] to multiple breast cancer liver metastases in a mouse liver lobe [308]. However, this model did not consider PD-L1 expression and its effect on the TME. Here, the mathematical 3D tumor model used in Goodin & Frieboes [289] is expanded to incorporate PD-L1 expression and exhaustion of CTL, an anti-PD-L1 inhibitor modeled after durvalumab, and nanotherapy (antigen-CNP) targeting DC-mediated CTL activation. This evaluation is performed on both mm-sized PDAC-LM and cm-scale PDAC to gauge the efficacy of systemically administered therapy.

5.2 Materials and Methods

5.2.1 Patient tumor samples and histological analysis

Immunohistochemical (IHC) staining of whole mount serial sections from a representative PDAC patient with a primary tumor and corresponding liver metastasis was performed. Both tissue samples were obtained via surgical resection. The research was approved by the ethics committee of Kiel University (reference number: A110/99).

Patient written consent was obtained. All IHC staining were performed as recently

described [52, 53]. Collagen staining was obtained via Sirius Red staining.

5.2.2 Model Main Equations

This study builds upon the 3D continuum model presented in Ng & Frieboes [82], which simulates a single tumor phenotype volume fraction represented as ϕ_V that interacts with ϕ_H and ϕ_E, representing host and ECM volume fractions, respectively. Tumor growth is promoted with sufficient oxygen and glucose and is restrained by hypoxia and necrosis (encompassing the dead tumor volume fraction ϕ_D). Tumor aerobic and anerobic respiration also affects local concentrations of bicarbonate, lactic acid, and H^+. ECM and host volume fractions compete for limited space, an interaction characterized by pressure and chemical potentials. Velocities describe the motion of tumor and ECM. Neo-vasculature formed in response to tumor angiogenic factors released by the TME maintains tumor proliferation while myofibroblasts secrete ECM.

Equation 5.2.1 through Equation 5.2.20 represent the key equations in non-dimensionalized form of this model as elaborated in [82] and [289]:

$$\frac{\partial \phi_V}{\partial t} + \nabla \cdot (\phi_V \boldsymbol{u}_\alpha) = M \nabla \cdot (\phi_V \nabla \mu_T) + S_V \qquad \text{Equation 5.2.1}$$

$$\mu_T = \frac{\partial F_b}{\partial \phi_T} - \epsilon_T^2 \cdot \nabla^2 \phi_T - \epsilon_{TE}^2 \cdot \nabla^2 \phi_E - \epsilon_{TG}^2 \cdot \nabla^2 \phi_G \qquad \text{Equation 5.2.2}$$

$$\mu_E = \frac{\partial F_b}{\partial \phi_E} + \frac{\partial \mathcal{W}}{\partial \phi_E} - \epsilon_E^2 \cdot \nabla^2 \phi_E - \epsilon_{TE}^2 \cdot \nabla^2 \phi_T - \epsilon_{EG}^2 \cdot \nabla^2 \phi_G \qquad \text{Equation 5.2.3}$$

$$\frac{\partial \mathcal{W}}{\partial \phi_E} = \epsilon_e \cdot [6 \cdot \phi_E (1 - \phi_E)] \cdot \sum_{i,j=1}^{3} \left[\frac{1}{2} \cdot (\mathcal{E}_T)_{ij} \cdot \mathbb{T}_{ij}^* - (\mathcal{E}_T^*)_{ij} \cdot \mathbb{T}_{ij} \right]$$

<div align="right">Equation 5.2.4</div>

$$\mathbb{T}_{mn}^* = 2 \cdot (1 - L_2^C) \cdot (\mathcal{E}_T)_{mn} + (L_1^E - L_1^C) \cdot \delta_{mn} \cdot \sum_{k=1}^{3} (\mathcal{E}_T)_{kk}$$

<div align="right">Equation 5.2.5</div>

$$\mathbb{T}_{mn} = 2 \cdot L_2 \cdot (\mathcal{E}_T)_{mn} + L_1 \cdot \delta_{mn} \cdot \sum_{s=1}^{3} (\mathcal{E}_T)_{ss}$$

<div align="right">Equation 5.2.6</div>

$$(\mathcal{E}_T)_{ij} = \mathcal{E}_{ij} - \mathcal{E}_{ij}^*$$

<div align="right">Equation 5.2.7</div>

$$\mathcal{E}_{ij}^* = Q_3(\phi_E) \cdot (\mathcal{E}_T^*)_{ij} + (\mathcal{E}_C^*)_{ij}$$

<div align="right">Equation 5.2.8</div>

$$(\mathcal{E}_T^*)_{ij} = (\mathcal{E}_E^*)_{ij} - (\mathcal{E}_C^*)_{ij}$$

<div align="right">Equation 5.2.9</div>

$$\mathcal{E}_{mn} = \frac{1}{2} \cdot \left(\frac{\partial u_m^d}{\partial x_n} + \frac{\partial u_n^d}{\partial x_m} \right)$$

<div align="right">Equation 5.2.10</div>

$$L_i = Q_3(\phi_E) \cdot (L_i^E - L_i^C) + L_i^C, i = 1,2$$

<div align="right">Equation 5.2.11</div>

$$Q_3(x) = Q_3(x) = \begin{cases} 0, x < 0 \\ x^2 \cdot (3 - 2x), 0 \leq x \leq 1 \\ 1, x > 1 \end{cases}$$

<div align="right">Equation 5.2.12</div>

$$\nabla \cdot \left[\tilde{k}_\alpha \cdot \left(\nabla \tilde{p} - \frac{\tilde{\gamma}_T}{\tilde{\epsilon}_T} \tilde{\mu}_T \nabla \tilde{\phi}_T - \frac{\tilde{\gamma}_E}{\tilde{\epsilon}_E} \tilde{\mu}_E \nabla \tilde{\phi}_E - \frac{\gamma_G}{\tilde{\epsilon}_G} \cdot \sum_{i \in G} \tilde{\mu}_i \nabla \tilde{\phi}_i \right) \right] = - \left(\tilde{S}_V + \tilde{S}_D + \tilde{S}_E + \tilde{S}_H + \sum_{i \in G} \tilde{S}_i \right)$$

<div align="right">Equation 5.2.13</div>

$$\tilde{\boldsymbol{u}}_\alpha = \tilde{k}_\alpha \cdot \left(\nabla \tilde{p} - \frac{\tilde{\gamma}_T}{\tilde{\epsilon}_T} \cdot \tilde{\mu}_T \nabla \tilde{\phi}_T - \frac{\tilde{\gamma}_E}{\tilde{\epsilon}_E} \cdot \mu_E \nabla \tilde{\phi}_E - \frac{\tilde{\gamma}_G}{\tilde{\epsilon}_G} \cdot \sum_{i \in G} \tilde{\mu}_i \nabla \tilde{\phi}_i \right)$$

<div align="right">Equation 5.2.14</div>

$$\nabla \cdot (D_n \nabla n) + k_{n1} n_C - (k_{n1} + k_{n2}) \cdot n = 0$$

<div align="right">Equation 5.2.15</div>

$$\nabla \cdot \left(D_{tgf} \nabla(tgf) \right) + \lambda_{tgf} - \left(\lambda_{tgf} + \lambda_{de,tgf} + \lambda_{U,tgf} \right) \cdot tgf = 0$$

<div align="right">Equation 5.2.16</div>

$$\nabla \cdot \left(D_{taf} \nabla(taf) \right) + \lambda_{taf} - \left(\lambda_{taf} + \lambda_{de,taf} + \lambda_{U,taf} \right) \cdot taf = 0$$

<div align="right">Equation 5.2.17</div>

$$\frac{\partial m}{\partial t} = \nabla \cdot (D_m \cdot \nabla m) + S_m$$

<div align="right">Equation 5.2.18</div>

$$\frac{\partial B_n^E}{\partial t} + \nabla \cdot (B_n^E u_E) = -\nabla \cdot \boldsymbol{J}_{BnE} + S_{BnE}$$

<div align="right">Equation 5.2.19</div>

$$\frac{\partial L_n^E}{\partial t} + \nabla \cdot (L_n^E u_E) = -\nabla \cdot \boldsymbol{J}_{LnE} + S_{LnE}$$

<div align="right">Equation 5.2.20</div>

where term values in Equation 5.2.1 through Equation 5.2.20 are given in **Table 38** and **Table 39**, G is the set of all simulated immune species, and $\delta_{mn} = \begin{cases} 0, m \neq n \\ 1, m = n \end{cases}$.

Table 40 summarizes the non-dimensionalization parameters used in **Table 38** and **Table 39**.

Lastly, for completeness, pre-existing blood (B_p^E) and lymphatic (L_p^E) vasculature defined per tissue volume modeled in [289, 308] as a mitotically senescent component of vasculature was assumed to not perform chemotaxis or haptotaxis, modeled using Equation 5.2.19 and Equation 5.2.20 from [82]:

$$\frac{\partial \sigma_p^E}{\partial t} + \nabla \cdot \left(\sigma_p^E u_E \right) = -\nabla \cdot \boldsymbol{J}_{\sigma pE} + S_{\sigma pE}$$

<div align="right">Equation 5.2.21</div>

$$\boldsymbol{J}_{\sigma pE} = 0$$

<div align="right">Equation 5.2.22</div>

$$S_{\sigma pE} = r_{de,\sigma pE} + r_{crush,\sigma pE}$$

<div align="right">Equation 5.2.23</div>

where all terms in Equation 3.2.21 through Equation 5.2.23 are analogously defined as their neo-vasculature counterparts in [82] for $\sigma = \{B, L\}$ and $\sigma_p = \sigma_p^E \phi_E$.

5.2.3 Simulation of Therapy

In this study, the 3D tumor model is expanded to simulate CTL exhausted from PD-L1 expression, a generic anti-PD-L1 therapeutic, PD-L1 expression, and nanoparticle-mediated effects on CTL entrance rates. New model variables are summarized in **Table 41**.

Exhausted CTL are assumed to be non-cytotoxic variants of CTL which do not move in response to chemical gradients (i.e., no chemotaxis) and are lost via apoptosis and necrosis. For this study, only monocytes (M_0), macrophages, including types M1 (M_1) and M2 (M_2), and CTL, both activated (T_C) and exhausted (T_{EC}), are simulated. Thus, $G = \{M_0, M_1, M_2, T_C, T_{EC}\}$. ϕ_G is defined as the sum of all immune cell fractions, including the exhausted volume fraction:

$$\phi_G = \sum_{i \in G} \phi_i$$

<div align="right">Equation 5.2.24</div>

Using the assumptions from [82] and [289], the following mass balance applies to exhausted CTL:

$$\frac{\partial \phi_{T_{EC}}}{\partial t} + \nabla \cdot \left(\phi_{T_{EC}} \cdot \boldsymbol{u}_\alpha\right) = M \cdot \nabla \cdot \left(\phi_{T_{EC}} \cdot \nabla \mu_{T_{EC}}\right) + S_{T_{EC}}$$

<div align="right">Equation 5.2.25</div>

$$S_{T_C} = r_{enter|T_C} - r_{exit|T_C} - r_{death|T_C} - r_{exhaust|T_C}$$

<div align="right">Equation 5.2.26</div>

$$S_{T_{EC}} = r_{exhaust|T_C} - r_{death|T_{EC}}$$

<div align="right">Equation 5.2.27</div>

$$r_{death|T_{EC}} = r_{apoptosis|T_{EC}} + r_{necrosis|T_{EC}}$$

<div align="right">Equation 5.2.28</div>

$$\mu_{T_{EC}} + \epsilon_{TG}^2 \cdot \nabla^2 \phi_T + \epsilon_{EG}^2 \cdot \nabla^2 \phi_E + \epsilon_G^2 \cdot \nabla^2 \phi_G + \sum_{l=1}^{L} \chi_{T_{EC},l} \sigma_l = 0$$

<div align="right">Equation 5.2.29</div>

where exhausted T cells have volume fraction $\phi_{T_{EC}}$, mobility M, chemical potential $\mu_{T_{EC}}$, and velocity $\boldsymbol{u}_\alpha$. Source term $S_{T_{EC}}$ comprises gain provided by CTL exhaustion ($r_{exhaust|T_C}$) and loss from apoptosis and necrosis ($r_{death|T_{EC}}$). Loss of T_C into T_{EC} is accounted for in the source term for activated CTL S_{T_C}. The chemical potential $\mu_{T_{EC}}$ is affected by interaction strengths between tumor (ϵ_{TG}^2), self and other immune species (ϵ_G^2), ECM (ϵ_{EG}^2), and each chemoattractant at concentration σ_l for $l \in \{1, \dots, L\}$

has a corresponding chemotaxis strength $\chi_{T_{EC},l}$ on T_{EC}. To simulate no chemotaxis of T_{EC}, $\chi_{T_{EC},l} = 0$. Rate term $r_{death|T_{EC}}$ is defined similarly to $r_{death|T_C}$ from [289]:

$$r_{death|T_{EC}} = r_{apoptosis|T_{EC}} + r_{necrosis|T_{EC}}$$

Equation 5.2.30

$$r_{apoptosis|T_{EC}} = \lambda_{apoptosis|T_{EC}} \cdot \mathcal{A}_{apoptosis|T_{EC}} \cdot \phi_{T_{EC}}$$

Equation 5.2.31

$$r_{necrosis|T_{EC}} = \lambda_{necrosis|T_{EC}} \cdot \mathcal{A}_{necrosis|T_{EC}} \cdot \phi_{T_{EC}}$$

Equation 5.2.32

$$\mathcal{A}_{apoptosis|T_{EC}} = 1$$

Equation 5.2.33

$$\mathcal{A}_{necrotic|T_{EC}} = 1 - \mathcal{H}\left(\frac{n}{n_{v,G}} - 1\right) \cdot \mathcal{H}\left(\frac{g}{g_{v,G}} - 1\right)$$

Equation 5.2.34

where $\mathcal{H}(x)$ is the right-continuous Heaviside function of x and the viability limits of oxygen and glucose for immune species are $n_{v,G}$ and $g_{v,G}$, respectively.

Necrosis can lead to an inflammatory environment characterized by increased leukocyte recruitment [315]. CTL can also be recruited by chemokines released from cancer cell death [316]. This effect is incorporated here by having lysing dead tumor cells (ϕ_D) release chemokines (CHE) that promote immune cell invasion. This phenomenon is incorporated into the chemokine variable che from [289] via an additional rate term:

$$\nabla \cdot (D_{che} \cdot \nabla che) + \lambda_{che} \cdot che_{sat} - (\lambda_{che} + \lambda_{de,che} + \lambda_{U,che}) \cdot che = 0$$

Equation 5.2.35

$$\lambda_{che} = \lambda_{V,che} \cdot \mathcal{A}_{V,che} + \lambda_{death,che}^V \cdot r_{L,D}$$

Equation 5.2.36

$$\mathcal{A}_{V,che} = \left(1 + \mathcal{F}_{che,n}^V \cdot \left(\frac{n_h - n}{n_h - n_{v,V}}\right) \cdot \mathcal{H}(n_h - n)\right) \cdot \frac{\phi_V}{\tilde{\phi}_\alpha}$$

Equation 5.2.37

where diffusivity, degradation, and uptake of che are D_{che}, $\lambda_{de,che}$, and $\lambda_{U,che}$, respectively, hypoxia induces raised CHE production by ϕ_V via an effective factor parameter $\mathcal{F}_{che,n}^V$, hypoxic threshold for oxygen in ϕ_V is n_h, $r_{L,D}$ is the lysis rate of ϕ_D as defined in [82], and the release rate of che by ϕ_D during lysis rate is $\lambda_{death,che}^V$.

CTL performs apoptosis when its cognate antigen is absent [168]. Thus, the rate of apoptosis is decreased in living and dead tumor tissue by modifying the adjustment factor $\mathcal{A}_{apoptosis|T_{EC}}$:

$$\mathcal{A}_{apoptosis|T_C} = 1 - \mathcal{F}_{che_{apop}|T_c} \cdot \frac{che}{che_{sat}}$$

<div align="right">Equation 5.2.38</div>

where $\mathcal{F}_{che_{apop}|T_c}$ is the effect of CHE on reducing CTL apoptosis.

CTL can enter a state of exhaustion from PD-L1 exposure and chronic T cell receptor stimulation [55, 56]. It is assumed here that PD1 is sufficiently expressed by CTL such that the outcome of the PD1-PD-L1 interaction can be inferred from PD-L1 expression. To represent exhaustion, a loss term $r_{exhaust,T_C}$ is added to the source term for CTL (S_{T_C}). The value of $r_{exhaust,T_C}$ varies in proportion to the amount of PD-L1 (P_{DL1}) that exists in the immediate vicinity of the CTL:

$$r_{exhaust,T_C} = \lambda_{exhaust|T_C} \cdot \mathcal{A}_{exhaust,T_C} \cdot \phi_{T_C}$$

<div align="right">Equation 5.2.39</div>

$$\mathcal{A}_{exhaust,T_C} = \frac{\mathcal{F}_{activation|T_C} \cdot \mathcal{A}_{I|T_C} + \mathcal{F}_{PDL1|T_C} \cdot \frac{P_{DL1}}{(P_{DL1})_{sat}}}{\mathcal{F}_{activation|T_C} + \mathcal{F}_{PDL1|T_C}}$$

<div align="right">Equation 5.2.40</div>

where $\lambda_{exahust,T_C}$ is the rate of CTL exhaustion, $P_{DL1_{sat}}$ is the saturated PD-L1 concentration, and $\mathcal{A}_{I|T_C}$ is the local activation level of T_C. For simplicity, the effect of activation is not evaluated in this study. Thus, $\mathcal{F}_{activiation|T_C} = 0$ and $\mathcal{A}_{I|\sigma} = 1$ for all $\sigma \in G$. The effect of other inhibitory receptors on CTL exhaustion, such as CTLA4 and LAG3 [56], is left to future work. Over time, proteins denature; thus, it is expected that PD-L1 has a denaturing rate. This is represented by a parameter $\lambda_{de|PDL1}$. It is assumed

that the value of $\lambda_{de|PDL1}$ is constant in the isothermal model domain and is negligibly affected by changes in TME pH.

Solid cell motility, k_α, is updated to include T_{EC} into the total immune species volume fraction ϕ_G, maintaining the form given in [289]:

$$k_\alpha = Q_3(\phi_E) \cdot (k_\alpha)_E + (1 - Q_3(\phi_E))$$
$$\cdot \left(Q_3\left(\frac{\phi_T}{\phi_C}\right) \cdot (k_\alpha)_T + \left(1 - Q_3\left(\frac{\phi_T}{\phi_C}\right)\right)\right)$$
$$\cdot \left[Q_3\left(\frac{\phi_G}{\phi_N}\right) \cdot (k_\alpha)_G + \left(1 - Q_3\left(\frac{\phi_G}{\phi_N}\right)\right) \cdot (k_\alpha)_H\right]\right)$$

Equation 5.2.41

Here, a generic drug that prevents PD-L1-induced CTL exhaustion, $D_{I_{PDL1}}$, is introduced. The following equation, adapted from [237, 291], simulates $D_{I_{PDL1}}$ extravasation into, decay within, and uptake from the domain:

$$\frac{\partial D_{I_{PDL1}}}{\partial t} = \nabla \cdot \left(D_{D_{I_{PDL1}}} \cdot \nabla D_{I_{PDL1}}\right) + \lambda_{extravasate,D_{I_{PDL1}}} \cdot \mathcal{A}_{extravasate,D_{I_{PDL1}}}$$
$$\cdot \left(\left(D_{I_{PDL1}}\right)_{sat} \cdot C_{D_{I_{PDL1}}}(t) - D_{I_{PDL1}}\right)$$
$$- \left(\lambda_{decay,D_{I_{PDL1}}} + \lambda_{uptake,D_{I_{PDL1}}}\right) \cdot D_{I_{PDL1}}$$

Equation 5.2.42

$$\lambda_{uptake,D_{I_{PDL1}}} = \lambda_{D_{I_{PDL1}},uptake,H} \cdot \frac{\phi_H}{\tilde{\phi}_\alpha} - \lambda_{D_{I_{PDL1}},uptake,V} \cdot \frac{\phi_V}{\tilde{\phi}_\alpha}$$

Equation 5.2.43

$$\mathcal{A}_{extravasate,D_{I_{PDL1}}} = \frac{B_n + B_p}{B_{max}} \cdot \left(1 - \frac{p_\alpha}{p_{t,B}}\right)$$

Equation 5.2.44

$$C_{D_{I_{PDL1}}}(t) = \begin{cases} \left(1 - e^{-\alpha_1 \cdot (t - t_i)}\right), t_i \leq t < t_f \\ \left(1 - e^{-\alpha_1(t_f - t_i)}\right) \cdot e^{-\alpha_2(t - t_f)}, t \geq t_f \end{cases}$$

Equation 5.2.45

where $C_{D_{I_{PDL1}}}(t)$ is the intravascular concentration of $D_{I_{PDL1}}$ that saturates at a concentration $\left(D_{I_{PDL1}}\right)_{sat}$ and has an initial and finishing time for drug administration at t_i and t_f, respectively, $p_{t,B}$ is the threshold of pressure corresponding to the onset of

blood vessel loss, and $D_{D_{I_{PDL1}}}$ is the diffusivity of $D_{I_{PDL1}}$. Uptake of $D_{I_{PDL1}}$ is assumed to

occur in host and viable tumor tissues at rates $\lambda_{D_{I_{PDL1}},uptake,H}$ and $\lambda_{D_{I_{PDL1}},uptake,V}$. Here,

for simplicity, drug uptake is not considered. Thus, $\lambda_{D_{I_{PDL1}},uptake,H} = \lambda_{D_{I_{PDL1}},uptake,V} =$

0. The rate of uptake by other PD-L1 species is assumed to be negligible. Drug release

behavior is adjusted by rate constants α_1 and α_2. Like in [308], $D_{D_{I_{PDL1}}}$ is computed

using region-specific diffusivities:

$$D_{D_{I_{PDL1}}} = D_{D_{I_{PDL1}},E} \cdot Q_3\left(\frac{\phi_E}{\tilde{\phi}_\alpha}\right) + D_{D_{I_{PDL1}},C} \cdot \left[1 - Q_3\left(\frac{\phi_E}{\tilde{\phi}_\alpha}\right)\right] \qquad \text{Equation 5.2.46}$$

$$D_{D_{I_{PDL1}},C} = D_{D_{I_{PDL1}},T} \cdot Q_3\left(\frac{\phi_T}{\phi_C}\right) + D_{D_{I_{PDL1}},H} \cdot \left(1 - Q_3\left(\frac{\phi_T}{\phi_C}\right)\right) \qquad \text{Equation 5.2.47}$$

where the diffusivities in tumor, ECM, and healthy regions are $D_{D_{I_{PDL1}},T}$,

$D_{D_{I_{PDL1}},E}$, and $D_{D_{I_{PDL1}},H}$, respectively, saturated solid volume fraction is $\tilde{\phi}_\alpha$, $\phi_C = \phi_T +$

ϕ_N, and $\phi_N = \phi_H + \phi_G$.

Because PD-L1 is a transmembrane ligand whose size is comparable to

chemoattractants as well as tumor angiogenic and growth factors, PD-L1 is modeled akin

to CHE, TAF (tumor angiogenic factors), and TGF (tumor growth factors) in [82, 289]:

$$\nabla \cdot \left(D_{tgf} \cdot \nabla tgf\right) + tgf_{sat} \cdot \lambda_{tgf} - \left(\lambda_{tgf} + \lambda_{de,tgf} + \lambda_{U,tgf}\right) \cdot tgf = 0 \qquad \text{Equation 5.2.48}$$

$$\lambda_{tgf} = \lambda_{V,tgf} \cdot \mathcal{A}_{V,tgf} + \lambda_{B,tgf} + \lambda_{L,tgf} + \lambda_{F,tgf} \cdot \mathcal{A}_{F,tgf} \qquad \text{Equation 5.2.49}$$

$$\lambda_{U,tgf} = \lambda_{U,V,tgf} \cdot \mathcal{A}_{U,V,tgf} \qquad \text{Equation 5.2.50}$$

where species V, B, L, and F produce TGF with rate constants $\lambda_{i,tgf}$, $\lambda_{U,tgf}$ is the

uptake of tgf by viable tumor cells, $\lambda_{de,tgf}$ is the degradation rate of tgf in the model

domain, and tgf_{sat} is the saturated concentration of tgf. Each species listed produces

tgf when conditions given by $\mathcal{A}_{i,tgf}$ for species i are met. Using the approach laid out

for tgf in [82], the PD-L1 governing quasi-steady state equation can be described as a

balance between the PD-L1 production rate (λ_{PDL1}), degradation rate ($\lambda_{de|PDL1}$), rate of

elimination by anti-PD-L1 therapy $D_{I_{PDL1}}$ ($\lambda_{D_{I_{PDL1}}}$), and effects of diffusion:

$$\nabla \cdot (D_{PDL1} \cdot \nabla P_{DL1}) + \lambda_{PDL1} \cdot (P_{DL1})_{sat} - \left(\lambda_{PDL1} + \lambda_{de|PDL1} + \lambda_{D_{I_{PDL1}}}\right) \cdot P_{DL1} = 0 \qquad \text{Equation 5.2.51}$$

where the diffusivity and saturated concentration of PD-L1 is $(P_{DL1})_{sat}$ and D_{PD1},

respectively. D_{PD1} is computed using effective diffusivity formula described in [289]:

$$D_{PDL1} = D_{PDL1,E} \cdot Q_3\left(\frac{\phi_E}{\tilde{\phi}_\alpha}\right) + D_{PDL1,C} \cdot \left[1 - Q_3\left(\frac{\phi_E}{\tilde{\phi}_\alpha}\right)\right] \qquad \text{Equation 5.2.52}$$

$$D_{PDL1,C} = D_{PDL1,T} \cdot Q_3\left(\frac{\phi_T}{\phi_C}\right) + D_{PDL1,H} \cdot \left(1 - Q_3\left(\frac{\phi_T}{\phi_C}\right)\right) \qquad \text{Equation 5.2.53}$$

where the diffusivity of D_{PD1} in ECM, tumor, immune, and host regions is

$D_{PDL1,E}$, $D_{PDL1,T}$, and $D_{PDL1,H}$, respectively. Because PD-L1 can be expressed by tumor

cells, myofibroblasts, and tumor-associated macrophages, the diffusivity through ECM

and healthy tissue will be zero, leaving PD-L1 to diffuse through the tumor phase of the

mixture model and maintain localized expression by immune species and myofibroblasts

[51, 300, 317]. Thus, $D_{PDL1,E} = D_{PDL1,H} = 0$.

PD-L1 expression by tumor-associated macrophages and hepatic myofibroblasts

increases *in vitro* when in contact with PDAC [53] and PDAC-LM [52], respectively.

MDSC have been shown to express PD-L1 and this aspect will be considered in future

work [300]. Thus:

$$\lambda_{PDL1} = \sum_{i \in \{V,F,M_1,M_2\}} \lambda_{i|PDL1} \cdot \mathcal{A}_{i|PDL1} \qquad \text{Equation 5.2.54}$$

$$\mathcal{A}_{V|PDL1} = \frac{\phi_V}{\tilde{\phi}_\alpha} \qquad \text{Equation 5.2.55}$$

$$\mathcal{A}_{M_1|PDL1} = \mathcal{A}_{I|M_1} \cdot Q_3\left(\frac{\phi_{M_1}}{\phi_{M_1,sat}}\right) \cdot \left(1 + \mathcal{F}_{PDL1,T|M_1} \cdot Q_3\left(\frac{\phi_T}{\phi_{M_1,T,sat}}\right)\right) \qquad \text{Equation 5.2.56}$$

$$\mathcal{A}_{M_2|PDL1} = \mathcal{A}_{I|M_2} \cdot Q_3\left(\frac{\phi_{M_2}}{\phi_{M_2,sat}}\right) \cdot \left(1 + \mathcal{F}_{PDL1,T|M_2} \cdot Q_3\left(\frac{\phi_T}{\phi_{M_2,T,sat}}\right)\right) \qquad \text{Equation 5.2.57}$$

$$\mathcal{A}_{F|PDL1} = \frac{F}{F_{max}} \cdot \left(1 + \mathcal{F}_{PDL1,T|F} \cdot Q_3\left(\frac{\phi_T}{\phi_{F,T,sat}}\right)\right) \qquad \text{Equation 5.2.58}$$

$$\lambda_{D_{I_{PDL1}}} = \lambda_{PDL1|D_{I_{PDL1}},PDL1} \cdot \frac{D_{I_{PDL1}}}{\left(D_{I_{PDL1}}\right)_{sat}} \qquad \text{Equation 5.2.59}$$

where rate of PD-L1 expression for species σ is $\lambda_{\sigma|PDL1}$, saturation concentration for myofibroblasts F is F_{max}, immune-immune and immune-tumor interactions for species τ are saturated at $\phi_{\tau,T,sat}$, and $\mathcal{F}_{PDL1,T|\tau}$ is the dimensionless factor for PD-L1 upregulation of species τ due to tumor tissue. Here, the saturation constant ϕ_{GG} from [289] is updated to species-specific saturation constants, $\phi_{\tau,sat}$ for any immune species τ, which is set to the value of ϕ_{GG} given in [308] by default. Finally, $\lambda_{D_{I_{PDL1}}}$ is proportional to local drug concentration $D_{I_{PDL1}}$ and a rate constant $\lambda_{PDL1|D_{I_{PDL1}},PDL1}$.

Like the model presented in [57, 59, 60, 318], it is assumed that tumor angiogenic factors are released by hypoxic tumor tissue. The equation in [82] is updated accordingly:

$$\mathcal{A}_{V,taf} = \frac{\phi_V}{\phi_\alpha} \cdot \left(\mathcal{F}_{taf}^V + \mathcal{F}_{n,taf}^V \cdot \frac{n_h - n}{n_h - n_{v,V}} \cdot \mathcal{H}\left(\frac{n_h - n}{n_h - n_{v,V}}\right)\right) \qquad \text{Equation 5.2.60}$$

where the hypoxic and viable tumor tissue thresholds of oxygen are n_h and $n_{v,V}$, respectively, $\mathcal{F}_{taf}^V$ is a nondimensional factor that describes the nominal level of TAF production by viable tumor tissue, and $\mathcal{F}_{n,taf}^V$ is a nondimensional factor for viable tumor tissue upregulation of TAF production in hypoxic conditions.

Like the macrophage model in [65], immune species are assumed to extravasate from blood vasculature in the presence of TAF. Thus, the entrance rate for all immune species $\sigma \in G, \sigma \neq T_C$ is updated:

$$\mathcal{A}_{enter|\sigma} = \left(\mathcal{F}_B^G + \mathcal{F}_B^{taf} \cdot \frac{taf}{taf_{sat}}\right) \cdot \left(1 - \frac{\phi_\sigma}{\tilde{\phi}_\alpha}\right) \cdot \left(1 - \frac{p_\alpha}{p_{t,B}}\right)$$

Equation 5.2.61

where the nominal rate of extravasation is set by dimensionless factor $\mathcal{F}_B^G$, the increase due to TAF expression is $\mathcal{F}_B^{taf}$, volume fraction for immune species σ is ϕ_σ, and extravasation is halted when solid pressure p_α exceeds the blood capillary pressure $p_{t,B}$.

The effects of peripheral dendritic cells due to antigen-CNP on T cell activation are incorporated into the entrance rate of CTL into the tumor domain:

$$r_{enter|T_c} = \lambda_{enter|T_C} \cdot \mathcal{A}_{enter|T_C} \cdot \tilde{\phi}_\alpha$$

Equation 5.2.62

$$\mathcal{A}_{enter|T_C} = \left(\mathcal{F}_B^G + \mathcal{F}_B^{taf} \cdot \frac{taf}{taf_{sat}}\right) \cdot \left(1 - \frac{\phi_\sigma}{\tilde{\phi}_\alpha}\right) \cdot Q_3 \left(1 - \frac{p_\alpha}{p_{t,B}}\right)$$
$$\cdot \left(1 + \mathcal{F}_{enter|T_C}^{D_{NP}} \cdot D_{NP,T_C}(t)\right)$$

Equation 5.2.63

$$D_{NP,T_C}(t) = \left(1 - e^{-\gamma_1 \cdot \left(t - t_{i,D_{NP}}\right)}\right) \cdot e^{-\gamma_2 \left(t - t_{i,D_{NP}}\right)}, t \geq t_{i,D_{NP}}$$

Equation 5.2.64

where the effect of antigen-CNP on CTL entrance rate begins at $t_{i,D_{NP}}$, has

maximum effect on CTL entrance $\mathcal{F}^{D_{NP}}_{enter|T_C}$, and decays as governed by rate constants γ_1

and γ_2.

The myofibroblast mitotic rate equation from [82] was modeled using equations

Equation 5.2.65 and Equation 5.2.66:

$$r_{M,FE} = \lambda_{M,FE} \cdot \mathcal{A}_{M,FE} \cdot F_E$$

<div align="right">Equation 5.2.65</div>

$$\mathcal{A}_{M,FE} = (1 - F_E) \cdot Q_3 \left(\frac{n - n_h}{n_\infty - n_h} \right) \cdot \left(1 + \mathcal{F}^M_{tgf,F} \cdot \frac{tgf}{tgf_{sat}} \cdot \mathcal{H}(tgf - tgf_{FE}) \right)$$

<div align="right">Equation 5.2.66</div>

where $\mathcal{F}^M_{tgf,F}$ is the dimensionless factor of myofibroblast upregulation due to

TGF, n_∞ is the concentration of oxygen at the model domain's borders, and tgf_{FE} is the

trigger threshold for TGF-induced mitotic upregulation of myofibroblasts. Here, the

definition of $\mathcal{A}_{M,FE}$ is updated to use a myofibroblast-specific hypoxic threshold $n_{h,F}$:

$$\mathcal{A}_{M,FE} = (1 - F_E) \cdot Q_3 \left(\frac{n - n_{h,F}}{n_\infty - n_{h,F}} \right)$$
$$\cdot \left(1 + \mathcal{F}^M_{tgf,F} \cdot \frac{tgf}{tgf_{sat}} \cdot \mathcal{H}(tgf - tgf_{FE}) \right)$$

<div align="right">Equation 5.2.67</div>

Finally, the ECM source term in [289] is updated to increase ECM deposition by

myofibroblasts in tumor tissue regions:

$$S_E = \sum_{\tau \in T} r_{\tau|E}$$

<div align="right">Equation 5.2.68</div>

$$r_{\tau|E} = \lambda_{\tau|E} \cdot \mathcal{A}_{\tau|E} \cdot \tau$$

<div align="right">Equation 5.2.69</div>

$$\mathcal{A}_{i|E} = \left(1 - \frac{\phi_E}{\tilde{\phi}_\alpha}\right) \cdot \mathcal{H}\left(1 - \frac{\phi_E}{\tilde{\phi}_\alpha}\right) \cdot \left(1 + \frac{tgf}{tgf_{sat}}\right)$$
$$\cdot \left(1 + \mathcal{F}_{n,E}^i \cdot \frac{n_h - n}{n_h - n_{v,F}} \cdot \mathcal{H}(n_h - n)\right) \cdot \mathcal{H}(n - n_{v,F}), i$$
$$\in \mathcal{R} \; \& \; i \neq F$$

<div align="right">Equation 5.2.70</div>

$$\mathcal{A}_{F|E} = \left(1 - \frac{\phi_E}{\tilde{\phi}_\alpha}\right) \cdot \mathcal{H}\left(1 - \frac{\phi_E}{\tilde{\phi}_\alpha}\right) \cdot \left(1 + \mathcal{F}_{F_E,tgf} \cdot \frac{tgf}{tgf_{sat}}\right)$$
$$\cdot \left(1 + \mathcal{F}_{n,E}^F \cdot \frac{n_h - n}{n_h - n_{v,F}} \cdot \mathcal{H}(n_h - n)\right)$$
$$\cdot \left(1 + \mathcal{F}_{F_E}^{T_{H2}} \cdot \mathcal{A}_{I|T_{H2}} \cdot Q_3\left(\frac{\phi_{T_{H2}}}{\phi_{T2.sat}}\right)\right) \cdot \mathcal{H}(tgf - tgf_{FE,E})$$
$$\cdot \mathcal{H}(n - n_{v,F})$$

<div align="right">Equation 5.2.71</div>

where $\mathcal{R} = \{B, L, F\}$, $B \equiv B_p + B_n$, $L \equiv L_p + L_n$, n_h is the hypoxic threshold of

oxygen, $n_{v,i}$ is the oxygen viability threshold for species i, $\mathcal{F}_{n,E}^\tau$ is the effective constant

for the increase in ECM secretion by species τ in response to hypoxia, $\mathcal{F}_{F_E,tgf}$ and $\mathcal{F}_{F_E}^{T_{H2}}$

are the effective factors of ECM secretion upregulation in myofibroblasts due to TGF and

type 2 helper T-cells, respectively, and $tgf_{FE,E}$ is the minimum concentration of tgf

required to promote ECM production. The contribution of helper T-cells in PDAC is left

for future work.

5.2.4 Model Non-dimensionalization

Non-dimensionalization of $\phi_{T_{EC}}$ and $\mu_{T_{EC}}$ follows the same approach given in [82],

where the scaling parameters used for non-dimensionalization are listed across **Table 38**

through **Table 43**. Nondimensionalization of diffusivities $D_{D_{I_{PDL1}}}$ and D_{PDL1} is performed

as described in [82]. The non-dimensionalized form for equations Equation 5.2.42

through Equation 5.2.45 is as shown in Equation 5.2.72 through Equation 5.2.75:

$$\frac{\partial \widetilde{D}_{I_{PDL1}}}{\partial t} = \nabla \cdot \left(\widetilde{D}_{D_{I_{PDL1}}} \cdot \nabla \widetilde{D}_{I_{PDL1}} \right) + \tilde{\lambda}_{extravasate,D_{I_{PDL1}}} \cdot \widetilde{\mathcal{A}_{extravasate,D_{I_{PDL1}}}}$$
$$\cdot \left(\widetilde{C_{D_{I_{PDL1}}}}(t) - \widetilde{D_{I_{PDL1}}} \right) - \left(\tilde{\lambda}_{decay,D_{I_{PDL1}}} + \tilde{\lambda}_{uptake,D_{I_{PDL1}}} \right)$$
$$\cdot \widetilde{D_{I_{PDL1}}}$$

<div align="right">Equation 5.2.72</div>

$$\tilde{\lambda}_{uptake,D_{I_{PDL1}}} = \tilde{\lambda}_{D_{I_{PDL1}},uptake,H} \cdot \tilde{\phi}_H - \tilde{\lambda}_{D_{I_{PDL1}},uptake,V} \cdot \tilde{\phi}_V$$

<div align="right">Equation 5.2.73</div>

$$\mathcal{A}_{extravasate,D_{I_{PDL1}}} = \frac{\widetilde{B_n} + \widetilde{B_p}}{\widetilde{B_{max}}} \cdot \left(1 - \frac{\widetilde{p_\alpha}}{\widetilde{p_{t,B}}} \right)$$

<div align="right">Equation 5.2.74</div>

$$\tilde{C}_{D_{I_{PDL1}}}(t) = \begin{cases} \left(1 - e^{-\widetilde{\alpha_1} \cdot (\tilde{t} - \tilde{t}_i)} \right), \tilde{t}_i \leq \tilde{t} < \tilde{t}_f \\ \left(1 - e^{-\widetilde{\alpha_1}(\tilde{t}_f - \tilde{t}_i)} \right) \cdot e^{-\widetilde{\alpha_2}(\tilde{t} - \tilde{t}_f)}, \tilde{t} \geq \tilde{t}_f \end{cases}$$

<div align="right">Equation 5.2.75</div>

where non-dimensionalization of any variable $\mathcal{V}$ is $\tilde{\mathcal{V}}$. Non-dimensionalization for P_{DL1}

for Equation 5.2.51 is performed akin to non-dimensionalization of TGF in [82] using

non-dimensionalized factor $(P_{DL1})_{sat}$. Non-dimensionalization of Equation 5.2.54

through Equation 5.2.59 is given across Equation 5.2.76 through Equation 5.2.80:

$$\mathcal{A}_{V|PDL1} = \tilde{\phi}_V$$

<div align="right">Equation 5.2.76</div>

$$\mathcal{A}_{M_1|PDL1} = \tilde{\mathcal{A}}_{I|M_1} \cdot Q_3 \left(\frac{\tilde{\phi}_{M_1}}{\tilde{\phi}_{M_1,sat}} \right) \cdot \left(1 + \mathcal{F}_{PDL1,T|M_1} \cdot Q_3 \left(\frac{\tilde{\phi}_T}{\tilde{\phi}_{M_1,T,sat}} \right) \right)$$

<div align="right">Equation 5.2.77</div>

$$\mathcal{A}_{M_2|PDL1} = \tilde{\mathcal{A}}_{I|M_2} \cdot Q_3 \left(\frac{\tilde{\phi}_{M_2}}{\tilde{\phi}_{M_2,sat}} \right) \cdot \left(1 + \mathcal{F}_{PDL1,T|M_2} \cdot Q_3 \left(\frac{\tilde{\phi}_T}{\tilde{\phi}_{M_2,T,sat}} \right) \right)$$

<div align="right">Equation 5.2.78</div>

$$\mathcal{A}_{F|PDL1} = \tilde{F} \cdot \left(1 + \mathcal{F}_{PDL1,T|F} \cdot Q_3 \left(\frac{\tilde{\phi}_T}{\tilde{\phi}_{F,T,sat}} \right) \right)$$

<div align="right">Equation 5.2.79</div>

$$\lambda_{D_{I_{PDL1}}} = \tilde{\lambda}_{PDL1|D_{I_{PDL1}},PDL1} \cdot \widetilde{D}_{I_{PDL1}}$$

<div align="right">Equation 5.2.80</div>

Equation 5.2.62 through Equation 5.2.64 are non-dimensionalized as shown in

equations Equation 5.2.81 through Equation 5.2.83:

$$\tilde{r}_{enter|T_c} = \tilde{\lambda}_{enter|T_C} \cdot \mathcal{A}_{enter|T_C}$$

<div align="right">Equation 5.2.81</div>

$$\mathcal{A}_{enter|T_C} = \left(\mathcal{F}_B^G + \mathcal{F}_B^{taf} \cdot \widetilde{taf}\right) \cdot (1 - \tilde{\phi}_\sigma) \cdot Q_3 \left(1 - \frac{\tilde{p}_\alpha}{\tilde{p}_{t,B}}\right)$$
$$\cdot \left(1 + \mathcal{F}_{enter|T_C}^{DNP} \cdot \widetilde{D_{NP,T_C}}(\tilde{t})\right)$$

Equation 5.2.82

$$\widetilde{D}_{NP,T_C}(\tilde{t}) = \left(1 - e^{-\tilde{\gamma}_1 \cdot \left(\tilde{t} - \tilde{t}_{i,D_{NP}}\right)}\right) \cdot e^{-\tilde{\gamma}_2 \cdot \left(\tilde{t} - \tilde{t}_{i,D_{NP}}\right)}, \tilde{t} \geq \tilde{t}_{i,D_{NP}}$$

Equation 5.2.83

where times t and $t_{i,D_{NP}}$ are non-dimensionalized using the non-dimensionalization time factor $\mathcal{T}$. Finally, dimensionless adjustment factors $\mathcal{A}_{enter|\sigma}$ for $\sigma \in G$, $\mathcal{A}_{M,FE}$, $\mathcal{A}_{V,taf}$, and $\mathcal{A}_{F|E}$ are trivially non-dimensionalized from prior forms given across [82, 289] using non-dimensionalization factors listed across **Table 38** through **Table 43**.

5.2.5 Boundary Conditions

Dirichlet and Neumann boundary conditions hold for the non-dimensionalized volume fraction and chemical potential of exhausted CTL, as well as PD-L1 and anti-PD-L1 drug concentrations:

$$\mathbf{n} \cdot \nabla \tilde{\phi}_{T_{EC}} = \tilde{\mu}_{T_{EC}} = \widetilde{P_{DL1}} = \mathbf{n} \cdot \nabla \widetilde{D}_{I_{PDL1}} = 0$$

Equation 5.2.84

where $\mathbf{n}$ is the outward normal of the boundary.

5.2.6 Model Discretization

Discretization of Equation 5.2.21, Equation 5.2.25, Equation 5.2.29, and Equation 5.2.51 followed the discretization performed for vasculature, volume fractions, chemical potential, and TGF, respectively [83, 289]. Following the methods in [308], discretization of $\widetilde{D}_{I_{PDL1}}$ was performed in time using the Crank-Nicholson method and in space using the operators defined in [83]. Drug distribution and effect, tumor growth, nutrient

metabolite production, and immune species interactions were simulated in parallel using coupled differential equations and solved using a Multigrid algorithm as described in [83, 147, 181]. From here onwards, accents indicating non-dimensionalized terms are omitted for readability.

5.3 Results

5.3.1 Primary and Metastatic PDAC Tumors

Representative pictures of primary and metastatic human PDAC tumors (**Figure 27** and **Figure 28**, respectively) show that PD-L1 was mostly located at tumor rim. Similarly, T cells, especially CD8+ T cells as well as tumor associated macrophages (CD163+ M2-like phenotype) were detected at rim (**Figure 27**). Myofibroblasts (αSMA+) were equally distributed between primary core and rim, while myofibroblast presence was accompanied by high collagen expression. CD8+ T cells and CD163+ tumor-associated macrophages were also predominantly located at the rim of the metastases (**Figure 28**). In contrast, myofibroblasts and collagen were detected at both metastatic core and rim. Overall, PD-L1 expression was associated with CD8+ T cells, tumor-associated macrophages and myofibroblasts, with the latter accompanied by high collagen expression.
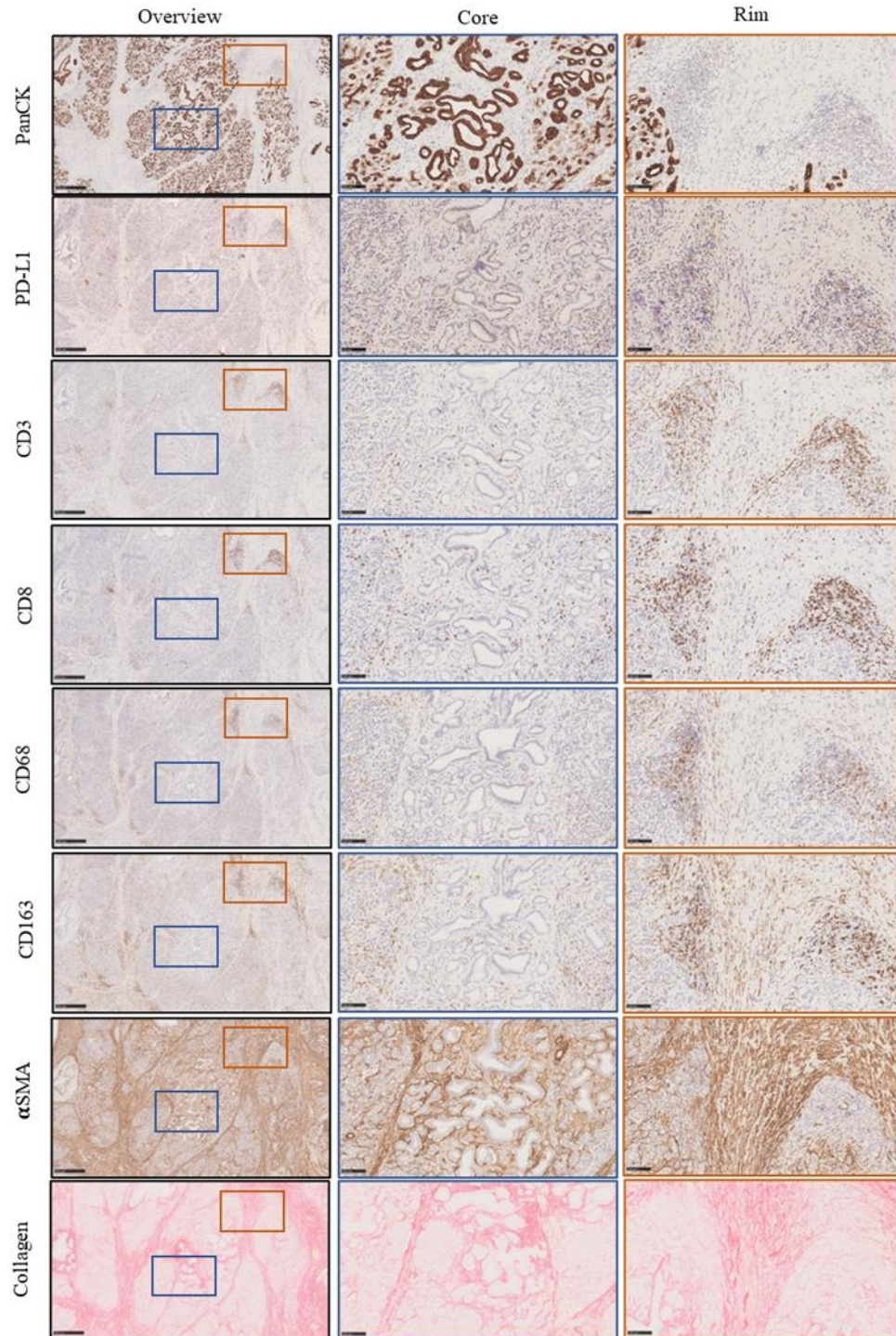
Figure 27 Spatial expression of Programmed Cell Death Ligand 1 (PD-L1) is associated with the presence of CD8+ T cells, tumor-associated macrophages and myofibroblasts, accompanied by high collagen occurrence, in a primary tumor of a

PDAC patient. Representative immunohistochemical staining for Pan-Cytokeratin (PanCK), PD-L1, Cluster of Differentiation (CD) 3, CD8, CD68, CD163, alpha-Smooth Muscle actin (αSMA) and Collagen in a primary tumor of PDAC. Left: Overview of primary tumor within a Field of view (FoV) in the tumor core (blue rectangle) and a FoV of tumor rim (orange rectangle) (scale bar = 500 μm). Middle: zoomed-in picture of the tumor core. Right: zoomed-in picture of the tumor rim. pictures of tumor center and invasion front. Scale bar = 100 μm for middle and right.
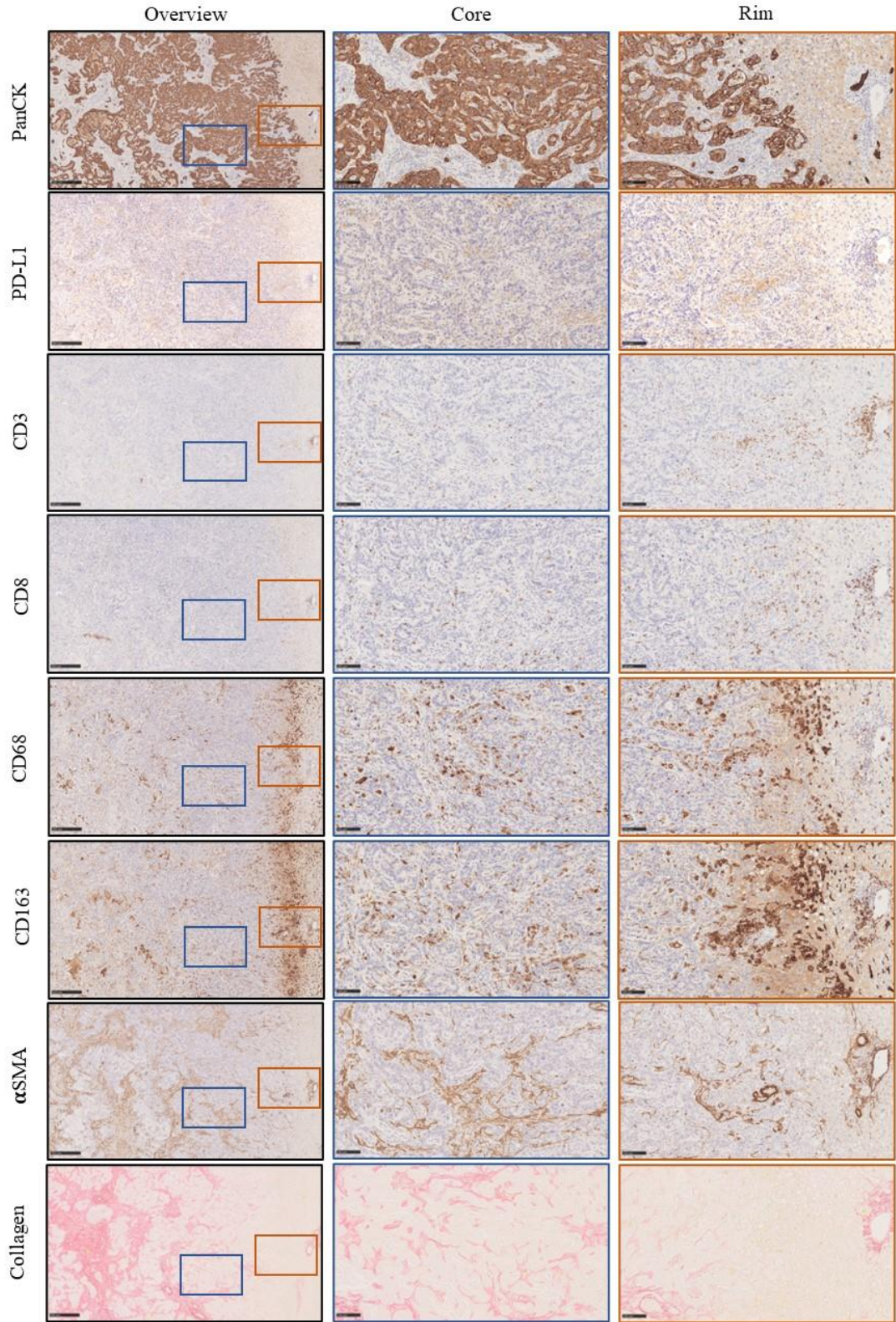
Figure 28 Spatial expression of PD-L1 is associated with the presence of CD8+ T cells, tumor-associated macrophages and myofibroblasts, accompanied by high collagen occurrence in a liver metastasis of a PDAC patient. Representative immunohistochemical staining for Pan-Cytokeratin (PanCK), PD-L1, Cluster of Differentiation (CD) 3, CD8, CD68, CD163, alpha-Smooth Muscle actin (αSMA) and Collagen in a corresponding liver metastasis of the PDAC patient. Left: Overview picture of the liver metastasis within a Field of view (FoV) in the tumor core (blue rectangle) and a FoV of the tumor rim (orange rectangle) (scale bar = 500 μm). Middle: zoomed-in picture of the tumor core. Right: zoomed-in picture of the tumor rim. pictures of tumor center and invasion front. Scale bar = 100 μm for middle and right.

5.3.2 Calibration of Antigen-CNP Therapy

The 3D model was first calibrated to match characteristics of antigen-CNP therapy. CTL concentration in response to antigen-CNP priming the antigen presenting cells (APC) (DCs or macrophages), which in turn activate the CTL, was calibrated to be ~3x higher after 3 days based on *in vitro* data from [307], assuming the model antigen has similar properties as SIINFEK (**Figure 29A**). Nominal CTL level was set to the concentration from primary PDAC observations in Kiryu et al. [319] and naïve T cell diameter from [241]. Vasculature was set to the initial condition used for PDAC in **Table 44.** Peak T cell concentration was calibrated to roughly 4.25 days, a value that is consistent with weak ligand activation of CTL which was measured at a peak between 4 and 5 days [320]. It is noted that stronger ligand binding leads to a delayed decrease in CTL response and, by extension, protracted elevated CTL concentration. Hence, this

analysis that considers a weak ligand activation curve evaluates a lower bound for CNP efficacy *in vivo*. To calibrate to cytotoxicity range seen in Walter et al. [307], a 200 μm diameter avascular tumor with $\phi_V = 0.1875$ in a 533.3 x 533.3 x 533.3 μm³ domain was measured after 24 hours of exposure to either (1) nominal CTL concentration or (2) antigen-CNP CTL concentration measured at 72 hours. To emulate *in vitro* conditions, an avascular tumor was simulated to proliferate without hypoxia (oxygen (n) = 0.85). Loss of activated CTL was simulated via apoptosis and exhaustion through tumor PD-L1 expression. Consistent with observations from [307], the tumor tissue was 50%-60% of untreated case after 1 day of exposure to CTL regardless of PD-L1 expression (**Figure 29B**).
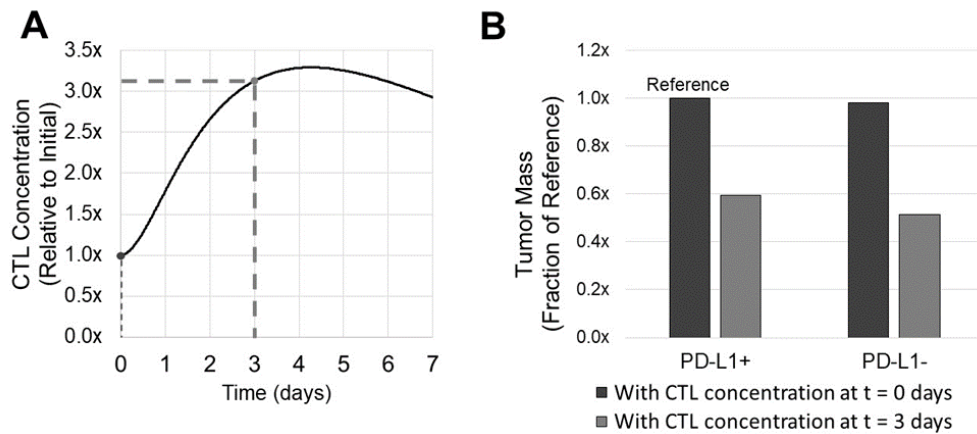
Figure 29 Calibration of antigen-CNP therapy assuming similar properties to SIINFEKL-CNP. (A) Relative to initial CTL concentration (time=0), antigen-CNP treatment increased CTL concentration to 3.1x after 3 days, consistent with in vitro observations [307]. CTL concentration peaked at 3.3x initial concentration at ~4.3 days.

(B) CTL concentration after 3 days of antigen-CNP treatment limited avascular tumor

mass to <60% of untreated case within 24 hours regardless of PD-L1 expression.

5.3.3 Calibration of anti-PD-L1 Therapy

PD-L1 expression rates were calibrated to *in vitro* tumor, macrophage, and

myofibroblast data by choosing $\phi_{M1} = \phi_{M2} = 0.03$, $\phi_V = 0.1875$, and $F = 0.2$.

Calibration was based on macrophage and hepatic myofibroblast PD-L1 expression

observed across [52, 53] and is summarized in **Table 45**. Efficacy of anti-PD-L1 drug at

peak bolus concentration was calibrated to hold PD-L1 expression at 1% saturation

concentration within a 200 μm diameter homogenous avascular tumor with $\phi_V =$

0.1875. Vasculature was set to the initial condition used for PDAC in **Table 44**. Drug

half-life was calibrated to match durvalumab's reported geometric-mean half-life of 17-

to 18-days [321, 322]. However, it is noted that the terminal half-life has been reported at

21 days [323].

5.3.4 Simulation of PDAC and PDAC-LM

To simulate primary PDAC at the centimeter-scale, domain size was set to 1.7067

x 1.7067 x 1.7067 cm^3. The *in silico* PDAC was shaped according to imaging

observations in Mahmoudi et al. [324], with initial conditions chosen and parameters

calibrated to meet *in vivo* stromal [325], macrophage [326, 327], and CTL [241, 319]

densities in PDAC assuming that both active and exhausted species contribute to T-cell

measurements in Kiryu et al. [319]. PDAC lesion was hypoxic, which is consistent with

sparse vascularization observed in Olive et al. [328]. Macrophage M1:M2 ratio was set to

1:1.5 as reported in Kurahara et al. [326]. Maximum apoptotic rates for CTL and macrophages were set to 0.15 day^{-1} based on the T cell model used in Curtis et al. [67], a value consistent with apoptosis rates for T cells in certain infections [329, 330]. It was assumed that the maximum apoptotic rate applied to both exhausted and non-exhausted CTL. Consistent with [51-53], PD-L1 expression by myofibroblasts and macrophages was elevated in tumor tissue. The initial condition and time selected for therapeutic administration (t = 3 days) are visualized in **Figure 30**, growing from 1.04 cm length on the i-axis to 1.06 cm over the course of 3 days.

Untreated

T = 0 Days   T = 3 Days

A

B
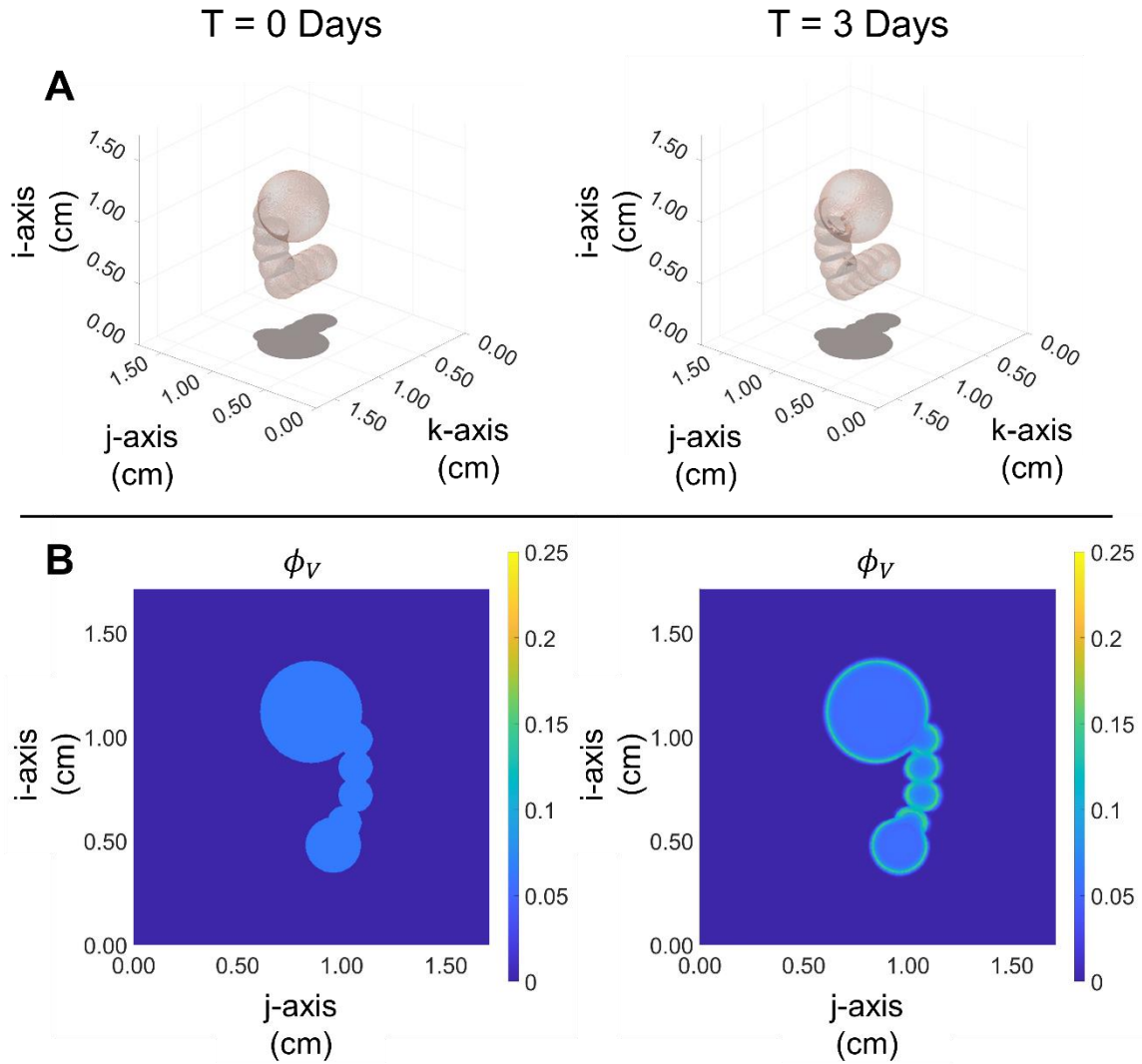
Figure 30 Simulation of primary PDAC with the 3D model. Viable tumor tissue (ϕ_V) is visualized from (A) oblique view and (B) side view at k = 0.852 cm. Growth is shown from initial condition (t = 0) and at (t = 3 days) when therapies were applied. Tumor tissue in (A) is defined as $\phi_V \geq 0.05$.

To simulate liver metastatic growth, PDAC-LM was grown from a 66.67 x 66.67 x 66.67 µm³ seed that reached an 827 µm diameter after 14 days in a 0.4267 x 0.4267 x

0.4267 cm^3 domain (**Figure 31**). Initial conditions for primary PDAC and PDAC-LM are given in **Table 44**. PDAC-LM was roughly spherical after 14 days of growth (matching clinical imaging [331]), was primarily hypoxic [332] and exhibited a replacement growth type hallmarked by negligible angiogenesis and normal stroma concentration [297]. The M1:M2 ratio was set to 1:1.8 as seen in breast cancer liver metastases [59]. Macrophage and T cell prevalence within the PDAC-LM mass was calibrated to fall within ranges reported in Daunke et al. [53], colorectal cancer liver metastases *in vivo* [333] using T-cell diameter from [241], and in breast cancer liver metastases *in vitro* [57]. PD-L1 was assumed to be consistently expressed in both PDAC and PDAC-LM [53]; thus, PD-L1 calibration from PDAC was used in PDAC-LM. Calibration of novel model parameters and parameters changed from [289, 308] are given in **Table 42** and **Table 43**, respectively. Simulation parameters changed for multigrid solver are given in **Table 46**.
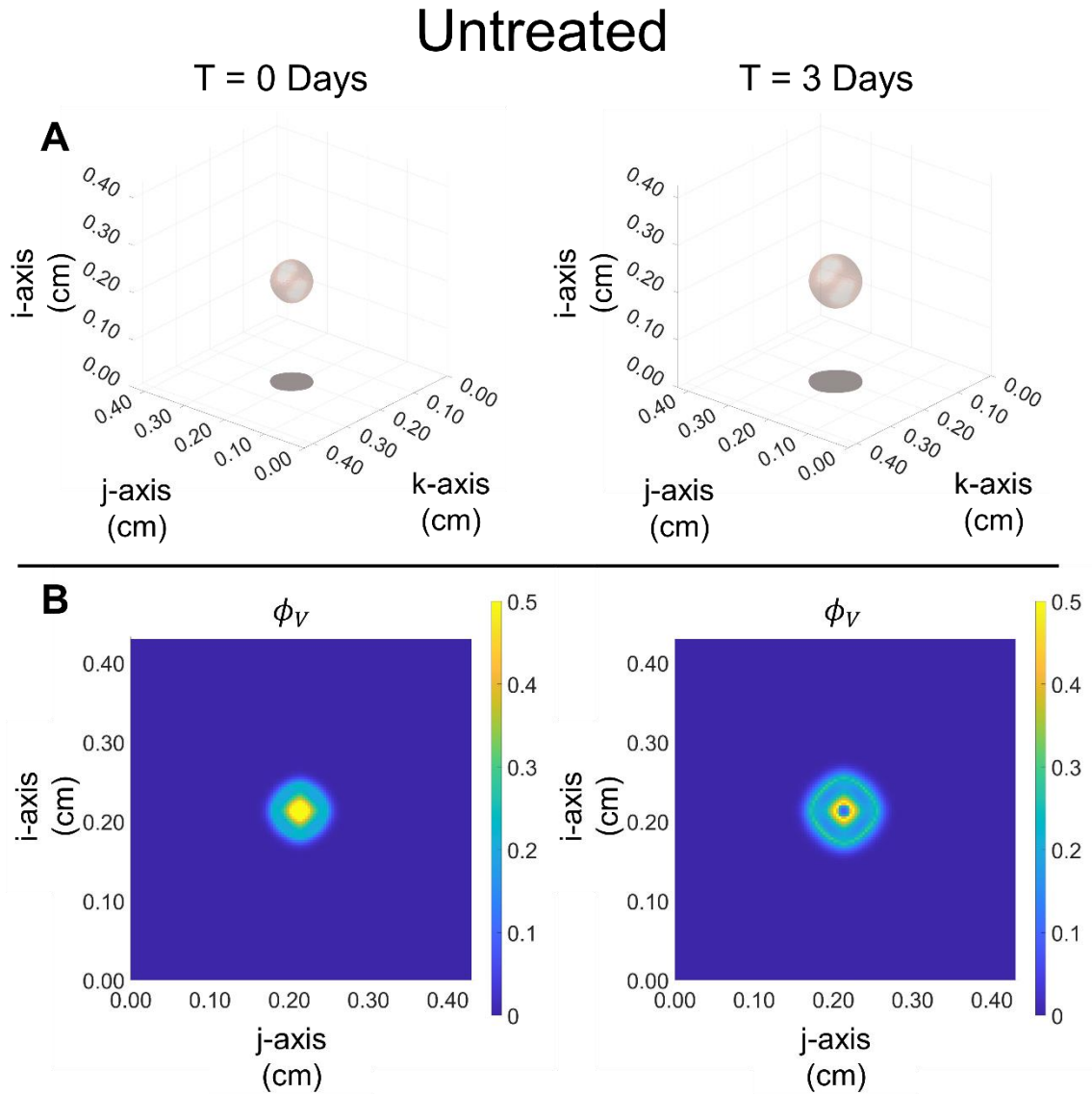
Figure 31 Simulation of PDAC-LM with the 3D model. Viable tumor tissue (ϕ_V) is visualized from (**A**) oblique view and (**B**) side view at k = 0.212 cm. Growth is shown from 0 and 3 days after the start of the treatment. Tumor tissue in (**A**) is defined as $\phi_V \geq$ 0.05.

5.3.5 Simulation of Therapeutic Effect

To quantify the efficacy of combination therapy of antigen-CNP and anti-PD-L1 approaches on systemic tumor load, PDAC and PDAC-LM were subjected to either the anti-PD-L1 therapeutic, SIINFEKL-CNP, or both simultaneously (Anti-PD-L1+antigen-CNP). Each treatment case was compared to a control (untreated) case. Preceding each treatment case, PDAC and PDAC-LM were grown from initial conditions for 3 and 14 days, respectively. PDAC and PDAC-LM tumor burden were measured across 10 days for each case. The tumor burden of PDAC and PDAC-LM in each therapeutic regimen is shown in **Figure 32A** and **Figure 32B**, respectively.
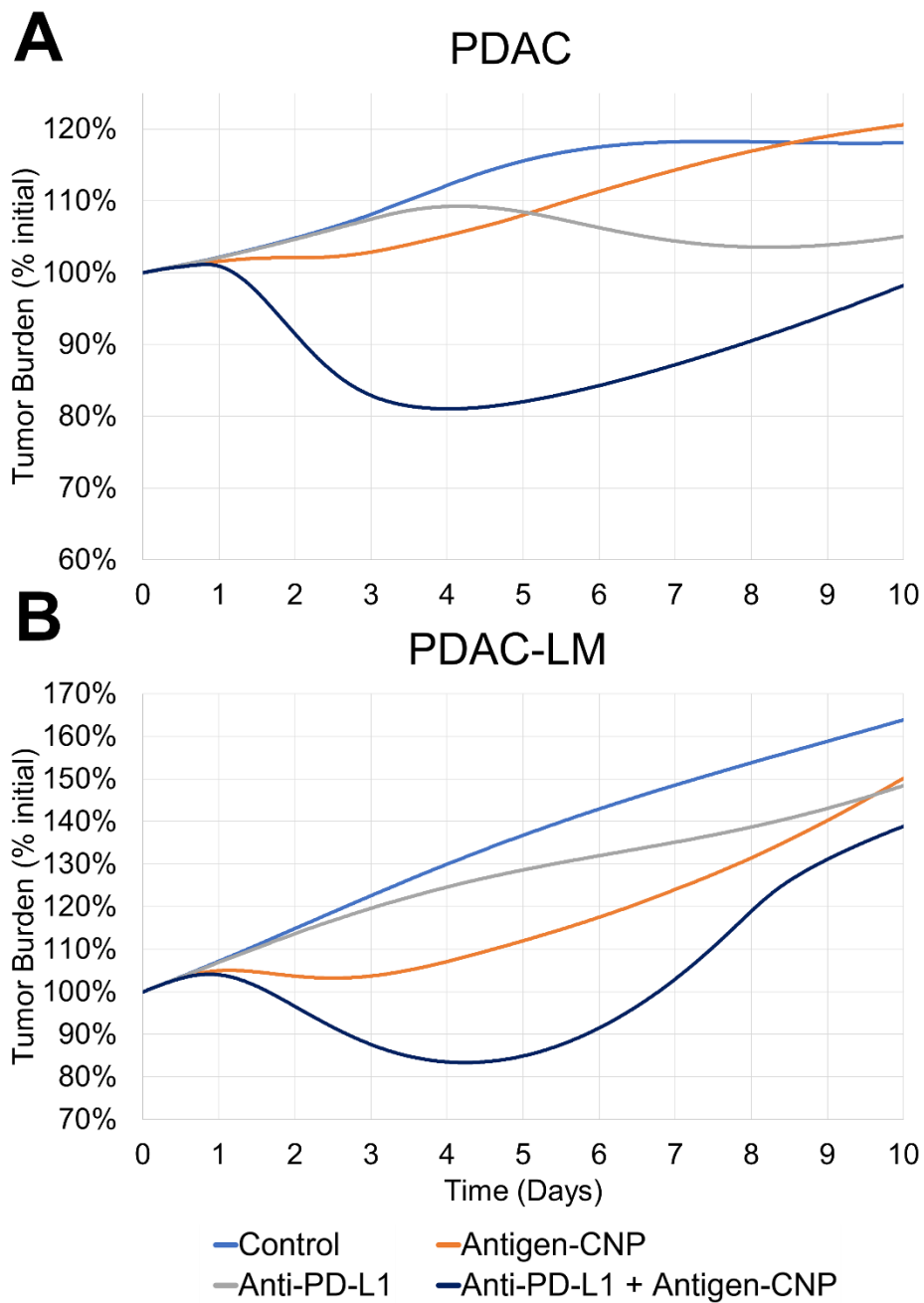
Figure 32 Response of PDAC (A) and PDAC-LM (B) to antigen-CNP and anti-PD-L1 therapies. Tumor radius is shown as percent of initial size at start of treatment (t = 0) as a function of treatment regimen (anti-PD-L1, antigen-CNP, or both applied simultaneously). 'Control' cases are untreated. Simultaneous application of anti-PD-L1

and antigen-CNP therapeutics yielded a synergistic effect in both primary and liver metastatic lesions.

In the control case, tumor burden of both PDAC and PDAC-LM increased over the course of 10 days to 118% and 164% of initial burden, respectively. Individually, anti-PD-L1 and antigen-CNP therapeutics were unable to decrease tumor burden beyond initial conditions for both primary and metastatic cases. In primary PDAC, antigen-CNP treatment was roughly equivalent to control, increasing tumor burden by 121% over 10 days, whereas the anti-PD-L1 therapy limited tumor growth to 105% initial. Similarly, tumor burden for antigen-CNP and anti-PD-L1 therapies for PDAC-LM was 150% and 148%, respectively. This result is consistent with ineffective durvalumab treatment observations *in vitro* [52, 53] against PDAC cell lines and in clinical trials with metastatic PDAC patients [24]. However, when applied simultaneously, tumor response improved in both cases: tumor burden of PDAC and PDAC-LM was minimized to 81.0% after 4.0 days and 83.4% after 4.2 days, respectively, indicating that anti-PD-L1 and antigen-CNP therapeutics exhibited a synergistic effect against primary and metastatic PDAC. **Figure 33** and **Figure 34** visualize treatment responses of PDAC and PDAC-LM, respectively, to anti-PD-L1 treatment + antigen-CNP after 1 and 3 days, indicating that increased CTL presence coupled with PD-L1 suppression decreased the overall tumor burden.
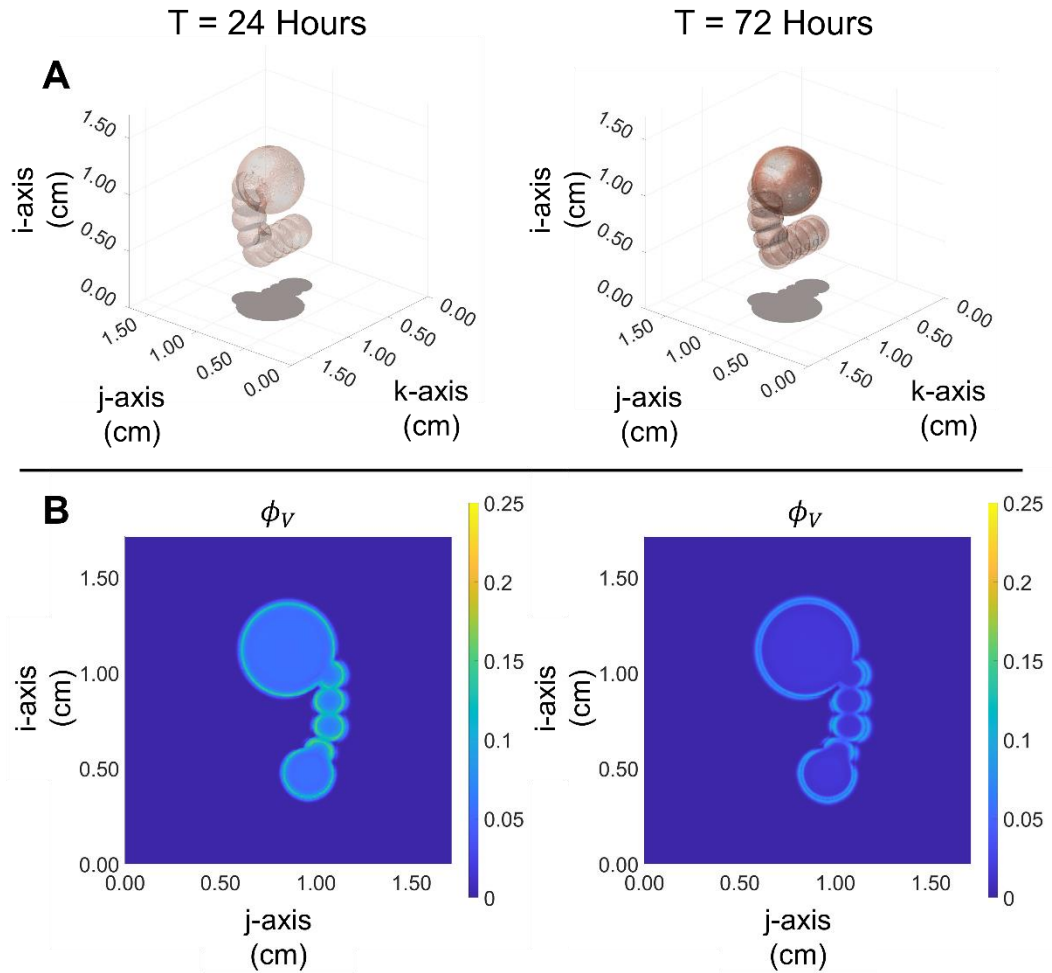
Figure 33 Simulation of simultaneous treatment of primary PDAC with anti-PD-L1 and antigen-CNP therapeutics. Viable tumor tissue is visualized from (**A**) oblique view and (**B**) side view at k = 0.852 cm at 1 and 3 days since therapeutic was applied. Tumor tissue in (**A**) is defined as $\phi_V \geq 0.05$. Darker blue hues within the tumor mass by 3 days indicate CTL were eliminating tumor tissue.
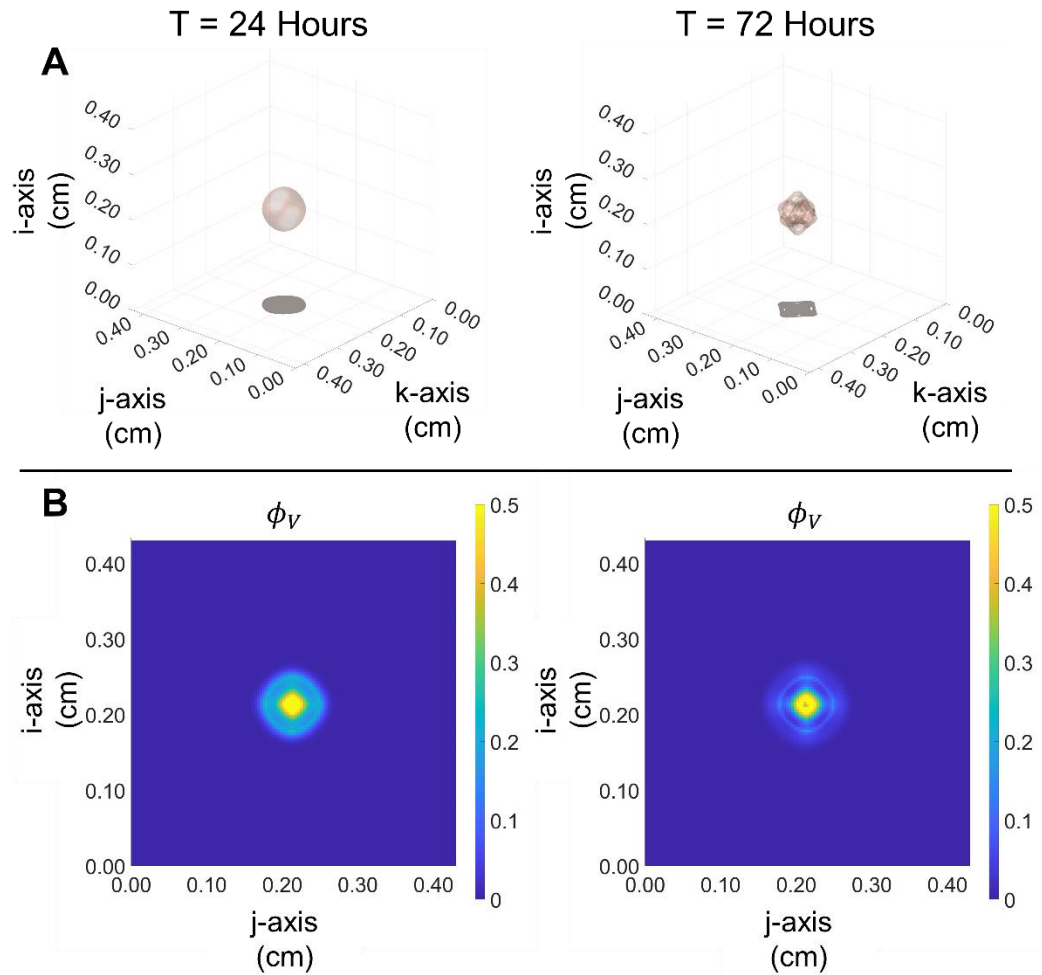
Figure 34 Simulation of simultaneous treatment of PDAC-LM with anti-PD-L1 and antigen-CNP. Viable tumor tissue (ϕ_V) is visualized from (A) oblique view and (B) side view at k = 0.212 cm at 1 day and 3 days after therapeutics were administered. Tumor tissue in (A) is defined as $\phi_V \geq 0.05$. Darker blue hues within the tumor mass by 3 days indicate CTL were eliminating tumor tissue.

5.4 Discussion

Despite significant improvements in cancer therapy of various solid tumors, the prognosis of PDAC patients has only marginally improved over the last decades. The pronounced immunosuppressive TME and the high metastatic potential might be two crucial factors contributing to the poor treatment responses [5, 10, 15, 292, 293]. The success of ICB to overcome PD-L1 mediated T cell exhaustion achieved in other cancers has not been translated to PDAC [24, 53]. In this study, a mathematical 3D model of tumor growth was applied to mm-scale PDAC metastasis (PDAC-LM) and centimeter-scale primary PDAC to simulate the interaction of PDAC with macrophages, myofibroblasts, and T cells during anti-PD-L1 therapy. Anti-PD-L1 treatment in combination with nanotherapy (antigen-CNP) targeting DC-mediated CTL activation was further evaluated. The modelling revealed an increased anti-tumor response when PD-L1 pathway inhibition and antigen-CNP were applied in combination. Of note, decrease in tumor burden was observed for both primary and liver metastatic tumors, suggesting this approach may be effective also in late-stage disease. To our knowledge, these results showcase the first centimeter-scale simulation of PDAC therapeutic response considering tumor stroma parameters from primary and metastatic PDAC tissues. Longer term, this platform aims to provide patient-specific predictions of therapeutic efficacy, with the goal to improve clinical outcomes.

In previous work, tumors were grown from a small initial size until treatment application [57, 308]. In the present model, the size of the simulated PDAC lesion was established at the centimeter-scale using an initial condition, representing a clinically

relevant scenario. While the PDAC shape used was consistent with clinical PDAC observations [324], the initial conditions assumed that tumor tissue has a homogenous composition of immune species and vasculature. However, over time, pressure and oxygen gradients caused spatial heterogeneity in both primary (**Figure 30**) and liver metastatic (**Figure 31**) cases. Simulation of differing PDAC-LM growth sizes as seen in Danet et al. [332] will be explored in future work. While the present simulation did include myofibroblast expression of PD-L1, recent evidence has suggested that PD-L1 expressing myofibroblasts inhibit CTL in a PD-L1 independent manner [52]. As myofibroblasts are particularly abundant in large PDAC-LM [298], therapeutic strategies affecting this immunomodulating stromal cell population may be attractive [303]. Moreover, further investigation is required to evaluate the effects of tumor stromal heterogeneity and PD-L1-induced myofibroblast inhibition on the therapy response.

Consistent with PDAC clinical trial results with PD-L1 inhibitors such as durvalumab [24], the anti-PD-L1 therapeutics without antigen-CNP therapy underperformed against PDAC and PDAC-LM. Thus, as outlined above, strategies beyond monotherapy with ICB must be evaluated to improve anti-tumor responses in PDAC patients. Recent preclinical studies have explored combinatorial strategies demonstrating promising results. Nanoparticles fashioned from human MiaPaCa-2 cells or M2-polarized macrophage cell membranes (CMNPs) were loaded with paclitaxel (PTX) or the colony-stimulating factor 1 receptor inhibitor, pexidartinib (PXDB), respectively, were found to act synergistically to affect PDAC cells in an *in vitro* tri-culture model consisting of activated fibroblasts, M2-polarized macrophages, and

MiaPaCa-2 cells [334]. A multi-paratopic VEGF decoy receptor developed to target PD-L1-expressing cancer-associated fibroblasts was found to synergize with gemcitabine to relieve desmoplasia in an orthotopic mouse PDAC model [303]. A synergistic interaction was identified between the MEK inhibitor trametinib and the multi-kinase inhibitor nintedanib targeting KRAS-directed oncogenic signaling in mesenchymal PDAC. Promoting intra-tumor infiltration of cytotoxic and effector T cells, this approach sensitized mesenchymal PDAC to PD-L1 immune checkpoint inhibition *in vivo* [304]. Recently, T cell-activating immune checkpoint therapies (agonist 41BB and antagonist LAG3) combined with a CXCR1/2 inhibitor targeting immunosuppressive myeloid cells resulted in complete responses in a mouse *in vivo* model [302].

Our simulation approach indicates that PD-L1 inhibition combined with nanotherapy targeting DC-mediated CTL activation may lead to improved CTL mediated anti-PDAC responses. The feasibility of such a combination requires further experimental validation *in vivo*. ICB has generally been associated with immune-related adverse events (irAE) [335], with durvalumab treated NSCLC patients experiencing manageable irAE in a recent phase III trial [336]. Whether a combination of ICB with nanotherapy targeting DC-mediated CTL activation leads to irAE remains to be elucidated. In this respect, the model presented herein could serve to evaluate therapeutic combinations with manageable irAE risk.

5.5 Supplementary Information

Non-dimensionalized Dependent Variable	Biological Representation	Scaling Factor
ϕ_V	Viable tumor cells volume fraction	$\tilde{\phi}_\alpha$ (fixed solid volume fraction)
ϕ_E	ECM volume fraction	$\tilde{\phi}_\alpha$
ϕ_H	Healthy host cells volume fraction	$\tilde{\phi}_\alpha$
u_α	Solid mass velocity	$\dfrac{\mathcal{L}}{\mathcal{T}}$
u_E	ECM Velocity within ECM	$\dfrac{\mathcal{L}}{\mathcal{T}}$
μ_T	Tumor cell potential	E_a^*
μ_E	ECM potential	E_a^*
$\tilde{u}^d$	Displacement vector	$\mathcal{L}$
p	Solid phase tumor cell pressure	$\mathcal{P}$
n	Concentration of oxygen	$\tilde{n}_\infty$
tgf	Tumor growth factors concentration	tgf_{sat}
taf	Tumor angiogenic factors concentration	taf_{sat}
m	Concentration of matrix degrading enzymes	m_{sat}
B_n^E	New blood vessels	$\tilde{B}_{max}$
L_n^E	New lymphatic vessels	$\tilde{L}_{max}$

Table 38 Dependent variables in Equation 5.2.1 through Equation 5.2.20 for the model in [82].

Parameter	Biological Representation	Parameter Definition	Non-dimensionalization
M_i	Mobility of cell species i	[82]	$\mathcal{M}$

S_V	Viable tumor cell source		
S_D	Dead/necrotic tumor cell source		$\tilde{\phi}_\alpha \cdot \mathcal{T}$
S_E	ECM source term		
S_{BnE}	Blood cell source term		$\tilde{B}_{max} \cdot \mathcal{T}$
$\mathcal{W}$	Elastic energy of ECM		$\tilde{\phi}_\alpha \cdot E_a^*$
L_1^E & L_2^E	Lamé constants for ECM components		L_2^E & L_2^E
L_1^C & L_2^C	Lamé constants for cell components		L_2^E & L_2^E
ϵ_E	Interaction strength of ECM with itself		$\bar{\bar{\epsilon}}$
ϵ_T	Interaction strength of tumor mass with itself		$\bar{\bar{\epsilon}}$
ϵ_e	Strain energy coefficient		$\bar{\bar{\epsilon}}_e$
γ_T	Tumor cell self-adhesion parameter		$\gamma_T = \dfrac{\epsilon_T \cdot \tilde{\phi}_\alpha \cdot \sqrt{\tilde{\phi}_\alpha \cdot E_a^*}}{\mathcal{L} \cdot \mathcal{P}}$
γ_E	ECM self-adhesion parameter		$\gamma_E = \dfrac{\epsilon_E \cdot \tilde{\phi}_\alpha \cdot \sqrt{\tilde{\phi}_\alpha \cdot E_a^*}}{\mathcal{L} \cdot \mathcal{P}}$
$\epsilon_{\sigma\tau}$	Interaction strength between species σ and τ	[82, 289]	$\bar{\bar{\epsilon}}$
$\mathcal{E}$	Infinitesimal strain		$\tilde{\bar{\bar{\mathcal{E}}}}$
$\mathcal{E}_E^*$	Eigenstrain tensor for ECM		$\bar{\bar{\mathcal{E}}}$
$\mathcal{E}_C^*$	Eigenstrain tensor for cells	[83]	$\bar{\bar{\mathcal{E}}}$
k_{n1}	Oxygen rate constants		$\lambda_{U,V,n}$
k_{n2}			$\lambda_{U,V,n}$
D_n	Diffusivity of oxygen in tumor	[82]	$D_{n,T}$

k_α	Motility of the solid phase		$\bar{\bar{k}}_\alpha$
D_{tgf}	Diffusivity of tumor growth factors		$D_{n,T}$
D_{tgf}	Diffusivity of tumor angiogenic factors		$D_{n,T}$
λ_{tgf}	Tumor growth factor rate constant		$\lambda_{U,V,n}$
$\lambda_{de,tgf}$	Degradation rate constant for tumor growth factors		$\lambda_{U,V,n}$
$\lambda_{U,tgf}$	Total uptake rate constant for tumor growth factors by tumor		$\lambda_{U,V,n}$
J_σ	Vasculature diffusive flux for $\sigma \in \{BnE, LnE\}$		$\tilde{\sigma}_{max} \cdot \mathcal{T}$

Table 39 Parameters in Equation 5.2.1 through Equation 5.2.20 for the model in [82, 83, 289]. Value for parameters used in this study are in [82] and [289].

Non-dimensionalization parameters	Description	Definition or Assigned Value
$\tilde{\phi}_\alpha$	Fixed solid volume fraction	0.8
E_a^*	Energy scale for adhesion	0.001
E_e^*	Energy scale for ECM elastic effects	0.001
$\bar{\bar{k}}_\alpha$	Characteristic motility of the solid phase (cells)	1.0
$\mathcal{L}$	Characteristic length	$\sqrt{\dfrac{D_{T,n}}{\lambda_{U,V,n}}}$
$\mathcal{T}$	Characteristic time	$\dfrac{1}{\lambda_{M,V}}$

$\mathcal{P}$	Characteristic pressure	$\dfrac{\mathcal{L}^2}{\bar{\bar{k}}_\alpha \cdot \mathcal{T}}$
$\mathcal{M}$	Characteristic mobility	$\dfrac{\mathcal{L}^2}{\mathcal{T} E_a^*}$
$\bar{\bar{\epsilon}}$	Characteristic interaction strength	$\mathcal{L} \cdot \sqrt{\dfrac{E_a^*}{\tilde{\phi}_\alpha}}$
$\bar{\bar{\mathcal{E}}}$	Characteristic strain	$\sqrt{\dfrac{E_a^* \cdot \tilde{\phi}_\alpha}{E_e^* \cdot \bar{\bar{\epsilon}} \cdot L_2^E}}$

Table 40 Non-dimensionalization parameters used in Table 38 and Table 39 [82].

Variable/Parameter Value	Description	Non-dimensionalization Factor
$\phi_{T_{EC}}$	Volume fraction of Exhausted T-cells	$\tilde{\phi}_\alpha$
$\mu_{T_{EC}}$	Chemical Potential of Exhausted T-cells	$\tilde{\phi}_\alpha$
P_{DL1}	Programmed Cell Death Ligand 1	$(P_{DL1})_{sat}$
$D_{I_{PDL1}}$	Anti-PD-L1 Drug	$\left(D_{I_{PDL1}}\right)_{sat}$

Table 41 Variables pertinent to model derivation for PDAC.

Parameter	Description	Scaling Factor	PDAC Value	PDAC-LM Value	Reference
$\lambda_{apoptosis\|T_{EC}}$	Apoptotic Rate for Exhausted T-cells	$\lambda_{M,V}$	0.15		Calibrated
$\lambda_{necrosis\|T_{EC}}$	Necrosis Rate for Exhausted T-cells	$\lambda_{M,V}$	0.0		Calibrated
$\mathcal{F}_{che_{apop}\|T_C}$	Factor of CHE to lessen CTL	Dimensionless	1.0		Calibrated

	exhaustion rate			
$\lambda_{exhaust|T_C}$	Exhaustion rate of CTL	$\lambda_{M,V}$	3.73	Calibrated
$\mathcal{F}_{activation|T_C}$	Factor of CTL exhaustion due to activation	Dimensionless	0.0	Calibrated
$\mathcal{F}_{PDL1|T_C}$	Factor of CTL exhaustion due to PD-L1 expression	Dimensionless	14.0	Calibrated
$\mathcal{F}_{F_E,tgf}$	Effective factor of TGF on myofibroblast release of ECM	Dimensionless	4.0	Calibrated
D_{PD1}	Diffusivity of PD-L1	$D_{U,V,n}$	Computed	Calibrated
$D_{PD1,H}$	Diffusivity of PD-L1 in healthy regions	$D_{U,V,n}$	0.0	Calibrated
$D_{PD1,E}$	Diffusivity of PD-L1 in ECM regions	$D_{U,V,n}$	0.0	Calibrated
$D_{PD1,T}$	Diffusivity of PD-L1 in tumor regions	$D_{U,V,n}$	0.5	Calibrated
λ_{PDL1}	Rate of PD-L1 Expression	$\lambda_{U,V,n}$	Computed	Calibrated
$\lambda_{V|PDL1}$	Rate of PD-L1 Expression by viable tumor mass	$\lambda_{U,V,n}$	0.25	Calibrated
$\lambda_{F|PDL1}$	Rate of PD-L1 Expression by myofibroblasts	$\lambda_{U,V,n}$	0.03	Calibrated to match [52]
$\lambda_{M_1|PDL1}$	Rate of PD-L1 Expression by M1	$\lambda_{U,V,n}$	2.0	Calibrated to match [53]
$\lambda_{M_2|PDL1}$	Rate of PD-L1 Expression by M2	$\lambda_{U,V,n}$	0.80	
$\mathcal{F}_{PDL1,T|M_1}$	Effective factor of	Dimensionless	2.0	

	upregulation of PD-L1 expression by M1 in tumor tissue			
$\mathcal{F}_{PDL1,T|M_2}$	Effective factor of upregulation of PD-L1 expression by M2 in tumor tissue	Dimensionless	5.0	
$\mathcal{F}_{PDL1,T|F}$	Effective factor of upregulation of PD-L1 expression by myofibroblasts in tumor tissue	Dimensionless	1.75	Calibrated to match [52]
$\phi_{M_1,T,sat}$	Saturation volume fraction of tumor tissue for PD-L1 production by M1	$\tilde{\phi}_\alpha$	0.05	Calibrated
$\phi_{M_2,T,sat}$	Saturation volume fraction of tumor tissue for PD-L1 production by M2	$\tilde{\phi}_\alpha$	0.05	Calibrated
$\phi_{F,T,sat}$	Saturation volume fraction of tumor tissue for PD-L1 production by myofibroblasts	$\tilde{\phi}_\alpha$	0.05	Calibrated
$\lambda_{de|PDL1}$	Degradation rate of PD-L1	$\lambda_{U,V,n}$	5.0	Calibrated
$\lambda_{PDL1|D_{I_{PDL1}},PDL1}$	Elimination rate of PD-L1 via $D_{I_{PDL1}}$	$\lambda_{U,V,n}$	4600	Calibrated

$D_{D_{I_{PDL1}}}$	Diffusivity of $D_{I_{PDL1}}$	$\dfrac{\mathcal{L}^2}{\mathcal{T}}$	Computed	Calibrated
$D_{D_{I_{PDL1}},H}$	Diffusivity of $D_{I_{PDL1}}$ in healthy regions	$\dfrac{\mathcal{L}^2}{\mathcal{T}}$	1.0	Calibrated
$D_{D_{I_{PDL1}},E}$	Diffusivity of $D_{I_{PDL1}}$ in ECM regions	$\dfrac{\mathcal{L}^2}{\mathcal{T}}$	1.0	Calibrated
$D_{D_{I_{PDL1}},T}$	Diffusivity of $D_{I_{PDL1}}$ in tumor regions	$\dfrac{\mathcal{L}^2}{\mathcal{T}}$	1.0	Calibrated
$\lambda_{extravasate,D_{I_{PDL1}}}$	Extravasation rate of $D_{I_{PDL1}}$	$\lambda_{M,V}$	9000	Calibrated
$\lambda_{decay,D_{I_{PDL1}}}$	Decay rate of $D_{I_{PDL1}}$	$\lambda_{M,V}$	0.03961	Calibrated to match [321, 322]
$\lambda_{uptake,D_{I_{PDL1}}}$	Uptake rate of $D_{I_{PDL1}}$	$\lambda_{M,V}$	Computed	Calibrated
$\lambda_{D_{I_{PDL1}},uptake,H}$	Uptake rate of $D_{I_{PDL1}}$ by viable tumor tissue	$\lambda_{M,V}$	0.0	Calibrated
$\lambda_{D_{I_{PDL1}},uptake,V}$	Uptake rate of $D_{I_{PDL1}}$ by host tissue	$\lambda_{M,V}$	0.0	Calibrated
$\lambda_{death,che}^{V}$	Rate of chemokine release from lysing dead tumor cells	$\dfrac{che_{sat}}{\lambda_{M,V}}$	1.25	Calibrated
α_1	Rate of drug concentration saturation in the blood vasculature	$\mathcal{T}^{-1}$	7.0	Calibrated
α_2	Rate of drug clearance in the blood vasculature	$\mathcal{T}^{-1}$	7.0	Calibrated
t_f	Finishing time for anti-PD-L1 therapy administration	$\mathcal{T}$	0.025	Calibrated_

$n_{h,F}$	Hypoxic threshold for myofibroblasts	n_∞	0.20	0.40	Calibrated
$\mathcal{F}_{enter|T_C}^{D_{NP}}$	Efficacy of antigen-CNP on increasing CTL Entrance rate	Dimensionless	15.0		Calibrated to match [307, 319]
γ_1	Rate of saturation of antigen-CNP effect	$\mathcal{T}^{-1}$	1.5		Calibrated to match [307, 320]
γ_2	Rate of decay of antigen-CNP effect	$\mathcal{T}^{-1}$	0.32		Calibrated to match [307, 320]
$\mathcal{F}_{taf}^{V}$	Nominal level of TAF expression by viable tumor tissue	Dimensionless	0.0		Calibrated to match [57, 59, 60, 318]
$\mathcal{F}_{B}^{G}$	Nominal extravasation level of immune species	Dimensionless	0.0		Calibrated to match [65]
$\phi_{M0,sat}$	Saturation volume fraction for M0 effect	$\tilde{\phi}_\alpha$	0.0085		Calibrated
$\phi_{M1,sat}$	Saturation volume fraction for M1 effect	$\tilde{\phi}_\alpha$	0.03	0.15	Calibrated (1)
$\phi_{M2,sat}$	Saturation volume fraction for M2 effect	$\tilde{\phi}_\alpha$	0.03	0.15	Calibrated (1)
$\phi_{T_c,sat}$	Saturation volume fraction for CTL effect	$\tilde{\phi}_\alpha$	0.02	0.06	Calibrated (1)
$\mathcal{F}_{F_E,tgf}$	Effective factor of TGF on myofibroblast	Dimensionless	4.0		Calibrated

	release of ECM					

Table 42 PDAC-specific model parameters. Computed parameters are defined as functions of model variables or constant-valued model parameters. Scaling factors are defined in [82, 289].

(1) Values were set to attain steady growth for primary and metastatic tumors.

Parameter	Description	Scaling Factor	Previous Value	Value in PDAC	Value in PDAC-LM	Reference
n_h	Hypoxic level of O$_2$	n_∞	0.489	0.375		Calibrated
$n_{v,B}$	O$_2$ viability limit of endothelial cells	n_∞	0.40	0.10		Calibrated
$n_{v,L}$	O$_2$ viability limit of lymphatic endothelial cells	n_∞	0.40	0.10		Calibrated
$n_{v,F}$	O$_2$ viability limit of myofibroblasts	n_∞	0.40	0.21		Calibrated
taf_{Bn}	Threshold of TAF corresponding to the onset of endothelial cell proliferation	taf_{sat}	0.2	0.01	0.2	Calibrated
taf_{Ln}	Threshold of TAF corresponding to onset of lymphatic endothelial cell proliferation	taf_{sat}	0.2	0.01	0.2	Calibrated
$p_{t,B}$	Threshold pressure corresponding to onset of blood vessel loss	$\mathcal{P}$	0.15	20.0	0.60	Calibrated
$p_{t,L}$	Threshold pressure corresponding to onset of lymphatic vessel loss	$\mathcal{P}$	0.15	20.0	0.60	Calibrated
$p_{c,\sigma}$	Threshold pressure corresponding to the maximum rate of preexisting vasculature vessel loss for $\sigma \in \{Bp, Lp\}$	$\mathcal{P}$	0.9	40.0	0.8	Calibrated
$p_{c,\psi}$	Threshold pressure corresponding to	$\mathcal{P}$	0.2	40.0	0.8	Calibrated

	the maximum rate of neo-vasculature vessel loss for $\psi \in \{Bn, Ln\}$					
$D_{m,E}$	Diffusivity of matrix degrading enzymes in ECM regions	$\frac{\mathcal{L}^2}{\mathcal{T}}$	0.05	0.25		Calibrated
$D_{m,\sigma}$	Diffusivity of matrix degrading enzymes in region σ for $\sigma \in \{T, H\}$	$\frac{\mathcal{L}^2}{\mathcal{T}}$	0.01	0.25		Calibrated
$\lambda_{InduceDeath|V}$	Tumor death rate in response to cytotoxic immune species	$\lambda_{M,V}$	0.2	3.0		Calibrated
$\lambda_{N,V}$	Necrosis rate constant of viable tumor cells	$\lambda_{M,V}$	1.0	3.0		Calibrated
$\lambda_{L,D}$	Lysis rate constant of dead tumor cells	$\lambda_{M,V}$	9.0	1.0		Calibrated
$\lambda_{enter,E|G}$	Entrance rate of immune species within ECM	$\lambda_{M,V}$	0.03	1.0		Calibrated to match [53, 241, 319, 326, 327, 333]
$\lambda_{enter,T|G}$	Entrance rate of immune species within tumor tissue	$\lambda_{M,V}$	0.03	1.0		Calibrated to match [53, 241, 319, 326, 327, 333]
$\lambda_{enter,H|G}$	Entrance rate of immune species within host tissue	$\lambda_{M,V}$	0.03	1.0		Calibrated to match [53, 241, 319, 326, 327, 333]
$\lambda_{diff|M_0}$	Rate of monocyte differentiation	$\lambda_{M,V}$	1.2	10.0		Calibrated
$\mathcal{F}_{F_{bias}}$	Bias for steady-state M1:M2 ratio	Dimensionless	0.14286	0.10	0.14286	Calibrated to match [59, 326]
$\mathcal{F}_{M_0}^{Bp}$	Monocyte extravasation factor for pre-existing blood vasculature	Dimensionless	7.0	0.10	4.0	Calibrated to match [53, 57, 326, 327]
$\mathcal{F}_{M_0}^{Bn}$	Monocyte extravasation factor for blood neo-vasculature	Dimensionless	1.75	0.10	4.0	Calibrated to match [53, 57, 326, 327]
$\mathcal{F}_{T_C}^{Bp}$	CTL extravasation factor via pre-existing blood vasculature	Dimensionless	0.0 (1)	0.018	0.375	Calibrated to match [53, 241, 319, 333]
$\mathcal{F}_{T_C}^{Bn}$	CTL extravasation factor for blood neo-vasculature	Dimensionless	0.0 (1)	0.018	0.375	Calibrated to match [53, 241, 319, 333]

$\lambda_{apoptosis\|\sigma}$	Apoptosis rate with respect to $\sigma \in \{M_1, M_2, T_C\}$	$\lambda_{M,V}$	0.10	0.15		Calibrated to match [67]
$\mathcal{F}_{InduceDeath,T_C}$	Effective factor of CTL tumor cytotoxicity	Dimensionless	0.0	0.75		Calibrated
$\mathcal{F}_{InduceDeath,M_1}$	Effective factor of M1 tumor cytotoxicity	Dimensionless	1.0	0.25		Calibrated
$\lambda_{M2,tgf}$	Release rate of TGF by M2	$\lambda_{U,V,n}$	0.0	0.05		Calibrated
$\lambda_{F,E}$	ECM rate of secretion by myofibroblasts	$\dfrac{\tilde{\phi}_\alpha \lambda_{M,V}}{F_{max}}$	2.0	0.15	0.05	Calibrated to match [325]
$\lambda_{de,C}$	Degradation rate of ECM macromolecules catalyzed by matrix degrading enzymes	$\tilde{\phi}_\alpha \lambda_{M,V} C_E$	0.7	4.0		Calibrated to match [325]
$\lambda_{Bp,n,E}$	Transfer coefficient of O2 via pre-existing blood vasculature in ECM regions	$\lambda_{U,V,n}$	0.5	0.12	0.25	Calibrated
$\lambda_{Bp,n,T}$	Transfer coefficient of O2 via pre-existing blood vasculature in tumor regions	$\lambda_{U,V,n}$	0.5	0.12	0.25	Calibrated
$\lambda_{Bp,n,H}$	Transfer coefficient of O2 via pre-existing blood vasculature in healthy regions	$\lambda_{U,V,n}$	0.5	0.12	0.25	Calibrated
$\lambda_{Bn,n,E}$	Transfer coefficient of O2 via blood neo-vasculature in ECM regions	$\lambda_{U,V,n}$	0.6	0.12	0.25	Calibrated
$\lambda_{Bn,n,T}$	Transfer coefficient of O2 via blood neo-vasculature in tumor 0.6regions	$\lambda_{U,V,n}$	0.6	0.12	0.25	Calibrated
$\lambda_{Bn,n,H}$	Transfer coefficient of O2 via blood neo-vasculature in host regions	$\lambda_{U,V,n}$	0.6	0.12	0.25	Calibrated
$\lambda_{Bp,g,E}$	Transfer coefficient of glucose via pre-existing blood vasculature in ECM regions	$\lambda_{U,V,n}$	0.1	0.02	0.1	Calibrated
$\lambda_{Bp,g,T}$	Transfer coefficient of glucose via pre-existing blood	$\lambda_{U,V,n}$	0.1	0.02	0.1	Calibrated

	vasculature in tumor regions					
$\lambda_{Bp,g,H}$	Transfer coefficient of glucose via pre-existing blood vasculature in healthy regions	$\lambda_{U,V,n}$	0.1	0.02	0.1	Calibrated
$\lambda_{Bn,g,E}$	Transfer coefficient of glucose via blood neo-vasculature in ECM regions	$\lambda_{U,V,n}$	1.0	0.02	1.0	Calibrated
$\lambda_{Bn,g,T}$	Transfer coefficient of glucose via blood neo-vasculature in tumor regions	$\lambda_{U,V,n}$	1.0	0.02	1.0	Calibrated
$\lambda_{Bn,g,H}$	Transfer coefficient of glucose via blood neo-vasculature in host regions	$\lambda_{U,V,n}$	1.0	0.02	1.0	Calibrated
$\lambda_{Bp,w,E}$	Transfer coefficient of carbon dioxide via pre-existing blood vasculature in ECM regions	$\lambda_{U,V,n}$	3.0	0.6	3.0	Calibrated
$\lambda_{Bp,w,T}$	Transfer coefficient of carbon dioxide via pre-existing blood vasculature in tumor regions	$\lambda_{U,V,n}$	3.0	0.6	3.0	Calibrated
$\lambda_{Bp,w,H}$	Transfer coefficient of carbon dioxide via pre-existing blood vasculature in healthy regions	$\lambda_{U,V,n}$	3.0	0.6	3.0	Calibrated
$\lambda_{Bn,w,E}$	Transfer coefficient of carbon dioxide via blood neo-vasculature in ECM regions	$\lambda_{U,V,n}$	1.0	0.6	1.0	Calibrated
$\lambda_{Bn,w,T}$	Transfer coefficient of carbon dioxide via blood neo-vasculature in tumor regions	$\lambda_{U,V,n}$	1.0	0.6	1.0	Calibrated
$\lambda_{Bn,w,H}$	Transfer coefficient of carbon dioxide via blood neo-vasculature in host regions	$\lambda_{U,V,n}$	1.0	0.6	1.0	Calibrated
$\lambda_{Bp,\ell,E}$	Transfer coefficient of	$\lambda_{U,V,n}$	3.0	0.6	3.0	Calibrated

	lactate ion via pre-existing blood vasculature in ECM regions					
$\lambda_{Bp,\ell,T}$	Transfer coefficient of lactate ion via pre-existing blood vasculature in tumor regions	$\lambda_{U,V,n}$	3.0	0.6	3.0	Calibrated
$\lambda_{Bp,\ell,H}$	Transfer coefficient of lactate ion via pre-existing blood vasculature in healthy regions	$\lambda_{U,V,n}$	3.0	0.6	3.0	Calibrated
$\lambda_{Bn,\ell,E}$	Transfer coefficient of lactate ion via blood neo-vasculature in ECM regions	$\lambda_{U,V,n}$	1.0	0.6	1.0	Calibrated
$\lambda_{Bn,\ell,T}$	Transfer coefficient of lactate ion via blood neo-vasculature in tumor regions	$\lambda_{U,V,n}$	1.0	0.6	1.0	Calibrated
$\lambda_{Bn,\ell,H}$	Transfer coefficient of lactate ion via blood neo-vasculature in host regions	$\lambda_{U,V,n}$	1.0	0.6	1.0	Calibrated
$\lambda_{V,tgf}$	Production rate constant of TGF by viable tumor cells	$\lambda_{U,V,n}$	0.371150	2.50		Calibrated
$\lambda_{V,taf}$	Production rate constant of TAF by viable tumor cells	$\lambda_{U,V,n}$	3.0	4.0		Calibrated
$\lambda_{M2,taf}$	Release rate of TAF by M2	$\lambda_{U,V,n}$	0.0	0.1		Calibrated
$\lambda_{U,B,taf}$	Uptake rate of constant of TAFs by endothelial cells	$\dfrac{\lambda_{U,V,n}}{B_{max}}$	0.001157	0.0	0.001157	Calibrated
$\lambda_{U,L,taf}$	Uptake rate of constant of TAFs by lymphatic endothelial cells	$\dfrac{\lambda_{U,V,n}}{L_{max}}$	0.001157	0.0	0.001157	Calibrated
$\lambda_{V,m}$	Production rate of matrix degrading enzymes by viable tumor cells	$\lambda_{M,V}$	3.0	2.5	0.5	Calibrated
$\lambda_{M,FE}$	Mitosis rate constant of myofibroblasts	$\lambda_{M,V}$	0.75	0.8		Calibrated
$\mathcal{F}^{M}_{tgf,F}$	Effective factor of TGF on the	Dimensio nless	2.0	5.0	0.5	Calibrated

	mitotic rate of myofibroblasts					
$\lambda_{de,BpE}$	Remodeling rate constant of pre-existing blood vasculature by matrix degrading enzymes	$\dfrac{\lambda_{M,V}}{m_{sat}}$	0.01	2.0	40.0	Calibrated
$\lambda_{crush,BpE}$	Maximum degradation rate constant of pre-existing blood vasculature due to solid tumor pressure	$\lambda_{M,V}$	0.05	0.01	0.05	Calibrated
$\mathcal{F}_{Bn}$	Fraction of blood neo-vasculature that are sprouting	Dimensionless	0.4	0.8		Calibrated
$\lambda_{m,BnE}$	Maximum mitosis rate constant for blood neo-vasculature	$\lambda_{M,V}$	18.0	0.8	0.25	Calibrated
$\lambda_{de,BnE}$	Remodeling rate constant of blood neo-vasculature by matrix degrading enzymes	$\dfrac{\lambda_{M,V}}{m_{sat}}$	5.0	0.02	5.0	Calibrated
$\lambda_{crush,BnE}$	Maximum degradation rate constant of blood neo-vasculature due to solid tumor pressure	$\lambda_{M,V}$	5.0	0.02	5.0	Calibrated
$\lambda_{de,LpE}$	Remodeling rate constant of pre-existing lymphatic vasculature by matrix degrading enzymes	$\dfrac{\lambda_{M,V}}{m_{sat}}$	0.01	0.002	0.01	Calibrated
$\lambda_{crush,LpE}$	Maximum degradation rate constant of pre-existing lymphatic vasculature due to solid tumor pressure	$\lambda_{M,V}$	0.05	0.01	0.05	Calibrated
$\mathcal{F}_{Ln}$	Fraction of lymphatic neo-vasculature that are sprouting	Dimensionless	0.3	0.8		Calibrated
$\lambda_{m,LnE}$	Maximum mitosis rate constant for lymphatic neo-vasculature	$\lambda_{M,V}$	2.0	0.8	0.25	Calibrated
$\lambda_{de,LnE}$	Remodeling rate constant of lymphatic neo-	$\dfrac{\lambda_{M,V}}{m_{sat}}$	4.0	0.02	4.0	Calibrated

	vasculature by matrix degrading enzymes					
$\lambda_{crush,LnE}$	Maximum degradation rate constant of lymphatic neo-vasculature due to solid tumor pressure	$\lambda_{M,V}$	4.0	0.02	4.0	Calibrated
$\mathcal{F}_{Halt_G|V,che}$	Effect of ϕ_V to mitigate chemokine-mediated macrophage chemotaxis	Dimensionless	0.40	0.0		Calibrated
tgf_{FE}	Threshold level of TGF corresponding to onset of upregulation of myofibroblast proliferation	tgf_{sat}	0.1	0.08		Calibrated
χ_{c,M_0}	Chemotaxis parameter for monocytes	$\dfrac{E_a^*}{che_{sat}}$	5.0	4.0		Calibrated
$\chi_{c,\sigma}$	Chemotaxis parameter for $\sigma \in \{M_1, M_2\}$	$\dfrac{E_a^*}{che_{sat}}$	15.0	4.0		Calibrated
χ_{c,T_C}	Chemotaxis parameter for CTL	$\dfrac{E_a^*}{che_{sat}}$	0.0	10.0		Calibrated
$\mathcal{F}_{Halt_G|V,che}$	Effective factor of ϕ_V mitigating immune species chemotaxis along CHE gradients	Dimensionless	0.4	0.0		Calibrated
$\lambda_{M_2,F_{M2}}$	Rate of release of F_{M2} by M2	$\lambda_{U,V,n}$	0.20	0.23	0.20	Calibrated
$\mathcal{F}_{F_{M2},V}^M$	Effect of F_{M2} on tumor mitotic rate	Dimensionless	0.95	0.0		Calibrated
$\mathcal{F}_{F_{M2},V}^{n_h}$	Effect of F_{M2} on tumor hypoxic threshold	Dimensionless	0.3	0.5		Calibrated

Table 43 Additional parameters used for this study. All other parameter values are set

as given across [82, 289, 308]. Scaling factors are defined in [82, 289].

(1) T-cells were not simulated in [289].

Variable	Condition Type	Value from [289]	Value in PDAC	Value in PDAC-LM
$\widehat{B}_E^{\widetilde{p}}$	Internal and Boundary	0.13	0.70	1.0
$\widehat{B}_E^{\widetilde{n}}$	Internal and Boundary	0.00	0.23	0.0
$\widetilde{\phi}_E$	Internal and Boundary	0.75	0.40	0.25
$\widetilde{F}_E$	Internal	0.20	0.20	0.80
$\widetilde{\phi}_{M_0}$	Internal	0.00980	0.0	

$\tilde{\phi}_{M_1}$	Internal	0.04891	0.0	
$\tilde{\phi}_{M_2}$	Internal	0.04076	0.0	
$\widehat{B_E^n}$	Within Tumor	0.00 (1)	0.28	0.0
$\widehat{B_E^p}$	Within Tumor	0.00 (1)	0.37	0.0
$\widehat{L_E^n}$	Within Tumor	0.00	0.0064	0.0
$\widehat{L_E^p}$	Within Tumor	0.00	0.017	0.0
$\widehat{F_E}$	Within Tumor	0.20	0.19	0.80
$\tilde{\phi}_E$	Within Tumor	0.75	0.48	0.25
$\tilde{\phi}_V$	Within Tumor	0.1875	0.063	0.1875
$\tilde{\phi}_D$	Within Tumor	0.0	3.9E-5	0.0
$\tilde{\phi}_{M_0}$	Within Tumor	0.00980	0.00028	0.0
$\tilde{\phi}_{M_1}$	Within Tumor	0.04891	0.0066	0.0
$\tilde{\phi}_{M_2}$	Within Tumor	0.04076	0.0099	0.0
$\tilde{\phi}_{T_C}$	Within Tumor	0.00 (2)	0.0012	0.0
$\tilde{\phi}_{T_{EC}}$	Within Tumor	0.00 (2)	0.0024	0.0

Table 44 Initial conditions for PDAC primary and liver metastatic lesions. All internal and boundary conditions not listed for PDAC or PDAC-LM are as given across [181] and [289].

(1) Blood vasculature was set to 0.1 to calibrate strength of anti-PDL1 therapy.

(2) T-cells were not simulated in [289].

Case	Multiplier	Range in Literature	Citation
PDAC	1.0x (Baseline)	-	-
PDAC + myofibroblasts	1.36x	1.28x - 1.32x (1)	[52]
PDAC + M1	1.95x	1.8x - 2.1x	
PDAC + M2	3.65x	3.2x - 4.3x	
Ratio of M1-only PD-L1 to M2-only PD-L1 (No Tumor)	2.09x	2.0x - 2.1x	[53]

Table 45 Calibration of PD-L1 expression by macrophages and myofibroblasts. Expression multipliers are relative to PDAC case (Baseline).

(1) Value falls within standard deviation from mean observations given in [52] (1.08x - 1.48x).

Parameter	Description	Value Assigned			
		Primary PDAC	PDAC-LM	PD-L1 Calibration	Antigen-CNP & Anti-PDL1 Therapies
#Simulated Points	Number of points within the cubic simulated domain	512^3	128^3	8	
#Levels used	Number of levels used in the Multigrid solver	5		2	

Table 46 Computed parameters from [83] used for PDAC simulations. Initial values are set pre-model runtime. Values not listed were set as in [83, 289].

CHAPTER 6: BREAST CANCER LIVER METASTASIS MICROENVIRONMENT

PREDICTED VIA MACHINE LEARNING FROM CLINICALLY MATCHED

PRIMARY TUMORS

6.1 Introduction

Breast cancer has the dubious distinction of being the most commonly diagnosed and second-deadliest female cancer in the U.S. [5]. Breast cancer liver metastases (BCLM) are diagnosed with primary breast cancer in up to 25% of cases [2, 5, 7-9] and present in ~71% of patient autopsies [337]. BCLM are prognostically grim, with median survival of 17.1 to 27.3 months and 5-year survival of ~20% [2-4], creating a critical need for effective therapies. BCLM typically appear as small, hypovascular nodules under contrast imaging [17], which do not rely on angiogenesis by receiving nutrients mainly from surrounding hepatic capillaries. Hence, transport of intravenously injected therapeutics is frequently impaired due to physiological drug resistance. [11-13].

The liver harbors various immune cell types, with macrophages being a primary population [338]. Macrophages are professional phagocytes, which readily take up nanomaterials and frequently congregate around inflamed tumor lesions [339]. We have previously shown that physiological resistance to therapy in BCLM could in principle be overcome by targeting phagocytic macrophages with nanotherapy [57-60, 308]. With

nanoalbumin-paclitaxel (nab-PTX) encapsulated into a solid multistage nanovector (nab-PTX-MSV) [57-60], macrophages were shown to take up significant numbers of nanovectors, thereby acting as depots to locally release drug in the vicinity of BCLM. Efficacy of this approach, evaluated *in vitro* [57, 59, 60], *in silico* [57, 59, 60, 308], and *in vivo* [58], depends on the BCLM characteristics and, particularly, the number and type of associated macrophages. Macrophages in the TME originate from monocyte (CD14) lineage [157, 257, 340] and can be traditionally classified into anti-tumor (M1) (CD68+ and CD163-CD206-) [60, 158, 194, 341-343] and pro-tumor variants (M2) (CD68+, CD163+, or CD206+) [60, 159, 235, 341, 342, 344, 345]. Interestingly, contrary to the general notion that M2 macrophages solely enhance tumor resistance to therapy and favor tumor growth [346], our *in silico* modelling validated through our prior studies underscored the potential role of M2 macrophages in sensitizing the TME to nanotherapy, suggesting that a balance between M1 and M2 phenotypes is required to achieve optimal anti-tumor response [59, 60]. Thus, defining macrophage-dependent immunotherapy parameters would benefit from understanding the patient-specific BCLM TME [347].

Multiple parameters interact in complex ways to define BCLM TME characteristics. Macrophage-mediated nanotherapeutic delivery relies on the macrophage ability to penetrate into BCLM. Transport is facilitated towards hypoxic regions (e.g., via HIF1α as a chemoattractant [348-350]) but can be inhibited by dense extracellular matrix (ECM) (primarily comprised of collagen) [15, 351] secreted by cancer-associated fibroblasts (αSMA) [352-354] and can be breached by tumor cells through Matrix Metalloproteinase 9 (MMP9) expression [355-357]. BCLM growth can be classified from

(ECM-preserving) replacement growth to less common (ECM-driven) desmoplastic growth [26, 239], which may differentially affect tumor response. Cancer cell proliferation (inferred from tumor cell expression of Ki-67 and phosphorylated extracellular signal-related kinase [pERK] [358-360]) as well as lesion vascularity (CD31) [361], could affect treatment response. Furthermore, expression of Programmed Death Ligand 1 (PD-L1), a common inhibitor of CD8a T-cell-mediated immunotherapy [300, 362] via the PD1/PD-L1 axis [51, 52, 362, 363], can be induced in primary breast tumors by local macrophages [364] and is highly expressed in synchronous axillary lymph node metastases of triple negative breast cancer [365]. Macrophage activity can be influenced by helper T-cells (CD4) [195, 200, 366], which can exert a pro-tumor [197, 198] or anti-tumor [174] effect. Natural killer (NK) cells (CD56) [367-369], an innate anti-tumor immune species common to the liver [164, 370], could also contribute to tumor response [164].

Obtaining information about BCLM characteristics for efficient immunotherapeutic targeting is challenging, however, since biopsy may have significant complications, resulting in poor patient survival [61], and resection is generally discouraged [12, 62, 63]. In comparison, biopsy from primary breast tumors is usually obtained and histological analysis is routinely performed [371, 372]. Ideally, BCLM TME characteristics could be derived and predicted from the primary lesion TME. Recent work [373] has indicated that metastasis of primary breast tissue was contingent on tumor E-cadherin (E-cad) expression. Furthermore, correlations have been identified between paired primary colorectal cancer and liver metastases [374], suggesting that metastatic

formation could in principle be inferred from primary tumor characteristics. This study

hypothesized that the BCLM TME could be inferred from the primary lesion TME.

Imaging Mass Cytometry (IMC) analysis of 23 different markers (including immune

cells, tumor markers, hypoxia, vascularity, and ECM) was performed on matched primary

breast cancer and BCLM patient samples to associate the TME of these two locations

using a machine learning (ML) approach, with the goal to predict the BCLM TME

characteristics based on the primary tumor TME.

6.2 Methods

6.2.1 Patient Samples

De-identified patient-matched primary breast cancer and BCLM (n=15 pairs)

paraffin slide samples were commercially obtained from BioCoreUSA (Philadelphia,

USA). No patient consent was required. Primary breast and BCLM samples were

obtained via resection or core needle biopsies, respectively. Matched samples from the

primary tumor were collected up to four years prior to the diagnosis and collection of

core biopsies from the matched BCLM in the same patient. The number in each group

was considered adequate for proof-of-concept testing [375] of the hypothesis that BCLM

TME characteristics could be predicted via ML analysis of the primary TME.

6.2.2 Sample Staining Analysis for IMC ROI

All patient slides were deparaffined and stained with Hematoxylin and Eosin

(H&E, Sigma, USA). Slides were holistically imaged, under brightfield microscopy at

10x magnification (Nikon Eclipse 80i) for examination of specific regions of interest

(ROI) to identify areas for IMC analysis. Due to the size of the histological cores, five and three ROIs per slide were analyzed in primary and matched BCLM samples, respectively. ROIs were selected based on the H&E staining focusing on the areas of high nuclear density (indicative of tumors), and areas bordering tumor tissue to capture TME. Each ROI was chosen at random within unique tumors and dependent on slide tissue size. IMC analysis was performed on 0.7mm x 0.7mm tissue samples in each ROI.

6.2.3 Imaging Mass Cytometry (IMC)

Imaging Mass Cytometry (IMC) allows simultaneous marker detection, making it suitable for profiling the TME. IMC data were preprocessed and checked for tissue integrity, staining quality, and signal range prior to analysis. For each ROI, single cells were segmented using *ilastik* [376] and *CellProfiler*, [377] based on DNA staining (Ir191) and other cell surface markers. Following segmentation, data were processed using Histology Topography Cytometry Analysis Toolbox (HistoCAT) [378], where mean marker intensities for single cells were extracted. Data were consolidated in R scripts for downstream analysis. Intensity values were clipped at 99.5 percentile to eliminate outliers and subsequently normalized to 0 to 1 range, giving equal weights to each marker. For samples from different tissue type, expression values were aligned using geometrical means of marker expression within the same tissue type before above-mentioned data normalization to remove tissue-type-specific background noise and to decrease batch effect. Normalized intensities were used to perform unsupervised clustering in Seurat [379] using *Louvain* algorithm [380, 381]. Cell clusters were annotated based on the mean expressions of markers and consolidated into 23 known cell types. Cell densities of

each cell type were calculated by normalizing counts by ROI. Neighborhood analysis

identified statistically significant neighboring status for each pair of cell types [378].

Neighborhood heatmaps normalized results to -1 to 1, where 1 (or red) denotes two cell

types are neighboring each other, -1 (or blue) denotes significant separation, and 0

indicates no significant spatial relationship. IMC ROI were excluded for subsequent

analysis if signal lacked tumor-specific markers (Ki-67, αSMA, or E-cad).

6.2.4 Machine Learning Preprocessing

All statistical and ML analyses were done in R 4.2.2 using cluster density data

from IMC ROI. To prevent biasing due to tissue type, preprocessing steps were

performed on breast and liver data separately. Cluster densities were first transformed

using base 10 logarithm to reduce heteroskedasticity [382]. Each ROI was then scaled by

total cluster intensities to control for differences in tissue mass represented per ROI. The

IMC data were processed and clustered in two analytical batches. Thus, each batch

(primary and BCLM data) was separately centered to focus on differences in expression

[382, 383]. Finally, each cluster was averaged across ROIs on a per-patient basis to create

one representative primary and BCLM sample pair per patient.

6.2.5 Machine Learning Analysis

To predict relative cluster density expression in BCLM TME from primary TME,

a comprehensive ML analysis was performed across all BCLM cluster densities using

caret package. For each cluster, patients were separated into low (<median) or high

(≥median) expression groups. Multiple ML models were tested, including neural

networks (neural networks with principal component step [*pcaNNet*], neural network [*nnet*], model averaged neural network [*avNNet*], multi-layer perceptron with multiple layers [*mlpWeightDecayML*]), k-nearest neighbors [*knn*], naïve bayes [*naive_bayes*], linear models (generalized [*glm*], boosted [*glmboost*]), random forests (random forest [*rf*], oblique random forest with SVM as splitting model [*ORFsvm*]), and support vector machines (linear kernel [*svmLinear*], radial basis function kernel [*svmRadial*], class weights [*svmRadialWeights*], and polynomial kernel [*svmPoly*]). For each model, features were ranked using *varImp*, with all feature subsets tested from the top 2 primary clusters as ranked by *varImp* to all primary clusters. Calculation of variable importance by *varImp* included model-specific learning methods (e.g., Random Forest) and generalized ROC curve analysis, such as for naïve bayes. Then, each model was re-trained on a feature subset generated by sequentially adding features in the order determined by *varImp* feature rankings. Five-fold cross validation with 20 resampling iterations was performed to obtain a total of 100 unique permutations. Kappa was selected as the optimization metric for *caret* model training.

To evaluate classifications, area under receiver-operating characteristic curve (AUROC) was calculated for each BCLM cluster and feature number combination, along with variable importance data. Performance metrics were calculated as the average across all folds and resampling iterations. AUROC 95% confidence intervals were generated using t-test distribution standard error. A single AUROC-optimized model was selected for each cluster. F1, which has been used to evaluate model performance in concert with AUROC [384, 385], was also computed. All plots were generated using *ggplot2* package.

6.2.6 Statistical Analysis

Correlations were done using Pearson or Spearman correlations, depending on the normality of the data per Shapiro-Wilks test using *corrplot* package. Like [386], strong correlation was defined as $|r| \geq 0.75$ or $|\rho| \geq 0.75$ for Pearson and Spearman, respectively. Bonferroni correction was applied to adjust for repeated t-test (for parametric data) or Wilcoxon rank sum test (for non-parametric data) across patient groups, with two-sided p-value < 0.0025 (p-adj) considered significant. PLS-DA was performed using *plsda* function from *mdatools* package.

6.3 Results

6.3.1 Study Methodology and Patient Characteristics

The study methodology is summarized in **Figure 35**. Characteristics related to the matched (primary and BCLM) breast cancer patient samples, as well as the number of IMC ROI samples preserved for analysis per patient, is summarized in **Table 47**. All patients were female. Average patient age was 49.2 years (SD 12.7 years) with BCLM core needle biopsy taken on average 2.5 years (SD 1.19 years) after primary resection. The majority of patients when initially diagnosed had AJCC stage III (n = 8) followed by stage I (n = 4) and stage II (n = 3). Most patients were T1 (n = 7) or T2 (n = 6), with only two patients being T3 (n = 1) or T4 (n = 1). Patients were roughly evenly distributed across all represented lymph node classifications: N0 (n = 3), N1 (n = 4), N2 (n = 5), and N3 (n = 3).
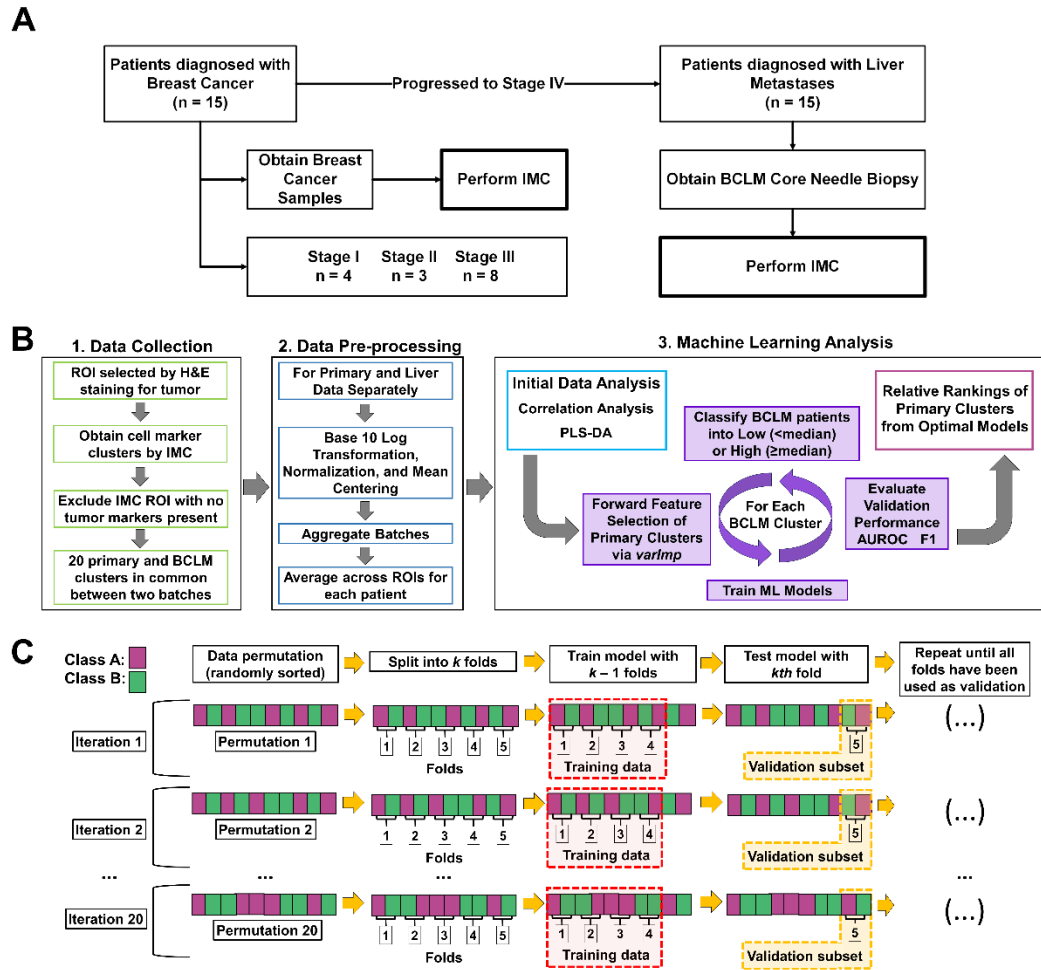
Figure 35 Workflow of study design. (A) Study profile. Primary breast cancer samples were taken from 15 patients. After subsequent diagnosis of breast cancer liver metastasis (BCLM), a core needle biopsy was also obtained. (B) Summary of Analysis. ROIs from primary and BCLM were identified using H&E staining for tumor tissue and TME. Multiple cell marker clusters were quantified by Imaging Mass Cytometry (IMC), producing 20 common clusters between two analytical batches. IMC ROIs missing multiple tumor markers (Ki-67, E-cad+, or αSMA) were excluded. Multiple machine learning models were trained to classify BCLM cluster expression into Low (< median) or High (≥ median) groups using primary cluster data. Forward feature selection was performed on preprocessed data using *varImp* to identify primary cell markers associated

236

with BCLM classification. (C) Diagram of model training and validation. Primary breast data was randomly sorted and split into k folds (subsets; here, k=5). Each model was trained with k-1 folds and validated with the kth fold. This process was repeated until all folds were used once as the validation set. Twenty permutations were performed in total, repeating the validation process for each fold within each permutation. Final results of each model are the averages of the validations across all folds and all iterations (n = 100).

Patient	Disease Status	Primary Tumor (T) classification	Regional Lymph Node (N) Classification	AJCC Staging	Age at Sample Collection	#IMC ROI samples used for ML analysis
1	Primary	1	2	IIIA	55	5
1	Metastatic	N/A	N/A	IV	57	4
2	Primary	2	2	IIIA	53	5
2	Metastatic	N/A	N/A	IV	56	5
3	Primary	Right :2 Left:2	Right :1a Left:0	Right: IIB Left: IIA	63	5
3	Metastatic	N/A	N/A	IV	64	4
4	Primary	3	3a	IIIC	35	5
4	Metastatic	N/A	N/A	IV	36	4
5	Primary	1a	0	IA	51	5
5	Metastatic	N/A	N/A	IV	53	2
6	Primary	1c	0	IA	30	4
6	Metastatic	N/A	N/A	IV	32	2
7	Primary	2	2a	IIIA	51	5
7	Metastatic	N/A	N/A	IV	52	2
8	Primary	4b	2a	IIIB	59	4
8	Metastatic	N/A	N/A	IV	61	3
9	Primary	2	3	IIIC	28	5
9	Metastatic	N/A	N/A	IV	31	5
10	Primary	2	2	IIIA	69	5
10	Metastatic	N/A	N/A	IV	73	5
11	Primary	Right :2 Left:1c	Right :3 Left:1	Right: IIIC Left: IIA	49	5
11	Metastatic	N/A	N/A	IV	53	3
12	Primary	1b	1mi	IB	45	5
12	Metastatic	N/A	N/A	IV	48	5
13	Primary	1c	1	IIA	32	5
13	Metastatic	N/A	N/A	IV	36	4
14	Primary	1c	0	IA	61	5
14	Metastatic	N/A	N/A	IV	65	3
15	Primary	1c	1	IIA	57	5
15	Metastatic	N/A	N/A	IV	58	4

Table 47 Breast cancer patient characteristics. N/A = Not Available. TNM metastasis classification was 0 and 1 for primary and metastatic disease statuses, respectively. Note: "1mi" denotes micrometastases (<2 mm), which were classified as 1.

6.3.2 Marker Clusters Identified from IMC Data

Representative paired primary and BCLM samples are shown in **Figure 36**. The IMC data were randomly distributed before and after mean aggregation (**Figure 40** and **Figure 41**, respectively). To confirm that the clusters were not skewed by analytical batch, a PLS-DA analysis of the post-preprocessed data was performed, showing that the batches were homogeneous (**Figure 42**). Tumor and TME IMC markers in preserved clusters are summarized in **Table 48**. Out of 23 marker clusters identified across batches, 20 were shared across batches and were kept for analysis. To evaluate whether BCLM patient IMC clusters could in principle be separated into Low (<median) or High (≥median) groups using primary cluster densities, a PLS-DA analysis showed that this separation was feasible ($p < 0.01$) (**Figure 43**) but was unsuccessful in 19 out of 20 cases when using covariates only ($p < 0.05$) (**Figure 44**).
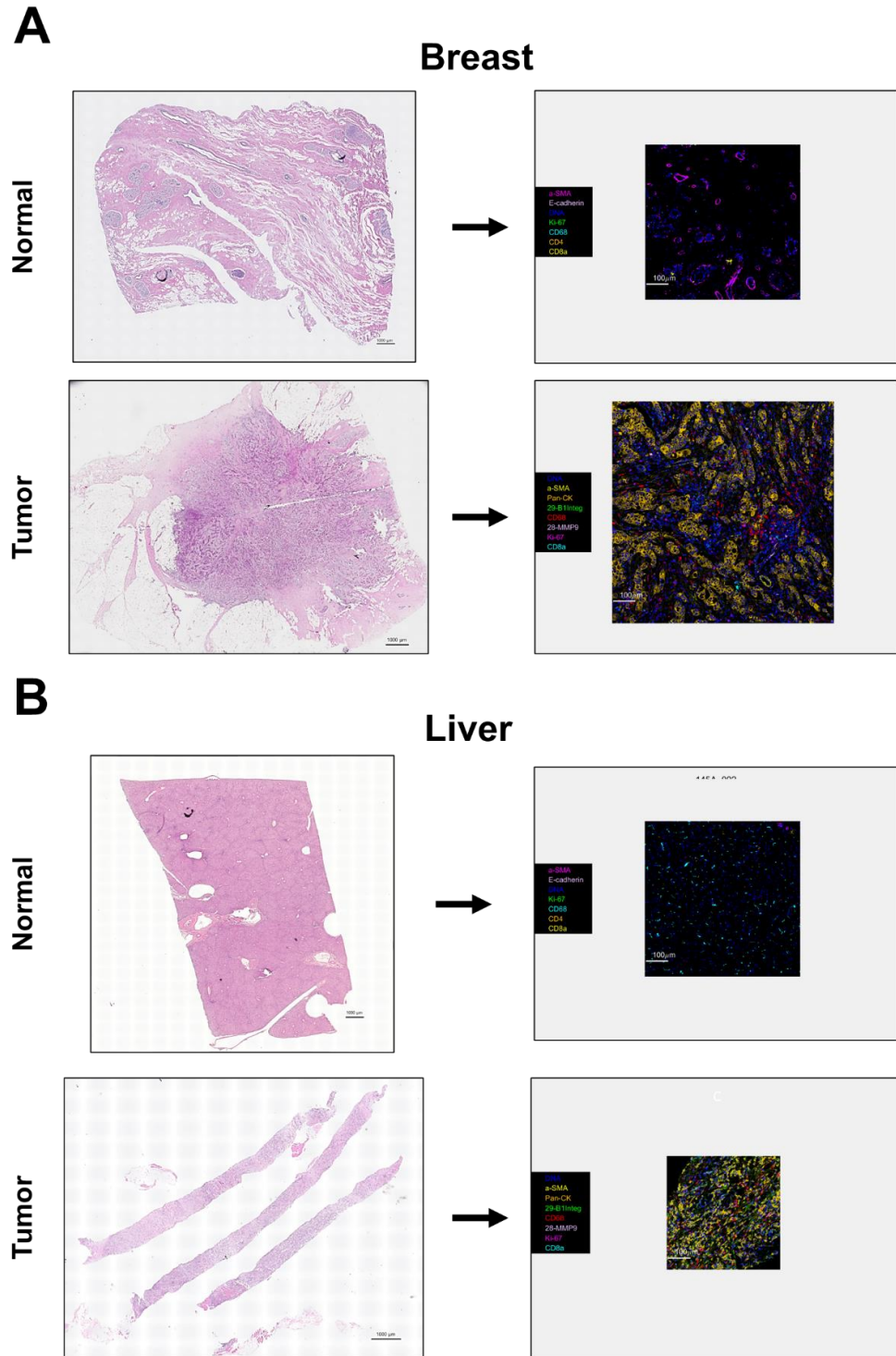
Figure 36 Representative H&E-stained slices of normal and tumor tissue, and corresponding IMC images from (A) breast and (B) liver tissue.

Biological Marker	Associated cell expressions in Tumor Microenvironment	References
CD14	Monocytes/Macrophage – LPS on bacteria Detector	[157, 257, 340, 387]
CD163	TAM, alternatively activated or anti-inflammatory macrophages (M2) Scavenger Receptor	[342, 388]
CD206	M2 Macrophages – mannose Receptor	[341, 389, 390]
CD31	Endothelial marker	[361]
CD4	Helper T-cells – transmembrane glycoprotein	[366, 391]
CD56	NK mainly and some T-cells, monocytes, and dendritic cells	[367-369]
CD68	Circulating/tissue macrophages (monocytic lineage), mainly M1 – promote phagocytosis	[343, 392]
CD8a	Cytotoxic T-cells and some NKs – transmembrane glycoprotein	[391, 393-395]
Collagen	Collagen marker	[351]
E-Cadherin (E-cad)	Expression in normal breast tissue	[373, 396, 397]
HIF1α	Hypoxia	[349, 350]
Ki-67	Cancer cells – proliferation	[358]
MMP9	Regulates and breaks down extracellular matrix in normal physiological conditions	[355-357]
PD1	immune cells including T-cells – Programmed cell death protein 1	[363]
PD-L1	Suppression of adaptive immunity – cancer prognostic marker	[300, 363, 398-400]
pERK	Signal transduction protein – regulates a variety of cellular processes	[359, 360]
αSMA	Alpha-smooth muscle actin	[352-354]

Table 48 Markers identified by IMC in BCLM and primary and breast cancer samples.

6.3.3 Correlation Analysis

To quantify the relationships between cluster densities, a correlation analysis was performed between primary and BCLM data (**Figure 37**). Within primary, CD163+ was positively correlated with CD163+MMP9+ (r = 0.751, p = 0.0013) and CD68+CD163+CD206+ (ρ = 0.762, p = 9.7E-4). For BCLM, CD68+MMP9+ was

positively correlated with MMP9+ (r = 0.861, p = 3.8E-5). Strong correlations between

primary clusters and BCLM clusters were observed: primary CD68+ expression was

negatively correlated with BCLM CD14+ (r = -0.751, p = 0.0012) and positively

correlated with BCLM CD31+ (r = 0.763, p = 9.3E-4). Additionally, primary

CD163+MMP9+ was positively correlated with BCLM CD163+MMP9+ (r = 0.763, p =

9.4E-4). No primary clusters were found to significantly differ after Bonferroni

adjustment between patients separated by low (<median) or high (≥median) BCLM

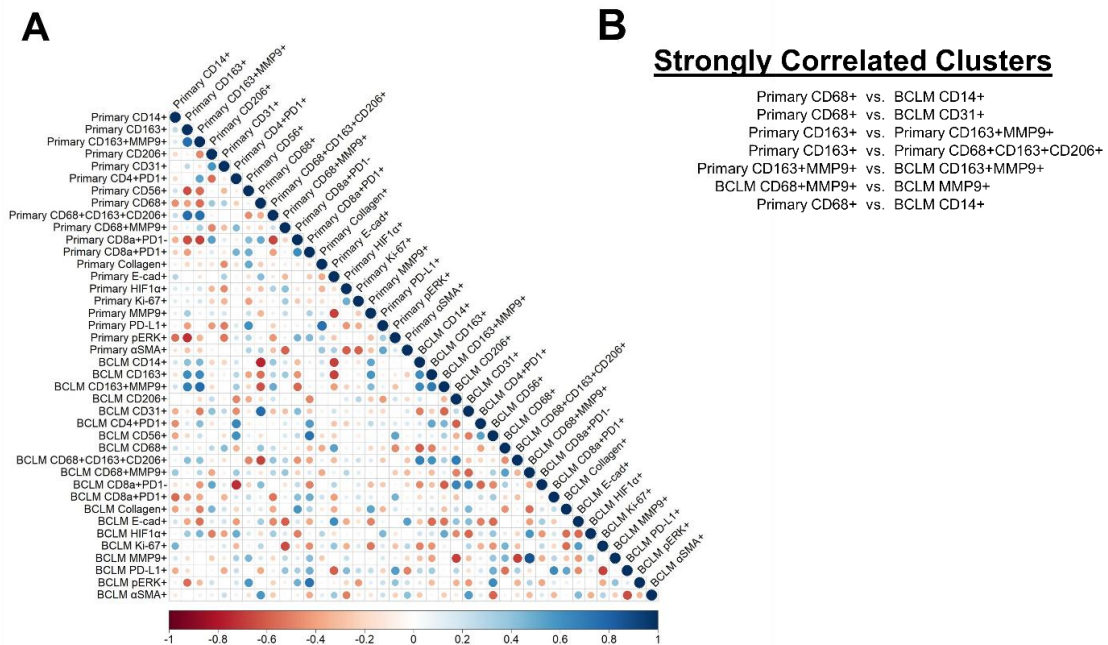cluster expression (p-adj = 0.0025).

Figure 37 Cluster correlations. (A) Correlations between primary (breast) and BCLM

(liver) IMC clusters. (B) Pairs of strongly correlated clusters (≥0.75).

6.3.4 Prediction of BCLM Markers from Primary Markers

To evaluate the predictive potential of the primary TME at predicting the BCLM TME, ML models were trained to classify cluster levels in patients as low expression (<median) or high expression (≥median). ML models were selected by maximum validation subset AUROC per BCLM cluster (**Table 50**). Validation subset AUROC for all optimized ML models was ≥0.75, with 95% confidence in all cases ≥0.70 (**Figure 38**). This performance was supported by F1 ≥0.70 for all ML models. The lowest AUROC and F1 was achieved for predicting BCLM CD56+, with *glmboost* validation subset AUROC = 0.770 (95% CI 0.705-0.835) and F1 = 0.726. Variable importance of primary clusters to predict BCLM clusters are in **Table 51** through **Table 70** and visualized in **Figure 45** through **Figure 49**. AUROC and F1 across feature subsets are visualized in **Figure 50** and **Figure 51**, respectively.
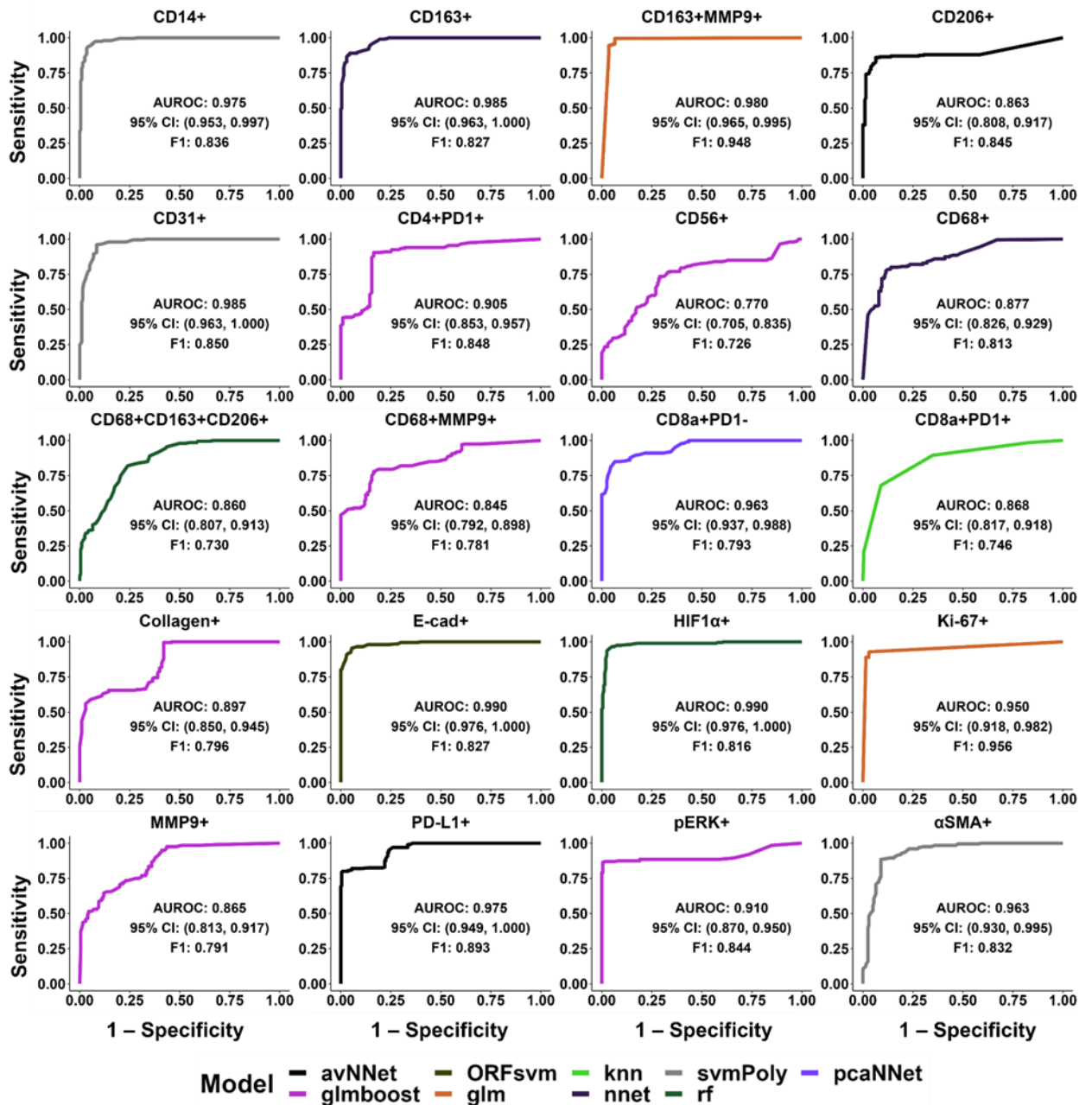
Figure 38 AUROC curves of models predicting BCLM IMC cluster density expression using primary cluster densities. One ML model was created per BCLM cluster.

To check whether covariates only instead of marker clusters could predict the BCLM TME, the ML workflow was performed using covariates as features. Covariates

included patient age at primary resection, time between primary and BCLM resections, T and N components from TNM score, and AJCC staging. Patients with more than one TNM grade were ascribed the more advanced grade. Seven out of 20 models with the maximum validation subset AUROC had AUROC <0.7 and 12 out of 20 models had a lower AUROC 95% confidence interval of <0.7 (**Figure 52**). Only CD68+CD163+CD206+ and MMP9+ had higher validation subset AUROC using covariates (0.945; 95% CI 0.922-0.968 and 0.897; 95% CI 0.853-0.942, respectively) than cluster density-informed ML models (0.860; 95% CI 0.807-0.913 and 0.865; 95% CI 0.813-0.917, respectively). These results indicate that covariates alone would generally be insufficient to predict the BCLM TME.

6.3.5 Identification of Key Primary Markers

Lastly, to identify which primary clusters were most important to predict the BCLM TME, the variable importance rank (1 [high importance] through 20 [low importance]) for each primary cluster was determined for each of the 20 BCLM cluster densities. Relative rankings (**Figure 39**) enable comparisons between differing ML rankings since the scale of *varImp* output differs based on the ML model selected. To prevent ranking biases, clusters with zero variable importance were uniformly set to the lowest importance rank. This analysis found that CD68+ had the highest average relative rank of all 20 clusters (5.55) while Collagen+ had the lowest (11.9) (**Table 49**).
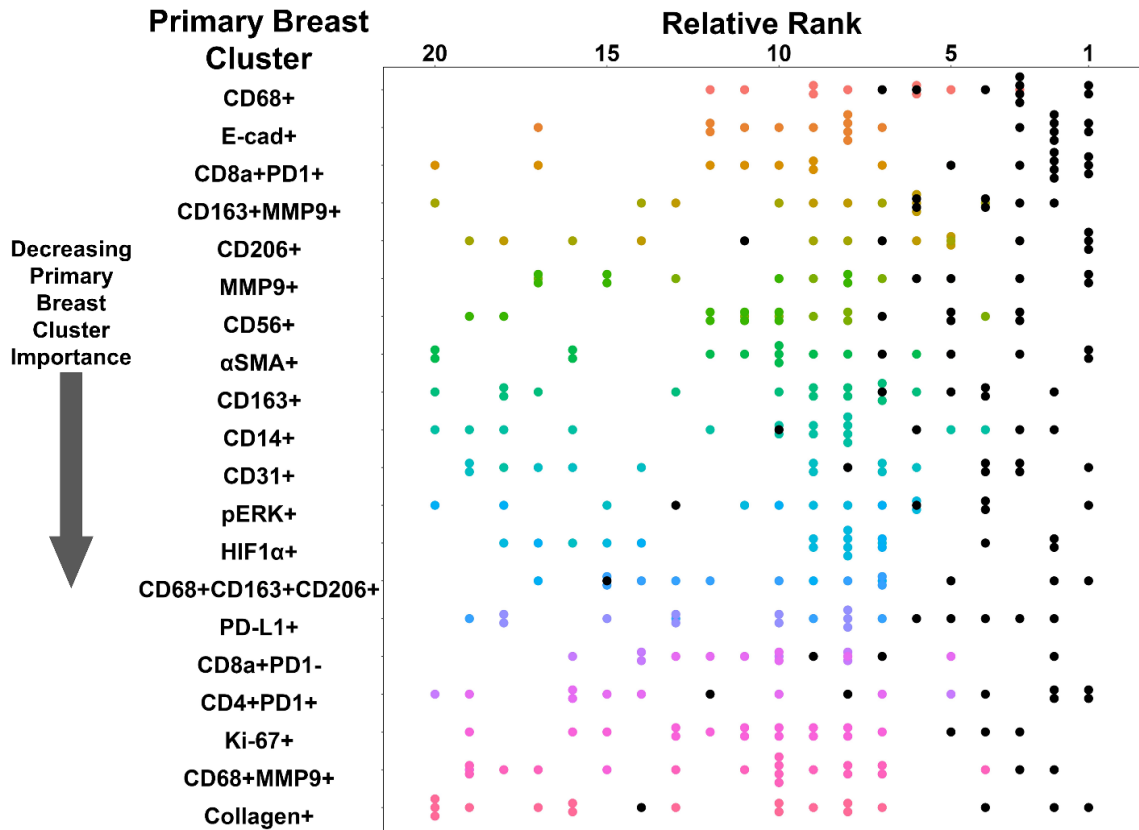
Figure 39 Primary IMC clusters sorted by average relative rank across all 20 ML models (highest rank denoted by lowest number). Higher primary clusters are more important to ML models than lower primary clusters. Black dots indicate instances where cluster was selected for ML predictions of BCLM cluster predictions. Clusters with zero variable importance were considered to have the minimum lowest relative rank. Clusters CD163+MMP9+ and CD206+ had tied importance.

Primary Marker	Average Relative Ranking
CD68+	5.55
E-cad+	6.83
CD8a+PD1+	7.40
CD163+MMP9+	8.10
CD206+	8.10
CD56+	9.15

MMP9+	9.15
αSMA+	9.44
CD163+	9.45
CD14+	9.55
CD31+	9.56
HIF1α+	9.61
pERK+	9.61
CD68+CD163+CD206+	9.70
PD-L1+	9.75
CD4+PD1+	9.85
CD8a+PD1-	9.85
Ki-67+	10.17
CD68+MMP9+	10.95
Collagen+	11.89

Table 49 Average relative rank for all primary clusters across all 20 BCLM predictions. Smaller values imply higher relative rank, suggesting primary marker was more important in predicting the BCLM TME.

6.4 Discussion

This proof-of-concept study provides evidence that the BCLM TME can in principle be predicted from the primary TME, which could longer term aid in tailoring immunotherapeutic regimens on a patient-specific basis. BCLM are a common hallmark of advanced stage breast cancer, which, due to low vascularization [9], often exhibit physiological resistance to intravenously delivered chemotherapeutics. The TME can play an important role not only in nanotherapy of BCLM but also other therapeutic approaches. This fact necessitates patient-specific evaluation of BCLM TME to optimize treatment efficacy. As a first step towards this goal, this study developed a ML workflow to predictively link the primary TME to the BCLM TME. The dataset of IMC cluster densities from BCLM liver core biopsies was adequately predicted using paired IMC cluster density data from the primary tumor. IMC markers included macrophage (CD68,

CD163, CD206) and monocytes (CD14), local immune response composition (CD56, CD4, CD8a), PD-L1 (PD1, PD-L1), and those denoting tumor tissue prevalence (Ki-67, pERK) and invasiveness (E-cad), hypoxia prevalence (HIF1α), vascularity (CD31) and ECM composition (αSMA, collagen, MMP9). The ML approached achieved a maximum AUROC ≥0.75 with 95% CI ≥0.7 for all markers.

Rankings of different primary clusters were computed, finding that primary CD68, a pan-macrophage marker [343], was the most significant feature overall at predicting the BCLM TME, with all 20 clusters being included for model predictions (**Figure 39**). This is consistent with previous work documenting macrophage influence in the TME and that the M1/M2 ratio can serve as a prognostic marker in multiple tumor types when considering conventional therapies [401-403]. M1 macrophages kill tumor cells via multiple pathways, including release of inflammatory cytokines (IL6, IL12, TNF, IL23, etc.), reactive oxygen species, nitrogen intermediates, and other factors [194, 404] while M2 promote immunosuppression, tumor growth, progression and resistance to therapy via secretion of factors such as transforming growth factor β (TGF-β), IL-10, IL-1, Vascular Endothelial Growth Factor A (VEGF-A) that mediates angiogenesis [159, 235, 345], and other growth factors [405]. Further, TGF-β has also been linked to ECM dysregulation across multiple cancer types [406]. CD4 T-cells can be influenced by macrophages [195, 200]. CD206 is expressed primarily by M2-like macrophages [341, 390] and dendritic cells [341, 389, 390, 407] and was tied with CD163+MMP9+ as the fourth most important feature by relative rank (**Figure 39**). The CD56+ primary cluster (rank 6 out of 20) indicates NK cell presence [367-369], which could potentially be

therapeutically targeted. In addition, CD163, a marker of tumor-associated macrophages, especially M2, was used in CD163+MMP9+ (rank 4 out of 20) and CD163+ (rank 9 out of 20) primary clusters (**Table 49**) [342]. Previous work has indicated that M2 macrophages could potentially sensitize tumors to nanotherapeutics such as MSV-nab-PTX [60]. Longer term, the results here could also aid in identifying patients that could benefit from T-cell-based immunotherapies since macrophages have been shown to limit cytotoxic T-cell efficacy in liver metastases [46, 408].

The CD8a+PD1+ cluster (rank 3 out of 20) combines CD8a, a cytotoxic T-cell cell surface marker [393, 394], and PD1, a marker expressed by CD8+ T-cells [363] that is associated with PD-L1-induced T-cell exhaustion [51, 52]. Exhausted cytotoxic T-cells exhibit reduced tumor cytotoxicity and are a hallmark of decreased immunotherapeutic efficacy [51, 52]. Blocking PD-L1 using durvalumab has recently improved survival in triple-negative breast cancer independently of pathological complete response [409]. Recently, macrophages and myofibroblasts have been found to be major PD-L1 expressors within pancreatic adenocarcinoma (PDAC) TME [53] and PDAC liver metastatic TME, respectively [52, 53]. Additionally, it was found that PD-L1 expression in liver metastasis of colorectal tumors was higher than in primary tumors [410]. Future work could investigate the potential of targeting potential PD1/PD-L1 expression, which may also be connected to macrophage and myofibroblast presence.

In addition to immune species in the TME, markers directly associated with primary tissue characteristics were also evident in the ML model rankings. E-cad, a cell-

cell adhesion protein with tumor suppressing properties [396, 397, 411], and MMP9, a matrix metalloprotease (MMP) that breaks down ECM [357], were ranked second and seventh, respectively (**Table 49**). Suppression of E-cad facilitates epithelial-to-mesenchymal transition (EMT) in primary tissue, a key step in metastatic formation [397, 411]. However, recent work has suggested that high expression of E-cad is required for metastatic formation while low E-cad may increase primary tumor invasiveness, suggesting that a E-cad-mediated therapeutic may aid in reducing metastatic formation [373]. While early literature linked MMP9 expression in mice with reduced angiogenesis [412] and raised innate anti-tumor immune response [413], it has been consistently associated with decreased survival [414-418] and has been viewed recently as a potential therapeutic target in breast cancer [356, 357, 419]. Overall, these findings suggest development of BCLM patient-specific therapeutic strategies may benefit from considering both immune species and tumor cells in the TME.

Despite the wide range of TME phenomena covered by the clusters detected in this study, they only represent a subset of the TME. T-cell markers such as forkhead box protein P3 (FoxP3) [420] or CD45 [421] could be included to further assess potential T-cell mediated therapeutic activity. Other immune markers, such as CD86 expressed by B-cells and antigen presenting cells, could be investigated [422]. Future work with larger sample sizes and diverse sampling pools could prospectively confirm and further refine ML model predictions, given that the availability of paired human primary and BCLM samples is limited. BCLM ROI were obtained via core needle biopsies, which, in the case of metastatic malignancies in the liver, have been found to afford more tissue for analysis

and improve diagnostic quality relative to fine needle aspiration liver biopsies [423]. Considering the clinical uniqueness of paired breast and BCLM samples this study emphasized cohort size; thus, BCLM ROI per patient was varied from two to five depending on number of ROI deemed eligible for analysis. Subsequent studies should focus on additional ROI to overcome this limitation. In addition, while primary biopsies and resections are routinely obtained [371, 372], other predictors of BCLM TME could be investigated. For example, blood-based metabolomics have shown promise to diagnose solid tumors and metastatic formation [424]. Metabolites obtained from lung cancer biopsies have been used to predict overall survival and progression free survival using Kaplan Meier [386] analysis and ensemble ML models [425]. Metabolites have informed a mechanistic model of lung tumor growth to predict survival [426]. Similar approaches could help bolster the TME links between primary breast tumors and BCLM to arrive at patient-specific optimal immunotherapeutic strategies.

6.5 Supplementary Information

6.5.1 Supplementary Tables

BCLM Cluster	ML Model Description from *caret*	R Library::R Function	Hyperparameter	Description	Value
CD14+	Least Squares Support Vector Machine with Polynomial Kernel	*kernlab::svmPoly()*	degree	Polynomial Degree	1
			scale	Scale	0.01
			tau	Regularization Parameter	128
CD163+	Neural Network	*nnet::nnet()*	size	#Hidden Units	15
			decay	Weight Decay	0.00750
CD163+MMP9+	Bayesian Generalized Linear Model	*stats::glm()*	N/A	N/A	N/A
CD206+	Model Averaged Neural Network	*nnet:avNNet()*	size	#Hidden Units	5

			decay	Weight Decay	1e-04
			bag	Bagging	FALSE
CD31+	Least Squares Support Vector Machine with Polynomial Kernel	*kernlab::svmPoly()*	degree	Polynomial Degree	3
			scale	Scale	10
			tau	Regularization Parameter	32
CD4+PD1+	Boosted Generalized Linear Model	*mboost::glmboost()*	mstop	# Boosting Iterations	500
			prune	AIC Prune	No
CD56+	Boosted Generalized Linear Model	*mboost::glmboost()*	mstop	# Boosting Iterations	100
			prune	AIC Prune	No
CD68+	Neural Network	*nnet::nnet()*	size	#Hidden Units	3
			decay	Weight Decay	0.000562
CD68+CD163+CD206+	Quantile Random Forest	*randomForest::rf()*	mtry	#Randomly Selected Predictors	2
CD68+MMP9+	Boosted Generalized Linear Model	*mboost::glmboost()*	mstop	# Boosting Iterations	500
			prune	AIC Prune	No
CD8a+PD1+	k-Nearest Neighbors	*caret::knn()*	kmax	Max. #Neighbors	7
			distance	Distance	7
			kernel	Kernel	7
CD8a+PD1-	Neural Networks with Feature Extraction	*nnet::pcaNNet()*	size	#Hidden Units	3
			decay	Weight Decay	0.1
Collagen+	Boosted Generalized Linear Model	*mboost::glmboost()*	mstop	# Boosting Iterations	150
			prune	AIC Prune	No
E-cad+	Oblique Random Forest	*obliqueRF::ORFsvm()*	mtry	#Randomly Selected Predictors	6
HIF1α+	Quantile Random Forest	*randomForest::rf()*	mtry	#Randomly Selected Predictors	3
Ki-67+	Bayesian Generalized Linear Model	*stats::glm()*	N/A	N/A	N/A
MMP9+	Boosted Generalized Linear Model	*mboost::glmboost()*	mstop	# Boosting Iterations	400
			prune	AIC Prune	No

			size	#Hidden Units	1
PD-L1+	Model Averaged Neural Network	*nnet:avNNet()*	decay	Weight Decay	1e-04
			bag	Bagging	False
pERK+	Boosted Generalized Linear Model	*mboost::glmboost()*	mstop	# Boosting Iterations	300
			prune	AIC Prune	no
αSMA+	Least Squares Support Vector Machine with Polynomial Kernel	*kernlab::svmPoly()*	degree	Polynomial Degree	2
			scale	Scale	1000
			tau	Regularization Parameter	64

Table 50 Hyperparameters used for AUROC-optimized Machine Learning models.

N/A = Not Applicable.

Cluster in Primary	Included In Optimal Model	Variable Importance
MMP9+	X	0.857
E-cad+	X	0.804
Ki-67+	X	0.768
CD163+MMP9+	X	0.732
CD68+		0.696
CD14+		0.679
PD-L1+		0.679
CD68+CD163+CD206+		0.661
CD56+		0.643
CD163+		0.625
CD8a+PD1-		0.625
CD4+PD1+		0.607
Collagen+		0.607
CD206+		0.607
pERK+		0.607
HIF1α+		0.571
CD8a+PD1+		0.554
CD31+		0.554
CD68+MMP9+		0.536
αSMA+		0.518

Table 51 Variable Importance for predicting BCLM CD14+ using primary clusters.

Larger values imply higher variable importance. Clusters used in the optimal model are

marked with "X."

Cluster in Primary	Included In Optimal Model	Variable Importance
E-cad+	X	20.253
CD163+	X	12.066
CD68+	X	11.295
CD163+MMP9+	X	9.002
MMP9+	X	7.475
pERK+	X	5.927
CD56+	X	5.530
CD4+PD1+	X	5.306
CD14+		3.569
Ki-67+		3.303

αSMA+		3.185
CD8a+PD1+		3.031
PD-L1+		2.882
CD8a+PD1-		2.301
HIF1α+		1.373
CD31+		1.222
CD68+CD163+CD206+		0.907
CD206+		0.804
CD68+MMP9+		0.539
Collagen+		0.029

Table 52 Variable Importance for predicting BCLM CD163+ using primary clusters.

Larger values imply higher variable importance. Clusters used in the optimal model are

marked with "X."

Cluster in Primary	Included In Optimal Model	Variable Importance
CD206+	X	0.0000511
CD4+PD1+	X	0.0000322
CD68+	X	0.0000281
CD163+	X	0.0000260
MMP9+		0.0000249
CD163+MMP9+		0.0000246
CD8a+PD1+		0.0000240
PD-L1+		0.0000237
CD68+CD163+CD206+		0.0000233
CD68+MMP9+		0.0000229
CD56+		0.0000188
CD14+		0.0000180
CD8a+PD1-		0.0000178

Table 53 Variable Importance for predicting BCLM CD163+MMP9+ using primary

clusters. Larger values imply higher variable importance. Clusters used in the optimal

model are marked with "X."

Cluster in Primary	Included In Optimal Model	Variable Importance

CD206+	X	0.732
CD8a+PD1+	X	0.696
CD68+		0.661
CD56+		0.661
CD4+PD1+		0.661
PD-L1+		0.643
CD68+CD163+CD206+		0.634
HIF1α+		0.571
αSMA+		0.571
MMP9+		0.554
pERK+		0.554
E-cad+		0.554
CD163+		0.536
CD8a+PD1-		0.536
Ki-67+		0.536
Collagen+		0.536
CD31+		0.536
CD14+		0.518
CD68+MMP9+		0.518
CD163+MMP9+		0.500

Table 54 Variable Importance for predicting BCLM CD206+ using primary clusters.

Larger values imply higher variable importance. Clusters used in the optimal model are

marked with "X."

Cluster in Primary	Included In Optimal Model	Variable Importance
CD68+	X	0.893
CD14+	X	0.839
CD206+	X	0.786
CD31+	X	0.786
CD56+	X	0.768
PD-L1+	X	0.750
CD163+MMP9+		0.679
CD8a+PD1-		0.679
CD8a+PD1+		0.679
Collagen+		0.679
E-cad+		0.625
αSMA+		0.607

CD68+MMP9+		0.607
CD68+CD163+CD206+		0.607
MMP9+		0.607
CD4+PD1+		0.589
HIF1α+		0.589
CD163+		0.554
Ki-67+		0.518
pERK+		0.518

Table 55 Variable Importance for predicting BCLM CD31+ using primary clusters.

Larger values imply higher variable importance. Clusters used in the optimal model are

marked with "X."

Cluster in Primary	Included In Optimal Model	Variable Importance
CD4+PD1+	X	72.705
CD8a+PD1+	X	12.524
αSMA+	X	9.352
CD163+MMP9+		8.851
CD206+		6.388
CD68+		5.221
CD31+		2.076
CD14+		0.000
CD68+MMP9+		0.000
CD163+		0.000
CD68+CD163+CD206+		0.000
MMP9+		0.000
CD56+		0.000
CD8a+PD1-		0.000
PD-L1+		0.000
Ki-67+		0.000
pERK+		0.000
HIF1α+		0.000
E-cad+		0.000
Collagen+		0.000

Table 56 Variable Importance for predicting BCLM CD4+PD1+ using primary

clusters. Larger values imply higher variable importance. Clusters used in the optimal

model are marked with "X."

Cluster in Primary	Included In Optimal Model	Variable Importance
CD8a+PD1+	X	43.623
Collagen+	X	15.671
CD206+		8.660
CD68+		7.337
CD68+CD163+CD206+		7.333
pERK+		6.803
CD68+MMP9+		6.004
CD14+		0.000
CD163+		0.000
CD163+MMP9+		0.000
MMP9+		0.000
CD56+		0.000
CD4+PD1+		0.000
CD8a+PD1-		0.000
PD-L1+		0.000
Ki-67+		0.000
HIF1α+		0.000
E-cad+		0.000
CD31+		0.000
αSMA+		0.000

Table 57 Variable Importance for predicting BCLM CD56+ using primary clusters.

Larger values imply higher variable importance. Clusters used in the optimal model are

marked with "X."

Cluster in Primary	Included In Optimal Model	Variable Importance
αSMA+	X	14.142
HIF1α+	X	11.103
E-cad+	X	9.592
CD31+	X	8.898
CD163+	X	7.808
CD14+	X	7.049
CD206+	X	6.721
Collagen+		5.287
CD68+		4.583

CD56+		4.334
Ki-67+		4.003
CD8a+PD1+		3.638
CD163+MMP9+		3.169
CD68+CD163+CD206+		1.972
CD68+MMP9+		1.825
CD8a+PD1-		1.552
MMP9+		1.505
pERK+		1.390
PD-L1+		1.163
CD4+PD1+		0.265

Table 58 Variable Importance for predicting BCLM CD68+ using primary clusters.

Larger values imply higher variable importance. Clusters used in the optimal model are

marked with "X."

Cluster in Primary	Included In Optimal Model	Variable Importance
CD68+	X	1.226
CD68+MMP9+	X	1.099
CD56+	X	0.972
pERK+	X	0.651
αSMA+	X	0.449
CD163+MMP9+		0.350
HIF1α+		0.228
CD14+		0.221
CD8a+PD1-		0.220
CD68+CD163+CD206+		0.199
CD8a+PD1+		0.198
Ki-67+		0.189
MMP9+		0.165
CD206+		0.157
CD4+PD1+		0.130
Collagen+		0.122
E-cad+		0.110
PD-L1+		0.102
CD31+		0.097
CD163+		0.089

Table 59 Variable Importance for predicting BCLM CD68+CD163+CD206+ using

primary clusters. Larger values imply higher variable importance. Clusters used in the

optimal model are marked with "X."

Cluster in Primary	Included In Optimal Model	Variable Importance
CD4+PD1+	X	75.195
CD8a+PD1-	X	10.525
CD56+	X	10.198
CD68+MMP9+		8.573
αSMA+		3.158
CD68+		2.885
CD68+CD163+CD206+		2.364
E-cad+		0.755
CD14+		0.000
CD163+		0.000
CD163+MMP9+		0.000
CD206+		0.000
MMP9+		0.000
CD8a+PD1+		0.000
PD-L1+		0.000
Ki-67+		0.000
pERK+		0.000
HIF1α+		0.000
Collagen+		0.000
CD31+		0.000

Table 60 Variable Importance for predicting BCLM CD68+MMP9+ using primary

clusters. Larger values imply higher variable importance. Clusters used in the optimal

model are marked with "X."

Cluster in Primary	Included In Optimal Model	Variable Importance
CD8a+PD1+	X	0.821
E-cad+	X	0.786
CD68+	X	0.750

CD4+PD1+	X	0.714
CD206+		0.696
CD163+MMP9+		0.679
pERK+		0.679
MMP9+		0.643
CD31+		0.643
CD8a+PD1-		0.607
CD68+MMP9+		0.589
CD56+		0.571
Ki-67+		0.571
HIF1α+		0.571
CD68+CD163+CD206+		0.554
CD14+		0.536
CD163+		0.518
PD-L1+		0.518
Collagen+		0.500
αSMA+		0.500

Table 61 Variable Importance for predicting BCLM CD8a+PD1- using primary

clusters. Larger values imply higher variable importance. Clusters used in the optimal

model are marked with "X."

Cluster in Primary	Included In Optimal Model	Variable Importance
CD68+CD163+CD206+	X	0.786
CD8a+PD1+	X	0.768
CD14+	X	0.750
CD163+MMP9+		0.696
CD8a+PD1-		0.696
pERK+		0.679
CD163+		0.661
E-cad+		0.625
CD206+		0.607
CD68+MMP9+		0.589
CD68+		0.571
CD56+		0.571
Ki-67+		0.571
CD4+PD1+		0.554
PD-L1+		0.554

αSMA+		0.554
MMP9+		0.536
HIF1α+		0.536
CD31+		0.536
Collagen+		0.518

Table 62 Variable Importance for predicting BCLM CD8a+PD1+ using primary

clusters. Larger values imply higher variable importance. Clusters used in the optimal

model are marked with "X."

Cluster in Primary	Included In Optimal Model	Variable Importance
MMP9+	X	47.340
CD163+MMP9+	X	38.648
PD-L1+	X	25.608
CD14+		12.889
CD8a+PD1+		7.033
αSMA+		5.544
CD68+		0.000
CD68+MMP9+		0.000
CD163+		0.000
CD68+CD163+CD206+		0.000
CD206+		0.000
CD56+		0.000
CD4+PD1+		0.000
CD8a+PD1-		0.000
Ki-67+		0.000
pERK+		0.000
HIF1α+		0.000
E-cad+		0.000
Collagen+		0.000
CD31+		0.000

Table 63 Variable Importance for predicting BCLM Collagen+ using primary

clusters. Larger values imply higher variable importance. Clusters used in the optimal

model are marked with "X."

Cluster in Primary	Included In Optimal Model	Variable Importance
αSMA+	X	0.911
E-cad+	X	0.857
CD68+MMP9+	X	0.839
HIF1α+	X	0.839
CD68+CD163+CD206+	X	0.830
CD163+MMP9+	X	0.821
CD163+	X	0.732
MMP9+		0.732
CD68+		0.714
CD56+		0.679
Ki-67+		0.679
CD8a+PD1-		0.661
PD-L1+		0.661
CD31+		0.661
CD4+PD1+		0.625
CD206+		0.607
Collagen+		0.589
pERK+		0.571
CD14+		0.554
CD8a+PD1+		0.518

Table 64 Variable Importance for predicting BCLM E-cad+ using primary clusters.

Larger values imply higher variable importance. Clusters used in the optimal model are marked with "X."

Cluster in Primary	Included In Optimal Model	Variable Importance
CD31+	X	0.790
PD-L1+	X	0.683
CD163+MMP9+	X	0.606
Collagen+	X	0.509
Ki-67+	X	0.421
CD68+	X	0.416
CD8a+PD1-	X	0.411
CD206+		0.340
CD163+		0.309
pERK+		0.274

CD56+		0.270
E-cad+		0.263
CD68+CD163+CD206+		0.254
HIF1α+		0.245
MMP9+		0.208
αSMA+		0.196
CD8a+PD1+		0.187
CD68+MMP9+		0.183
CD4+PD1+		0.178
CD14+		0.167

Table 65 Variable Importance for predicting BCLM HIF1α+ using primary clusters.

Larger values imply higher variable importance. Clusters used in the optimal model are

marked with "X."

Cluster in Primary	Included In Optimal Model	Variable Importance
CD206+	X	0.0001178
CD4+PD1+	X	0.0001025
MMP9+	X	0.0000995
CD163+	X	0.0000988
PD-L1+	X	0.0000978
CD163+MMP9+	X	0.0000978
CD68+	X	0.0000969
CD14+		0.0000952
CD68+MMP9+		0.0000949
CD8a+PD1+		0.0000933
CD56+		0.0000930
CD68+CD163+CD206+		0.0000904
CD8a+PD1-		0.0000878

Table 66 Variable Importance for predicting BCLM Ki-67+ using primary clusters.

Larger values imply higher variable importance. Clusters used in the optimal model are
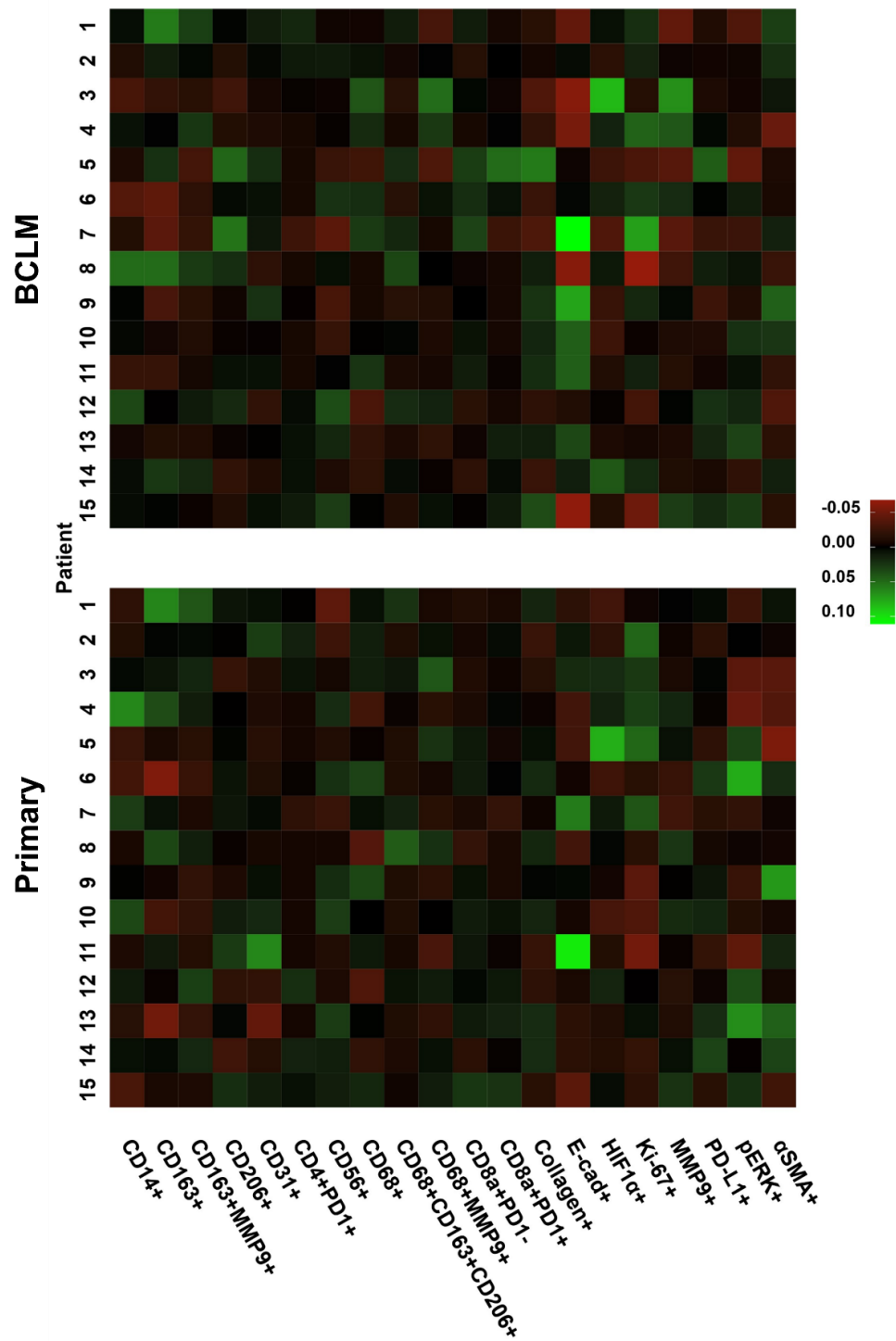
marked with "X."

Cluster in Primary	Included In Optimal Model	Variable Importance

Cluster in Primary	Included In Optimal Model	Variable Importance
Collagen+	X	44.789
CD8a+PD1+	X	37.826
CD31+	X	22.642
CD68+	X	15.997
CD56+	X	13.865
CD206+		3.397
MMP9+		2.660
HIF1α+		1.757
E-cad+		1.226
CD14+		0.000
CD68+MMP9+		0.000
CD163+		0.000
CD163+MMP9+		0.000
CD68+CD163+CD206+		0.000
CD4+PD1+		0.000
CD8a+PD1-		0.000
PD-L1+		0.000
Ki-67+		0.000
pERK+		0.000
αSMA+		0.000

Table 67 Variable Importance for predicting BCLM MMP9+ using primary clusters. Larger values imply higher variable importance. Clusters used in the optimal model are marked with "X."

Cluster in Primary	Included In Optimal Model	Variable Importance
pERK+	X	0.857
E-cad+	X	0.821
CD8a+PD1+	X	0.786
Ki-67+	X	0.750
CD14+		0.714
CD31+		0.696
CD163+		0.679
CD68+MMP9+		0.661
HIF1α+		0.661
αSMA+		0.643
CD8a+PD1-		0.643
CD68+		0.625

		0.607
PD-L1+		0.607
CD163+MMP9+		0.589
CD68+CD163+CD206+		0.589
CD4+PD1+		0.571
MMP9+		0.554
CD56+		0.554
CD206+		0.536
Collagen+		0.518

Table 68 Variable Importance for predicting BCLM PD-L1+ using primary clusters.

Larger values imply higher variable importance. Clusters used in the optimal model are

marked with "X."

Cluster in Primary	Included In Optimal Model	Variable Importance
CD8a+PD1+	X	64.582
CD68+CD163+CD206+	X	19.871
CD31+	X	17.611
pERK+	X	12.553
CD206+		11.857
CD163+		6.104
HIF1α+		5.579
CD68+		3.060
Ki-67+		0.917
CD14+		0.000
CD68+MMP9+		0.000
CD163+MMP9+		0.000
MMP9+		0.000
CD56+		0.000
CD4+PD1+		0.000
CD8a+PD1-		0.000
PD-L1+		0.000
E-cad+		0.000
Collagen+		0.000
αSMA+		0.000

Table 69 Variable Importance for predicting BCLM pERK+ using primary clusters.

Larger values imply higher variable importance. Clusters used in the optimal model are

marked with "X."

Cluster in Primary	Included In Optimal Model	Variable Importance
E-cad+	X	0.804
HIF1α+	X	0.786
CD68+	X	0.768
PD-L1+	X	0.750
CD8a+PD1+	X	0.696
MMP9+	X	0.679
αSMA+	X	0.679
CD31+	X	0.643
CD8a+PD1-	X	0.607
CD14+	X	0.589
CD206+	X	0.589
CD4+PD1+	X	0.589
pERK+	X	0.589
Collagen+	X	0.589
CD68+CD163+CD206+	X	0.571
Ki-67+		0.536
CD68+MMP9+		0.518
CD163+		0.518
CD56+		0.518
CD163+MMP9+		0.518

Table 70 Variable Importance for predicting BCLM αSMA+ using primary clusters.

Larger values imply higher variable importance. Clusters used in the optimal model are

marked with "X."

6.5.2 Supplementary Figures

Figure 40 Heatmap of IMC cluster densities for all patients originating from breast primary and breast cancer liver metastases (BCLM) before mean-aggregation of ROIs.

Figure 41 Heatmap of IMC cluster densities originating from BCLM (top) and primary breast tumors (bottom) after mean-aggregation of ROIs.
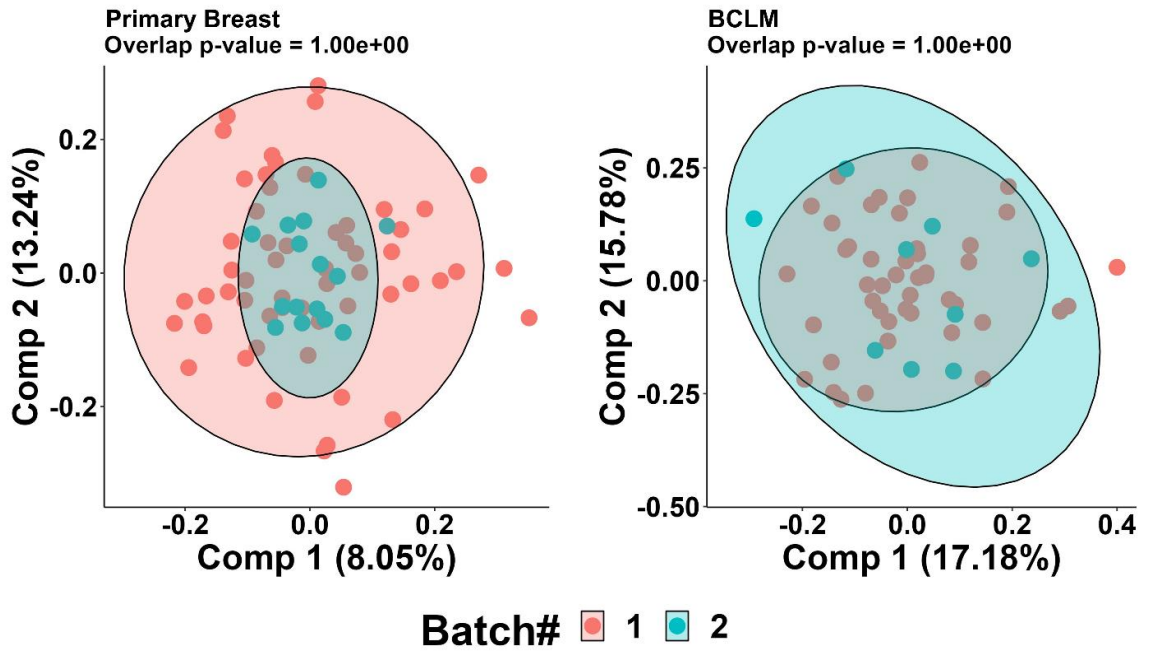
Figure 42 PLS-DA of primary breast and BCLM IMC ROI data by batch number showing that the batches were homogeneous.
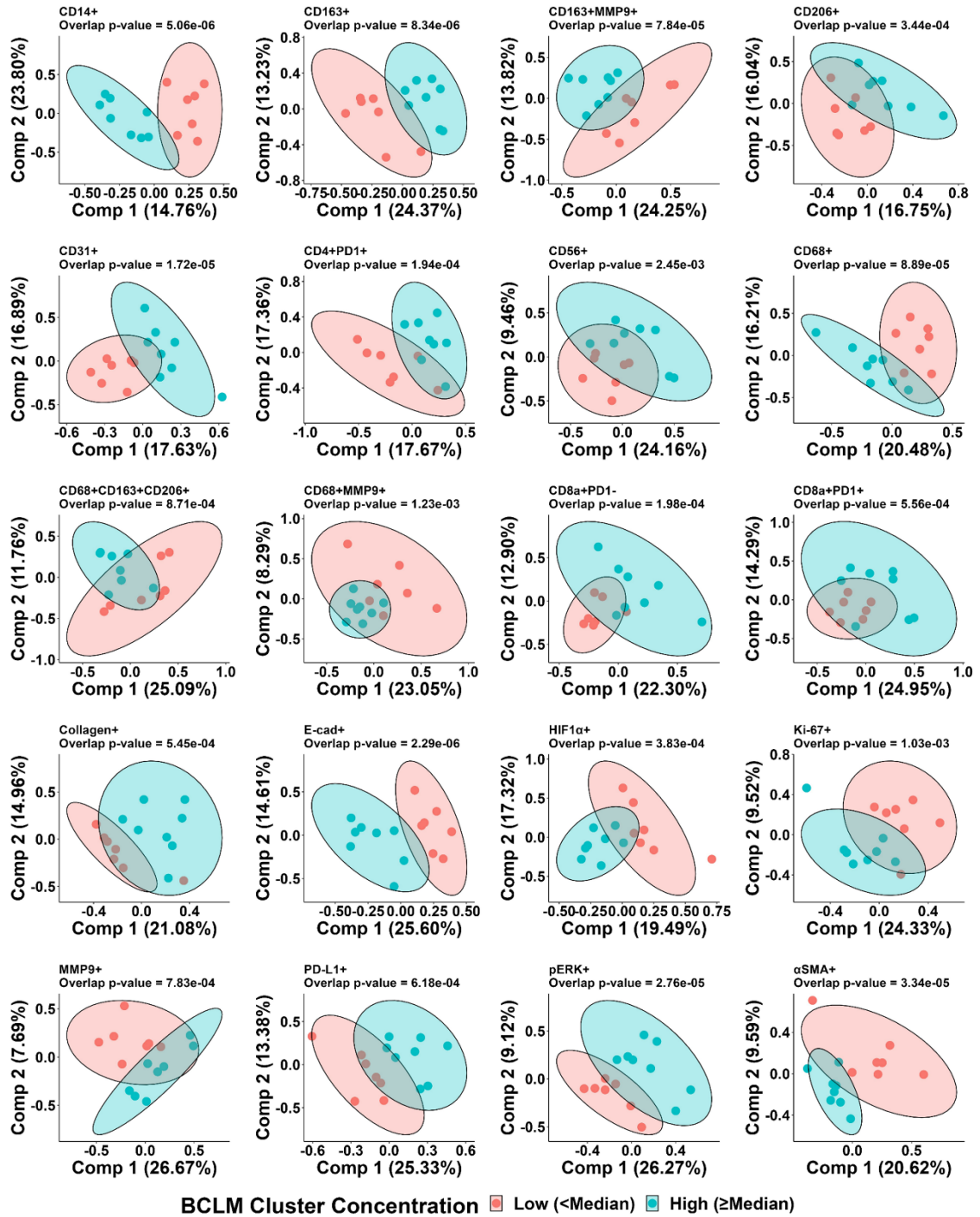
Figure 43 PLS-DA score plots of classifying BCLM patient IMC clusters into Low (<median) or High (≥median) groups using primary cluster densities.
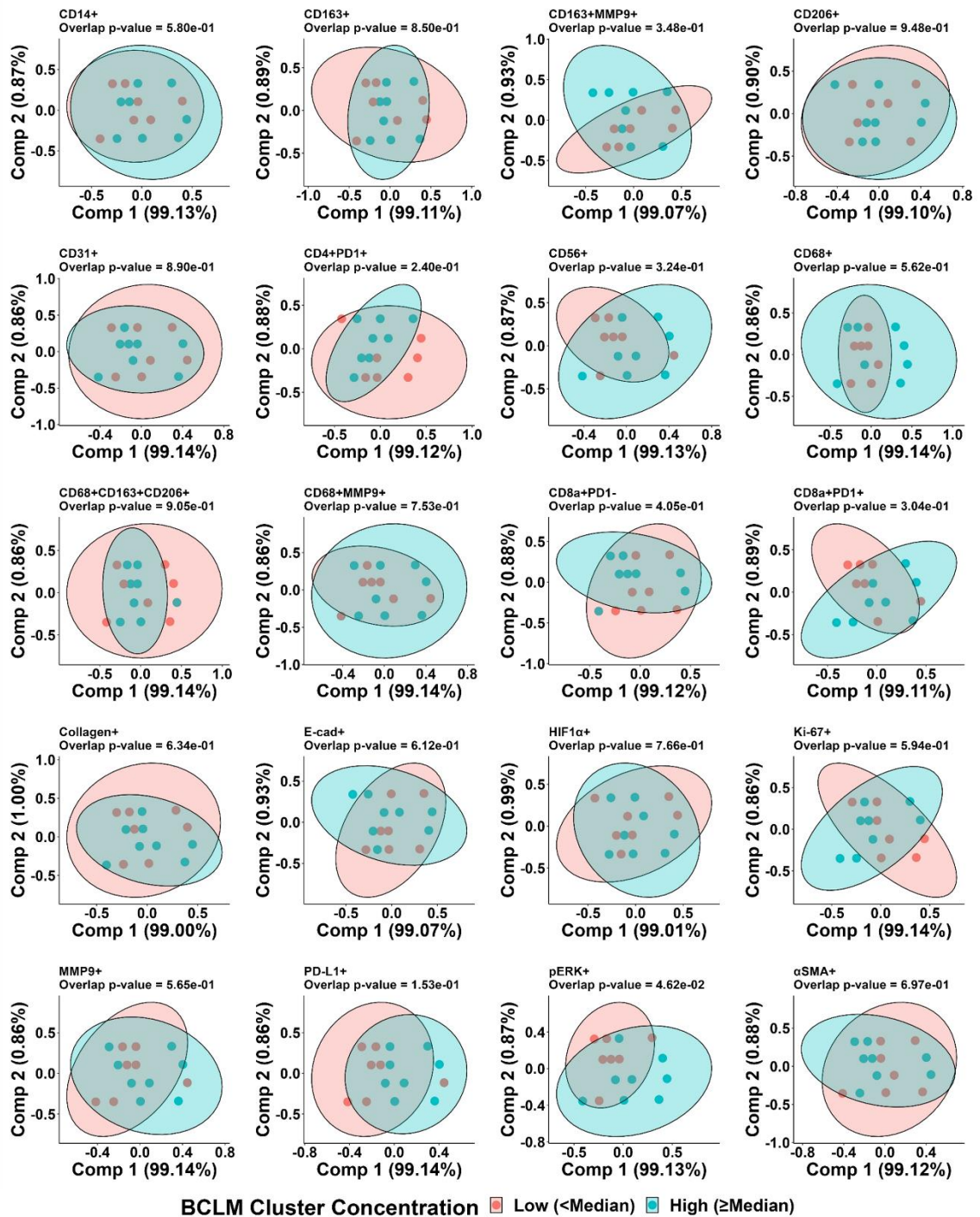
Figure 44 PLS-DA score plots of classifying BCLM patient IMC clusters into Low (<median) or High (≥median) groups using only covariates age and difference in age

from patient breast sample or BCLM sample. Performance of PLS-DA was subpar

even with categorical features added.
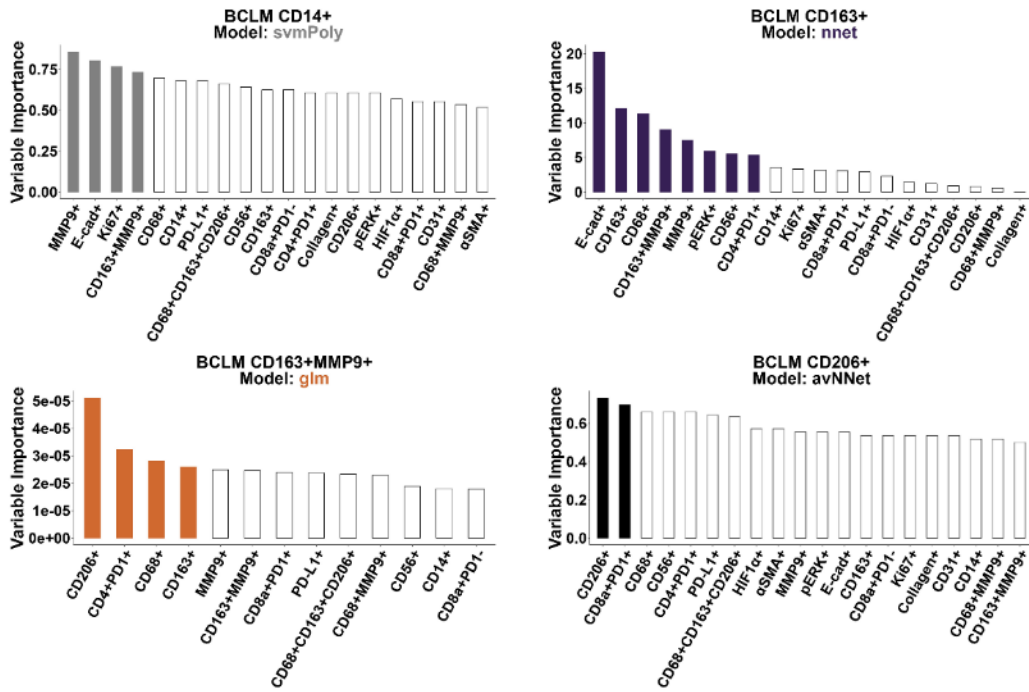
Figure 45 Variable importance for prediction of BCLM CD14+, CD163+,

CD163+MMP9+, and CD206+ using ML models. IMC clusters given zero variable

importance by *varImp* are not shown. Dark bars denote clusters used by the optimized
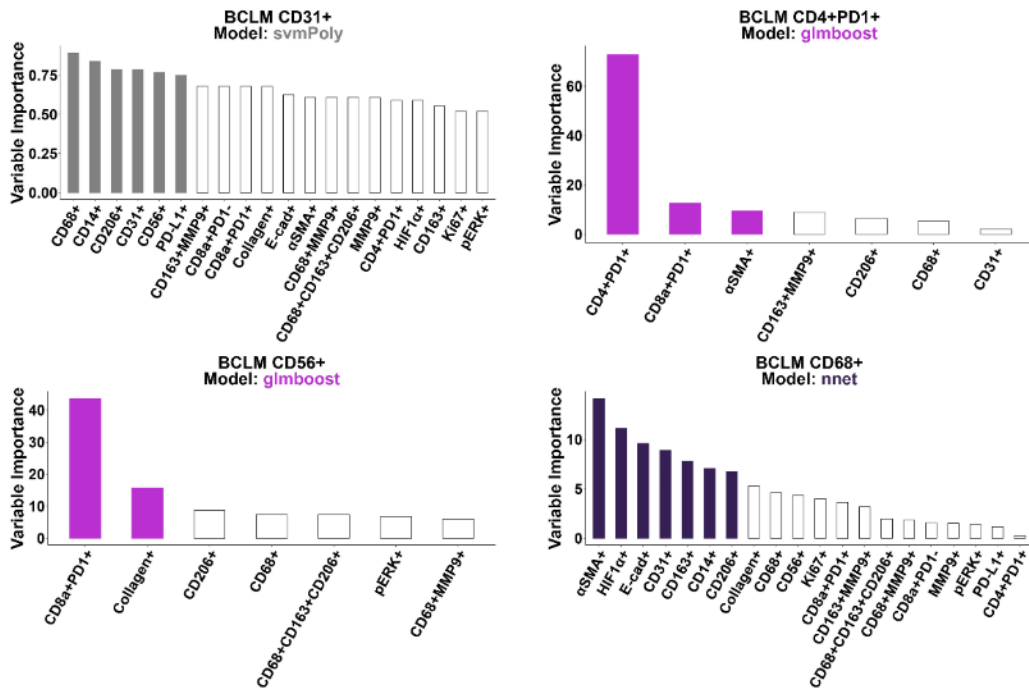
model.

Figure 46 Variable importance for prediction of BCLM CD31+, CD4+PD1+, CD56+, and CD68+ using ML models. IMC clusters given zero variable importance by *varImp* are not shown. Dark bars denote clusters used by the optimized model.
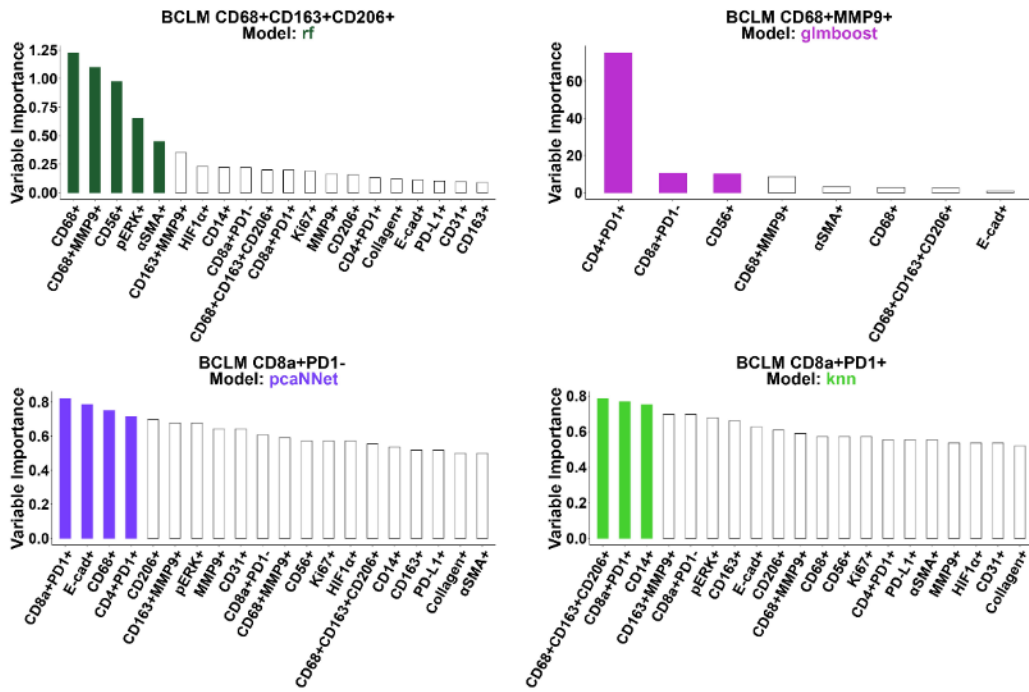
Figure 47 Variable importance for prediction of BCLM CD68+CD163+CD206+, CD68+MMP9+, CD8a+PD1-, and CD8a+PD1+ using ML models. IMC clusters given zero variable importance by *varImp* are not shown. Dark bars denote clusters used by the optimized model.
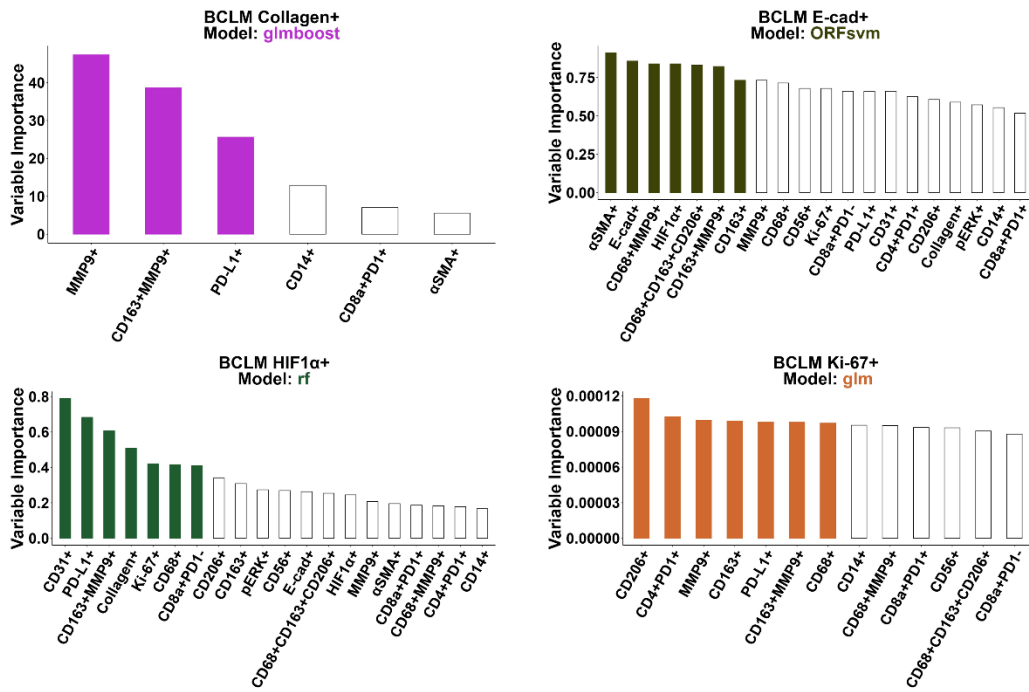
Figure 48 Variable importance for prediction of BCLM Collagen+, E-cad+, HIF1α+, and Ki-67+ using ML models. IMC clusters given zero variable importance by *varImp* are not shown. Dark bars denote clusters used by the optimized model.
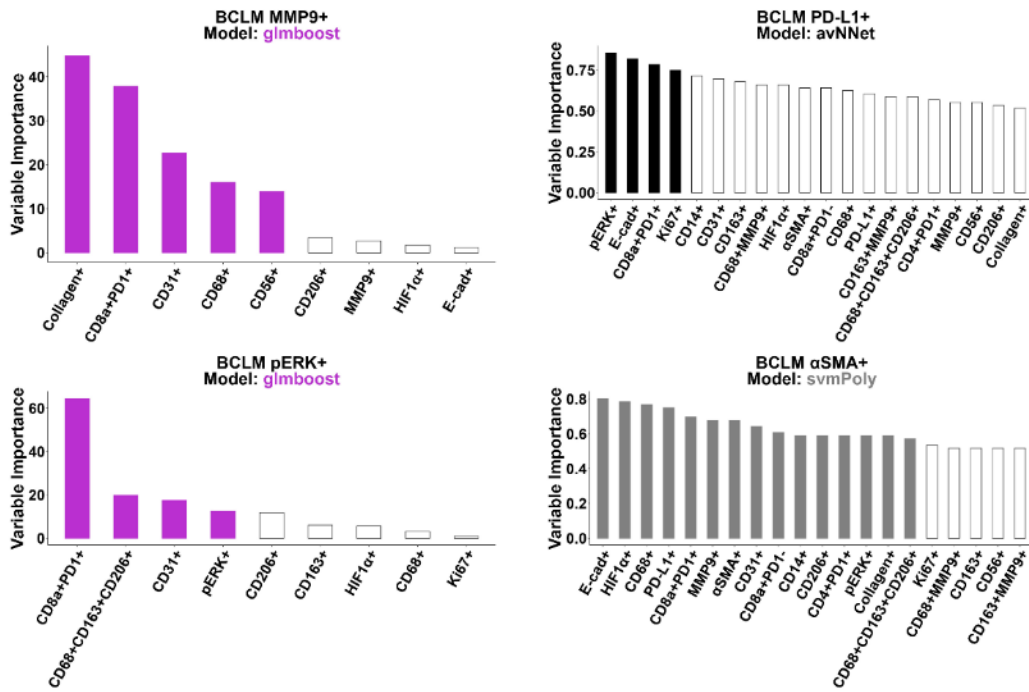
Figure 49 Variable importance for prediction of BCLM MMP9+, PD-L1+, pERK+, and αSMA+ using ML models. IMC clusters given zero variable importance by *varImp* are not shown. Dark bars denote clusters used by the optimized model.
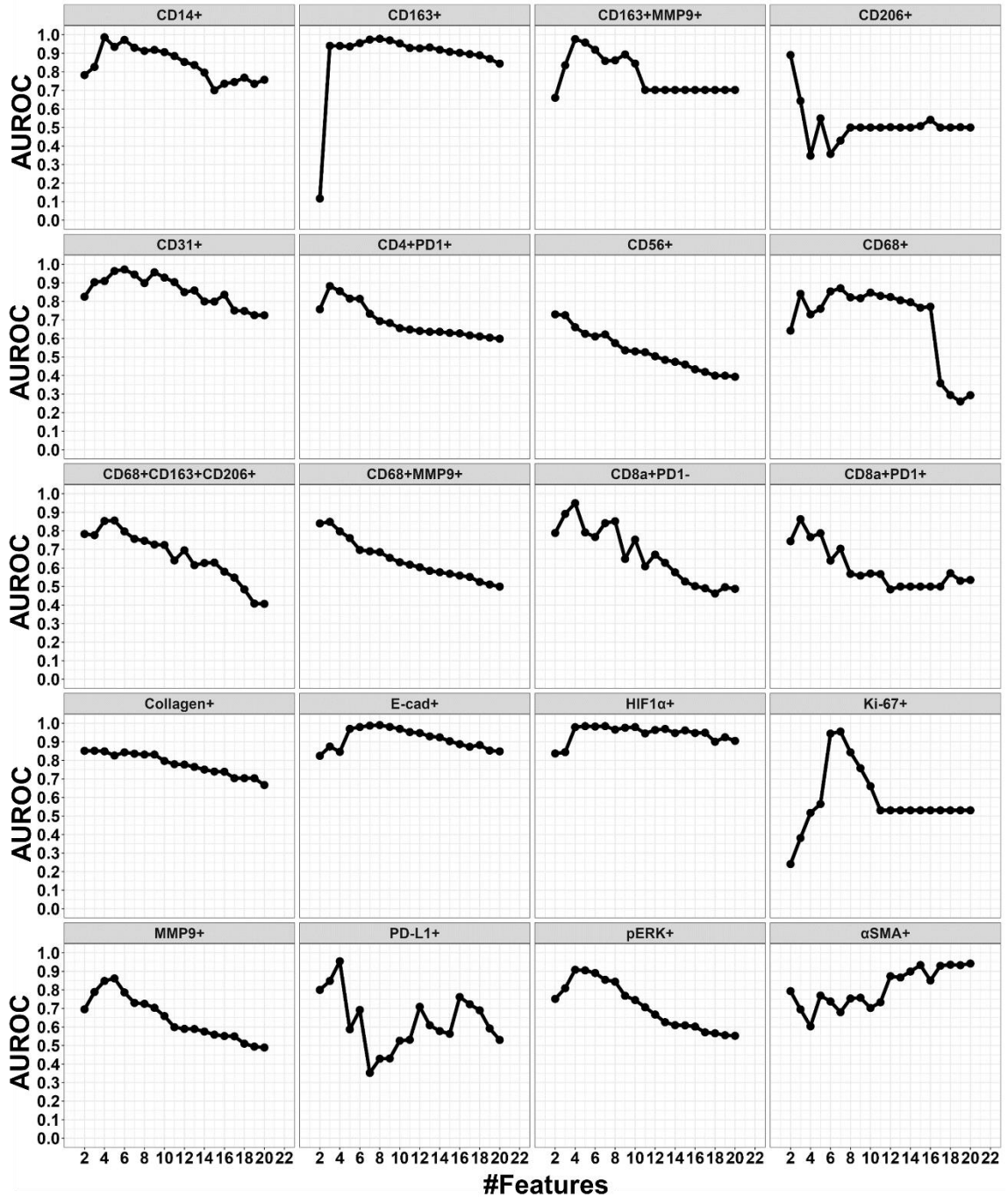
Figure 50 AUROC achieved by ML models using primary IMC clusters across a variable number of features to predict BCLM cluster concentrations (as stated in gray box of each panel).
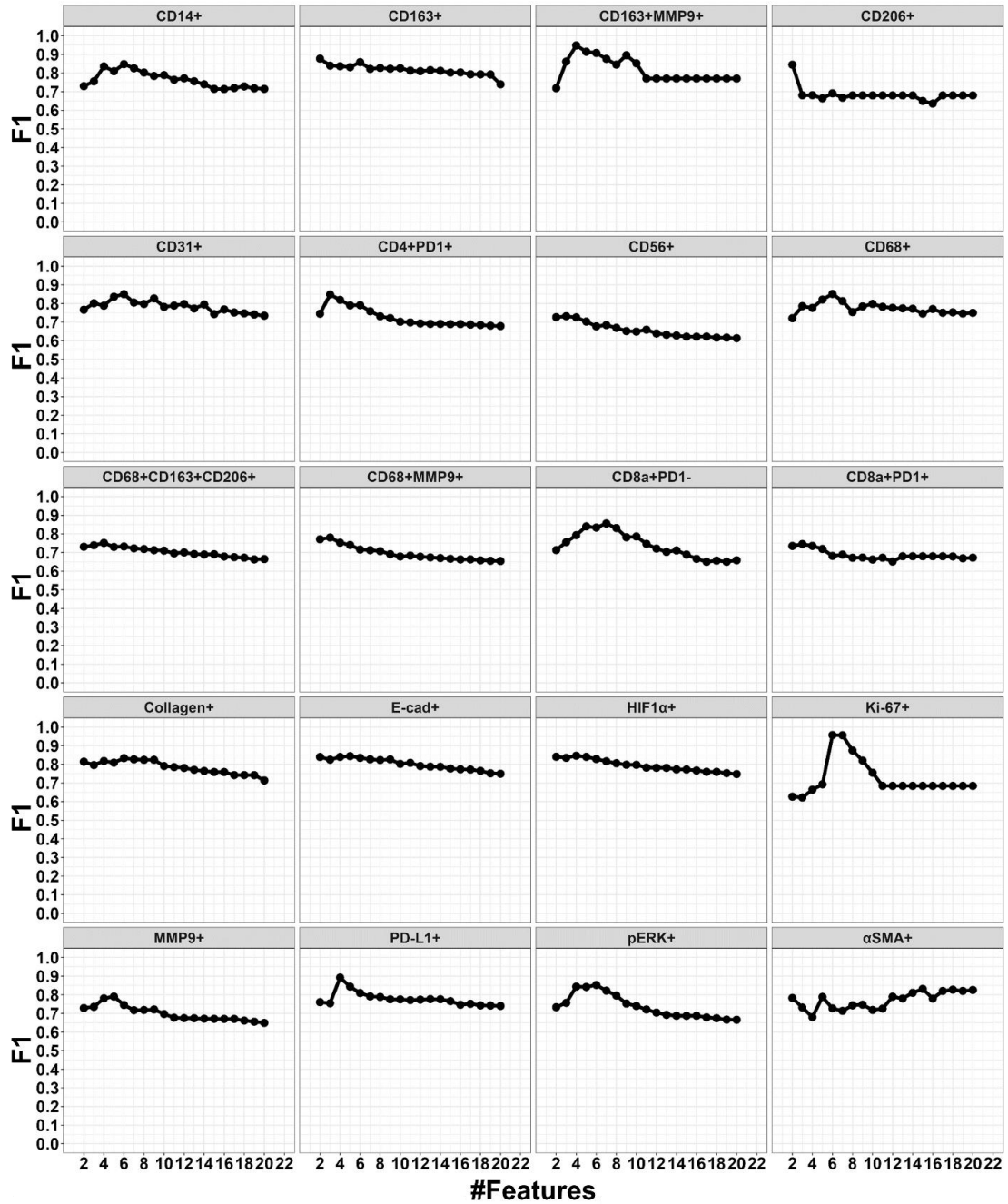
Figure 51 Metric F1 achieved by ML models using primary IMC clusters across a variable number of features to predict BCLM cluster concentrations (as stated in gray box of each panel).
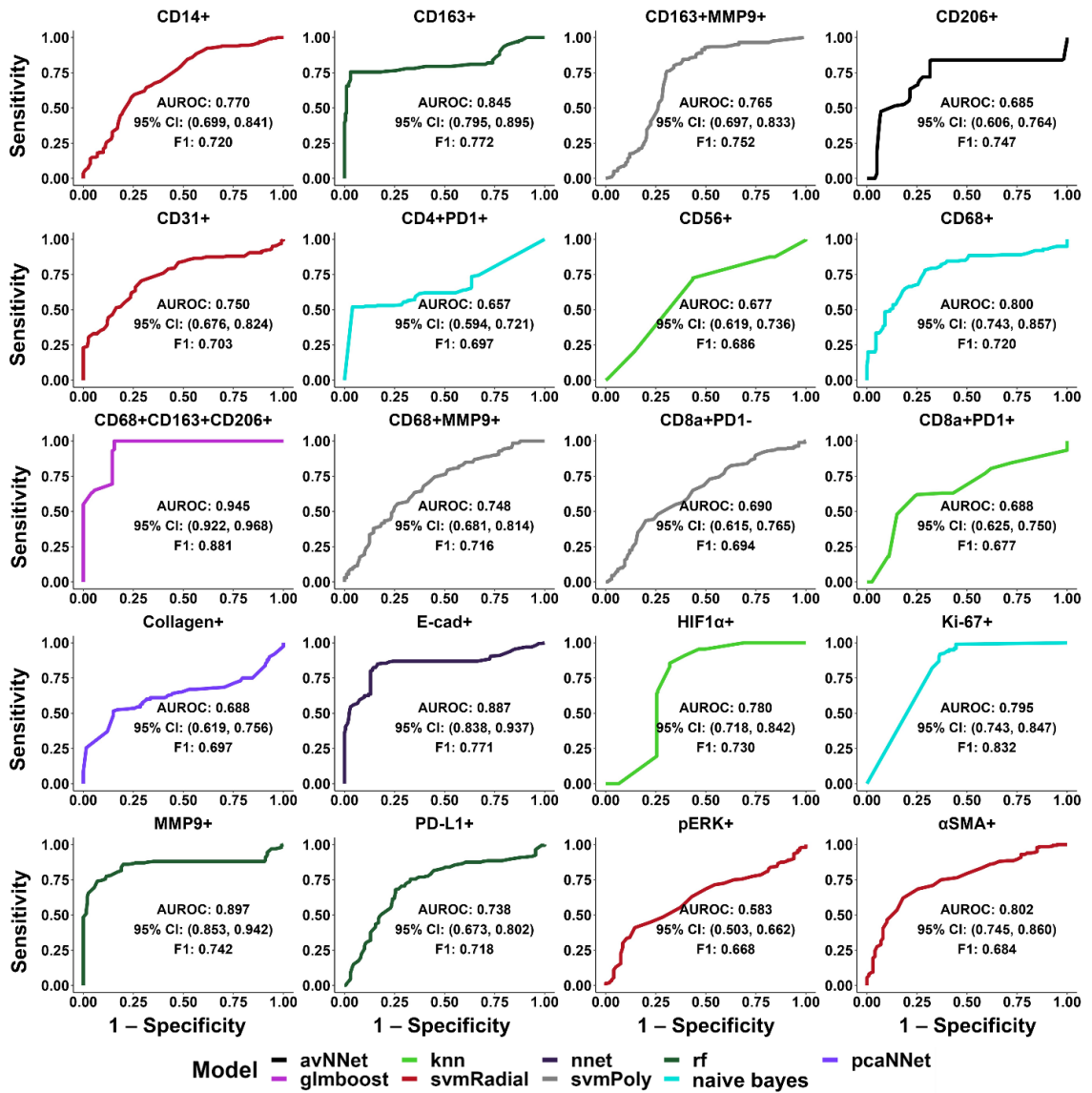
Figure 52 AUROC curves of covariates classifying patients by BCLM IMC cluster densities.

CHAPTER 7: OVERALL DISCUSSION AND CONCLUSIONS

This work documents the development of a 3D model to simulate centimeter-scale TME at sub-millimeter resolution to evaluate BCLM and primary and liver metastatic PDAC response to novel therapies, focusing on immunotherapy. The TME represents a highly complex pathophysiology, itself a product of multiple concurrent interactions, whose conduciveness to an ever-expanding pool of treatments and treatment regimens is difficult to predict for particular patients. In this dissertation, a Multigrid V-cycle solver was parallelized over an MPI-CUDA framework to solve a triphasic continuum mathematical model of tumor growth. Threads were synchronized during red-black Gauss-Seidel iterations and restriction and prolongation procedures. In doing so, model performance was improved by 14.7x in an initial time step and 10.7x on a per-smoothing step basis when accelerating Multigrid solving with a Titan RTX and a single general compute process (GCP). Using a 256^3 domain size, model performance improved 6.7x when scaling from 1 GCP to 64 GCP with 2 GCP allocated per Nvidia V100 GPU (32 GPUs total). A simulation of a growing cm-scale tumor in a 512^3 domain for 8 simulated days was performed in ~58 hours (~2.4 days). Given recent interest in training large language [427] and diffusion [428] models, GPU-bound frameworks may increase in prevalence, offering more opportunities for tumor model deployment.

The model's scope was extended to include immune species while preserving a triphasic structure. The activity level of local immune-immune interactions was quantified as having pro-tumor or anti-tumor effects which, in turn, affected phenomena in the TME. Pro-tumor species increased ECM deposition, production of tumor angiogenic factors, vascularity, and intra-tumoral pressure relative to an immune-free tumor mass. Meanwhile, anti-tumor species suppressed tumor growth sufficiently to prevent growth-induced hypoxia formation. This work also briefly investigated MDSC, a potential target for immunotherapy due to its inhibitory effects during immune-checkpoint therapy [47-49]. In this model, affecting MDSC activation levels and entrance rates was sufficient to vary tumor burden from 20% to 58% of the initial condition over the course of 4 days. Along with all the other results, this suggests that this model could aid in evaluating the efficacy of immunotherapies in the immunosuppressive TME.

This model was then applied to simulation of BCLM. Consistent with previously published results from a 2D tumor model [57, 59, 60], the model confirmed that MSV-nab-PTX produced greater tumor response than intravenously delivered PTX. Further, MSV-nab-PTX efficacy was improved in a TME containing both M1 and M2 macrophages, consistent with prior *in vitro* observations [59, 60]. Tumor burden in female BALB/C mice livers (n = 3) was quantified and then simulated in an *in silico* mouse liver lobe containing hundreds of BCLM of varying sizes. There, administering MSV-nab-PTX every 6 days curbed overall tumor burden, with smaller intervals between doses improving tumor response.

This model was also used to simulate treatment of primary and metastatic PDAC across 10 days of growth and compared changes in tumor burden to a control (untreated) case. Analysis found that anti-PDL1 and antigen-loaded chitosan therapies slowed, but did not eliminate, tumor burden in either site. However, the approaches combined synergistically in both PDAC and PDAC-LM, lowering burden to 81.0% at 4.0 days and 83.4% after 4.2 days, respectively. This suggests that this model has identified a potential route for reducing systemic tumor burden in advanced stage PDAC cases with hepatic metastases. Overall, these BCLM and PDAC applications demonstrate that this model can evaluate novel immunotherapeutic strategies in liver metastatic TME and, in the case of PDAC, centimeter-scale primary tumors. Longer-term this approach could be applied across a broader spectrum of therapeutic approaches and tumor types to identify potential routes of improved tumor response.

Lastly, as a first step towards informing the model with clinical data from the TME, 20 IMC clusters from 15 BCLM patients were classified as above-median or below-median expression using primary breast IMC data. The predicted IMC clusters were comprised of markers representing multiple components of the TME, including immune species (CD68, CD163, CD206, CD14, CD56, CD4, CD8a), PD1/PD-L1 expression (PD1, PD-L1), vascularity (CD31), hypoxia (HIFα), ECM (αSMA, collagen, MMP9), and tumor tissue (Ki-67, pERK, and E-cad). Trained ML models attained acceptable model performance, with validation subset AUROC ≥ 0.75 and 95% CI ≥ 0.7 with F1 ≥ 0.70. Pan-macrophage marker CD68 was found to be the most important component in making ML predictions. This finding was consistent with observations that

tumor associated macrophages can influence TME neovascularization and immunosuppression, as well as tumor invasiveness and metastasis [402]. Notably, because all IMC clusters were used by optimum ML models, a comprehensive view of the primary tumor's TME was leveraged to predict the BCLM TME. In future work, this approach could inform 3D model parameters with the goal of performing simulations of patient-specific immunotherapy.

While these results mark the first steps in attaining *in silico* analysis of cm-scale tumor response, several limitations exist in these studies. While BCLM and PDAC simulations were calibrated to a variety of observations in literature, model predictions have not been externally validated against clinical, *in vivo*, or *in vitro* results. The model excludes events and locations outside the TME, antigen presentation to naïve T-cells by dendritic cells in lymph nodes and lymphopoiesis in the bone marrow and thymus [168], as well as multiple immune species, including pro- and anti-neutrophils, plasma cells, and Th17 cells [247, 249, 250, 429]. Further, the model yields deterministic results, contrasting with *in vitro* [57, 59, 60] and *in vivo* results [58] for which replicates would document inter-sample variation. Mechanistic tumor models have incorporated semi-stochasticity to better reflect population variation [57, 59, 60, 426], which, in future work, may be incorporated to this model. The ability to simulate the temporal growth of a cm-scale tumor from an initial "seed" is an ongoing challenge that may require prolonged use of GPU resources. Other techniques for informing 3D model parameters, such as from metabolomics [426], could be investigated in the future. Recognizing that the tumor mass can often be isolated to a specific region of the simulated domain, reintroducing an

adaptive grid meshing approach from [83] capable of dynamically allocating resources to variable sub-domain sizes may improve model performance at cm-scale. Exploration of other Multigrid level cycling techniques, such as the F-cycle and W-cycle, could also be evaluated in future work [147]. Model sensitivity to different grid resolutions and time step sizes could be investigated. Finally, ML model predictions of BCLM TME from primary lesions could be confirmed and refined using increased sample sizes. In spite of these limitations, this work overall advances the goal towards patient-specific simulation of response to cancer immunotherapy.

REFERENCES

1. Hanahan, D., *Hallmarks of Cancer: New Dimensions.* Cancer Discov, 2022. **12**(1): p. 31-46.
2. Zhao, H.Y., et al., *Incidence and prognostic factors of patients with synchronous liver metastases upon initial diagnosis of breast cancer: a population-based study.* Cancer Manag Res, 2018. **10**: p. 5937-5950.
3. Ji, L., et al., *Risk and prognostic factors of breast cancer with liver metastases.* BMC Cancer, 2021. **21**(1): p. 238.
4. Zhang, N., et al., *Different risk and prognostic factors for liver metastasis of breast cancer patients with de novo and relapsed distant metastasis in a Chinese population.* Front Oncol, 2023. **13**: p. 1102853.
5. Siegel, R.L., A.N. Giaquinto, and A. Jemal, *Cancer statistics, 2024.* CA Cancer J Clin, 2024. **74**(1): p. 12-49.
6. Butepage, G., et al., *Overall survival of individuals with metastatic cancer in Sweden: a nationwide study.* BMC Public Health, 2022. **22**(1): p. 1913.
7. Ruiz, A., et al., *Surgical resection versus systemic therapy for breast cancer liver metastases: Results of a European case matched comparison.* Eur J Cancer, 2018. **95**: p. 1-10.
8. O'Shaughnessy, J., *Extending survival with chemotherapy in metastatic breast cancer.* Oncologist, 2005. **10 Suppl 3**: p. 20-9.
9. Ozaki, K., et al., *Liver Metastases: Correlation between Imaging Features and Pathomolecular Environments.* Radiographics, 2022. **42**(7): p. 1994-2013.
10. Iacobuzio-Donahue, C.A., et al., *DPC4 gene status of the primary carcinoma correlates with patterns of failure in patients with pancreatic cancer.* J Clin Oncol, 2009. **27**(11): p. 1806-13.
11. Valderrama-Trevino, A.I., et al., *Hepatic Metastasis from Colorectal Cancer.* Euroasian J Hepatogastroenterol, 2017. **7**(2): p. 166-175.
12. Yamamoto, M., et al., *Clinical practice guidelines for the management of liver metastases from extrahepatic primary cancers 2021.* J Hepatobiliary Pancreat Sci, 2021. **28**(1): p. 1-25.
13. Chao, Y., et al., *Hepatocyte induced re-expression of E-cadherin in breast and prostate cancer cells increases chemoresistance.* Clin Exp Metastasis, 2012. **29**(1): p. 39-50.
14. Wachsmann, M.B., L.M. Pop, and E.S. Vitetta, *Pancreatic ductal adenocarcinoma: a review of immunologic aspects.* J Investig Med, 2012. **60**(4): p. 643-63.

15.   Banerjee, K., et al., *Emerging trends in the immunotherapy of pancreatic cancer.* Cancer Lett, 2018. **417**: p. 35-46.

16.   Ho, W.J., E.M. Jaffee, and L. Zheng, *The tumour microenvironment in pancreatic cancer - clinical challenges and opportunities.* Nat Rev Clin Oncol, 2020. **17**(9): p. 527-540.

17.   Sheafor, D.H., et al., *Comparison of unenhanced, hepatic arterial-dominant, and portal venous-dominant phase helical CT for the detection of liver metastases in women with breast carcinoma.* AJR Am J Roentgenol, 1999. **172**(4): p. 961-8.

18.   Gonzalez, H., C. Hagerling, and Z. Werb, *Roles of the immune system in cancer: from tumor initiation to metastatic progression.* Genes Dev, 2018. **32**(19-20): p. 1267-1284.

19.   Gun, S.Y., et al., *Targeting immune cells for cancer therapy.* Redox Biol, 2019. **25**: p. 101174.

20.   Galli, F., et al., *Relevance of immune cell and tumor microenvironment imaging in the new era of immunotherapy.* J Exp Clin Cancer Res, 2020. **39**(1): p. 89.

21.   Provenzano, P.P., et al., *Enzymatic targeting of the stroma ablates physical barriers to treatment of pancreatic ductal adenocarcinoma.* Cancer Cell, 2012. **21**(3): p. 418-29.

22.   Merika, E.E., et al. *Desmoplasia in Pancreatic Cancer. Can We Fight It?* Gastroenterology Research and Practice., 2012.

23.   Whatcott, C.J., et al., *Desmoplasia in Primary Tumors and Metastatic Lesions of Pancreatic Cancer.* Clin Cancer Res, 2015. **21**(15): p. 3561-8.

24.   O'Reilly, E.M., et al., *Durvalumab With or Without Tremelimumab for Patients With Metastatic Pancreatic Ductal Adenocarcinoma: A Phase 2 Randomized Clinical Trial.* JAMA Oncol, 2019. **5**(10): p. 1431-1438.

25.   Jain, R.K., *Delivery of molecular and cellular medicine to solid tumors.* Adv Drug Deliv Rev, 2001. **46**(1-3): p. 149-68.

26.   Stessels, F., et al., *Breast adenocarcinoma liver metastases, in contrast to colorectal cancer liver metastases, display a non-angiogenic growth pattern that preserves the stroma and lacks hypoxia.* Br J Cancer, 2004. **90**(7): p. 1429-36.

27.   Charmsaz, S., et al., *Novel Strategies for Cancer Treatment: Highlights from the 55th IACR Annual Conference.* Cancers (Basel), 2019. **11**(8).

28.   Esfahani, K., et al., *A review of cancer immunotherapy: from the past, to the present, to the future.* Curr Oncol, 2020. **27**(Suppl 2): p. S87-S97.

29.   Hamdan, F. and V. Cerullo, *Cancer immunotherapies: A hope for the uncurable?* Frontiers in Molecular Medicine, 2023. **3**.

30.   Galluzzi, L., et al., *Classification of current anticancer immunotherapies.* Oncotarget, 2014. **5**(24): p. 12472-508.

31.   Shalhout, S.Z., et al., *Therapy with oncolytic viruses: progress and challenges.* Nat Rev Clin Oncol, 2023. **20**(3): p. 160-177.

32.   Fyfe, G., et al., *Results of treatment of 255 patients with metastatic renal cell carcinoma who received high-dose recombinant interleukin-2 therapy.* J Clin Oncol, 1995. **13**(3): p. 688-96.

33.   Achkar, T., et al., *High-dose interleukin 2 in patients with metastatic renal cell carcinoma with sarcomatoid features.* PLoS One, 2017. **12**(12): p. e0190084.

34. Amaria, R.N., et al., *Update on use of aldesleukin for treatment of high-risk metastatic melanoma.* Immunotargets Ther, 2015. **4**: p. 79-89.

35. Davar, D., et al., *High-dose interleukin-2 (HD IL-2) for advanced melanoma: a single center experience from the University of Pittsburgh Cancer Institute.* J Immunother Cancer, 2017. **5**(1): p. 74.

36. Zhang, P., G. Zhang, and X. Wan, *Challenges and new technologies in adoptive cell therapy.* J Hematol Oncol, 2023. **16**(1): p. 97.

37. Plosker, G.L. and S.J. Keam, *Trastuzumab: a review of its use in the management of HER2-positive metastatic and early-stage breast cancer.* Drugs, 2006. **66**(4): p. 449-75.

38. Maadi, H., et al., *Trastuzumab Mechanism of Action; 20 Years of Research to Unravel a Dilemma.* Cancers (Basel), 2021. **13**(14): p. 3540.

39. Hodi, F.S., et al., *Improved survival with ipilimumab in patients with metastatic melanoma.* N Engl J Med, 2010. **363**(8): p. 711-23.

40. Abou-Alfa, G.K., et al., *Tremelimumab plus Durvalumab in Unresectable Hepatocellular Carcinoma.* NEJM Evid, 2022. **1**(8): p. EVIDoa2100070.

41. Plosker, G.L., *Sipuleucel-T: in metastatic castration-resistant prostate cancer.* Drugs, 2011. **71**(1): p. 101-8.

42. Kantoff, P.W., et al., *Sipuleucel-T immunotherapy for castration-resistant prostate cancer.* N Engl J Med, 2010. **363**(5): p. 411-22.

43. Lin, M.J., et al., *Cancer vaccines: the next immunotherapy frontier.* Nat Cancer, 2022. **3**(8): p. 911-926.

44. Boorjian, S.A., et al., *Intravesical nadofaragene firadenovec gene therapy for BCG-unresponsive non-muscle-invasive bladder cancer: a single-arm, open-label, repeat-dose clinical trial.* Lancet Oncol, 2021. **22**(1): p. 107-117.

45. Lemos de Matos, A., L.S. Franco, and G. McFadden, *Oncolytic Viruses and the Immune System: The Dynamic Duo.* Mol Ther Methods Clin Dev, 2020. **17**: p. 349-358.

46. Waldman, A.D., J.M. Fritz, and M.J. Lenardo, *A guide to cancer immunotherapy: from T cell basic science to clinical practice.* Nat Rev Immunol, 2020. **20**(11): p. 651-668.

47. Li, T., et al., *Targeting MDSC for Immune-Checkpoint Blockade in Cancer Immunotherapy: Current Progress and New Prospects.* Clin Med Insights Oncol, 2021. **15**: p. 11795549211035540.

48. Tang, H., H. Li, and Z. Sun, *Targeting myeloid-derived suppressor cells for cancer therapy.* Cancer Biol Med, 2021. **18**(4): p. 992-1009.

49. Law, A.M.K., F. Valdes-Mora, and D. Gallego-Ortega, *Myeloid-Derived Suppressor Cells as a Therapeutic Target for Cancer.* Cells, 2020. **9**(3): p. 561.

50. Mitra, A., et al., *From bench to bedside: the history and progress of CAR T cell therapy.* Front Immunol, 2023. **14**: p. 1188049.

51. Rahn, S., et al., *POLE Score: a comprehensive profiling of programmed death 1 ligand 1 expression in pancreatic ductal adenocarcinoma.* Oncotarget, 2019. **10**(16): p. 1572-1588.

52. Beckinger, S., et al., *Hepatic myofibroblasts exert immunosuppressive effects independent of the immune checkpoint regulator PD-L1 in liver metastasis of pancreatic ductal adenocarcinoma.* Front Oncol, 2023. **13**: p. 1160824.

53. Daunke, T., et al., *Expression and role of the immune checkpoint regulator PD-L1 in the tumor-stroma interplay of pancreatic ductal adenocarcinoma.* Front Immunol, 2023. **14**: p. 1157397.

54. Wherry, E.J., et al., *Molecular signature of CD8+ T cell exhaustion during chronic viral infection.* Immunity, 2007. **27**(4): p. 670-84.

55. Jiang, Y., Y. Li, and B. Zhu, *T-cell exhaustion in the tumor microenvironment.* Cell Death Dis, 2015. **6**(6): p. e1792.

56. Chow, A., et al., *Clinical implications of T cell exhaustion for cancer immunotherapy.* Nat Rev Clin Oncol, 2022. **19**(12): p. 775-790.

57. Leonard, F., et al., *Enhanced performance of macrophage-encapsulated nanoparticle albumin-bound-paclitaxel in hypo-perfused cancer lesions.* Nanoscale, 2016. **8**(25): p. 12544-52.

58. Tanei, T., et al., *Redirecting Transport of Nanoparticle Albumin-Bound Paclitaxel to Macrophages Enhances Therapeutic Efficacy against Liver Metastases.* Cancer Res, 2016. **76**(2): p. 429-39.

59. Leonard, F., et al., *Macrophage Polarization Contributes to the Anti-Tumoral Efficacy of Mesoporous Nanovectors Loaded with Albumin-Bound Paclitaxel.* Front Immunol, 2017. **8**: p. 693.

60. Leonard, F., et al., *Nonlinear response to cancer nanotherapy due to macrophage interactions revealed by mathematical modeling and evaluated in a murine model via CRISPR-modulated macrophage polarization.* Cancer Immunol Immunother, 2020. **69**(5): p. 731-744.

61. Cresswell, A.B., F.K. Welsh, and M. Rees, *A diagnostic paradigm for resectable liver lesions: to biopsy or not to biopsy?* HPB (Oxford), 2009. **11**(7): p. 533-40.

62. Rodes Brown, S. and R.C. Martin, 2nd, *Management of liver dominant metastatic breast cancer: surgery, chemotherapy, or hepatic arterial therapy - benefits and limitations.* Minerva Chir, 2012. **67**(4): p. 297-308.

63. Yoo, T.G., et al., *Systematic review of early and long-term outcome of liver resection for metastatic breast cancer: Is there a survival benefit?* Breast, 2017. **32**: p. 162-172.

64. Mahlbacher, G.E., K.C. Reihmer, and H.B. Frieboes, *Mathematical modeling of tumor-immune cell interactions.* J Theor Biol, 2019. **469**: p. 47-60.

65. Mahlbacher, G., et al., *Mathematical modeling of tumor-associated macrophage interactions with the cancer microenvironment.* J Immunother Cancer, 2018. **6**(1): p. 10.

66. Frieboes, H.B., et al., *Three-dimensional multispecies nonlinear tumor growth-II: Tumor invasion and angiogenesis.* J Theor Biol, 2010. **264**(4): p. 1254-78.

67. Curtis, L.T., S. Sebens, and H.B. Frieboes, *Modeling of tumor response to macrophage and T lymphocyte interactions in the liver metastatic microenvironment.* Cancer Immunol Immunother, 2021. **70**(5): p. 1475-1488.

68. Miller, H.A. and H.B. Frieboes, *Evaluation of Drug-Loaded Gold Nanoparticle Cytotoxicity as a Function of Tumor Vasculature-Induced Tissue Heterogeneity.* Ann Biomed Eng, 2019. **47**(1): p. 257-271.

69. Wang, Y., et al., *Mathematical model predicts tumor control patterns induced by fast and slow cytotoxic T lymphocyte killing mechanisms.* Sci Rep, 2023. **13**(1): p. 22541.

70. Lapin, A., et al., *Integrating a dynamic central metabolism model of cancer cells with a hybrid 3D multiscale model for vascular hepatocellular carcinoma growth.* Sci Rep, 2022. **12**(1): p. 12373.

71. Ruiz-Martinez, A., et al., *Simulations of tumor growth and response to immunotherapy by coupling a spatial agent-based model with a whole-patient quantitative systems pharmacology model.* PLoS Comput Biol, 2022. **18**(7): p. e1010254.

72. Agarwal, B., A.M. Correa, and L. Ho, *Survival in pancreatic carcinoma based on tumor size.* Pancreas, 2008. **36**(1): p. e15-20.

73. Li, D., et al., *Impact of tumor size on survival of patients with resected pancreatic ductal adenocarcinoma: a systematic review and meta-analysis.* BMC Cancer, 2018. **18**(1): p. 985.

74. Rihan, F.A., et al., *A time delay model of tumour-immune system interactions: Global dynamics, parameter estimation, sensitivity analysis.* Applied Mathematics and Computation, 2014. **232**: p. 606-623.

75. Wilkie, K.P. and P. Hahnfeldt, *Modeling the Dichotomy of the Immune Response to Cancer: Cytotoxic Effects and Tumor-Promoting Inflammation.* Bull Math Biol, 2017. **79**(6): p. 1426-1448.

76. de Pillis, L.G., A.E. Radunskaya, and C.L. Wiseman, *A validated mathematical model of cell-mediated immune response to tumor growth.* Cancer Res, 2005. **65**(17): p. 7950-8.

77. Benchaib, M.A., et al., *Mathematical Modeling Reveals That the Administration of EGF Can Promote the Elimination of Lymph Node Metastases by PD-1/PD-L1 Blockade.* Front Bioeng Biotechnol, 2019. **7**: p. 104.

78. Makhlouf, A.M., L. El-Shennawy, and H.A. Elkaranshawy, *Mathematical Modelling for the Role of CD4(+)T Cells in Tumor-Immune Interactions.* Comput Math Methods Med, 2020. **2020**: p. 7187602.

79. Makaryan, S.Z., C.G. Cess, and S.D. Finley, *Modeling immune cell behavior across scales in cancer.* Wiley Interdiscip Rev Syst Biol Med, 2020. **12**(4): p. e1484.

80. Antonopoulos, M., et al., *Three-dimensional tumor growth in time-varying chemical fields: a modeling framework and theoretical study.* BMC Bioinformatics, 2019. **20**(1): p. 442.

81. Lorenzo, G., et al., *Tissue-scale, personalized modeling and simulation of prostate cancer growth.* Proc Natl Acad Sci U S A, 2016. **113**(48): p. E7663-E7671.

82. Ng, C.F. and H.B. Frieboes, *Model of vascular desmoplastic multispecies tumor growth.* J Theor Biol, 2017. **430**: p. 245-282.

83. Ng, C.F. and H.B. Frieboes, *Simulation of Multispecies Desmoplastic Cancer Growth via a Fully Adaptive Non-linear Full Multigrid Algorithm.* Front Physiol, 2018. **9**: p. 821.

84. Wise, S.M., et al., *Three-dimensional multispecies nonlinear tumor growth--I Model and numerical method.* J Theor Biol, 2008. **253**(3): p. 524-43.

85. Oden, J.T., A. Hawkins, and S. Prudhomme, *General Diffuse-Interface Theories and an Approach to Predictive Tumor Growth Modeling.* Mathematical Models & Methods in Applied Sciences, 2010. **20**(3): p. 477-517.

86.   Cristini, V., et al., *Nonlinear simulations of solid tumor growth using a mixture model: invasion and branching.* J Math Biol, 2009. **58**(4-5): p. 723-63.

87.   Hawkins-Daarud, A., et al., *Bayesian calibration, validation, and uncertainty quantification of diffuse interface models of tumor growth.* J Math Biol, 2013. **67**(6-7): p. 1457-85.

88.   Cristini, V., et al., *Nonlinear modeling and simulation of tumor growth*, in *Selected topics in cancer modeling.* 2008, Birkhäuser: Boston. p. 1-69.

89.   Frigeri, S., M. Grasselli, and E. Rocca, *On a diffuse interface model of tumour growth.* European Journal of Applied Mathematics, 2015. **26**: p. 215-243.

90.   Cavaterra, C., E. Rocca, and H. Wu, *Long-Time Dynamics and Optimal Control of a Diffuse Interface Model for Tumor Growth.* Applied Mathematics & Optimization, 2019. **83**(2): p. 739-787.

91.   Colli, P., et al., *Optimal distributed control of a diffuse interface model of tumor growth.* Nonlinearity, 2017. **30**(6): p. 2518-2546.

92.   Ward, J.P. and J.R. King, *Mathematical modelling of avascular-tumour growth.* IMA J Math Appl Med Biol, 1997. **14**(1): p. 39-69.

93.   Please, C.P., G. Pettet, and D.L.S. McElwain, *A new approach to modelling the formation of necrotic regions in tumours.* Applied Mathematics Letters, 1998. **11**(3): p. 89-94.

94.   Ward, J.P. and J.R. King, *Mathematical modelling of avascular-tumour growth. II: Modelling growth saturation.* IMA J Math Appl Med Biol, 1999. **16**(2): p. 171-211.

95.   Please, C.P., G.J. Pettet, and D.L.S. McElwain, *Avascular tumour dynamics and necrosis.* Mathematical Models & Methods in Applied Sciences, 1999. **9**(4): p. 569-579.

96.   Breward, C.J., H.M. Byrne, and C.E. Lewis, *The role of cell-cell interactions in a two-phase model for avascular tumour growth.* J Math Biol, 2002. **45**(2): p. 125-52.

97.   Ambrosi, D. and L. Preziosi, *On the closure of mass balance models for tumor growth.* Mathematical Models & Methods in Applied Sciences, 2002. **12**(5): p. 737-754.

98.   Breward, C.J., H.M. Byrne, and C.E. Lewis, *A multiphase model describing vascular tumour growth.* Bull Math Biol, 2003. **65**(4): p. 609-40.

99.   Byrne, H.M., et al., *A two-phase model of solid tumour growth.* Applied Mathematics Letters, 2003. **16**(4): p. 567-573.

100. Byrne, H. and L. Preziosi, *Modelling solid tumour growth using the theory of mixtures.* Math Med Biol, 2003. **20**(4): p. 341-66.

101. Franks, S.J., et al., *Modelling the early growth of ductal carcinoma in situ of the breast.* J Math Biol, 2003. **47**(5): p. 424-52.

102. Franks, S.J., et al., *Mathematical modelling of comedo ductal carcinoma in situ of the breast.* Math Med Biol, 2003. **20**(3): p. 277-308.

103. Roose, T., et al., *Solid stress generated by spheroid growth estimated using a linear poroelasticity model.* Microvasc Res, 2003. **66**(3): p. 204-12.

104. Araujo, R.P. and D.L.S. McElwain, *A mixture theory for the genesis of residual stresses in growing tissues I: A general formulation.* Siam Journal on Applied Mathematics, 2005. **65**(4): p. 1261-1284.

105. Araujo, R.P. and D.L.S. Mcelwain, *A Mixture Theory for the Genesis of Residual Stresses in Growing Tissues Ii: Solutions to the Biphasic Equations for a Multicell Spheroid.* Siam Journal on Applied Mathematics, 2005. **66**(2): p. 447-467.

106. Chaplain, M.A., L. Graziano, and L. Preziosi, *Mathematical modelling of the loss of tissue compression responsiveness and its role in solid tumour development.* Math Med Biol, 2006. **23**(3): p. 197-229.

107. Tosin, A., *Multiphase modeling and qualitative analysis of the growth of tumor cords.* Networks and Heterogeneous Media, 2008. **3**(1): p. 43-83.

108. Ambrosi, D. and L. Preziosi, *Cell adhesion mechanisms and stress relaxation in the mechanics of tumours.* Biomech Model Mechanobiol, 2009. **8**(5): p. 397-413.

109. Ambrosi, D., et al., *Traction patterns of tumor cells.* J Math Biol, 2009. **58**(1-2): p. 163-81.

110. Preziosi, L. and A. Tosin, *Multiphase modelling of tumour growth and extracellular matrix interaction: mathematical tools and applications.* J Math Biol, 2009. **58**(4-5): p. 625-56.

111. Preziosi, L. and A. Tosin, *Multiphase and Multiscale Trends in Cancer Modelling.* Mathematical Modelling of Natural Phenomena, 2009. **4**(3): p. 1-11.

112. Tracqui, P., *Biophysical models of tumour growth.* Reports on Progress in Physics, 2009. **72**(5): p. 056701.

113. Wise, S.M., J.S. Lowengrub, and V. Cristini, *An Adaptive Multigrid Algorithm for Simulating Solid Tumor Growth Using Mixture Models.* Math Comput Model, 2011. **53**(1-2): p. 1-20.

114. Anderson, A.R. and M.A. Chaplain, *Continuous and discrete mathematical models of tumor-induced angiogenesis.* Bull Math Biol, 1998. **60**(5): p. 857-99.

115. McDougall, S.R., et al., *Mathematical modelling of flow through vascular networks: implications for tumour-induced angiogenesis and chemotherapy strategies.* Bull Math Biol/, 2002 **64**: p. 673-702.

116. Plank, M.J. and B.D. Sleeman, *A reinforced random walk model of tumour angiogenesis and anti-angiogenic strategies.* Math Med Biol, 2003. **20**(2): p. 135-81.

117. Plank, M.J. and B.D. Sleeman, *Lattice and non-lattice models of tumour angiogenesis.* Bull Math Biol, 2004. **66**(6): p. 1785-819.

118. Ng, C.F. and H.B. Frieboes, *Model of vascular desmoplastic multispecies tumor growth.* Journal of Theoretical Biology, 2017. **430**: p. 245-282.

119. Ng, C.F. and H.B. Frieboes, *Simulation of Multispecies Desmoplastic Cancer Growth via a Fully Adaptive Non-linear Full Multigrid Algorithm.* Frontiers in Physiology, 2018. **9**.

120. Wcisło, R. and W. Dzwinel, *Particle Model of Tumor Growth and Its Parallel Implementation*, in *Parallel Processing and Applied Mathematics*. 2010, Berlin, Heidelberg : Springer Berlin Heidelberg. p. 322-331.

121. Wcisło, R., P. Gosztyła, and W. Dzwinel. *N-body parallel model of tumor proliferation*. in *Proceedings of the 2010 Summer Computer Simulation Conference*. 2010.

122. Ghaffarizadeh, A., S.H. Friedman, and P. Macklin, *BioFVM: an efficient, parallelized diffusive transport solver for 3-D biological simulations.* Bioinformatics, 2016. **32**(8): p. 1256-8.

123. Chen, N., et al., *A parallel implementation of the Cellular Potts Model for simulation of cell-based morphogenesis.* Comput Phys Commun, 2007. **176**(11-12): p. 670-681.

124. Berghoff, M., J. Rosenbauer, and A. Schug, *Massively Parallel Large-scale Multi-model Simulation of Tumor Development.* 2019.

125. Berghoff, M., J. Rosenbauer, and A. Schug. *Massively Parallel Large-Scale Multi-Model Simulation of Tumour Development Including Treatments.* in *NIC Symposium 2020.* 2020. John von Neumann-Institut für Computing.

126. Berghoff, M., I. Kondov, and J. Hötzer, *Massively Parallel Stencil Code Solver with Autonomous Adaptive Block Distribution.* Ieee Transactions on Parallel and Distributed Systems, 2018. **29**(10): p. 2282-2296.

127. Tapia, J.J. and R. D'Souza, *Data-Parallel Algorithms for Large-Scale Real-Time Simulation of the Cellular Potts Model on Graphics Processing Units.* 2009 Ieee International Conference on Systems, Man and Cybernetics (Smc 2009), Vols 1-9, 2009: p. 1411-1418.

128. Tapia, J.J. and R.M. D'Souza, *Parallelizing the Cellular Potts Model on graphics processing units.* Computer Physics Communications, 2011. **182**(4): p. 857-865.

129. Salguero, A.G., M.I. Capel, and A.J. Tomeu, *Parallel Cellular Automaton Tumor Growth Model.* Practical Applications of Computational Biology and Bioinformatics, 2019. **803**: p. 175-182.

130. Salguero, A.G., A.J. Tomeu-Hardasmal, and M.I. Capel, *Dynamic Load Balancing Strategy for Parallel Tumor Growth Simulations.* J Integr Bioinform, 2019. **16**(1).

131. Tomeu, A.J., A.G. Salguero, and M.I. Capel, *Speeding Up Tumor Growth Simulations Using Parallel Programming and Cellular Automata.* Ieee Latin America Transactions, 2016. **14**(11): p. 4611-4619.

132. Dong, S., et al., *Simulation of 3D tumor cell growth using nonlinear finite element method.* Comput Methods Biomech Biomed Engin, 2016. **19**(8): p. 807-18.

133. Łoś, M., et al., *Parallel fast isogeometric L2 projection solver with GALOIS system for 3D tumor growth simulations.* Computer Methods in Applied Mechanics and Engineering, 2019. **343**: p. 1-22.

134. Klusek, A., et al., *Efficient model of tumor dynamics simulated in multi-GPU environment.* International Journal of High Performance Computing Applications, 2019. **33**(3): p. 489-506.

135. Swartz, M.A. and A.W. Lund, *Lymphatic and interstitial flow in the tumour microenvironment: linking mechanobiology with immunity.* Nat Rev Cancer, 2012. **12**(3): p. 210-9.

136. Asaadi, H., D. Khaldi, and B. Chapman, *A Comparative Survey of the HPC and Big Data Paradigms: Analysis and Experiments.* 2016 Ieee International Conference on Cluster Computing (Cluster), 2016: p. 423-432.

137. Kamburugamuve, S., et al., *Anatomy of machine learning algorithm implementations in MPI, Spark, and Flink.* The International Journal of High Performance Computing Applications, 2017. **32**(1): p. 61-73.

138. Reyes-Ortiz, J.L., L. Oneto, and D. Anguita, *Big Data Analytics in the Cloud: Spark on Hadoop vs MPI/OpenMP on Beowulf.* Inns Conference on Big Data 2015 Program, 2015. **53**: p. 121-130.

139. Canon, S., et al., *Matrix factorizations at scale: A comparison of scientific data analytics in spark and C+MPI using three case studies*, in *2016 IEEE International Conference on Big Data (Big Data)*. 2016. p. 204-213.

140. Reiter, S., et al., *A massively parallel geometric multigrid solver on hierarchically distributed grids.* Computing and Visualization in Science, 2014. **16**(4): p. 151-164.

141. Nugent, L.J. and R.K. Jain, *Extravascular diffusion in normal and neoplastic tissues.* Cancer Res, 1984. **44**(1): p. 238-44.

142. Frieboes, H.B., et al., *Prediction of drug response in breast cancer using integrative experimental/computational modeling.* Cancer Res, 2009. **69**(10): p. 4484-92.

143. Benedusi, P., et al., *A Parallel Multigrid Solver for Time-Periodic Incompressible Navier–Stokes Equations in 3D*, in *Numerical Mathematics and Advanced Applications ENUMATH 2015*, B. Karasözen, et al., Editors. 2016, Springer, Cham. p. 265-273.

144. Jacobsen, D., J. Thibault, and I. Senocak, *An MPI-CUDA Implementation for Massively Parallel Incompressible Flow Computations on Multi-GPU Clusters*, in *48th AIAA Aerospace Sciences Meeting Including the New Horizons Forum and Aerospace Exposition*. 2010: Orlando, FL.

145. Huang, H., et al., *An MPI-CUDA Implementation and Optimization for Parallel Sparse Equations and Least Squares (LSQR).* Proceedings of the International Conference on Computational Science, Iccs 2012, 2012. **9**: p. 76-85.

146. Lončar, V., et al., *OpenMP, OpenMP/MPI, and CUDA/MPI C programs for solving the time-dependent dipolar Gross-Pitaevskii equation.* Computer physics communications, 2016. **209**: p. 190-196.

147. Trottenberg, U., et al., *Multigrid*. 2001, San Diego: Academic Press.

148. Leo, P.H., J.S. Lowengrub, and H.J. Jou, *A diffuse interface model for microstructural evolution in elastically stressed solids.* Acta Materialia, 1998. **46**(6): p. 2113-2130.

149. Wise, S., J. Kim, and J. Lowengrub, *Solving the regularized, strongly anisotropic Cahn-Hilliard equation by an adaptive nonlinear multigrid method.* Journal of Computational Physics, 2007. **226**(1): p. 414-446.

150. Wise, S.M., J.S. Lowengrub, and V. Cristini, *An adaptive multigrid algorithm for simulating solid tumor growth using mixture models.* Mathematical and Computer Modelling, 2011. **53**: p. 1-20.

151. Kim, J. and J. Lowengrub, *Phase field modeling and simulation of three-phase flows.* Interfaces and Free Boundaries, 2005. **7**(4): p. 435-466.

152. Wu, J. and L.L. Lanier, *Natural killer cells and cancer.* Adv Cancer Res, 2003. **90**: p. 127-56.

153. Ma, Y., et al., *Dendritic cells in the cancer microenvironment.* J Cancer, 2013. **4**(1): p. 36-44.

154. Italiani, P. and D. Boraschi, *From Monocytes to M1/M2 Macrophages: Phenotypical vs. Functional Differentiation.* Front Immunol, 2014. **5**: p. 514.

155. Olingy, C.E., H.Q. Dinh, and C.C. Hedrick, *Monocyte heterogeneity and functions in cancer.* J Leukoc Biol, 2019. **106**(2): p. 309-322.

156. Wu, L., et al., *Tumor-Associated Neutrophils in Cancer: Going Pro.* Cancers (Basel), 2019. **11**(4).

157. Ginhoux, F. and S. Jung, *Monocytes and macrophages: developmental pathways and tissue homeostasis.* Nat Rev Immunol, 2014. **14**(6): p. 392-404.

158. Edin, S., et al., *The distribution of macrophages with a M1 or M2 phenotype in relation to prognosis and the molecular characteristics of colorectal cancer.* PLoS One, 2012. **7**(10): p. e47045.

159. Furler, R.L., et al., *TGF-beta Sustains Tumor Progression through Biochemical and Mechanical Signal Transduction.* Cancers (Basel), 2018. **10**(6): p. 199.

160. Ley, K., *The second touch hypothesis: T cell activation, homing and polarization.* F1000Res, 2014. **3**: p. 37.

161. Wu, W.K., et al., *IL-10 regulation of macrophage VEGF production is dependent on macrophage polarisation and hypoxia.* Immunobiology, 2010. **215**(9-10): p. 796-803.

162. Hanke, N., et al. *Dendritic Cell Tumor Killing Activity and Its Potential Applications in Cancer Immunotherapy.* Critical Reviews in Immunology, 2013. **33**, 1-21 DOI: 10.1615/CritRevImmunol.2013006679.

163. Guillerey, C., N.D. Huntington, and M.J. Smyth, *Targeting natural killer cells in cancer immunotherapy.* Nat Immunol, 2016. **17**(9): p. 1025-36.

164. Vivier, E., et al., *Targeting natural killer cells and natural killer T cells in cancer.* Nat Rev Immunol, 2012. **12**(4): p. 239-52.

165. Gershkovitz, M., et al., *TRPM2 modulates neutrophil attraction to murine tumor cells by regulating CXCL2 expression.* Cancer Immunol Immunother, 2019. **68**(1): p. 33-43.

166. Bodogai, M., et al., *Immunosuppressive and Prometastatic Functions of Myeloid-Derived Suppressive Cells Rely upon Education from Tumor-Associated B Cells.* Cancer Res, 2015. **75**(17): p. 3456-65.

167. Monu, N.R. and A.B. Frey, *Myeloid-derived suppressor cells and anti-tumor T cells: a complex relationship.* Immunol Invest, 2012. **41**(6-7): p. 595-613.

168. Murphy, K. and C. Weaver, *Janeway's immunobiology.* 2016: Garland science.

169. Bruno, A., et al., *Orchestration of angiogenesis by immune cells.* Front Oncol, 2014. **4**: p. 131.

170. Sarvaria, A., J.A. Madrigal, and A. Saudemont, *B cell regulation in cancer and anti-tumor immunity.* Cell Mol Immunol, 2017. **14**(8): p. 662-674.

171. Namm, J.P., et al., *B lymphocytes as effector cells in the immunotherapy of cancer.* J Surg Oncol, 2012. **105**(4): p. 431-5.

172. Peng, B., Y. Ming, and C. Yang, *Regulatory B cells: the cutting edge of immune tolerance in kidney transplantation.* Cell Death Dis, 2018. **9**(2): p. 109.

173. Farhood, B., M. Najafi, and K. Mortezaee, *CD8(+) cytotoxic T lymphocytes in cancer immunotherapy: A review.* J Cell Physiol, 2019. **234**(6): p. 8509-8521.

174. Xu, X., et al., *Expression of Th1- Th2- and Th17-associated cytokines in laryngeal carcinoma.* Oncol Lett, 2016. **12**(3): p. 1941-1948.

175. Kondelkova, K., et al., *Regulatory T cells (TREG) and their roles in immune system with respect to immunopathological disorders.* Acta Medica (Hradec Kralove), 2010. **53**(2): p. 73-7.

176. Sawant, D.V., et al., *Adaptive plasticity of IL-10(+) and IL-35(+) T(reg) cells cooperatively promotes tumor T cell exhaustion.* Nat Immunol, 2019. **20**(6): p. 724-735.

177. Grossman, W.J., et al., *Human T regulatory cells can use the perforin pathway to cause autologous target cell death.* Immunity, 2004. **21**(4): p. 589-601.

178. Ghiringhelli, F., et al., *CD4+CD25+ regulatory T cells inhibit natural killer cell functions in a transforming growth factor-beta-dependent manner.* J Exp Med, 2005. **202**(8): p. 1075-85.

179. Smyth, M.J., et al., *CD4+CD25+ T regulatory cells suppress NK cell-mediated immunotherapy of cancer.* J Immunol, 2006. **176**(3): p. 1582-7.

180. de Pillis, L.G., A.E. Radunskaya, and C.L. Wiseman, *A validated mathematical model of cell-mediated immune response to tumor growth.* Cancer research, 2005. **65**(17): p. 7950-8.

181. Goodin, D.A. and H.B. Frieboes, *Simulation of 3D centimeter-scale continuum tumor growth at sub-millimeter resolution via distributed computing.* Comput Biol Med, 2021. **134**: p. 104507.

182. Ambrosi, D. and L. Preziosi, *On the closure of mass balance models for tumor growth.* Math. Mod. Meth. Appl. Sci. , 2002. **12**: p. 737–754.

183. Tosin, A., *Multiphase modeling and qualitative analysis of the growth of tumor cords.* Networks Heterogen. Media, 2008. **3**: p. 43–84.

184. Preziosi, L. and A. Tosin, *Multiphase and multiscale trends in cancer modelling.* Math. Model. Nat. Phenom., 2009. **4**: p. 1–11.

185. Cristini, V., et al., *Nonlinear simulations of solid tumor growth using a mixture model: invasion and branching.* J. Math. Biol., 2009. **58**.

186. Hawkins-Daarud, A., et al., *Bayesian calibration, validation, and uncertainty quantification of diffuse interface models of tumor growth.* J. Math. Biol., 2013. **67**: p. 1457-1485.

187. Chow, M.T. and A.D. Luster, *Chemokines in cancer.* Cancer Immunol Res, 2014. **2**(12): p. 1125-31.

188. Hughes, C.E. and R.J.B. Nibbs, *A guide to chemokines and their receptors.* FEBS J, 2018. **285**(16): p. 2944-2971.

189. Okeke, E.B. and J.E. Uzonna, *The Pivotal Role of Regulatory T Cells in the Regulation of Innate Immune Cells.* Front Immunol, 2019. **10**: p. 680.

190. Fu, C. and A. Jiang, *Dendritic Cells and CD8 T Cell Immunity in Tumor Microenvironment.* Front Immunol, 2018. **9**: p. 3059.

191. Hedrick, C.C. and I. Malanchi, *Neutrophils in cancer: heterogeneous and multifaceted.* Nat Rev Immunol, 2022. **22**(3): p. 173-187.

192. Moulin, V., et al., *B lymphocytes regulate dendritic cell (DC) function in vivo: increased interleukin 12 production by DCs from B cell-deficient mice results in T helper cell type 1 deviation.* J Exp Med, 2000. **192**(4): p. 475-82.

193. Hilligan, K.L. and F. Ronchese, *Antigen presentation by dendritic cells and their instruction of CD4+ T helper cell responses.* Cell Mol Immunol, 2020. **17**(6): p. 587-599.

194. Disis, M.L., *Immune regulation of cancer.* J Clin Oncol, 2010. **28**(29): p. 4531-8.

195. Martinez, F.O. and S. Gordon, *The M1 and M2 paradigm of macrophage activation: time for reassessment.* F1000Prime Rep, 2014. **6**: p. 13.

196.   Lakomy, D., et al., *Cytotoxic dendritic cells generated from cancer patients.* J Immunol, 2011. **187**(5): p. 2775-82.

197.   Knutson, K.L. and M.L. Disis, *Tumor antigen-specific T helper cells in cancer immunity and immunotherapy.* Cancer Immunol Immunother, 2005. **54**(8): p. 721-8.

198.   Corthay, A., et al., *Primary antitumor immune response mediated by CD4+ T cells.* Immunity, 2005. **22**(3): p. 371-83.

199.   Gordon, S., *Alternative activation of macrophages.* Nat Rev Immunol, 2003. **3**(1): p. 23-35.

200.   Muraille, E., O. Leo, and M. Moser, *TH1/TH2 paradigm extended: macrophage polarization as an unappreciated pathogen-driven escape mechanism?* Front Immunol, 2014. **5**: p. 603.

201.   Suzuki, E., et al., *Gemcitabine selectively eliminates splenic Gr-1+/CD11b+ myeloid suppressor cells in tumor-bearing animals and enhances antitumor immune activity.* Clin Cancer Res, 2005. **11**(18): p. 6713-21.

202.   Hu, C.E., et al., *Up-regulated myeloid-derived suppressor cell contributes to hepatocellular carcinoma development by impairing dendritic cell function.* Scand J Gastroenterol, 2011. **46**(2): p. 156-64.

203.   Markowitz, J., et al., *Nitric oxide mediated inhibition of antigen presentation from DCs to CD4(+) T cells in cancer and measurement of STAT1 nitration.* Sci Rep, 2017. **7**(1): p. 15424.

204.   Swain, S.L., K.K. McKinstry, and T.M. Strutt, *Expanding roles for CD4(+) T cells in immunity to viruses.* Nat Rev Immunol, 2012. **12**(2): p. 136-48.

205.   Wang, Y., et al., *Myeloid-Derived Suppressor Cells Impair B Cell Responses in Lung Cancer through IL-7 and STAT5.* J Immunol, 2018. **201**(1): p. 278-295.

206.   Zhang, S., H. Zhang, and J. Zhao, *The role of CD4 T cell help for CD8 CTL activation.* Biochem Biophys Res Commun, 2009. **384**(4): p. 405-8.

207.   Green, A.M., R. Difazio, and J.L. Flynn, *IFN-gamma from CD4 T cells is essential for host survival and enhances CD8 T cell function during Mycobacterium tuberculosis infection.* J Immunol, 2013. **190**(1): p. 270-7.

208.   Sharma, S., et al., *T cell-derived IL-10 promotes lung cancer growth by suppressing both T cell and APC function.* Journal of Immunology, 1999. **163**(9): p. 5020-5028.

209.   Saraiva, M. and A. O'Garra, *The regulation of IL-10 production by immune cells.* Nat Rev Immunol, 2010. **10**(3): p. 170-81.

210.   Haist, M., et al., *The Functional Crosstalk between Myeloid-Derived Suppressor Cells and Regulatory T Cells within the Immunosuppressive Tumor Microenvironment.* Cancers (Basel), 2021. **13**(2): p. 210.

211.   Guermonprez, P., et al., *Antigen presentation and T cell stimulation by dendritic cells.* Annu Rev Immunol, 2002. **20**: p. 621-67.

212.   Oh, D.Y., et al., *Intratumoral CD4(+) T Cells Mediate Anti-tumor Cytotoxicity in Human Bladder Cancer.* Cell, 2020. **181**(7): p. 1612-1625 e13.

213.   Barron, L. and T.A. Wynn, *Fibrosis is regulated by Th2 and Th17 responses and by dynamic interactions between fibroblasts and macrophages.* Am J Physiol Gastrointest Liver Physiol, 2011. **300**(5): p. G723-8.

214. Hashimoto, S., et al., *IL-4 and IL-13 induce myofibroblastic phenotype of human lung fibroblasts through c-Jun NH2-terminal kinasedependent pathway.* Journal of Allergy and Clinical Immunology, 2001. **107**(6): p. 1001.

215. Cogswell, D.A. and W.C. Carter, *Thermodynamic phase-field model for microstructure with multiple components and phases: the possibility of metastable phases.* Phys Rev E Stat Nonlin Soft Matter Phys, 2011. **83**(6 Pt 1): p. 061602.

216. Strell, C. and F. Entschladen, *Extravasation of leukocytes in comparison to tumor cells.* Cell Commun Signal, 2008. **6**(1): p. 10.

217. Hampton, H.R. and T. Chtanova, *Lymphatic Migration of Immune Cells.* Front Immunol, 2019. **10**: p. 1168.

218. Luetke-Eversloh, M., M. Killig, and C. Romagnani, *Signatures of human NK cell development and terminal differentiation.* Front Immunol, 2013. **4**: p. 499.

219. Masson, F., et al., *Brain microenvironment promotes the final functional maturation of tumor-specific effector CD8+ T cells.* J Immunol, 2007. **179**(2): p. 845-53.

220. Thompson, E.D., et al., *Tumor masses support naive T cell infiltration, activation, and differentiation into effectors.* J Exp Med, 2010. **207**(8): p. 1791-804.

221. Ning-Bo, H., et al. *Macrophages in Tumor Microenvironments and the Progression of Tumors*. Journal of Immunology Research, 2012. **2012**, DOI: 10.1155/2012/948098.

222. Horikawa, M., et al., *Regulatory B cell production of IL-10 inhibits lymphoma depletion during CD20 immunotherapy in mice.* J Clin Invest, 2011. **121**(11): p. 4268-80.

223. Wennhold, K., A. Shimabukuro-Vornhagen, and M. von Bergwelt-Baildon, *B Cell-Based Cancer Immunotherapy.* Transfus Med Hemother, 2019. **46**(1): p. 36-46.

224. Jin, T., X. Xu, and D. Hereld, *Chemotaxis, chemokine receptors and human disease.* Cytokine, 2008. **44**(1): p. 1-8.

225. Harris, T.H., et al., *Generalized Levy walks and the role of chemokines in migration of effector CD8+ T cells.* Nature, 2012. **486**(7404): p. 545-8.

226. Xuan, W., et al., *The chemotaxis of M1 and M2 macrophages is regulated by different chemokines.* J Leukoc Biol, 2015. **97**(1): p. 61-9.

227. Galeano Nino, J.L., et al., *Cytotoxic T cells swarm by homotypic chemokine signalling.* Elife, 2020. **9**.

228. Loef, E.J., et al., *Live-Cell Microscopy Reveals That Human T Cells Primarily Respond Chemokinetically Within a CCL19 Gradient That Induces Chemotaxis in Dendritic Cells.* Front Immunol, 2021. **12**: p. 628090.

229. Biswas, S.K., P. Allavena, and A. Mantovani, *Tumor-associated macrophages: functional diversity, clinical significance, and open questions.* Semin Immunopathol, 2013. **35**(5): p. 585-600.

230. Schioppa, T., et al., *Regulation of the chemokine receptor CXCR4 by hypoxia.* J Exp Med, 2003. **198**(9): p. 1391-402.

231. Esmann, L., et al., *Phagocytosis of apoptotic cells by neutrophil granulocytes: diminished proinflammatory neutrophil functions in the presence of apoptotic cells.* J Immunol, 2010. **184**(1): p. 391-400.

232. Hellberg, L., et al., *Proinflammatory stimuli enhance phagocytosis of apoptotic cells by neutrophil granulocytes.* ScientificWorldJournal, 2011. **11**: p. 2230-6.

233. Vaught, D.B., J.C. Stanford, and R.S. Cook, *Efferocytosis creates a tumor microenvironment supportive of tumor survival and metastasis.* Cancer Cell Microenviron, 2015. **2**(1).

234. Lugano, R., M. Ramachandran, and A. Dimberg, *Tumor angiogenesis: causes, consequences, challenges and opportunities.* Cell Mol Life Sci, 2020. **77**(9): p. 1745-1770.

235. Hwang, I., et al., *Tumor-associated macrophage, angiogenesis and lymphangiogenesis markers predict prognosis of non-small cell lung cancer patients.* J Transl Med, 2020. **18**(1): p. 443.

236. Mantovani, A., et al., *Macrophage polarization: tumor-associated macrophages as a paradigm for polarized M2 mononuclear phagocytes.* Trends Immunol, 2002. **23**(11): p. 549-55.

237. Curtis, L.T., et al., *An interdisciplinary computational/experimental approach to evaluate drug-loaded gold nanoparticle tumor cytotoxicity.* Nanomedicine (Lond), 2016. **11**(3): p. 197-216.

238. Mollica Poeta, V., et al., *Chemokines and Chemokine Receptors: New Targets for Cancer Immunotherapy.* Front Immunol, 2019. **10**: p. 379.

239. Rashid, N.S., et al., *Breast cancer liver metastasis: current and future treatment approaches.* Clin Exp Metastasis, 2021. **38**(3): p. 263-277.

240. Guo, G., et al., *Immune cell concentrations among the primary tumor microenvironment in colorectal cancer patients predicted by clinicopathologic characteristics and blood indexes.* J Immunother Cancer, 2019. **7**(1): p. 179.

241. Tasnim, H., et al., *Quantitative Measurement of Naive T Cell Association With Dendritic Cells, FRCs, and Blood Vessels in Lymph Nodes.* Front Immunol, 2018. **9**: p. 1571.

242. Stankovic, B., et al., *Immune Cell Composition in Human Non-small Cell Lung Cancer.* Front Immunol, 2018. **9**: p. 3101.

243. Yang, L., et al., *Expansion of myeloid immune suppressor Gr+CD11b+ cells in tumor-bearing host directly promotes tumor angiogenesis.* Cancer Cell, 2004. **6**(4): p. 409-21.

244. Marvel, D. and D.I. Gabrilovich, *Myeloid-derived suppressor cells in the tumor microenvironment: expect the unexpected.* J Clin Invest, 2015. **125**(9): p. 3356-64.

245. Antonia, S.J., et al., *Durvalumab after Chemoradiotherapy in Stage III Non-Small-Cell Lung Cancer.* N Engl J Med, 2017. **377**(20): p. 1919-1929.

246. Han, J., et al., *Memory CD8(+) T cell responses to cancer.* Semin Immunol, 2020. **49**: p. 101435.

247. Knochelmann, H.M., et al., *When worlds collide: Th17 and Treg cells in cancer and autoimmunity.* Cell Mol Immunol, 2018. **15**(5): p. 458-469.

248. Revel, M., et al., *Complement System: Promoter or Suppressor of Cancer Progression?* Antibodies (Basel), 2020. **9**(4): p. 57.

249. Sharonov, G.V., et al., *B cells, plasma cells and antibody repertoires in the tumour microenvironment.* Nat Rev Immunol, 2020. **20**(5): p. 294-307.

250. Lecot, P., et al., *Neutrophil Heterogeneity in Cancer: From Biology to Therapies.* Front Immunol, 2019. **10**: p. 2155.

251. Murray, P.J., et al., *Macrophage activation and polarization: nomenclature and experimental guidelines.* Immunity, 2014. **41**(1): p. 14-20.
252. Weigert, A., et al., *Tumor cell apoptosis polarizes macrophages role of sphingosine-1-phosphate.* Mol Biol Cell, 2007. **18**(10): p. 3810-9.
253. Krzywinska, E. and C. Stockmann, *Hypoxia, Metabolism and Immune Cell Function.* Biomedicines, 2018. **6**(2): p. 56.
254. Lammermann, T. and R.N. Germain, *The multiple faces of leukocyte interstitial migration.* Semin Immunopathol, 2014. **36**(2): p. 227-51.
255. Subimerb, C., et al., *Circulating CD14(+) CD16(+) monocyte levels predict tissue invasive character of cholangiocarcinoma.* Clin Exp Immunol, 2010. **161**(3): p. 471-9.
256. Ziai, J., et al., *CD8+ T cell infiltration in breast and colon cancer: A histologic and statistical analysis.* PLoS One, 2018. **13**(1): p. e0190158.
257. Kapellos, T.S., et al., *Human Monocyte Subsets and Phenotypes in Major Chronic Inflammatory Diseases.* Front Immunol, 2019. **10**: p. 2035.
258. Ong, S.M., et al., *A Novel, Five-Marker Alternative to CD16-CD14 Gating to Identify the Three Human Monocyte Subsets.* Front Immunol, 2019. **10**: p. 1761.
259. Al-Hity, G., et al., *An integrated framework for quantifying immune-tumour interactions in a 3D co-culture model.* Commun Biol, 2021. **4**(1): p. 781.
260. Holl, E.K., et al., *Examining Peripheral and Tumor Cellular Immunome in Patients With Cancer.* Front Immunol, 2019. **10**: p. 1767.
261. Frieboes, H.B., et al., *An integrated computational/experimental model of tumor invasion.* Cancer Res, 2006. **66**(3): p. 1597-604.
262. Frieboes, H.B., et al., *Computer simulation of glioma growth and morphology.* Neuroimage, 2007. **37 Suppl 1**(Suppl 1): p. S59-70.
263. Bearer, E.L., et al., *Multiparameter computational modeling of tumor invasion.* Cancer Res, 2009. **69**(10): p. 4493-501.
264. Frieboes, H.B., et al., *Physical oncology: a bench-to-bedside quantitative and predictive approach.* Cancer Res, 2011. **71**(2): p. 298-302.
265. Frieboes, H.B., et al., *An integrated computational/experimental model of lymphoma growth.* PLoS Comput Biol, 2013. **9**(3): p. e1003008.
266. Boujelben, A., et al., *Multimodality imaging and mathematical modelling of drug delivery to glioblastomas.* Interface Focus, 2016. **6**(5): p. 20160039.
267. Painter, K.J. and T. Hillen, *Mathematical modelling of glioma growth: the use of Diffusion Tensor Imaging (DTI) data to predict the anisotropic pathways of cancer invasion.* J Theor Biol, 2013. **323**: p. 25-39.
268. Wishart, D.S., *Metabolomics for Investigating Physiological and Pathophysiological Processes.* Physiol Rev, 2019. **99**(4): p. 1819-1875.
269. Hanahan, D. and R.A. Weinberg, *Hallmarks of cancer: the next generation.* Cell, 2011. **144**(5): p. 646-74.
270. Miller, H.A., J. Lowengrub, and H.B. Frieboes, *Modeling of Tumor Growth with Input from Patient-Specific Metabolomic Data.* Ann Biomed Eng, 2022.
271. Everts, B., *Metabolomics in Immunology Research.* Methods Mol Biol, 2018. **1730**: p. 29-42.

272. van der Windt, G.J. and E.L. Pearce, *Metabolic switching and fuel choice during T-cell differentiation and memory development.* Immunol Rev, 2012. **249**(1): p. 27-42.

273. Le Bourgeois, T., et al., *Targeting T Cell Metabolism for Improvement of Cancer Immunotherapy.* Front Oncol, 2018. **8**: p. 237.

274. Van den Bossche, J., L.A. O'Neill, and D. Menon, *Macrophage Immunometabolism: Where Are We (Going)?* Trends Immunol, 2017. **38**(6): p. 395-406.

275. Zinser, J.W., et al., *Clinical course of breast cancer patients with liver metastases.* J Clin Oncol, 1987. **5**(5): p. 773-82.

276. Hoe, A.L., G.T. Royle, and I. Taylor, *Breast liver metastases--incidence, diagnosis and outcome.* J R Soc Med, 1991. **84**(12): p. 714-6.

277. Siegel, R.L., et al., *Cancer statistics, 2022.* CA Cancer J Clin, 2022. **72**(1): p. 7-33.

278. Oliveira, R.C., et al., *Liver Metastases and Histological Growth Patterns: Biological Behavior and Potential Clinical Implications-Another Path to Individualized Medicine?* J Oncol, 2019. **2019**: p. 6280347.

279. Horn, S.R., et al., *Epidemiology of liver metastases.* Cancer Epidemiol, 2020. **67**: p. 101760.

280. Tsilimigras, D.I., et al., *Liver metastases.* Nat Rev Dis Primers, 2021. **7**(1): p. 27.

281. Liu, L.X., *zhang WH, Jiang HC Current treatment for liver metastases from colorectal cancer.* World Journal of Gastroenterology, 2003. **9**: p. 193.

282. Elias, D., et al., *An attempt to clarify indications for hepatectomy for liver metastases from breast cancer.* Am J Surg, 2003. **185**(2): p. 158-64.

283. Sparreboom, A., et al., *Comparative preclinical and clinical pharmacokinetics of a cremophor-free, nanoparticle albumin-bound paclitaxel (ABI-007) and paclitaxel formulated in Cremophor (Taxol).* Clin Cancer Res, 2005. **11**(11): p. 4136-43.

284. Ferlay, J., et al., *Cancer incidence and mortality worldwide: sources, methods and major patterns in GLOBOCAN 2012.* Int J Cancer, 2015. **136**(5): p. E359-86.

285. Frentzas, S., et al., *Vessel co-option mediates resistance to anti-angiogenic therapy in liver metastases.* Nat Med, 2016. **22**(11): p. 1294-1302.

286. Van den Eynden, G.G., et al., *The multifaceted role of the microenvironment in liver metastasis: biology and clinical implications.* Cancer Res, 2013. **73**(7): p. 2031-43.

287. Jain, R.K., J.D. Martin, and T. Stylianopoulos, *The role of mechanical forces in tumor growth and therapy.* Annu Rev Biomed Eng, 2014. **16**(1): p. 321-46.

288. Byrd, B.K., et al., *The shape of breast cancer.* Breast Cancer Res Treat, 2020. **183**(2): p. 403-410.

289. Goodin, D.A. and H.B. Frieboes, *Evaluation of innate and adaptive immune system interactions in the tumor microenvironment via a 3D continuum model.* J Theor Biol, 2023. **559**: p. 111383.

290. Weaver, B.A., *How Taxol/paclitaxel kills cancer cells.* Mol Biol Cell, 2014. **25**(18): p. 2677-81.

291. Curtis, L.T. and H.B. Frieboes, *Modeling of Combination Chemotherapy and Immunotherapy for Lung Cancer.* Annu Int Conf IEEE Eng Med Biol Soc, 2019. **2019**: p. 273-276.

292. Rahib, L., et al., *Projecting cancer incidence and deaths to 2030: the unexpected burden of thyroid, liver, and pancreas cancers in the United States.* Cancer Res, 2014. **74**(11): p. 2913-21.

293. Quante, A.S., et al., *Projections of cancer incidence and cancer-related deaths in Germany by 2020 and 2030.* Cancer Med, 2016. **5**(9): p. 2649-56.

294. Azmi, A.S., *Molecular diagnostics and treatment of pancreatic cancer : systems and network biology approaches*. 2014, Elsevier/AP: Amsterdam.

295. Becker, A.E., et al., *Pancreatic ductal adenocarcinoma: risk factors, screening, and early detection.* World J Gastroenterol, 2014. **20**(32): p. 11182-98.

296. Park, W., A. Chawla, and E.M. O'Reilly, *Pancreatic Cancer: A Review.* JAMA, 2021. **326**(9): p. 851-862.

297. Watanabe, K., et al., *The "histological replacement growth pattern" represents aggressive invasive behavior in liver metastasis from pancreatic cancer.* Cancer Med, 2020. **9**(9): p. 3130-3141.

298. Nielsen, S.R., et al., *Macrophage-secreted granulin supports pancreatic cancer metastasis by inducing liver fibrosis.* Nat Cell Biol, 2016. **18**(5): p. 549-60.

299. Sahin, I.H., et al., *Immunotherapy in pancreatic ductal adenocarcinoma: an emerging entity?* Ann Oncol, 2017. **28**(12): p. 2950-2961.

300. Prima, V., et al., *COX2/mPGES1/PGE2 pathway regulates PD-L1 expression in tumor-associated macrophages and myeloid-derived suppressor cells.* Proc Natl Acad Sci U S A, 2017. **114**(5): p. 1117-1122.

301. Xiang, Z., et al., *Comprehensive Evaluation of Anti-PD-1, Anti-PD-L1, Anti-CTLA-4 and Their Combined Immunotherapy in Clinical Trials: A Systematic Review and Meta-analysis.* Front Pharmacol, 2022. **13**: p. 883655.

302. Gulhati, P., et al., *Targeting T cell checkpoints 41BB and LAG3 and myeloid cell CXCR1/CXCR2 results in antitumor immunity and durable response in pancreatic cancer.* Nat Cancer, 2023. **4**(1): p. 62-80.

303. Kim, D.K., et al., *PD-L1-directed PlGF/VEGF blockade synergizes with chemotherapy by targeting CD141(+) cancer-associated fibroblasts in pancreatic cancer.* Nat Commun, 2022. **13**(1): p. 6292.

304. Falcomata, C., et al., *Selective multi-kinase inhibition sensitizes mesenchymal pancreatic cancer to immune checkpoint blockade by remodeling the tumor microenvironment.* Nat Cancer, 2022. **3**(3): p. 318-336.

305. Qian, X., W. Hu, and J. Yan, *Nano-Chemotherapy synergize with immune checkpoint inhibitor- A better option?* Front Immunol, 2022. **13**: p. 963533.

306. Bockorny, B., et al., *Motixafortide and Pembrolizumab Combined to Nanoliposomal Irinotecan, Fluorouracil, and Folinic Acid in Metastatic Pancreatic Cancer: The COMBAT/KEYNOTE-202 Trial.* Clin Cancer Res, 2021. **27**(18): p. 5020-5027.

307. Walter, F., et al., *Chitosan nanoparticles as antigen vehicles to induce effective tumor specific T cell responses.* PLoS One, 2020. **15**(9): p. e0239369.

308. Goodin, D.A., et al., *Multiple breast cancer liver metastases response to macrophage-delivered nanotherapy evaluated via a 3D continuum model.* Immunology, 2023. **169**(2): p. 132-140.

309. Syed, M., et al., *Immune-checkpoint inhibitor therapy response evaluation using oncophysics-based mathematical models.* Wiley Interdiscip Rev Nanomed Nanobiotechnol, 2023. **15**(2): p. e1855.

310. Butner, J.D., et al., *Early prediction of clinical response to checkpoint inhibitor therapy in human solid tumors through mathematical modeling.* Elife, 2021. **10**.

311. Butner, J.D., et al., *A mathematical model for the quantification of a patient's sensitivity to checkpoint inhibitors and long-term tumour burden.* Nat Biomed Eng, 2021. **5**(4): p. 297-308.

312. Butner, J.D., et al., *Mathematical prediction of clinical outcomes in advanced cancer patients treated with checkpoint inhibitor immunotherapy.* Sci Adv, 2020. **6**(18): p. eaay6298.

313. Yamamoto, K.N., et al., *Computational modeling of pancreatic cancer patients receiving FOLFIRINOX and gemcitabine-based therapies identifies optimum intervention strategies.* PLoS One, 2019. **14**(4): p. e0215409.

314. Curtis, L.T., et al., *A Computational/Experimental Assessment of Antitumor Activity of Polymer Nanoassemblies for pH-Controlled Drug Delivery to Primary and Metastatic Tumors.* Pharm Res, 2016. **33**(10): p. 2552-64.

315. Rock, K.L. and H. Kono, *The inflammatory response to cell death.* Annu Rev Pathol, 2008. **3**(1): p. 99-126.

316. Roussot, N., F. Ghiringhelli, and C. Rebe, *Tumor Immunogenic Cell Death as a Mediator of Intratumor CD8 T-Cell Recruitment.* Cells, 2022. **11**(22): p. 3672.

317. Alsaab, H.O., et al., *PD-1 and PD-L1 Checkpoint Signaling Inhibition for Cancer Immunotherapy: Mechanism, Combinations, and Clinical Outcome.* Front Pharmacol, 2017. **8**: p. 561.

318. Macklin, P., et al., *Multiscale modelling and nonlinear simulation of vascular tumour growth.* J Math Biol, 2009. **58**(4-5): p. 765-98.

319. Kiryu, S., et al., *Prognostic value of immune factors in the tumor microenvironment of patients with pancreatic ductal adenocarcinoma.* BMC Cancer, 2021. **21**(1): p. 1197.

320. Zehn, D., S.Y. Lee, and M.J. Bevan, *Complete but curtailed T-cell response to very low-affinity antigen.* Nature, 2009. **458**(7235): p. 211-4.

321. Syed, Y.Y., *Durvalumab: First Global Approval.* Drugs, 2017. **77**(12): p. 1369-1376.

322. FDA. *HIGHLIGHTS OF PRESCRIBING INFORMATION IMFINZI.* 2020 [cited 2022; Available from: https://www.accessdata.fda.gov/drugsatfda_docs/label/2020/761069s018lbl.pdf.

323. Baverel, P.G., et al., *Population Pharmacokinetics of Durvalumab in Cancer Patients and Association With Longitudinal Biomarkers of Disease Status.* Clin Pharmacol Ther, 2018. **103**(4): p. 631-642.

324. Mahmoudi, T., et al., *Segmentation of pancreatic ductal adenocarcinoma (PDAC) and surrounding vessels in CT images using deep convolutional neural networks and texture descriptors.* Sci Rep, 2022. **12**(1): p. 3092.

325. Leppanen, J., et al., *Tenascin C, Fibronectin, and Tumor-Stroma Ratio in Pancreatic Ductal Adenocarcinoma.* Pancreas, 2019. **48**(1): p. 43-48.

326. Kurahara, H., et al., *Significance of M2-polarized tumor-associated macrophage in pancreatic cancer.* J Surg Res, 2011. **167**(2): p. e211-9.

327. Krombach, F., et al., *Cell size of alveolar macrophages: an interspecies comparison.* Environ Health Perspect, 1997. **105 Suppl 5**(Suppl 5): p. 1261-3.

328. Olive, K.P., et al., *Inhibition of Hedgehog signaling enhances delivery of chemotherapy in a mouse model of pancreatic cancer.* Science, 2009. **324**(5933): p. 1457-61.

329. De Boer, R.J., et al., *Recruitment times, proliferation, and apoptosis rates during the CD8(+) T-cell response to lymphocytic choriomeningitis virus.* J Virol, 2001. **75**(22): p. 10663-9.

330. Powell, T.J., et al., *CD8+ T cells responding to influenza infection reach and persist at higher numbers than CD4+ T cells independently of precursor frequency.* Clin Immunol, 2004. **113**(1): p. 89-100.

331. Elbanna, K.Y., H.J. Jang, and T.K. Kim, *Imaging diagnosis and staging of pancreatic ductal adenocarcinoma: a comprehensive review.* Insights Imaging, 2020. **11**(1): p. 58.

332. Danet, I.M., et al., *Liver metastases from pancreatic adenocarcinoma: MR imaging characteristics.* J Magn Reson Imaging, 2003. **18**(2): p. 181-8.

333. Dagenborg, V.J., et al., *Low Concordance Between T-Cell Densities in Matched Primary Tumors and Liver Metastases in Microsatellite Stable Colorectal Cancer.* Front Oncol, 2021. **11**: p. 671629.

334. Tapeinos, C., et al., *Evaluation of cell membrane-derived nanoparticles as therapeutic carriers for pancreatic ductal adenocarcinoma using an in vitro tumour stroma model.* J Control Release, 2023. **362**: p. 225-242.

335. Conroy, M. and J. Naidoo, *Immune-related adverse events and the balancing act of immunotherapy.* Nat Commun, 2022. **13**(1): p. 392.

336. Naidoo, J., et al., *Characterizing immune-mediated adverse events with durvalumab in patients with unresectable stage III NSCLC: A post-hoc analysis of the PACIFIC trial.* Lung Cancer, 2022. **166**: p. 84-93.

337. Cummings, M.C., et al., *Metastatic progression of breast cancer: insights from 50 years of autopsies.* J Pathol, 2014. **232**(1): p. 23-31.

338. Wen, Y., et al., *Hepatic macrophages in liver homeostasis and diseases-diversity, plasticity and therapeutic opportunities.* Cell Mol Immunol, 2021. **18**(1): p. 45-56.

339. Xiang, X., et al., *Targeting tumor-associated macrophages to synergize tumor immunotherapy.* Signal Transduct Target Ther, 2021. **6**(1): p. 75.

340. Burel, J.G., et al., *Circulating T cell-monocyte complexes are markers of immune perturbations.* Elife, 2019. **8**.

341. Xu, Z.J., et al., *The M2 macrophage marker CD206: a novel prognostic indicator for acute myeloid leukemia.* Oncoimmunology, 2020. **9**(1): p. 1683347.

342. Allison, E., et al., *Breast Cancer Survival Outcomes and Tumor-Associated Macrophage Markers: A Systematic Review and Meta-Analysis.* Oncol Ther, 2023. **11**(1): p. 27-48.

343. Jamiyan, T., et al., *CD68- and CD163-positive tumor-associated macrophages in triple negative cancer of the breast.* Virchows Arch, 2020. **477**(6): p. 767-775.

344. Chanmee, T., et al., *Tumor-associated macrophages as major players in the tumor microenvironment.* Cancers (Basel), 2014. **6**(3): p. 1670-90.

345. Liu, Z., et al., *TGF-beta1 secreted by M2 phenotype macrophages enhances the stemness and migration of glioma cells via the SMAD2/3 signalling pathway.* Int J Mol Med, 2018. **42**(6): p. 3395-3403.

346. Mantovani, A., et al., *Tumour-associated macrophages as treatment targets in oncology.* Nat Rev Clin Oncol, 2017. **14**(7): p. 399-416.

347. Williamson, T., N. Sultanpuram, and H. Sendi, *The role of liver microenvironment in hepatic metastasis.* Clin Transl Med, 2019. **8**(1): p. 21.

348. Bai, R., et al., *The hypoxia-driven crosstalk between tumor and tumor-associated macrophages: mechanisms and clinical treatment strategies.* Mol Cancer, 2022. **21**(1): p. 177.

349. Lee, J.W., et al., *Hypoxia signaling in human diseases and therapeutic targets.* Exp Mol Med, 2019. **51**(6): p. 1-13.

350. de Heer, E.C., M. Jalving, and A.L. Harris, *HIFs, angiogenesis, and metabolism: elusive enemies in breast cancer.* J Clin Invest, 2020. **130**(10): p. 5074-5087.

351. Aumailley, M. and B. Gayraud, *Structure and biological activity of the extracellular matrix.* J Mol Med (Berl), 1998. **76**(3-4): p. 253-65.

352. Muchlinska, A., et al., *Alpha-smooth muscle actin-positive cancer-associated fibroblasts secreting osteopontin promote growth of luminal breast cancer.* Cell Mol Biol Lett, 2022. **27**(1): p. 45.

353. Kalluri, R., *The biology and function of fibroblasts in cancer.* Nat Rev Cancer, 2016. **16**(9): p. 582-98.

354. Wang, J., R. Zohar, and C.A. McCulloch, *Multiple roles of alpha-smooth muscle actin in mechanotransduction.* Exp Cell Res, 2006. **312**(3): p. 205-14.

355. Yousef, E.M., et al., *MMP-9 expression varies according to molecular subtypes of breast cancer.* BMC Cancer, 2014. **14**(1): p. 609.

356. Augoff, K., et al., *MMP9: A Tough Target for Targeted Therapy for Cancer.* Cancers (Basel), 2022. **14**(7): p. 1847.

357. Kwon, M.J., *Matrix metalloproteinases as therapeutic targets in breast cancer.* Front Oncol, 2022. **12**: p. 1108695.

358. Zhang, A., et al., *The Role of Ki67 in Evaluating Neoadjuvant Endocrine Therapy of Hormone Receptor-Positive Breast Cancer.* Front Endocrinol (Lausanne), 2021. **12**: p. 687244.

359. Sugiura, R., R. Satoh, and T. Takasaki, *ERK: A Double-Edged Sword in Cancer. ERK-Dependent Apoptosis as a Potential Therapeutic Strategy for Cancer.* Cells, 2021. **10**(10).

360. Bartholomeusz, C., et al., *High ERK protein expression levels correlate with shorter survival in triple-negative breast cancer patients.* Oncologist, 2012. **17**(6): p. 766-74.

361. Schluter, A., et al., *CD31 and VEGF are prognostic biomarkers in early-stage, but not in late-stage, laryngeal squamous cell carcinoma.* BMC Cancer, 2018. **18**(1): p. 272.

362. Planes-Laine, G., et al., *PD-1/PD-L1 Targeting in Breast Cancer: The First Clinical Evidences Are Emerging. A Literature Review.* Cancers (Basel), 2019. **11**(7): p. 1033.

363. Sharpe, A.H. and K.E. Pauken, *The diverse functions of the PD1 inhibitory pathway.* Nat Rev Immunol, 2018. **18**(3): p. 153-167.

364. Zhang, H., et al., *Roles of tumor-associated macrophages in anti-PD-1/PD-L1 immunotherapy for solid cancers.* Mol Cancer, 2023. **22**(1): p. 58.

365. Li, M., et al., *Heterogeneity of PD-L1 expression in primary tumors and paired lymph node metastases of triple negative breast cancer.* BMC Cancer, 2018. **18**(1): p. 4.

366. Luckheeram, R.V., et al., *CD4(+)T cells: differentiation and functions.* Clin Dev Immunol, 2012. **2012**: p. 925135.

367. Van Acker, H.H., et al., *CD56 in the Immune System: More Than a Marker for Cytotoxicity?* Front Immunol, 2017. **8**: p. 892.

368. Marcelin, H.N., et al., *Circulating natural killer cells and their association with breast cancer and its clinico-pathological characteristics.* Ecancermedicalscience, 2023. **17**: p. 1567.

369. Verma, C., et al., *Natural killer (NK) cell profiles in blood and tumour in women with large and locally advanced breast cancer (LLABC) and their contribution to a pathological complete response (PCR) in the tumour following neoadjuvant chemotherapy (NAC): differential restoration of blood profiles by NAC and surgery.* J Transl Med, 2015. **13**: p. 180.

370. Mikulak, J., et al., *Hepatic Natural Killer Cells: Organ-Specific Sentinels of Liver Immune Homeostasis and Physiopathology.* Front Immunol, 2019. **10**: p. 946.

371. Barba, D., et al., *Breast cancer, screening and diagnostic tools: All you need to know.* Crit Rev Oncol Hematol, 2021. **157**: p. 103174.

372. Brown, J.Q., et al., *Optical assessment of tumor resection margins in the breast.* IEEE J Sel Top Quantum Electron, 2010. **16**(3): p. 530-544.

373. Padmanaban, V., et al., *E-cadherin is required for metastasis in multiple models of breast cancer.* Nature, 2019. **573**(7774): p. 439-444.

374. He, Y., et al., *Multi-perspective comparison of the immune microenvironment of primary colorectal cancer and liver metastases.* Journal of Translational Medicine, 2022. **20**(1).

375. Julious, S.A., *Sample size of 12 per group rule of thumb for a pilot study.* Pharm Stat., 2005. **4**: p. 287–291.

376. Berg, S., et al., *ilastik: interactive machine learning for (bio)image analysis.* Nat Methods, 2019. **16**(12): p. 1226-1232.

377. Stirling, D.R., et al., *CellProfiler 4: improvements in speed, utility and usability.* BMC Bioinformatics, 2021. **22**(1): p. 433.

378. Schapiro, D., et al., *histoCAT: analysis of cell phenotypes and interactions in multiplex image cytometry data.* Nat Methods, 2017. **14**(9): p. 873-876.

379. Hao, Y., et al., *Integrated analysis of multimodal single-cell data.* Cell, 2021. **184**(13): p. 3573-3587 e29.

380. Xu, Y., et al., *Patients with Lung Cancer of Different Racial Backgrounds Harbor Distinct Immune Cell Profiles.* Cancer Res Commun, 2022. **2**(8): p. 884-893.
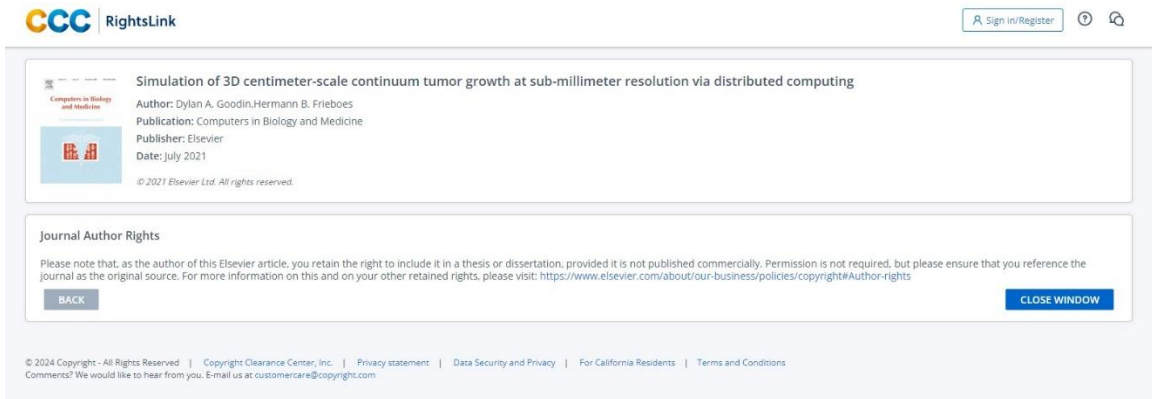
381. Chung, A.W., et al., *A phase 1/2 clinical trial of the nitric oxide synthase inhibitor L-NMMA and taxane for treating chemoresistant triple-negative breast cancer.* Sci Transl Med, 2021. **13**(624): p. eabj5070.

382. van den Berg, R.A., et al., *Centering, scaling, and transformations: improving the biological information content of metabolomics data.* BMC Genomics, 2006. **7**(1): p. 142.

383. Baxter, M.E., et al., *Metabolomic differentiation of tumor core versus edge in glioma.* Neurosurg Focus, 2023. **54**(6): p. E4.

384. Alakus, T.B. and I. Turkoglu, *Comparison of deep learning approaches to predict COVID-19 infection.* Chaos Solitons Fractals, 2020. **140**: p. 110120.

385. Iwendi, C., et al., *COVID-19 Patient Health Prediction Using Boosted Random Forest Algorithm.* Front Public Health, 2020. **8**: p. 357.

386. Miller, H.A., et al., *Lung cancer metabolomic data from tumor core biopsies enables risk-score calculation for progression-free and overall survival.* Metabolomics, 2022. **18**(5): p. 31.

387. Park, B.S. and J.O. Lee, *Recognition of lipopolysaccharide pattern by TLR4 complexes.* Exp Mol Med, 2013. **45**(12): p. e66.

388. Onofre, G., et al., *Scavenger receptor CD163 and its biological functions.* Acta Medica (Hradec Kralove), 2009. **52**(2): p. 57-61.

389. Geijtenbeek, T.B. and S.I. Gringhuis, *Signalling through C-type lectin receptors: shaping immune responses.* Nat Rev Immunol, 2009. **9**(7): p. 465-79.

390. Hussell, T. and T.J. Bell, *Alveolar macrophages: plasticity in a tissue-specific context.* Nat Rev Immunol, 2014. **14**(2): p. 81-93.

391. Li, Y., Y. Yin, and R.A. Mariuzza, *Structural and biophysical insights into the role of CD4 and CD8 in T cell activation.* Front Immunol, 2013. **4**: p. 206.

392. Zhang, J., et al., *Role of CD68 in tumor immunity and prognosis prediction in pan-cancer.* Sci Rep, 2022. **12**(1): p. 7844.

393. Zhang, N. and M.J. Bevan, *CD8(+) T cells: foot soldiers of the immune system.* Immunity, 2011. **35**(2): p. 161-8.

394. Mak, T.W. and M.E. Saunders, *T Cell Development*, in *The Immune Response*, T.W. Mak and M.E. Saunders, Editors. 2006, Academic Press: Burlington. p. 341-372.

395. Addison, E.G., et al., *Ligation of CD8alpha on human natural killer cells prevents activation-induced apoptosis and enhances cytolytic activity.* Immunology, 2005. **116**(3): p. 354-61.

396. Horne, H.N., et al., *E-cadherin breast tumor expression, risk factors and survival: Pooled analysis of 5,933 cases from 12 studies in the Breast Cancer Association Consortium.* Sci Rep, 2018. **8**(1): p. 6574.

397. Na, T.Y., et al., *The functional activity of E-cadherin controls tumor cell metastasis at multiple steps.* Proc Natl Acad Sci U S A, 2020. **117**(11): p. 5931-5937.

398. Sabatier, R., et al., *Prognostic and predictive value of PDL1 expression in breast cancer.* Oncotarget, 2015. **6**(7): p. 5449-64.

399. Gibbons Johnson, R.M. and H. Dong, *Functional Expression of Programmed Death-Ligand 1 (B7-H1) by Immune Cells and Tumor Cells.* Front Immunol, 2017. **8**: p. 961.

400. Keir, M.E., et al., *PD-1 and its ligands in tolerance and immunity.* Annu Rev Immunol, 2008. **26**(1): p. 677-704.

401. Boutilier, A.J. and S.F. Elsawa, *Macrophage Polarization States in the Tumor Microenvironment.* Int J Mol Sci, 2021. **22**(13): p. 6995.

402. Komohara, Y., M. Jinushi, and M. Takeya, *Clinical significance of macrophage heterogeneity in human malignant tumors.* Cancer Sci, 2014. **105**(1): p. 1-8.

403. Jayasingam, S.D., et al., *Evaluating the Polarization of Tumor-Associated Macrophages Into M1 and M2 Phenotypes in Human Cancer Tissue: Technicalities and Challenges in Routine Clinical Practice.* Front Oncol, 2019. **9**: p. 1512.

404. Mantovani, A., et al., *Innate immunity, inflammation and tumour progression: double-edged swords.* J Intern Med, 2019. **285**(5): p. 524-532.

405. Mantovani, A., et al., *Macrophages as tools and targets in cancer therapy.* Nat Rev Drug Discov, 2022. **21**(11): p. 799-820.

406. Chakravarthy, A., et al., *TGF-beta-associated extracellular matrix genes link cancer-associated fibroblasts to immune evasion and immunotherapy failure.* Nat Commun, 2018. **9**(1): p. 4692.

407. Suzuki, Y., et al., *Macrophage mannose receptor, CD206, predict prognosis in patients with pulmonary tuberculosis.* Sci Rep, 2018. **8**(1): p. 13129.

408. Yu, J., et al., *Liver metastasis restrains immunotherapy efficacy via macrophage-mediated T cell elimination.* Nat Med, 2021. **27**(1): p. 152-164.

409. Loibl, S., et al., *Neoadjuvant durvalumab improves survival in early triple-negative breast cancer independent of pathological complete response.* Ann Oncol, 2022. **33**(11): p. 1149-1158.

410. Wei, X.L., et al., *PD-L1 expression in liver metastasis: its clinical significance and discordance with primary tumor in colorectal cancer.* J Transl Med, 2020. **18**(1): p. 475.

411. Wang, Y. and B.P. Zhou, *Epithelial-mesenchymal transition in breast cancer progression and metastasis.* Chin J Cancer, 2011. **30**(9): p. 603-11.

412. Bendrik, C., et al., *Gene transfer of matrix metalloproteinase-9 induces tumor regression of breast cancer in vivo.* Cancer Res, 2008. **68**(9): p. 3405-12.

413. Leifler, K.S., et al., *Inflammation induced by MMP-9 enhances tumor regression of experimental breast cancer.* J Immunol, 2013. **190**(8): p. 4420-30.

414. Li, H.C., et al., *Prognostic value of matrix metalloproteinases (MMP-2 and MMP-9) in patients with lymph node-negative breast carcinoma.* Breast Cancer Res Treat, 2004. **88**(1): p. 75-85.

415. Mylona, E., et al., *The clinicopathological and prognostic significance of membrane type 1 matrix metalloproteinase (MT1-MMP) and MMP-9 according to their localization in invasive breast carcinoma.* Histopathology, 2007. **50**(3): p. 338-47.

416. Vizoso, F.J., et al., *Study of matrix metalloproteinases and their inhibitors in breast cancer.* Br J Cancer, 2007. **96**(6): p. 903-11.

417. Zhao, S., et al., *High expression of CD147 and MMP-9 is correlated with poor prognosis of triple-negative breast cancer (TNBC) patients.* Med Oncol, 2013. **30**(1): p. 335.

418. Joseph, C., et al., *Elevated MMP9 expression in breast cancer is a predictor of shorter patient survival.* Breast Cancer Res Treat, 2020. **182**(2): p. 267-282.
419. Juric, V., et al., *MMP-9 inhibition promotes anti-tumor immunity through disruption of biochemical and physical barriers to T-cell trafficking to tumors.* PLoS One, 2018. **13**(11): p. e0207255.
420. Lu, L., J. Barbi, and F. Pan, *The regulation of immune tolerance by FOXP3.* Nat Rev Immunol, 2017. **17**(11): p. 703-717.
421. Rheinlander, A., B. Schraven, and U. Bommhardt, *CD45 in human physiology and clinical medicine.* Immunol Lett, 2018. **196**: p. 22-32.
422. Collins, M., V. Ling, and B.M. Carreno, *The B7 family of immune-regulatory ligands.* Genome Biol, 2005. **6**(6): p. 223.
423. Suo, L., et al., *For diagnosis of liver masses, fine-needle aspiration versus needle core biopsy: which is better?* J Am Soc Cytopathol, 2018. **7**(1): p. 46-49.
424. Larkin, J.R., et al., *Metabolomic Biomarkers in Blood Samples Identify Cancers in a Mixed Population of Patients with Nonspecific Symptoms.* Clin Cancer Res, 2022. **28**(8): p. 1651-1661.
425. Miller, H.A., V.H. van Berkel, and H.B. Frieboes, *Lung cancer survival prediction and biomarker identification with an ensemble machine learning analysis of tumor core biopsy metabolomic data.* Metabolomics, 2022. **18**(8): p. 57.
426. Miller, H.A., J. Lowengrub, and H.B. Frieboes, *Modeling of Tumor Growth with Input from Patient-Specific Metabolomic Data.* Ann Biomed Eng, 2022. **50**(3): p. 314-329.
427. Singhal, K., et al., *Large language models encode clinical knowledge.* Nature, 2023. **620**(7972): p. 172-180.
428. Guo, Z., et al., *Diffusion models in bioinformatics and computational biology.* Nature Reviews Bioengineering, 2023. **2**(2): p. 136-154.
429. Marques, H.S., et al., *Relationship between Th17 immune response and cancer.* World J Clin Oncol, 2021. **12**(10): p. 845-867.

APPENDIX I: COPYRIGHT

This dissertation uses material in Chapters 2 through 4 with permission from published journal articles. Permission to use these articles is documented below:
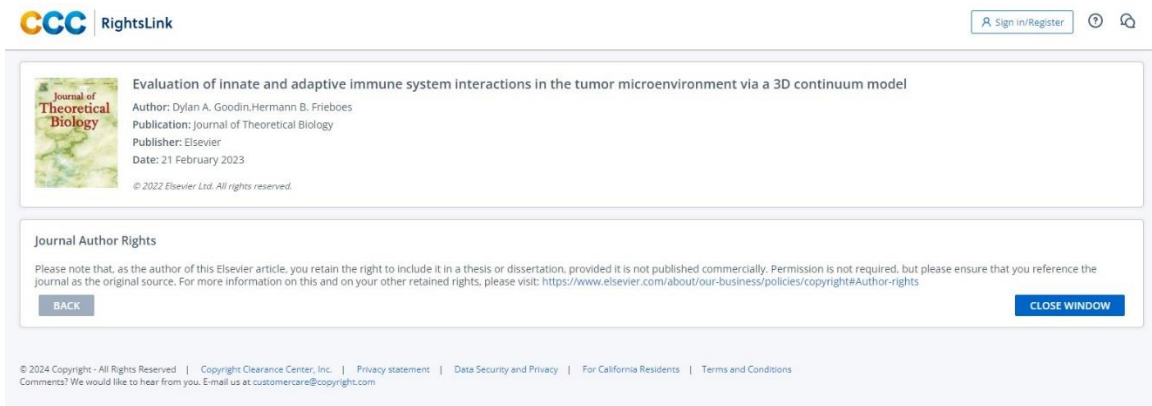
Multiple breast cancer liver metastases response to macrophage-delivered nanotherapy evaluated via a 3D continuum model

Author: Hermann B. Frieboes, Biana Godin, Anjana Tiwari, et al

Publication: Immunology

Publisher: John Wiley and Sons

Date: Dec 20, 2022

© 2022 John Wiley & Sons Ltd.

Order Completed

Your confirmation email will contain your order number for future reference.

🖨 Printable Details

License Number	5743680878688
License date	Mar 07, 2024

📄 Licensed Content

Licensed Content Publisher	John Wiley and Sons
Licensed Content Publication	Immunology
Licensed Content Title	Multiple breast cancer liver metastases response to macrophage-delivered nanotherapy evaluated via a 3D continuum model
Licensed Content Author	Hermann B. Frieboes, Biana Godin, Anjana Tiwari, et al
Licensed Content Date	Dec 20, 2022
Licensed Content Volume	169
Licensed Content Issue	2
Licensed Content Pages	9

📋 Order Details

Type of use	Dissertation/Thesis
Requestor type	Author of this Wiley article
Format	Print and electronic
Portion	Full article
Will you be translating?	No

CURRICULUM VITAE

Dylan A. Goodin

580 S Preston St. (Delia Baxter Research Building) Room 107, Louisville, KY 40202

Email: dagood05@louisville.edu

Profile

Hardworking and motivated Ph.D. candidate with background in mathematical modelling of cancer, immunotherapeutic evaluation, numerical methods, coding parallel processing, algorithm design, and machine learning. Specializes in synergistically combining computational, mathematical, and biological techniques to produce data-driven insights into human disease.

Research Interests

- Evaluation of immune species interactions, such as within the tumor microenvironment.
- Data-driven analysis of immune species prevalence and distribution in chronic conditions, such as in the tumor microenvironment.
- Analysis of and performance improvement of computational biological systems, such as tumor models.
- Application of predictive modelling approaches to outcome of immune species prevalence and activation status, such as in cancer.

Education

University of Louisville – Ph.D., Interdisciplinary Studies with Specialization in Translational Bioengineering
Anticipated Graduation date: May 2024
Louisville, KY

August 2019 – Present

University of Louisville - Graduate Certificate of AI in Medicine

August 2021

        o   Inaugural Recipient.

University of Louisville – Masters in Engineering
Louisville, KY

<div align="right">August 2018 – August 2019</div>

Thesis: Simulation of a continuum tumor model using distributed computing

University of Louisville – Bachelor of Science, Bioengineering
Louisville, KY

<div align="right">August 2014 – August 2018</div>

Research and Teaching Experience

Graduate Research Assistant, J.B. Speed School of Engineering, Department of Bioengineering

- Implemented a parallel processing framework to dramatically improve performance of a continuum mathematical model of tumor growth.
- Expanded model scope to include both innate and adaptive immune species.
- Tested and validated model performance on cluster computing.
- Evaluated tumor response to recently developed immunotherapeutic approaches.
- Trained machine learning models to multivariable clinical and imaging mass cytometry data.
- Designed and graded projects for an undergraduate student class on biosystems and signals.
- Mentored multiple high school, undergraduate, and masters-level students in student-specific research endeavors with the goal of producing publication-ready material.
- Oversaw day-to-day activities in the laboratory, ensuring safe and effective research was performed.

Frieboes Laboratory – University of Louisville

<div align="right">August 2018 – Present</div>

Undergraduate Research Assistant, J.B. Speed School of Engineering, Department of Bioengineering

- Performed discretization of a continuum model of tumor growth.
- Designed a parallel processing framework to improve performance of a continuum model of tumor growth.

Frieboes Laboratory – University of Louisville

<div align="right">August 2016 – August 2018</div>

Publications

- **Dylan A. Goodin**, Hermann B. Frieboes, Simulation of 3D centimeter-scale continuum tumor growth at sub-millimeter resolution via distributed computing, Computers in Biology and Medicine, Volume 134, 2021, 104507, ISSN 0010-4825, https://doi.org/10.1016/j.compbiomed.2021.104507.
- **Dylan A. Goodin**, Hermann B. Frieboes, Evaluation of innate and adaptive immune system interactions in the tumor microenvironment via a 3D continuum model, Journal of Theoretical Biology, Volume 559, 2023, 111383, ISSN 0022-5193, https://doi.org/10.1016/j.jtbi.2022.111383.
- **Goodin DA**, Chau E, Tiwari A, Godin B, Frieboes HB. Multiple breast cancer liver metastases response to macrophage-delivered nanotherapy evaluated via a 3D continuum model. Immunology. 2023 Jun;169(2):132-140. doi: 10.1111/imm.13615. Epub 2022 Dec 20. PMID: 36465031.
- Rai V, Kyser AJ, **Goodin DA**, Mahmoud MY, Steinbach-Rankins JM, Frieboes HB. Computational Modeling of Probiotic Recovery from 3D-Bioprinted Scaffolds for Localized Vaginal Application. Ann 3D Print Med. 2023 Aug;11:100120. doi: 10.1016/j.stlm.2023.100120. Epub 2023 Jul 4. PMID: 37583971; PMCID: PMC10424195.
- Mistry, A.M.; Daneshmand, J.; Seo, S.J.; Lehman, N.L.; Miller, D.M.; **Goodin, D.A.**; Frieboes, H.B.; Chen, J.; Masters, A.; Williams, B.J.; et al. Spatially Resolved Microglia/Macrophages in Recurrent Glioblastomas Overexpress Fatty Acid Metabolism and Phagocytic Genes. Curr. Oncol. 2024, 31, 1183-1194. https://doi.org/10.3390/curroncol31030088

Works in review or revision (* denotes co-authorship)

- Olivia S. Cooney*; **Dylan A Goodin***; Tyler J. Mouw, M.D.; Robert C.G. Martin, M.D., Ph.D. Hermann Frieboes, Ph.D. Intra-Abdominal Temperature Variation During Hyperthermic Intraperitoneal Chemotherapy Evaluated via Computational Fluid Dynamics Modeling. (In submission at *Annals of Biomedical Engineering*)
- Marianna Weaver*, **Dylan Goodin***, Hunter Miller, Dipan Karmali, Apur Agarwal, Hermann Frieboes, Sally Suliman. Prediction of Prolonged Mechanical Ventilation in the Intensive Care Unit via Machine Learning: a COVID-19 Perspective. (In submission at *Archivos de Bronconeumologia*)

Works in progress

- **Dylan A. Goodin**, Tina Daunke, Silje Beckinger, Sandra Krüger, Christoph Röcken, Susanne Sebens, Hermann B. Frieboes. Synergistic effect of anti-PDL1 and cytotoxic T-cell-activating nanotherapy in primary and liver metastatic pancreatic ductal adenocarcinoma evaluated via 3D mathematical modeling.
- **Dylan A. Goodin**, Eric Chau, Junjun Zheng, Cailin O'Connell, Anjana Tiwari, Yitian Xu, Shu-Hsia Chen, Biana Godin, Hermann B. Frieboes. Breast cancer liver metastasis microenvironment predicted via machine learning from clinically matched primary tumors.

Abstracts and Presentations

- **Dylan Goodin**, Hermann Frieboes. Improving the Performance of Multiscale Tissue Modeling Using a CUDA-Based Framework. (October 2019. Biomedical Engineering Society. Philadelphia, PA.)
- **Dylan A. Goodin**, Eric Chau, Anjana Tiwari, Biana Godin, Hermann B Frieboes. 3D Continuum Simulation of Nanotherapy Targeting Multiple Breast Cancer Liver Metastases. (October 2022. University of Kentucky Computational Commonwealth Summit).
- Anjana Tiwari, Eric Chau, Karem A. Court, Jenna Carr, **Dylan Goodin**, Hermann Frieboes, Biana Godin. Overcoming drug transport barriers in breast cancer liver metastasis by using macrophages as carriers: valuation in 2D and 3D models. (March 2023, SABCS 2023).
- **Dylan A. Goodin**, Hunter A. Miller, Brian Williams, Hermann B. Frieboes. Prediction of Glioblastoma Patient Survival using Tumor Core vs. Edge Metabolites. (October 2023. University of Kentucky Computational Commonwealth Summit).

Awards

- Jerry and Pat Sturgeon Academic Excellence Award, UofL Speed School Bioengineering Spring 2019 Award.
- Best Graduate Student Peer-Reviewed Journal Paper, UofL Speed School Bioengineering Spring 2022 Award.
- Best Graduate Student Peer-Reviewed Journal Paper, UofL Speed School Bioengineering Spring 2023 Award.
- 2nd Place Poster Presentation. Computational Commonwealth Summit, University of Kentucky. Fall 2023.
- Exemplary Doctoral Dissertation Award, UofL Speed School Bioengineering Spring 2024 Award.

Skills/Knowledge in Experimental Techniques

Metabolite extraction for mass spectrometry-based metabolomics studies
- Human lung and glioblastoma tissue biopsies.
- Human hair samples.

Skills/Knowledge in Mathematical Modeling and Programming

Mathematical Modelling
- Derivation of model equations
    - Immune species integration with three-dimensional diffuse-interface model of tumor growth.
    - Quantification of immune species interaction between immune species, tumor, extracellular matrix, and vasculature.

- o Quasi-steady state modelling.
- o T-cell exhaustion.
- o Immunotherapeutic application.
- o Drug delivery for bacterial vaginosis.
- o Numerical Methods/Solving
  - o Crank-Nicholson discretization.
  - o Geometric Multigrid.

Ansys
- o Modeled temperature fluid flow during Hyperthermic intraperitoneal chemotherapy using Fluent.
- o Conducted mesh and time step independence analyses.
- o Assisted in development of mesh-compatible abdominal structures.

MATLAB
- o Created generalized C/C++ code generator for solving model matrices.
- o Visualize 3D mathematical fields using isosurface generation.

C#
- o Post-processing of 3D model results to produce analysis-ready data.

C/C++ (Programming language)
- o Modelling and simulation of 3D tumor microenvironment
  - o Simulation of immunotherapies across multiple treatment strategies, including intravenous, macrophage-mediated, and extra-domain effects.
  - o Immune species interactions with tumor microenvironment, including innate (macrophages, natural killer cells, etc.) and adaptive (B-cells and T-cells).
  - o Exhaustion of T-cell species.
  - o Calibration of vasculature growth, immune species prevalence, tumor growth behavior, and tumor distribution using *in vitro* and *in vivo* data.

Message Passing Interface (MPI)
- o Developed and implemented a Multigrid solver across scores of threads.
  - o Synchronized data between CPU threads and Nvidia CUDA GPU calculations.

NVIDIA CUDA (GPU Acceleration of C/C++)
- o Developed and implemented Red-Black Gauss Seidel Relaxation and Multigrid prolongation and relaxation algorithms on Nvidia CUDA to increase model throughput.

Bash/Slurm
- o Job allocation of 30+ GPU resources and 60+ CPU resources in cluster environment.
- o Shell scripting for efficient and generalized utilization of cluster resources.

R Programming
- Analysis of clinical data and imaging mass cytometry data
  - Ongoing development and maintenance of machine learning workflow comprising custom code that interfaces with *caret* and *caretEnsemble* packages.
  - Imputation using the *mice* package.
  - Implemented metrics that quantify separation from principal component analysis and Partial Least Squares Discriminant Analysis score plots from *mdatools*.
  - Data visualization using *ggplot2*.
  - Statistical analyses, including propensity score matching (*matchit*, *cobalt*, *gtsummary*).
  - Survival analysis, including Kaplan Meier curves and Cox proportional hazards.